Savannah River
NUCLEAR SOLUTIONS™
FLUOR • NEWPORT NEWS NUCLEAR • HONEYWELL

K-TRT-G-00008, REV. 0

COMPREHENSIVE GEOCHARACTERIZATION OF THE SANTEE FORMATION AND ITS IMPLICATIONS FOR ENGINEERING BEHAVIOR

K-TRT-G-00008, Rev. 0

Comprehensive Geocharacterization of the Santee Formation and Its Implications for Engineering Behavior

Prepared By

6-22-15

Rucker J. Williams, *SRNS Design Engineering, Geotechnical Engineering*

Approved By

6-25-15

Ghada Elchoufi, *SRNS Design Engineering,*

TABLE OF CONTENTS

1. Summary

The Georgia Institute of Technology (Georgia Tech) was contracted by the Department of Energy (DOE) to understand better the formation and geologic evolution of the Santee Formation and to assess the impacts of the resulting physical and mechanical properties for engineering applications.

The work was performed under the DOE contract DE-FC09-08SR22631, Comprehensive Geocharacterization of the Santee Formation. The final report from this contract is attached as Appendix A.

Appendix A – Georgia Tech Final Report

(275 pages including this page)

COMPREHENSIVE GEOCHARACTERIZATION OF THE SANTEE FORMATION AND ITS IMPLICATIONS FOR ENGINEERING BEHAVIOR

Susan E. Burns, Paul W. Mayne, J. Carlos Santamarina

January 8, 2014

TABLE OF CONTENTS

TABLE OF FIGURES

EXECUTIVE SUMMARY

In this work, a series of geotechnical studies were undertaken to better quantify how and why the soil and rock formations within the Santee formed and dissolutioned, to detail the properties and behavior of the Santee formation materials, and to assess how those geologic processes affected and/or altered the conditions of the overlying soil column of interbedded sands and clays above it. The research program involved an integrated approach of experimental, analytical, and numerical components in order to consider a comprehensive understanding of the situation. The investigation: (1) performed a comprehensive assessment of the historical literature and data collected to date from the site, (2) identified unknowns, uncertainties, and/or gaps in the basic laboratory and field data, (3) performed additional lab and field investigations to quantify unknown properties and to give insight into the behavior of the formation materials, and (4) performed numerical and analytical modeling of the proposed design solutions.

The SRS is underlain by complex geologic formations, which have undergone significant transformations since their deposition some 30 million years ago. Most strikingly, a lower unit termed the Santee/Tinker formation (which in many cases includes Utley limestone as well) has developed an apparent random assortment of soft zones, voids, and cave features from processes related to diagenesis, dissolutioning, and cementation. Within the large scale excavation at Plant Vogtle, the soft zones, voids, and caves were observed in seven different manifestations, including:

- Soft zone of soil surrounded by stiffer soil matrix
- Soft zone forming through dissolution of Santee or Utley limestone
- Soft zone existing within Santee or weathered Utley limestone

- Soft zone formed in Santee weathered Utley and roofed by Utley limestone
- Soft zone formed in weathered Utley and roofed by Griffin's Landing and Irwinton Sand (verge of collapse)
- Collapsed soft zone with Griffin's Landing and Irwinton Sand infill
- Soft zone formed in Utley limestone

Some of these soft zones/caves exist today, but could collapse under unfavorable conditions, while in other cases, the soft zones/caves have already collapsed. In the latter case, the overlying soil column experienced a massive subsidence that may have affected the geostatic stress state and associated profile of soil parameters. Since recent excavations for the nearby Plant Vogtle uncovered and verified the presence of small- to medium- to very large-cavernous features (both water-filled and sediment-filled) in similar and related geologic units, the potential for such anomalous occurrences cannot be ruled out for the adjacent SRS terrain.

Site exploration for new and existing facilities at SRS should consist of a balance of geophysical, in-situ field-testing, and laboratory methods for careful and considerate geotechnical characterization. Future explorations should continue a series of CPT soundings to appropriate depths to fully penetrate the Santee/Tinker and sampling in boreholes made using either rotary, hydraulic push, and/or sonic methods to define the presence, extent, size, and type of the Santee soft zones/voids. In cases where early refusal are met by CPT, the sounding should continue using a drill-out of the caprock or specialized CPT method (i.e., ROTAP, EAPS).

As part of standard analyses and design, soft zone analyses must be conducted on a case-by-case basis, taking into consideration the local conditions at the site, including stratigraphy and material properties. If soft zones or voids are detected beneath cemented caprocks, analyses must include:

Step 1: simulations of cavity volume contraction without cohesive strength in the caprock as an upper bound safe scenario.

Step 2: assessment of caprock stability in case that excessive displacements are computed from the first step.

Details on methods, procedures, results and comprehensive reference lists are presented in:

Cha, M. (2012), Mineral dissolution in sediments, Ph.D. thesis, 152 pp, Georgia Institute of Technology, Atlanta, GA.

Chong, S.H. (2014). Details on methods, procedures, results and a comprehensive reference list will be presented in the thesis by Song Hun Chong (in preparation).

Ku, T. (2012), Geostatic stress state evaluation by directional shear wave velocities, with application towards geocharacterization at Aiken, SC, Georgia Institute of Technology, Atlanta, GA.

Larrahondo, J.M. (2011), Carbonate diagenesis and chemical weathering in the Southeastern United States: some implications on geotechnical behavior, Georgia Institute of Technology, Atlanta, GA.

Results will be updated in publications – Refer to http://pmrl.ce.gatech.edu/RandP.html

1. Background

1.1 Soft Zone Occurrence and Implications

The Savannah River Site (SRS) is a US government facility operated by the Department of Energy (DOE) located near Aiken, South Carolina, about 25 miles southeast from the city of Augusta, GA, on the South Carolina side of the Savannah River. The complex is comprised of 803 km^2 of terrain that is located in west central South Carolina and borders Georgia (Figure 1). The SRS consists of 30 separate facilities related to the development of nuclear materials processing and storage.

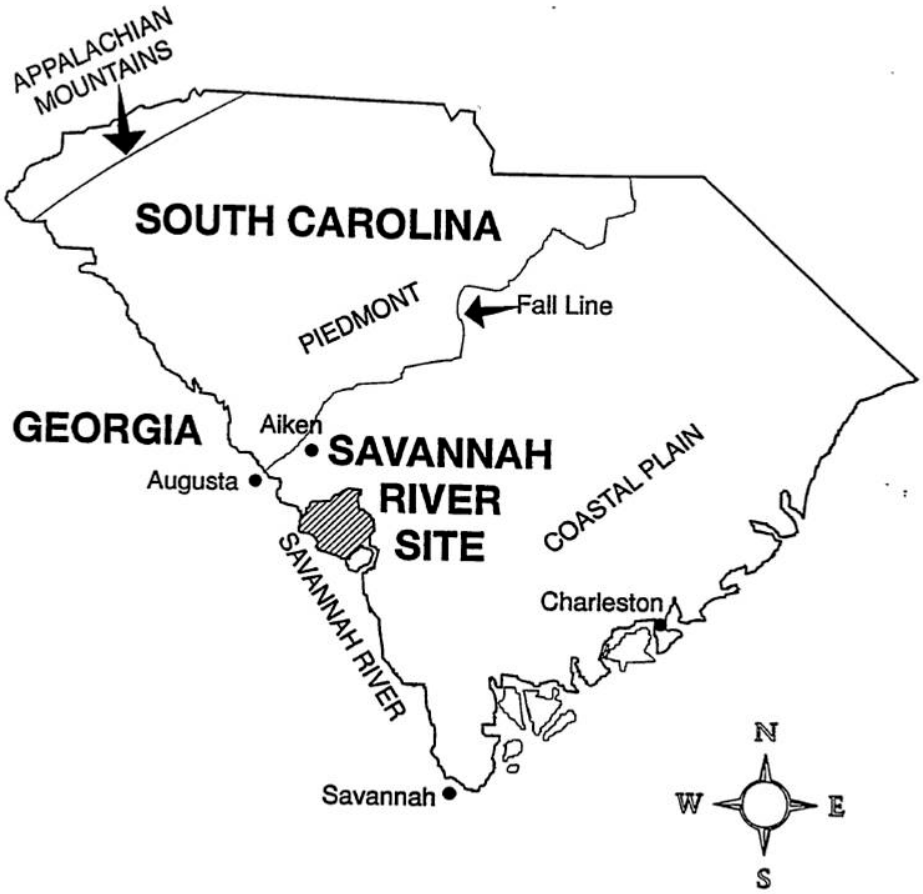

Figure 1-1. Location of Savannah River Site, South Carolina (Cumbest et al. 1996).

Since the initial development of SRS after World War II, it has been documented that the geologic soil column has unusual characteristics, particularly the presence of voids, caves, and/or soft zones at depths of about 30 to 45 m. The presence of the voids is of concern because of the potential effects of collapse on near-surface critical facilities. Additionally, SRS is located only 215 km from Charleston SC, where a large $M_w = 7.3$ earthquake occurred in 1886.

At the initiation of this investigation, the soft zones were envisioned as volumes of high water content, loose deposits of sands mixed with fines. The concept of cavities existing at depth, filled or partially filled, was not considered a likely alternative; however, the Vogtle excavation revealed multiple manifestations of geologic formations that were not previously considered under the simplified model of “soft zones”. In the Utley limestone encountered at nearby Plant Vogtle, Georgia, the soft zone-void-cave features were observed to range in size from 0.3 m to over 30 m in width and 0.5 to 2 m in height and may occur with or without a thick, hard shell-like enclosure that was embedded in the soil matrix. During the course of this investigation, seven scenarios were identified as possible configurations for the soft zones and their development (note all images taken by either Syms / Glidden, or Larrahondo):

- Soft zone of soil surrounded by stiffer soil matrix (no image)
- Soft zone forming through dissolution of Santee or Utley limestone (Figure 1-2)
- Soft zone existing within Santee or weathered Utley limestone (Figure 1-3)
- Soft zone formed in Santee weathered Utley and roofed by Utley limestone (Figure 1-4)
- Soft zone formed in weathered Utley and roofed by Griffin’s Landing and Irwinton Sand (verge of collapse) (Figure 1-5)
- Collapsed soft zone with Griffin’s Landing and Irwinton Sand infill (Figure 1-6)

- Soft zone formed in Utley limestone (Figure 1-7)

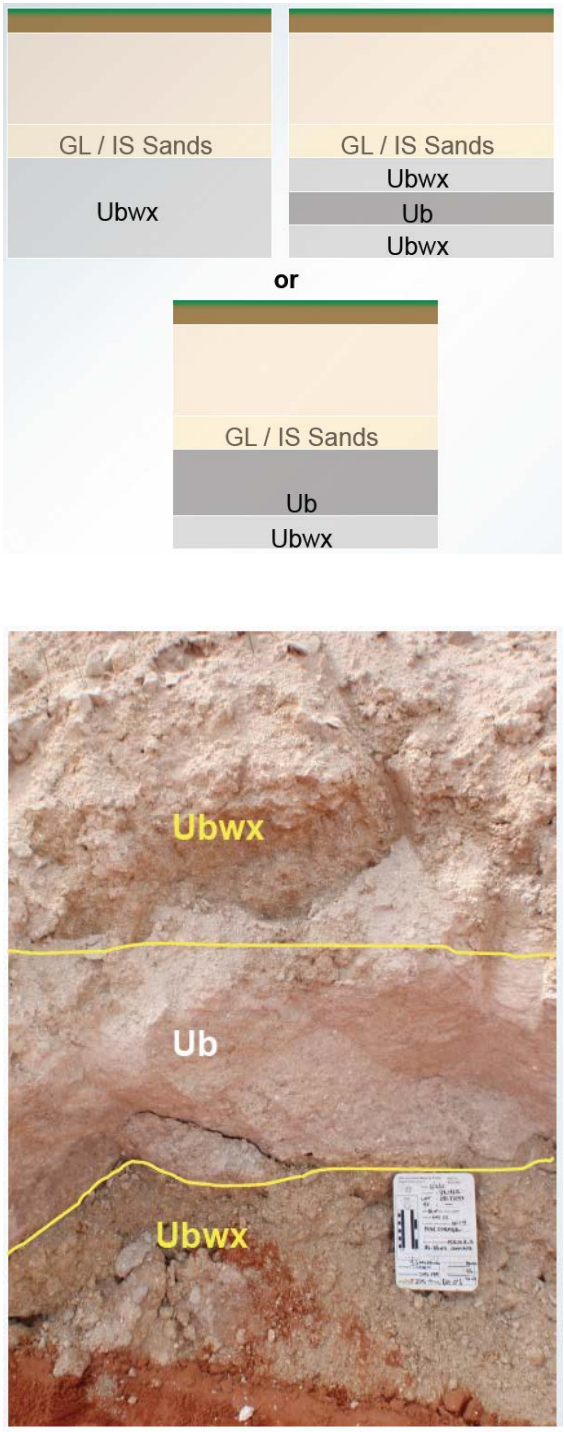

Figure 1-2. Prevoid formation: soil diagenesis before cavity formation.

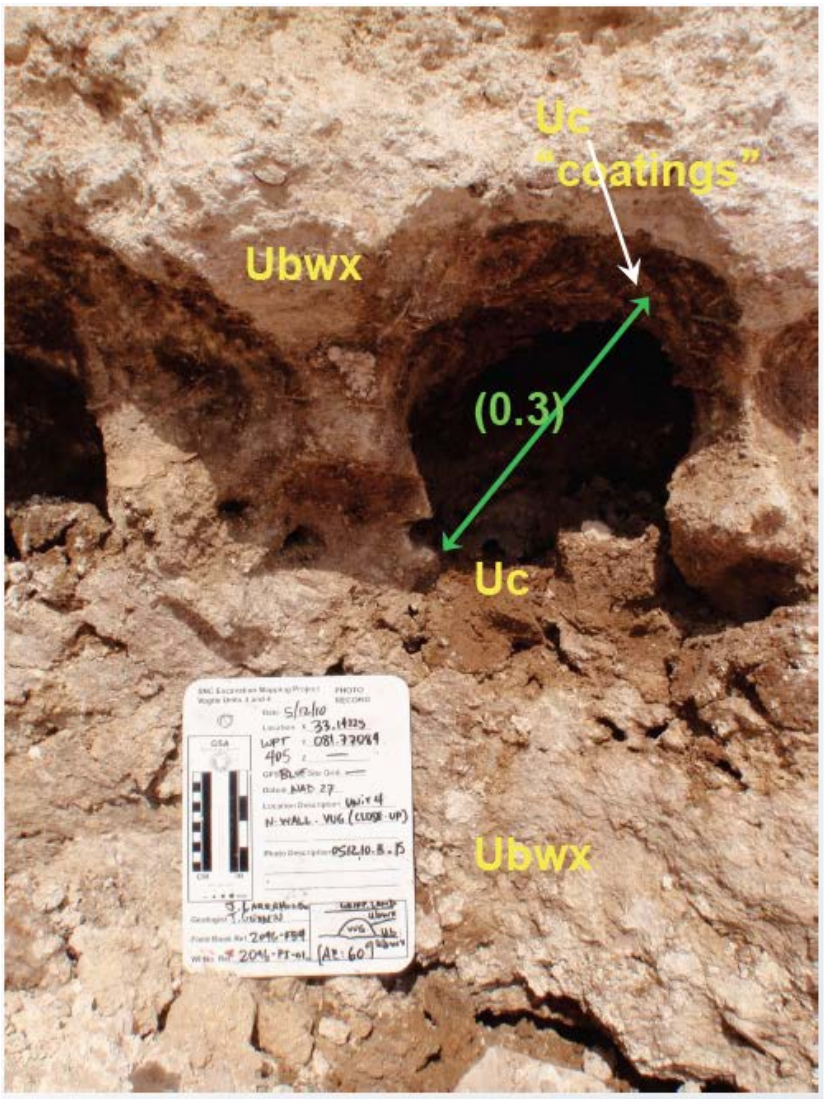

Figure 1-3. Void formation in weathered Utley (Ubwx).

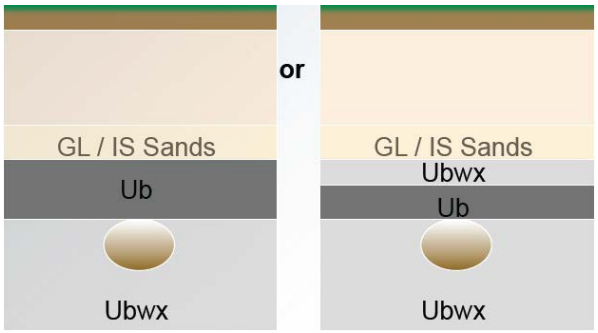

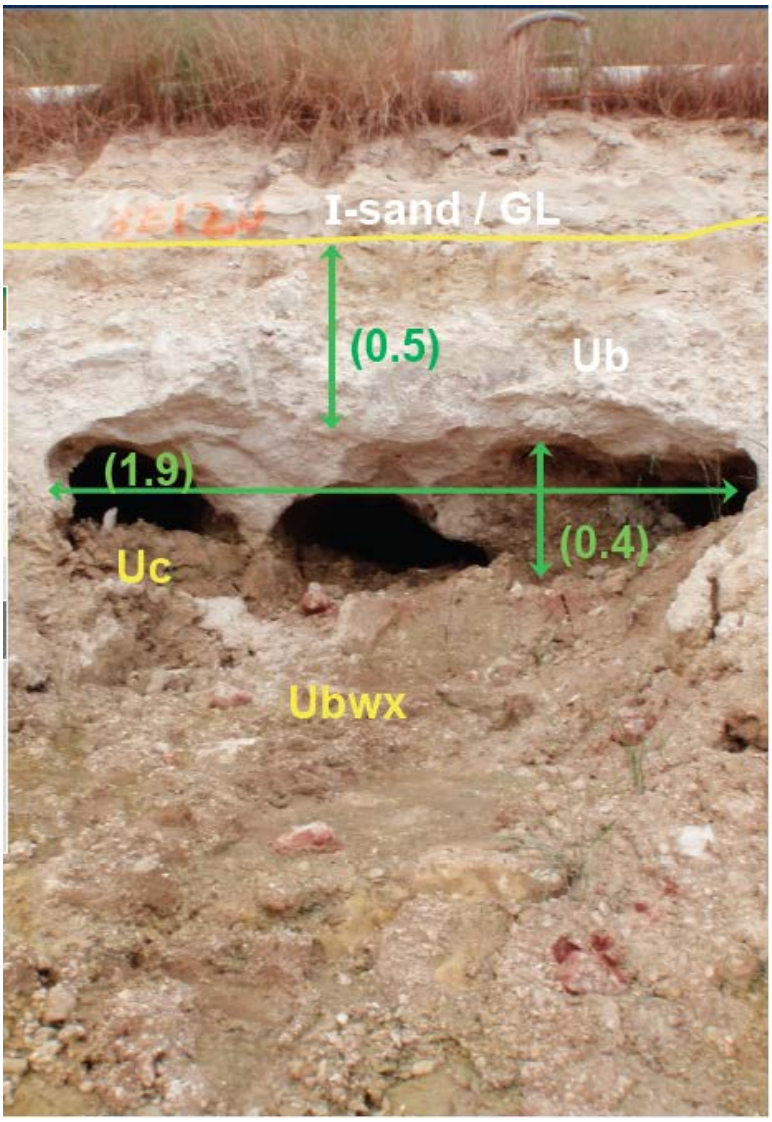

Figure 1-4. Void formation in weathered Utley (Ubwx), roofed by intact Utley (Ub).

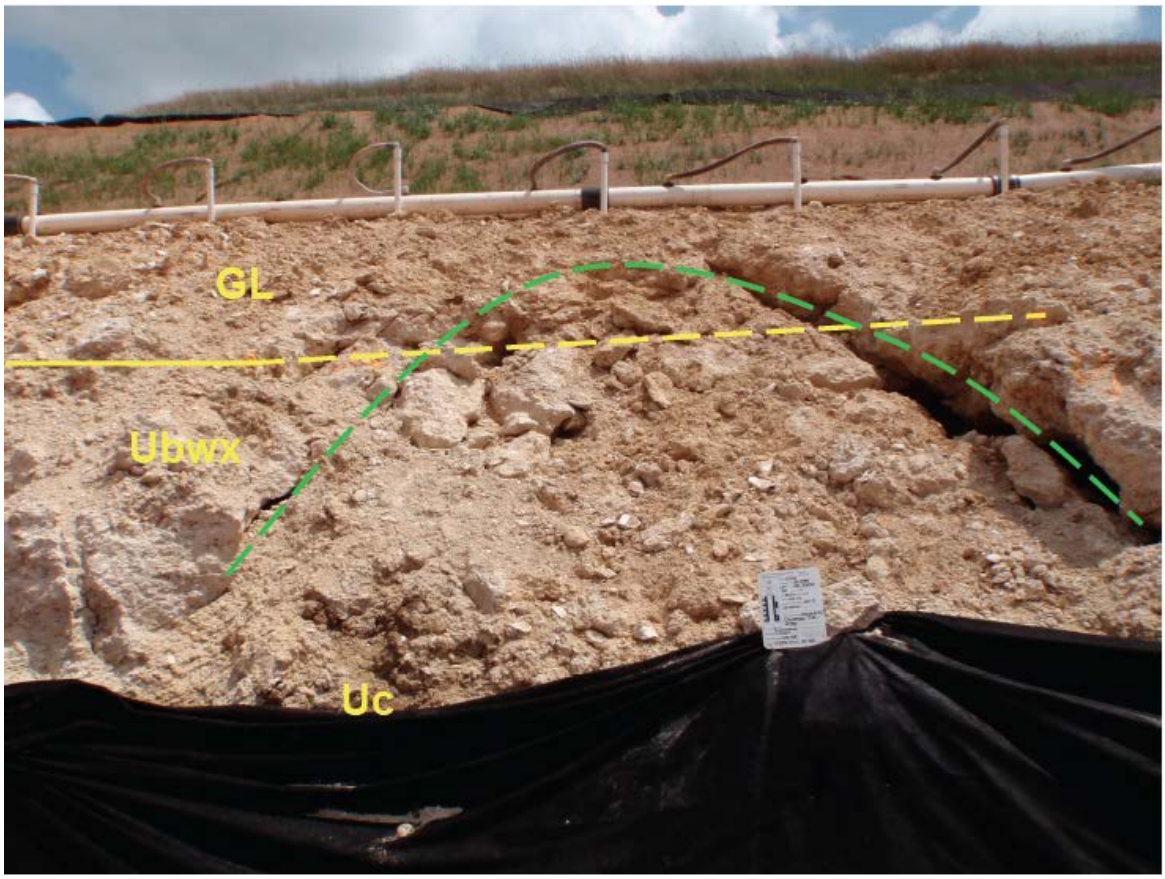

Figure 1-5. Void in weathered Utley (Ubwx) roofed by Griffin's Landing or Irwinton Sand with imminent or partial collapse.

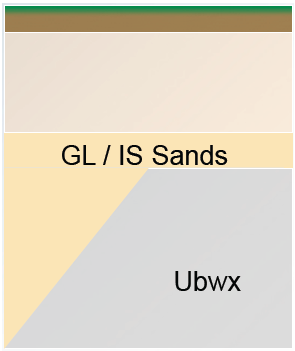

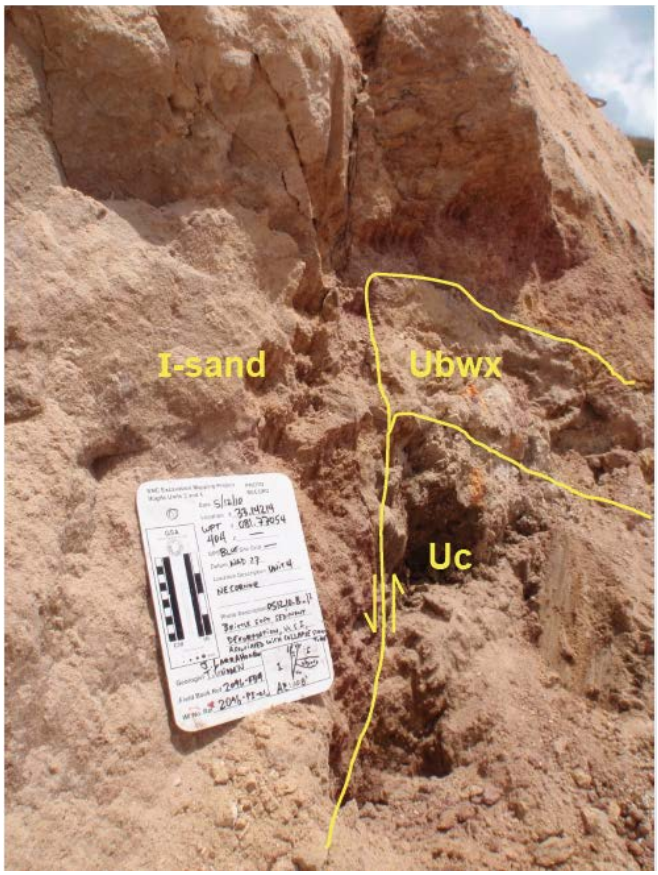

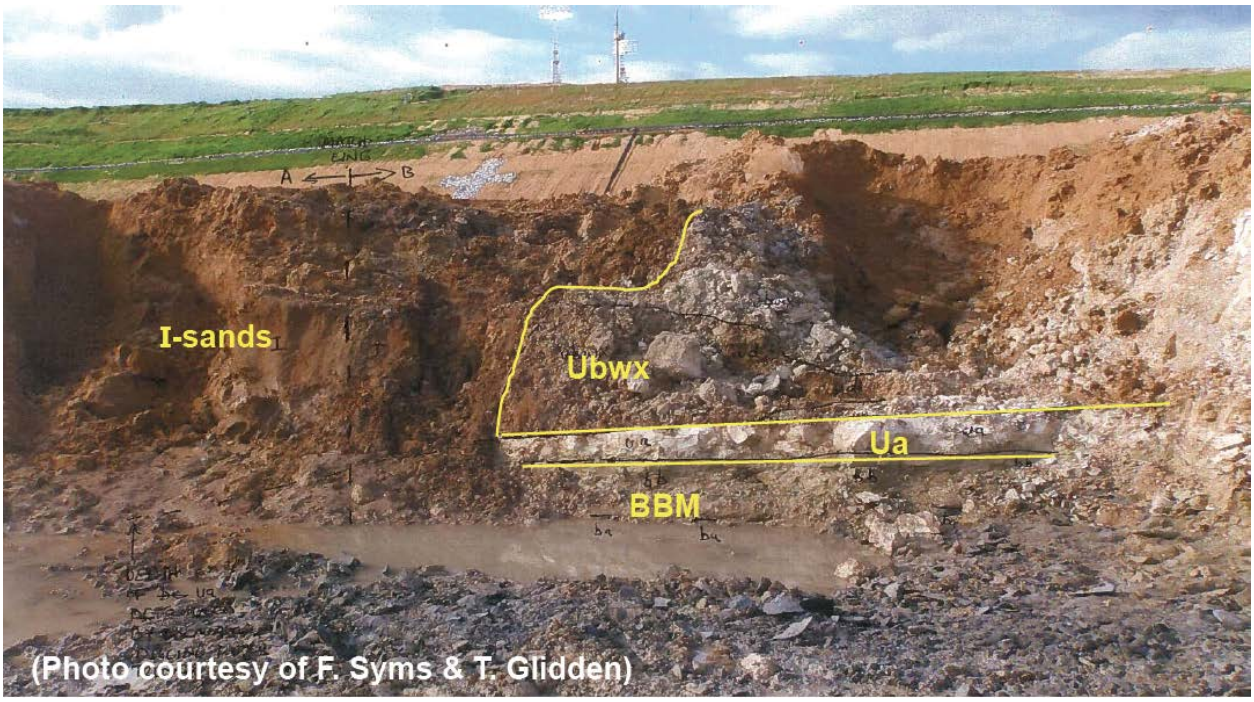

Figure 1-6. Collapsed void with Irwinton sand infill.

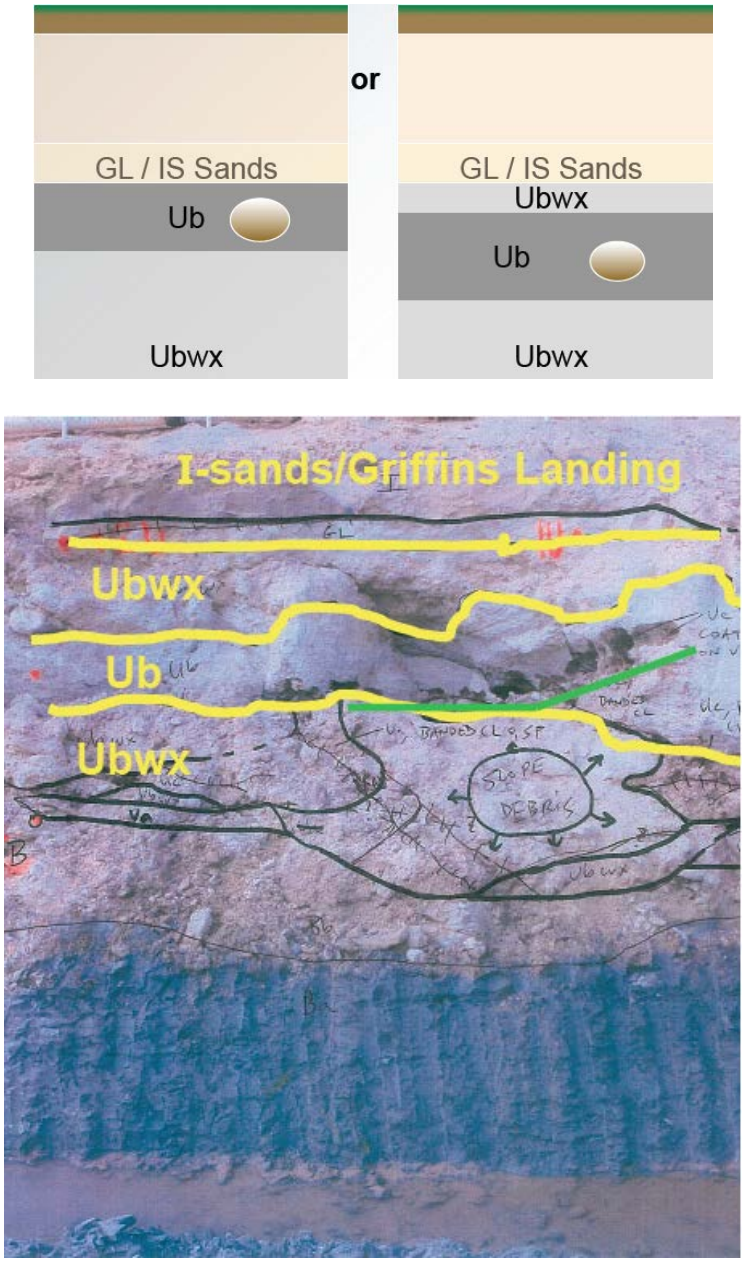

Figure 1-7. Void formation with in nonweathered Utley (Ub).

The impact of the presence and formation of the cavities on the engineering behavior of the soils at the site will be discussed in further detail throughout the report.

1.2 Program Objectives

At the initiation of the project, the objectives of this research program were to (1) perform a comprehensive assessment of the historical literature and data collected to date relevant to the formation, development, and performance of the soft zones at the Savannah River Site (SRS), (2) identify unknowns, uncertainties, and/or gaps in the basic laboratory and field data (if any), (3) conduct additional needed laboratory and field investigations, and (4) perform numerical and analytical modeling of the settlement induced by reduction of soft zone size, as well as a case study from the SRS. As the investigation progressed, an additional objective was added, which included the location, identification, and characterization of the soft zones within the Santee formation.

2. Geologic Setting

2.1 Regional Geology

The SRS lies within the Atlantic Coastal Plain geologic province. At SRS, the exposed overburden soils in the upper 60 m depths consist of very old Eocene sediments, primarily marine deposits of sands, clayey sands, and silty sands, with interbedded clay strata which exhibit a variable and complicated constituency and stress history profile. Within South Carolina, these sediments thicken in a southeasterly direction, as illustrated by Figure 2.

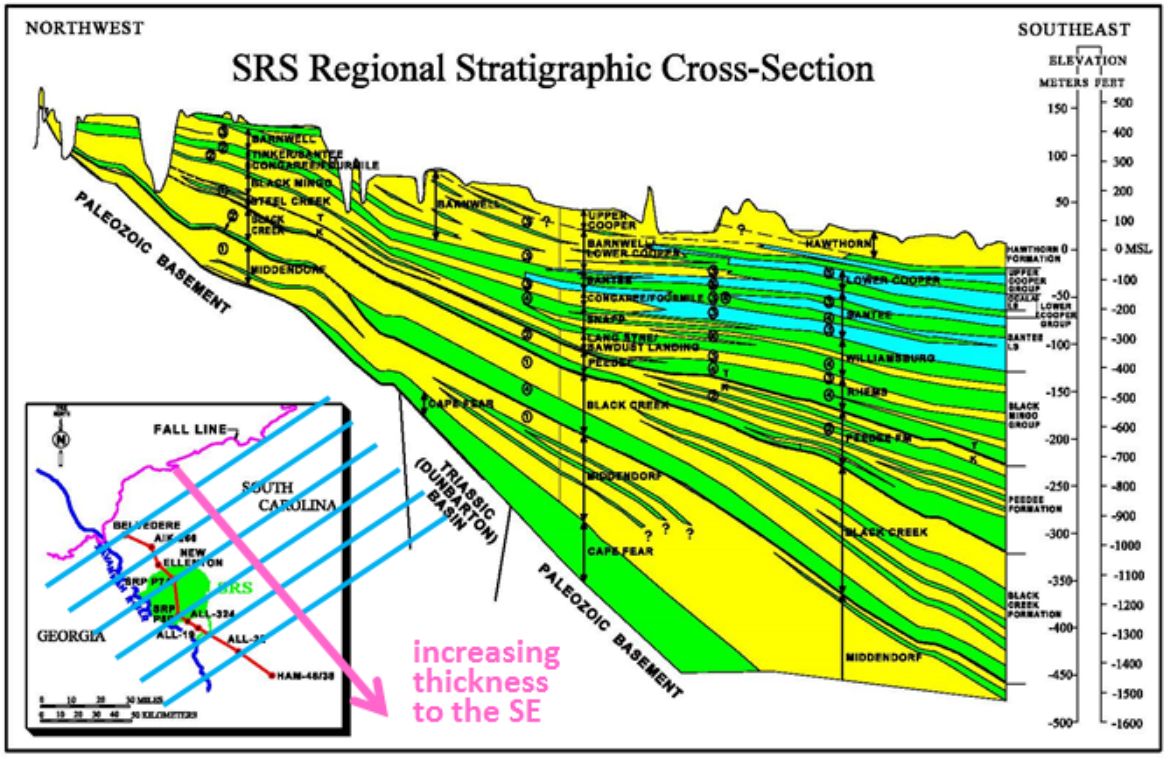

Figure 2-1. Regional stratigraphic cross-section at SRS (Washington Savannah River Co. 2007).

2.2 Depositional and Diagenetic History

Numerous studies have described the SRS litho- and bio-stratigraphy (Fallaw and Price, 1995; Harris et al., 1997; Powell, 1984; Rine and Engelhardt, 1999; Thayer et al., 1994; WSRC,

1999; Wyatt and Harris, 2004). The materials of most interest for this work are located in the Middle Eocene group and are approximately 39 million years old (Haq et al., 1987; Harris et al., 1997), particularly the Santee Formation and the Utley Limestone Member. These materials lie unconformably between approximately 30 and 45 m of depth. The Santee Formation is a predominately calcareous deposit of skeletal marine origin consisting of slightly to moderately indurated calcarenite, calcilutite, and sandy to muddy limestone, with some carbonate mineral replacement by silica (Fallaw and Price, 1995; Harris et al., 1997). The Santee Formation, as well as the Warley Hill and Congaree Formations, represent distinct depositional sequences consisting of transgressive and highstand seawater periods (Wyatt and Harris, 2004). The Santee Limestone represents the third advance to the NW of a transgressive carbonate mineral platform that first developed in early Paleocene time near the coast of South Carolina and Georgia. The Utley Limestone Member has been documented to belong to the Middle Eocene as well as to the "Late Eocene" epoch (Syms and Glidden, 2011). The Utley Limestone Member is a lightly to highly cemented and indurated skeletal limestone that has been interpreted at times as the carbonate mineral sequence of the Clinchfield Formation (Wyatt and Harris, 2004). Correlation between the stratigraphy at the SRS and the Plant Vogtle Site is given in Figure 2-2. Figure 2-3 shows the elevation correlation between the Investigation Site and the SRS. Due to the complex depositional history, the depths of the formations across the site are variable, and will be cited more specifically at selected locations across SRS in the following sections.

Savannah River Site

Age	*Unit*		
Eocene	Barnwell Group	Tobacco Rd Fm	
		Dry Branch Fm	Irwinton Sand Mbr
			Twiggs Clay Mbr
			Griffings Landing Mbr
		Santee Limestone	Timms Branch Mbr
	Orangeburg Group		McBean Mbr
			Blue Bluff Mbr
		Warley Hill Fm	
		Congaree Fm	

Plant Vogtle Site

Age		*Unit*			
Eocene	Late	Barnwell Group	Tobacco Rd Sand		Ocmulgee Fm	Crystal River Fm
			Dry Branch Fm.	Irwinton Sand Mbr / Twiggs clay Mbr	Griffins Ldg Mbr / Twiggs Clay Mbr	Williston Fm
			Clinchfield Fm / **Utley Limestone Member**			
	Middle	Lisbon Fm	McBean Limestone Mbr	Blue Bluff Mbr		Unnamed limestone
			Unnamed sands & limestone			

Figure 2-2. General stratigraphic equivalence between the SRS (left) and the investigation site (right), courtesy of Dr. F. Syms.

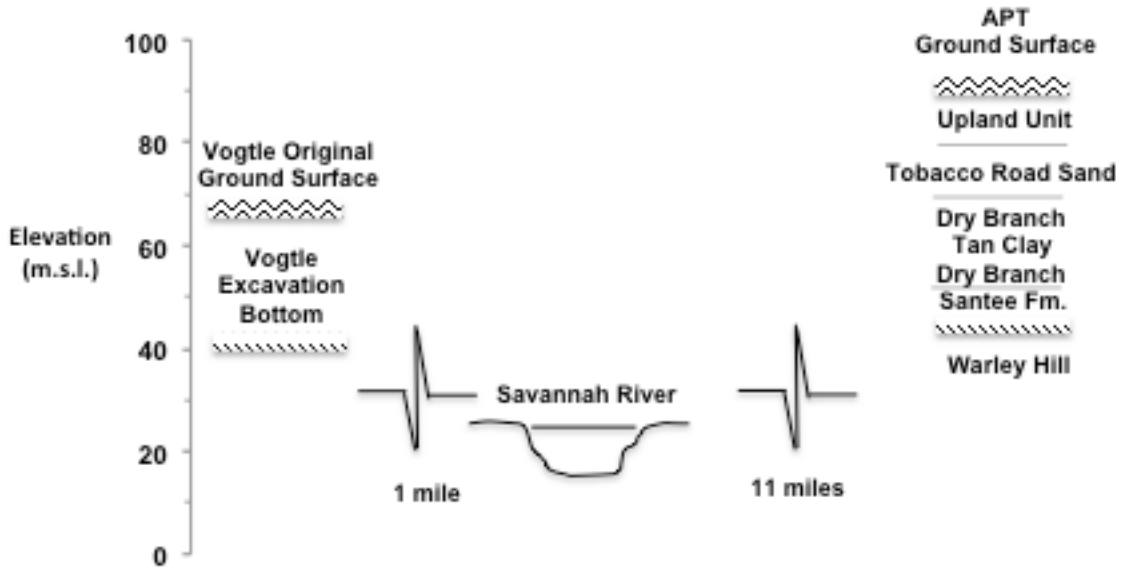

Figure 2-3. Elevation correlation: the Investigation Site vs. SRS.

The Middle Eocene sediments underlying the SRS are largely calcareous. These sediments are known to vary in overall thickness from as little as 2 m updip (i.e., toward the NW region of the Site) to 95 m downdip (i.e., the SE region) (Harris et al., 1997). The calcareous strata thin consistently in the NW direction at approximately 1.1 m/km. Field investigation has demonstrated that in the central portion of the SRS, the Santee is only sporadic and in fact, in the extreme NW region of SRS, calcareous sediments are virtually absent.

Deposition of carbonate, clastic, and mixed carbonate-clastic sediments during the Eocene resulted in a complex distribution of carbonate sequences across the SRS. In general, the paleo-shoreline resulted in primarily clastic sediments in the north-west portion of the site (roughly north and east of Upper Three Runs creek) with carbonates thickening to the south-east following the general dip of the coastal plain. The paleo-shoreline roughly parallels the fall-line (striking north-east) which marks the contact between basement (Piedmont province) and the

Coastal Plain sedimentary wedge. Thus facility locations (existing or proposed) respective to potential proximity to carbonate units in the subsurface can be determined from geographic location. For instance, the A/M-Area, which lies in the northern part of the SRS, has very little to no carbonate in the subsurface Coastal Plain sediments. The General Separations Area (GSA) lies in the approximate center of the SRS and during the middle Eocene was near the paleo-shoreline where fluctuations in sea levels resulted in depositional settings of both carbonate and mixed carbonated clastic deposition (sea level transgressions) as well as erosional events (sea level regressions). K-Area and P-Area are geographically located further south-east of the GSA and the carbonate sequence is more extensive due the geographic location being more seaward during the Eocene, and less affected by near-shore sea level fluctuations. This trend increases in the Eocene and older sediments to the south and east as the distance from the shoreline and water depth increased until sea levels dropped in the late Eocene to modern levels. Thus, a first order potential existence of soft zones for existing facilities or areas of interest can generally be determined geographic location. A second order prediction can be determined from regional subsurface maps and cross-sections (Aadland, Harris, Syms).

A large body of literature is available regarding diagenetic processes in the US Coastal Plain Middle-Eocene carbonate mineral sediments as well as their relationship with sedimentology. Figure 2-4 presents a flowchart review of relevant literature on SRS diagenesis, which will be discussed in detail subsequently. This figure displays four major processes that impact the formation of softzones, namely: seawater (marine) influx, freshwater influx, dissolution, and lithification diagenesis.

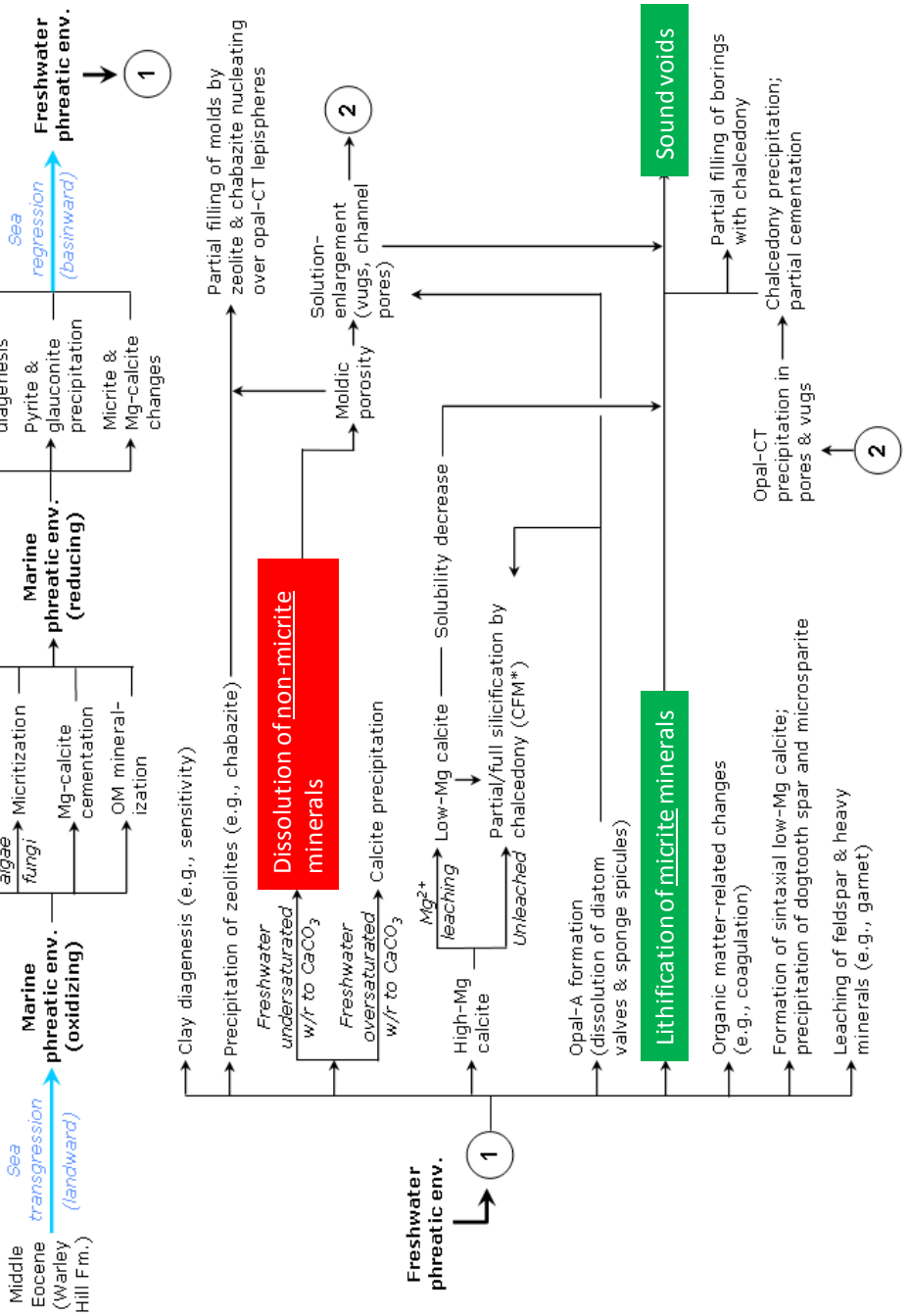

Figure 2-4. Summary of major diagenetic controls in SRS calcareous sediments (Fallaw and Price, 1995; Harris et al., 1997; Maliva and Siever, 1988; Thayer et al., 1994; WSRC, 1999)

For this 2013 review study of geotechnical data, three primary areas within the SRS were selected because of recent construction activity and the availability of digital electronic data at these particular areas: (1) Accelerator Production of Tritium (APT), (2) Salt Waste Processing Facility (SWPF), and (3) the K-Area Complex (KAC). In addition, information from geologic mapping during heavy construction and other relevant data were available from the nearby Plant Vogtle, Georgia. These four specific locations are shown on Figure 2-5 and suggest that, because of their general position relative to the Fall Line, the interface depths and thicknesses of various strata would be of comparable magnitudes at all four locations.

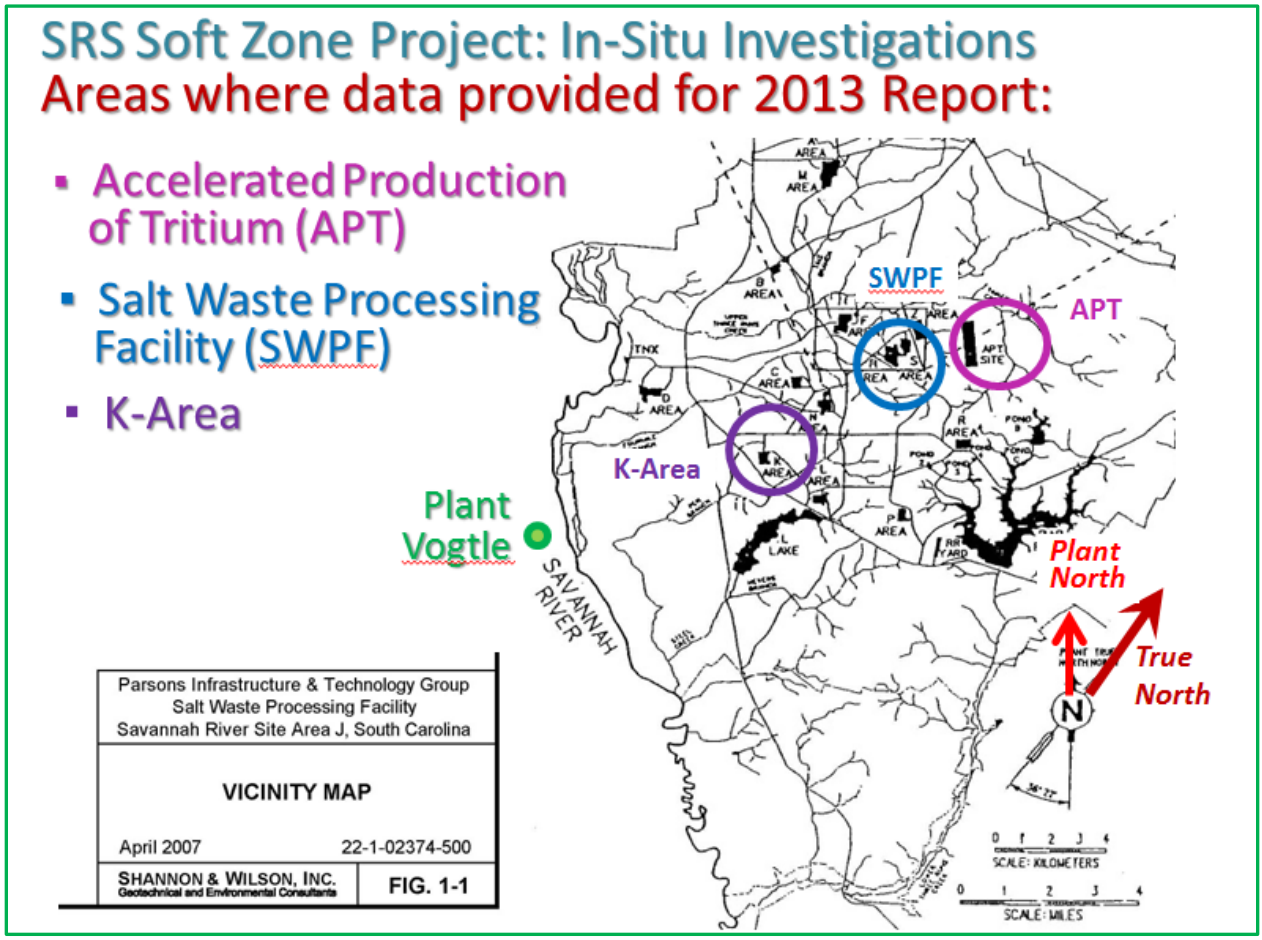

Figure 2-5. Locations of 4 areas of focus for 2013 geotechnical site investigation study at SRS.

2.3 Current Soil Stratigraphy

At the SRS locations, the uppermost sandy soils < 25± m depth appear to be composed primarily of quartz, silica, with glauconite inclusions, while the lower sands below 25± m depth may also contain calcareous and carbonate components depending upon their location at SRS. Consistent with the depositional history, the lower sands in the northwest sections of SRS have little to no carbonates, while carbonate contents increase in a southeasterly direction at SRS, as shown by Figure 2-7 developed by Syms (2010).

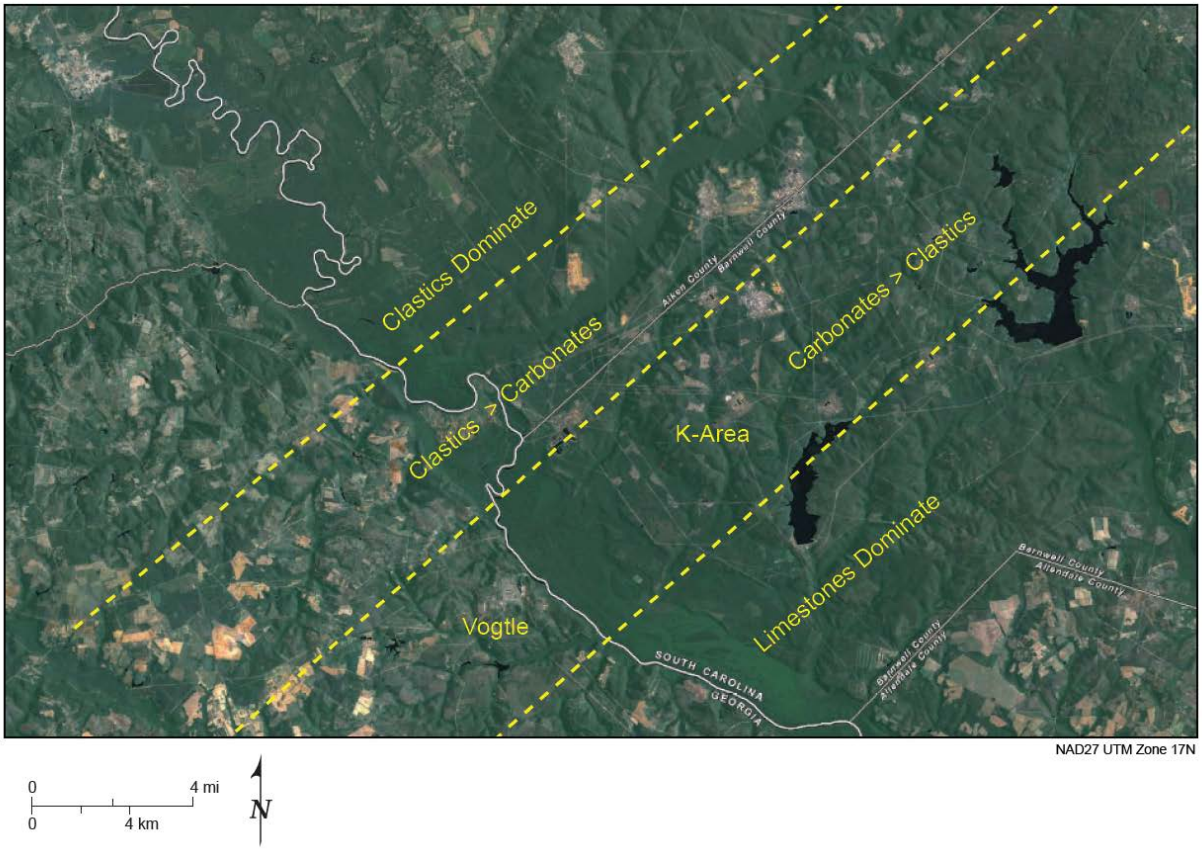

Figure 2-6. General zonation showing change in the predominance of clastics and carbonates across the SRS (Syms 2010).

These old sediments are overconsolidated at shallow depths < 10 m. However, at depths exceeding 10 m, using conventional methods of sampling, laboratory testing, and in-situ interpretative procedures, the soils appear to be either underconsolidated, normally-consolidated, and/or overconsolidated, depending upon both the specific location across the site and depth in the profile. Significant lateral variability in the interpreted preconsolidation stress is evident at any given area. This is apparent regardless of field test type (SPT = standard penetration test, CPT = cone penetration test, or DMT = flat dilatometer test) or laboratory test method (consolidation, triaxial, resonant column). Moreover, the shear wave velocity profile from various techniques (CHT = crosshole test, DHT = downhole test, SASW = spectral analysis of surface waves, SPL = suspension logging) are rather unusual, with V_s decreasing with depth in the upper 15 m, then remaining rather constant to depths of 45 m or so.

Since 1952, many thousands of soil test borings, cone soundings, probings, soil samplings, geophysical tests, and other field investigations have been conducted at SRS by various geotechnical consultants and testing firms. A summary report by Li et al. (2010) indicates a total of 3608 borings, 3321 CPTs, 6493 wells, and 573 other tests. A historical review and synopsis of the subsurface conditions, particularly the unusual aspects related to soft zones, voids, caves, and dissolution features of the lower Santee Formation at depths of 35 to 45 m depths are summarized by Aadland et al. (1999). An updated geologic mapping and interpretation is given by Syms (2010). Of additional concern in this 2013 study is the notion that the geostatic stress regime of the overlying deposits has been altered and changed by collapse features in the lower Santee, thus affecting the overlying soil column and associated geotechnical parameters where localized collapse has occurred.

A simplified stratigraphic profile at the SRS area termed the APT site is shown in Figure 2-7. The APT site was initially chosen as the prime testing grounds for this 2013 study because a detailed geotechnical investigation had been conducted circa 1999 but the facility was not built, thus allowing for the potential for additional new testing, site visits, and field measurements, if desired, without the impedance of restricted access and security. At the APT site, the generalized profiles includes the following geologic strata (from shallowest to deepest): (a) Upland Deposits/Altamaha Formation; (b) Tobacco Road sand; (c) Dry Branch sands; (d) Tan clay; (e) Dry Branch/Clinchfield sands; (f) Santee Formation/Tinker-Santee Formation; and (g) green to rusty brown glauconitic Warley Hill Formation. Groundwater is generally found at depths of about 15 m. The Santee formation shows consistent but variably occurring soft zones and/or the presence of voids and caves. These anomalies are due to dissolutioning of calcite and complex geochemical processes that formed karstic features, soft zones, fluid-filled encapsulations, and other anomalies at depths of between 40 to 50 m below grade.

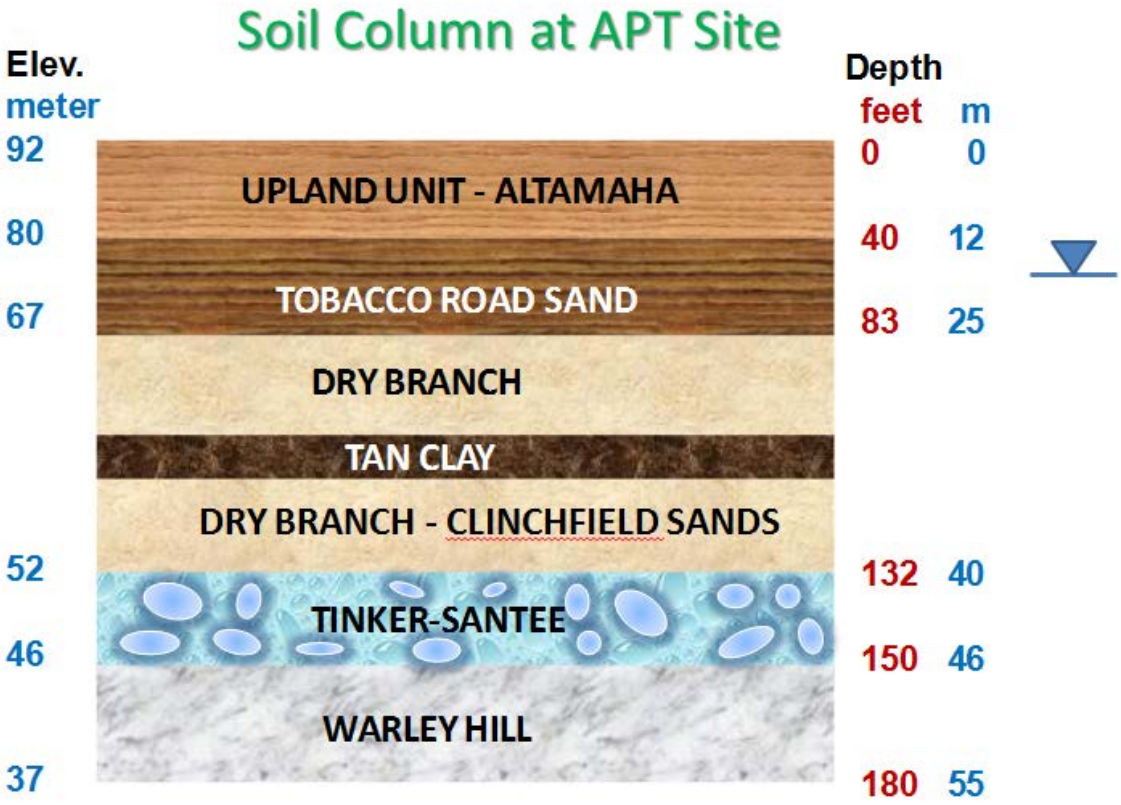

Figure 2-7. Simplified geostratigraphic soil profile at the SRS APT site (adapted from Burns & Roe Enterprises Inc., 2001).

In the Santee formation, the soft zone-void-cave features range in size from 0.3 m to over 30 m in width and 0.5 to 2 m in height and may occur with or without a hard shell-like enclosure that is embedded in the soil matrix. These are unusual features though compared with other marine deposits along the Atlantic seaboard, such as the Cooper Marl, Yorktown Formation, Miocene Marl, or Calvert Clay, which are also associated with calcite, calcareous, and carbonate compositions. The presence of caves and soft infilled encapsulated bodies of the Santee have indeed been confirmed in recent deep excavations for the new power units 3 and 4 of the Plant Vogtle nuclear station near Augusta, Georgia, that is located only 2 km west of SRS. The

investigation encountered the caves at similar elevations in a geologically similar unit known as the Utley Limestone (Syms 2010).

During the removal and replacement operations for 30-m deep excavations made for two new reactors at Plant Vogtle in 2009-2011, geologic mapping of the unearthed strata and subsurface conditions was documented (Syms 2010). Figure 2-8 shows one of several sets of discovered caves at the Plant Vogtle site. The existence of dissolution features and soft zones/voids at depth could possibly have adverse effects on near-surface buildings and ancillary structures at the SRS because of concerns associated with possible collapse, subsidence, and/or settlements. In the field mapping by Syms (2010), a number of the localized soft zones/caves/voids showed a collapsed structure, with brittle cemented sections in broken pieces. At other locations, the excavation operations broke through these encapsulated shells and released either water, slurry, and/or clay-rich fluid suspension into the construction area.

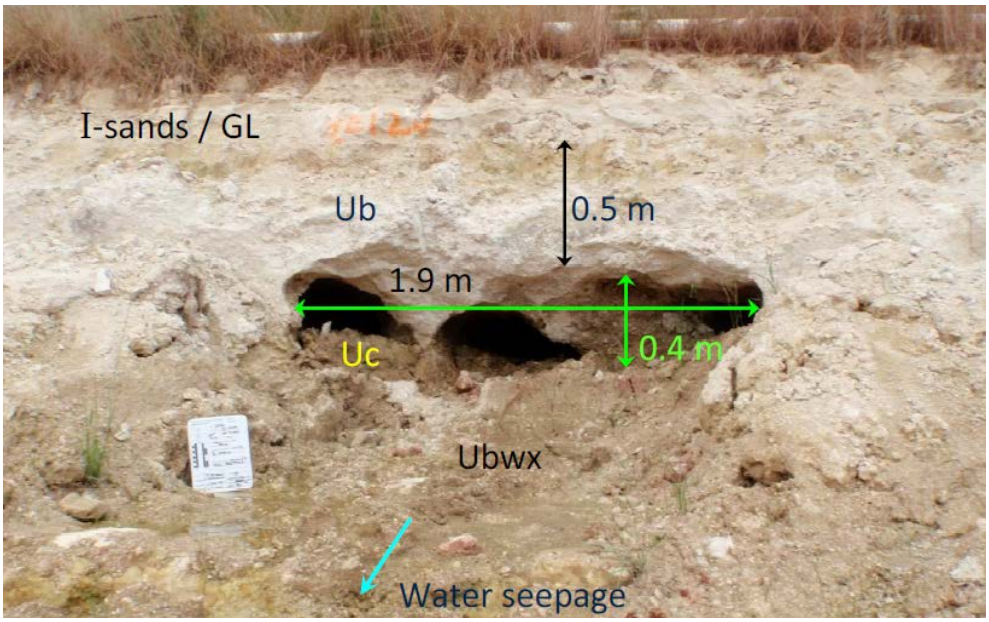

Figure 2-8. Photo of cave feature in soil observed in deep excavations at Plant Vogtle, Augusta (Larrahondo-Cruz 2011). ***Notes: Ub – hard Utley limestone, Ubwx – brittle Utley limestone, Uc – Putley soil (very soft clay deposits, bottom of observed caves)***

3. Case Study-Vogtle

3.1 Background

A summary of the historical knowledge of conditions at the SRS and Plant Vogtle is included under separate cover, in a report by Syms titled "K-Area – Vogtle Geologic Comparative Study: Assessment of 105-K Subsurface Conditions", November 2010". A brief summary of the geologic conditions encountered in the course of this investigation, along with the results of imaging and mineralogy studies follows.

3.2 Vogtle Excavation Observations

The Utley Limestone Member (Plant Vogtle) is composed of the following sub-units (Syms and Glidden, 2011):

- Hard Utley limestone (Ub): hard, strongly cemented limestone. Very light gray, massive to thickly-bedded, ledge-forming wackestone to packstone; abundance of mollusc, bivalve, and echinoderm fossils; violent reaction to HCl. This limestone typically required mechanical ram-hoe excavation for removal at the Investigation Site. The degree of cementation slightly decreased within the northern third of the excavations.
- Weathered Utley limestone (Ubwx): friable (can be disturbed by hand), very light gray to pale yellow, slightly to highly cemented shell hash. Its brittle character increases as a function of fossil content and porosity. Reacts to HCl. Occasional yellow coloration indicates iron oxide staining.
- Micritic Utley (Ua): lime mud with occasional shell hash inclusions. Reported as segregated bodies of micrite with shell hash matrix.

- "Putley" (Uc): glauconite-rich, brown, laminated to thinly bedded, soft sandy clay with calcareous laminae. Normally found either at the bottom of existing dissolution caves or intermixed with Ub or Ubwx in ancient collapse features. Slight reaction to HCl.

Within the Vogtle excavations, the southern half of the excavations were composed primarily of Ub and Ubwx, were well-cemented and variably weathered, with little to no dissolution features observed (Figure 3-1 and Figure 3-2). Figure 3-2 shows the photographs of the excavation walls taken during construction, along with the corresponding geologic interpretations (Ubwx shown in brown and Ub shown in orange). Significantly different features were also noted in the texture of the cores that were observed using SEM (Figure 3-3 and Figure 3-4).

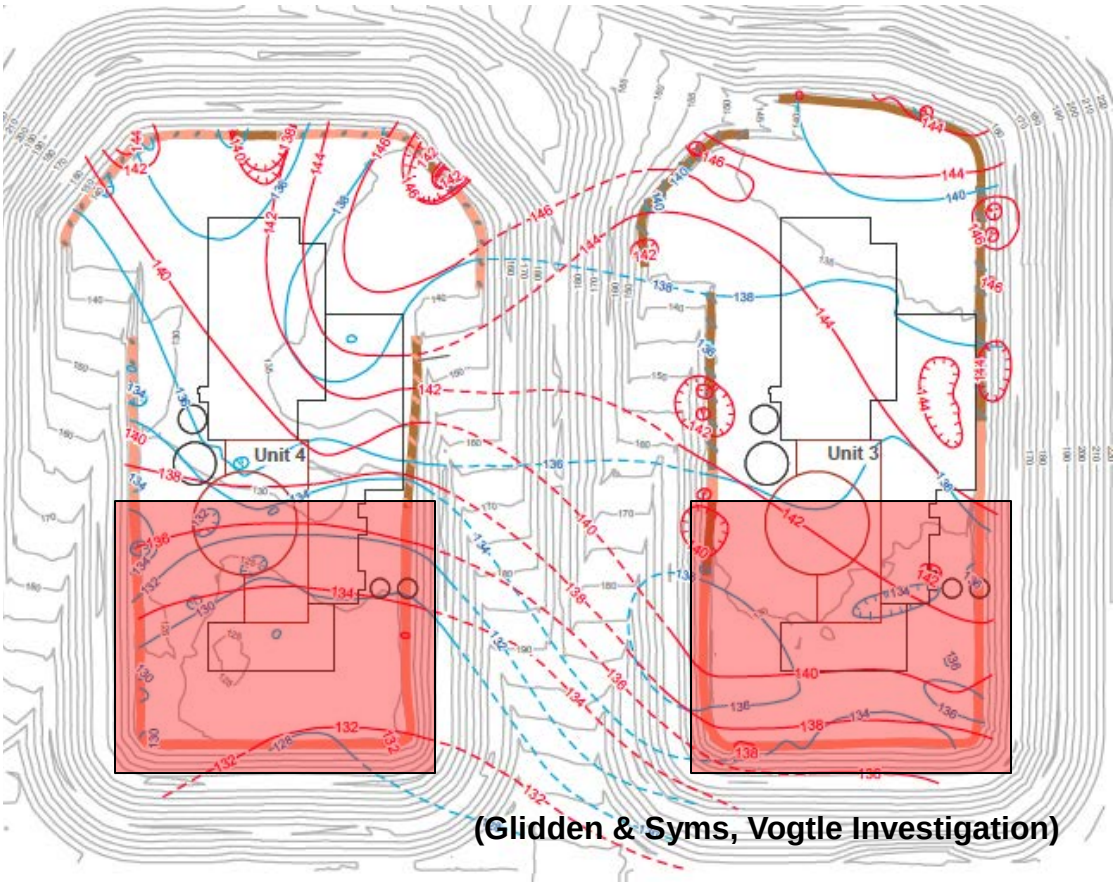

Figure 3-1. Occurrence of Ub and Ubwx in Units 3 and 4. The gray contours represent the as built subgrade of the Plant Vogtle excavation; the red contours represent the top of the Utley formation; blue contours represent the top of the Blue Bluff Marl formation. The red shaded boxes indication zones where significant dissolution was encountered.

FWLA Utley facies

1 Well-cemented Packstone & Wackstone, variably weathered (Ua, Ub, Ubwx)

2 Laminated Sand, Silt, & Clay; Fossiliferous, Glauconitic, Highly Weathered (Uc); with indurated Utley Limestone Cobbles (Ub, Ubwx) and erosional remnants of Facies 1

3 Facies 1 with substantial dissolution and laterally Ddiscontinuous zones of Facies 2

4 Disturbed exposures, primarily Facies 2 and Facies 3

5 Total to near total removal of Facies 1 with Uc and Irwinton Sands infill

As-built subgrade map, 5 ft contour

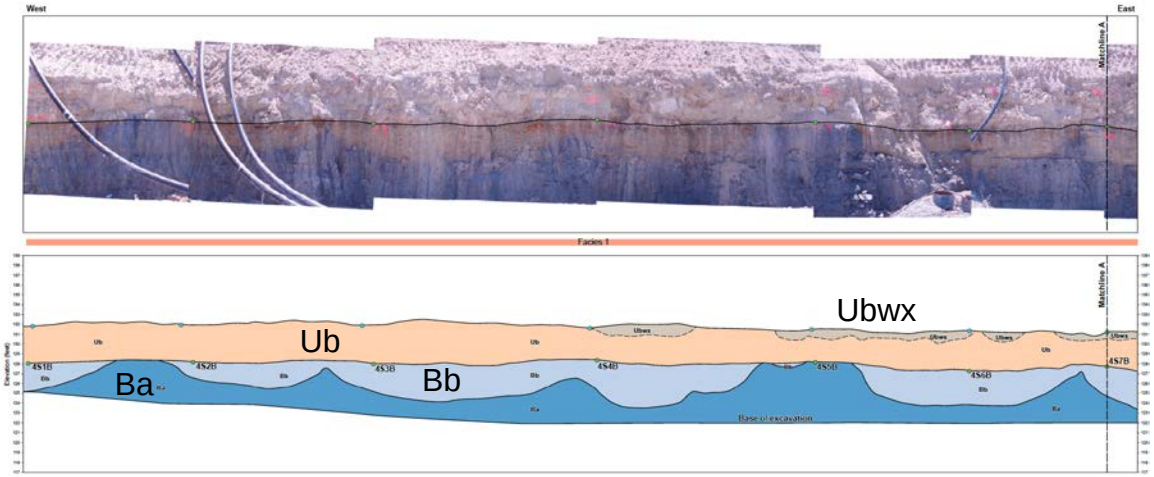

Figure 3-2. Unit 4, South Wall (Glidden & Syms, Vogtle Investigation); (Ubwx shown in grey; Ub shown in orange; Blue Bluff Marl in blue).

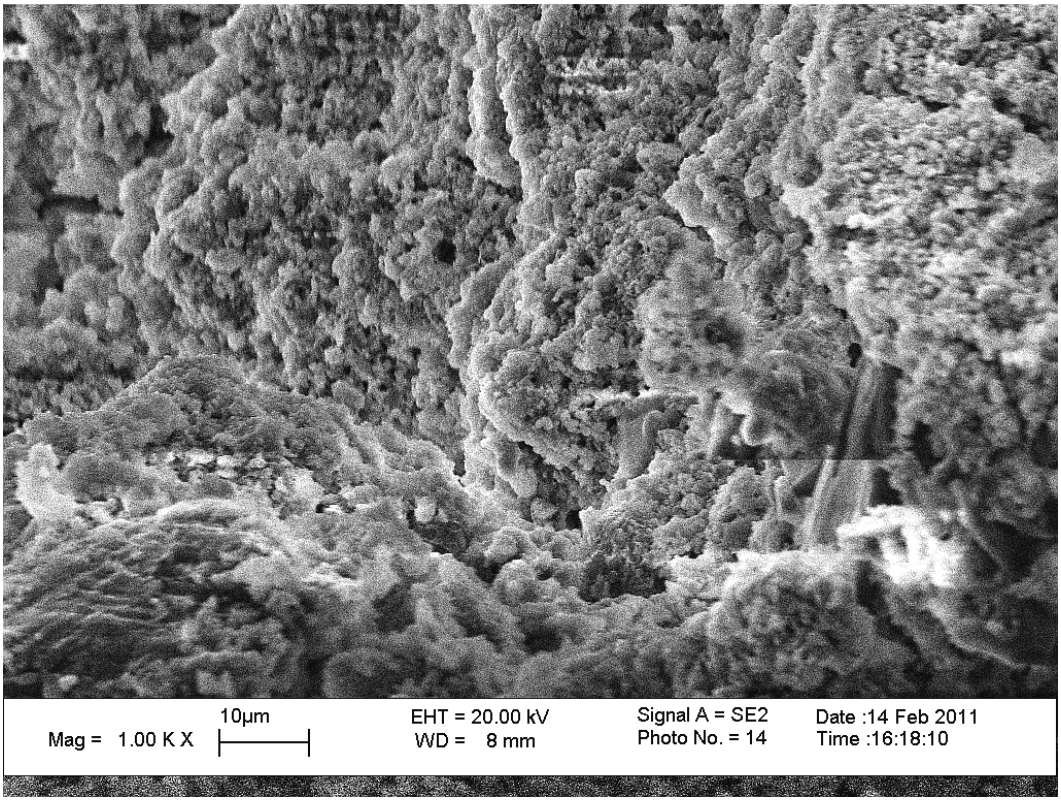

Figure 3-3. SEM image of Ubwx core.

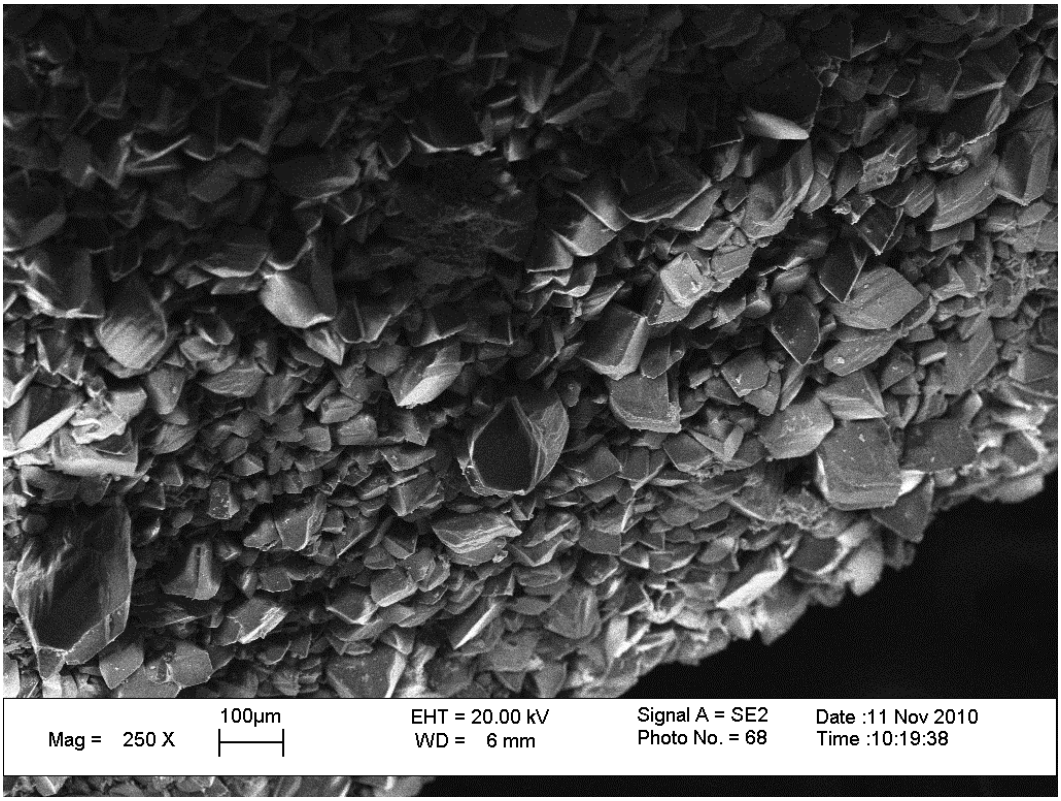

Figure 3-4. SEM image of Ub core.

In contrast, the northern section of the excavation showed more extensive weathering, with dissolution features and large deposits of Uc (Figure 3-5, Figure 3-6, and Figure 3-7). XRD analysis performed on the Uc (Putley) indicated the presence of smectitie (2:1) clay, kaolinite (1:1 clay), with minor amounts of glauconite, calcite, and apatite (Figure 3-8 and Figure 3-9). In the Vogtle excavation, the presence of a dissolution feature was always associated with the occurrence of Uc, which was often found in large deposits and in the absence of Ub and Ubwx.

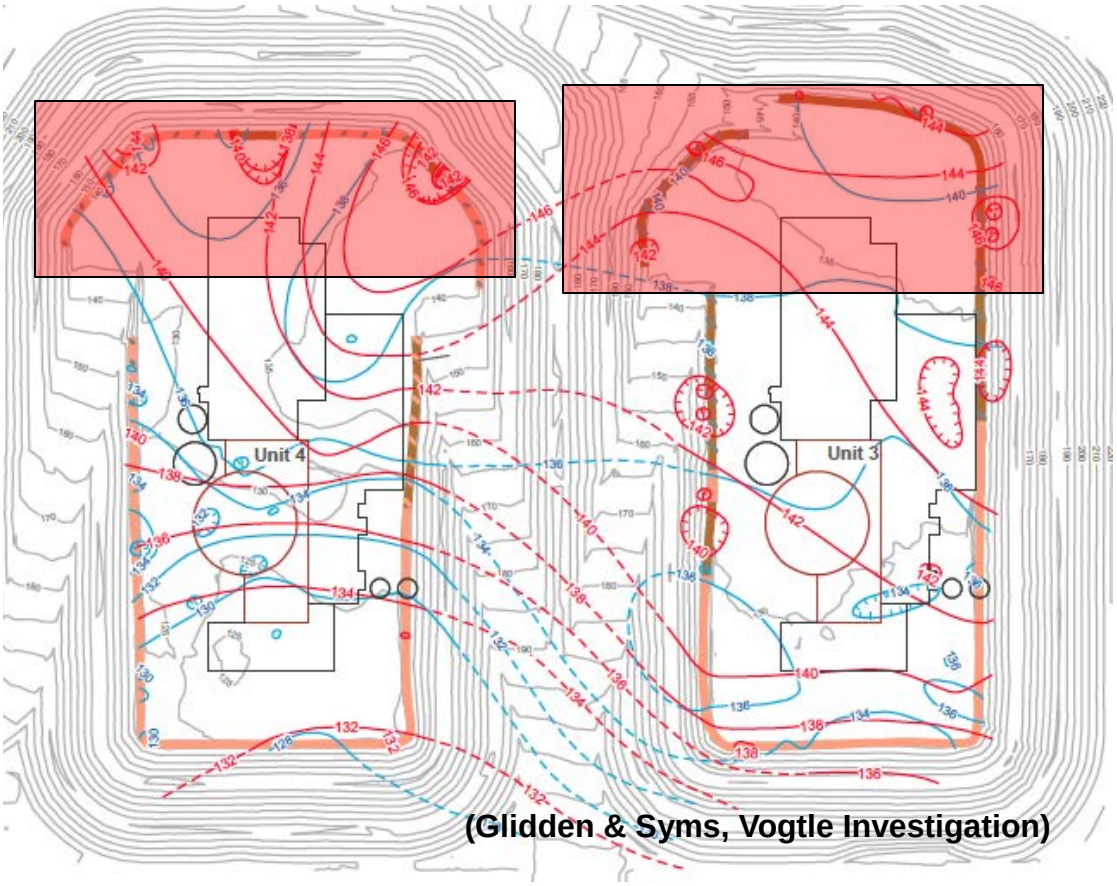

Figure 3-5. Occurrence of Uc in Units 3 and 4. The gray contours represent the as built subgrade of the Plant Vogtle excavation; the red contours represent the top of the Utley formation; blue contours represent the top of the Blue Bluff Marl formation. The red shaded boxes indication zones where significant dissolution was encountered.

FWLA Utley facies

1 Well-cemented Packstone & Wackstone, variably weathered (Ua, Ub, Ubwx)

2 Laminated Sand, Silt, & Clay; Fossiliferous, Glauconitic, Highly Weathered (Uc); with indurated Utley Limestone Cobbles (Ub, Ubwx) and erosional remnants of Facies 1

3 Facies 1 with substantial dissolution and laterally Ddiscontinuous zones of Facies 2

4 Disturbed exposures, primarily Facies 2 and Facies 3

5 Total to near total removal of Facies 1 with Uc and Irwinton Sands infill

As-built subgrade map, 5 ft contour

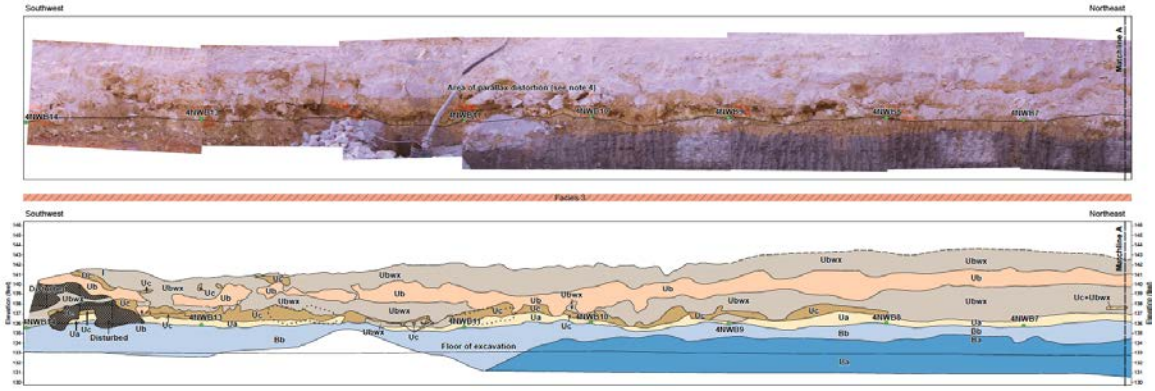

Figure 3-6. Unit 4, Northwest wall (Glidden & Syms, Vogtle Investigation).

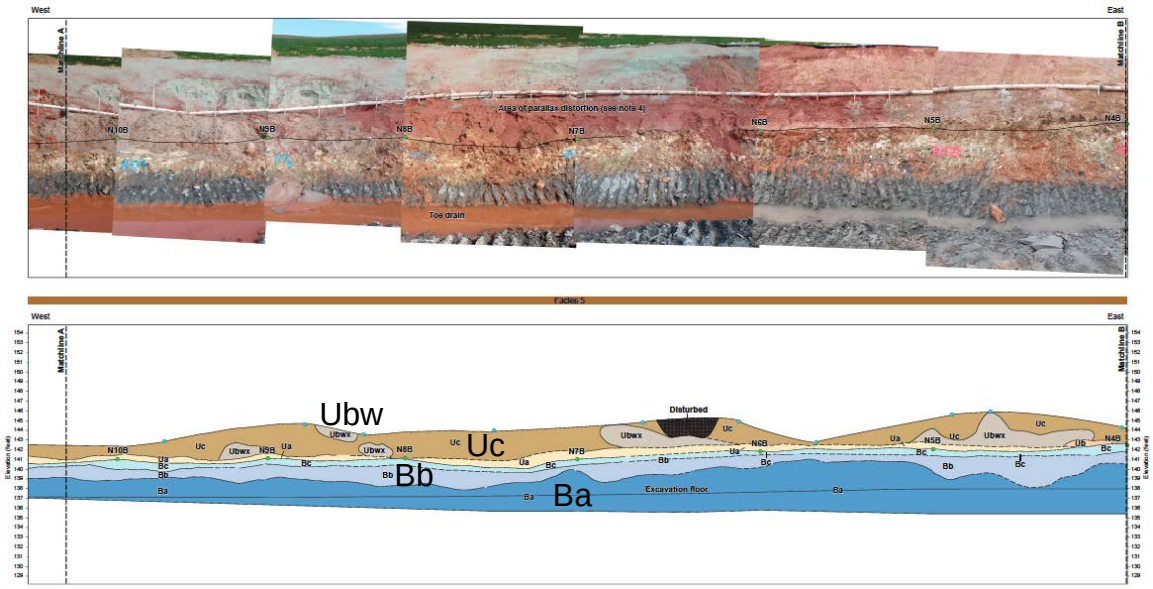

Figure 3-7. Unit 3, North wall (Glidden & Syms, Vogtle Investigation); (Ubwx shown in grey; Ub shown in orange; Blue Bluff Marl in blue).

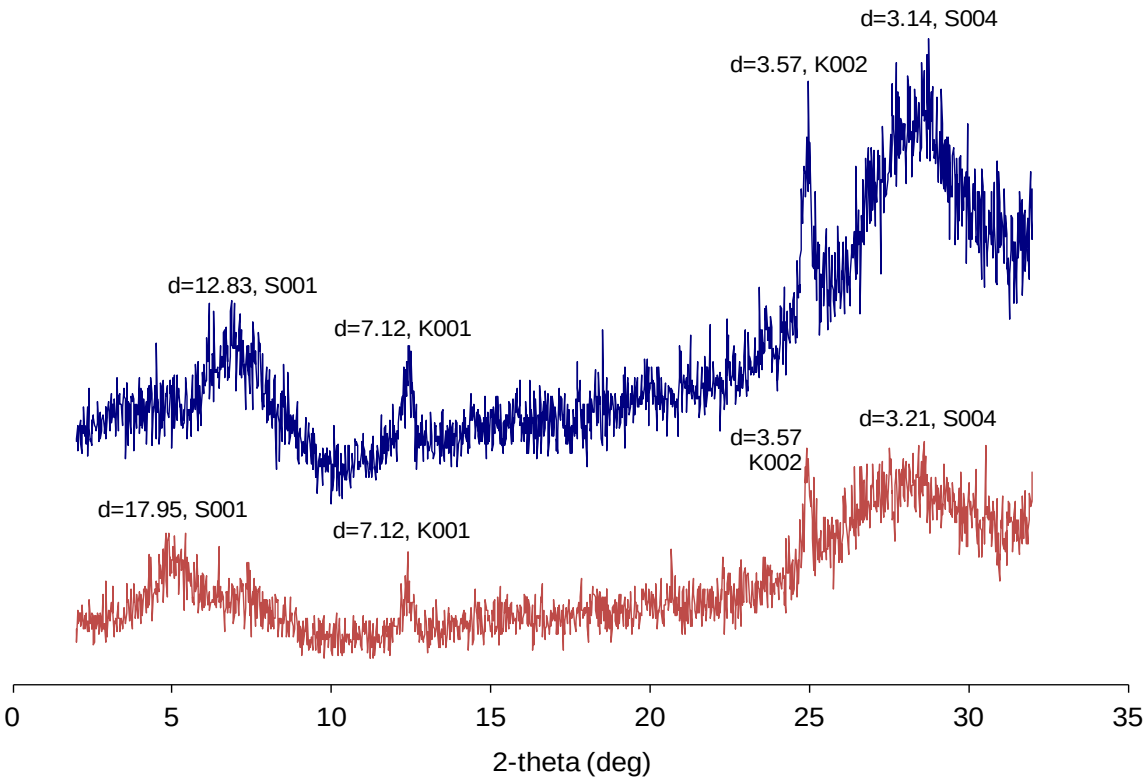

Figure 3-8. Oriented XRD patterns for Putley (Uc) soil. The patterns indicate the presence of smectite (S) and kaolinite (K). Air dried in blue, ethylene glycol solvated in red.

Figure 3-9. Uc Putley sample.

4. Laboratory Testing and Experiments

A laboratory investigation was performed to quantify the present day properties of the samples taken from the Vogtle excavation, as well as give indication as to the geological origins of the deposits. Measurements performed included EDS, XRD, SEM, N_2-adsorption, stable isotopes, K-Ar dating, P/S wave velocities, tensile strength, porosity, and solubility/groundwater studies, which highlighted the contrast between hard and weathered limestones and allowed calculation of parameters for geochemical modeling.

4.1 Chemical Analysis and Mineral Characterization

In order to yield insight into the origin of the Utley/Santee deposits, age dating was performed on samples obtained from the Vogtle excavation. Samples of Ub and Ubwx were tested using the strontium isotope method, samples of Uc (Putley) were tested using the potassium argon method, and several speleothems that were found within the caves at Vogtle were tested using uranium-thorium methods.

4.1.1 Ub and Ubwx: Strontium Isotope Analysis

Samples of Ub and Ubwx were tested using strontium isotope analysis (Geochron Laboratories). The method measured the relative concentration of $^{87}Sr/^{86}Sr$ in the samples, and then correlated that ratio with statistical LOWESS fit to the marine $^{87}Sr/^{86}Sr$ record to determine age (McArthur et al., 2001). Both limestone samples indicated an age of approximately 35 million years, which is consistent with the previous geological findings at SRS.

Figure 4-1. Ub and Ubwx cores: strontium isotope analysis indicated an age of 35 million years.

4.1.2 Uc (Putley): Potassium – Argon Age Dating Analysis

A sample of Uc (Putley) was analyzed using potassium-argon age dating. Over time, ^{40}K will decay to ^{40}Ar; however, the argon is unable to diffuse through the crystal due to its large size, which allows determination of the time since mineral formation through the relative amounts of ^{40}K to ^{40}Ar. The samples were analyzed by Joan Larrahondo, working under the close supervision of Dr. Marion Wampler and Dr. Crawford Elliot at Georgia State University. The Uc was subjected to chemical pretreatment, size separation, 24hr vacuum, followed by 24hr vacuum at 150°C, and was tested using mass spectrometry at the exit of an argon extraction line

that included cold finger traps for H_2O, CO_2, and NH_3 and Ti traps: hot and cooling (Dalrymple & Lanphere, 1969). The potassium content was measured by Flame Atomic Absorption Spectrometry (FAAS). The results of the potassium argon age dating were determined for a composite sample (less than 2 micron), and by size fraction (Table 1).

Table 1. Uc (Putley) Age Dating Results as a Function of Size

Fraction	K (% by mass)	^{40}Ar (nmol/kg)	Age (M yr)
< 2 µm	3.1	578.7	105.3 ± 3.3
1 - 2 µm	3.0	504.6	95.0 ± 3.2
0.25 - 1.0 µm	3.4	405.3	68.3 ± 1.6
< 0.25 µm	2.3	200.5	49.6 ± 1.5

Results indicated that the Uc (Putley) is on the order of 100 million years old, with the smaller particles representing more recent growth and younger geologic age. For reference the Santee formation is on the order of 40 million years old and the overlying Twiggs clay is on the order of 34.3 million years old, as indicated from glauconite age dating. These data indicate that the Uc is likely detrital, having been transported, and not formed in place, to its current location, although it is likely that under stagnant groundwater conditions, some continued particle growth is occurring. This is supported by the younger age measured for the smallest particles.

4.1.3 Speleothems: Uranium Thorium Age Dating

Uranium thorium age dating was performed on three speleothem samples by the USGS laboratory in Denver, Colorado, by Dr. James B. Paces. The method measured the relative concentration of ^{234}U to ^{230}Th to establish secular equilibrium between the concentration U

relative Th. ^{230}Th present was primarily from the in situ decay of U, and the distance from equilibrium allowed determination of age of the specimens. The samples were acid digested and mixed with isotope tracers (^{236}U-^{233}U-^{229Th}). Uranium and thorium were then separated by ion chromatography, and strontium was isolated by a Sr selective resin. The isotope ratios were quantified on a Thermo Finnigan Triton thermal ionization mass spectrometer (TIMS) equipped with an RPQ electrostatic filter, using:

- U- series isotope ratios (^{234}U/^{235}U, ^{236}U/^{235}U, ^{230}Th/^{229}Th, and ^{232}Th/^{229}Th) single ETP electron multiplier operating in peak- jumping mode
- Sr ratios multiple faraday cup in multi- dynamic peak- hopping mode

Three speleothem samples with the following characteristics were tested:

Sample SRS 1 (Figure 4-2:)

- 14- cm- tall stalagmite with fine growth laminations with 1- to 2- cm- thick basal coating of coarse- grained, acicular carbonate flowstone
- Exterior surface possibly recrystallized
- Texture also suggests postdepositional dissolution
- Samples taken included
    - basal acicular calcite (A,B: oldest portion of the speleothem)
    - basal laminar calcite (C: younger sample)
    - intermediate laminar calcite (D, E, and F: younger samples)
    - Outermost laminar calcite (G and H: younger samples)

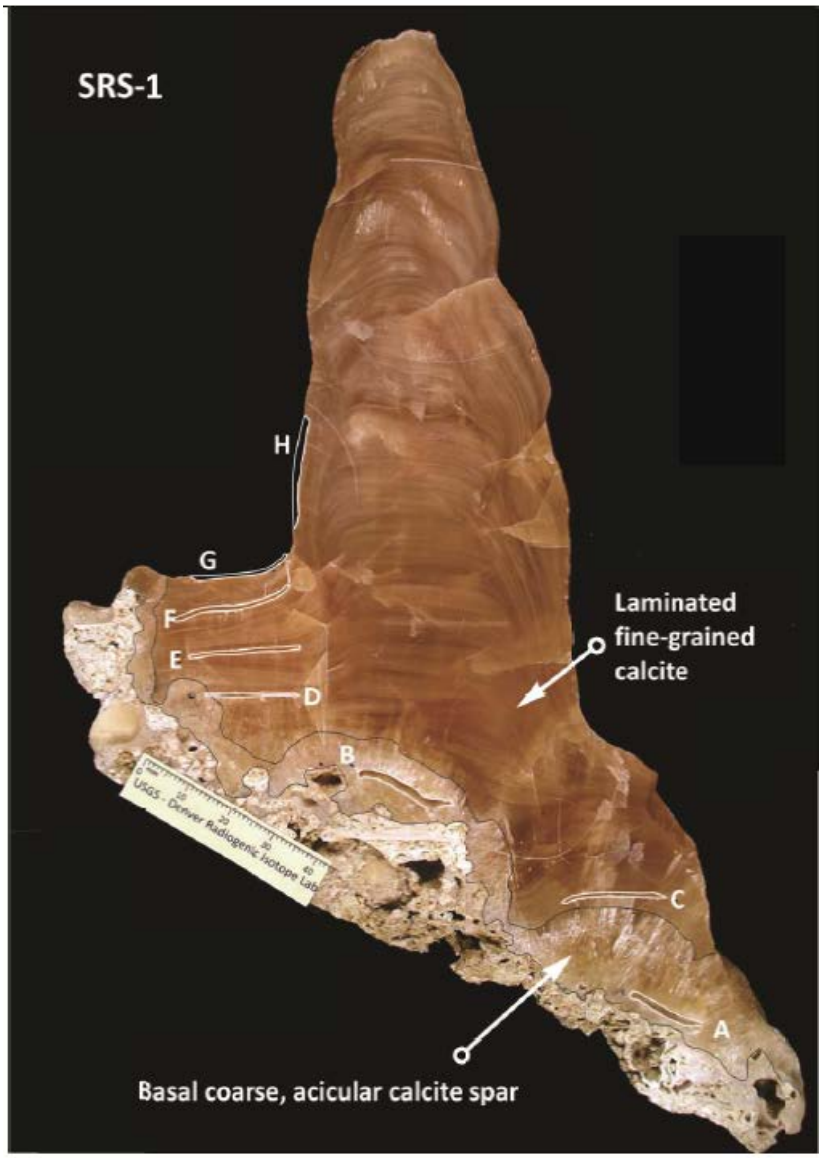

Figure 4-2. Photograph of SRS‐ 1 speleothem, showing locations of subsamples excavated from the basal acicular calcite flowstone (SRS-1A, S SRS-1B) and additional samples from laminated stalagmite (SRS-1C through SRS-1H).

Sample SRS 2 (Figure 4-3):

- 13-cm long by 3-cm diameter stalactite containing a central capillary tube
- Very coarse-grained calcite spar likely caused by extensive recrystallization (faint concentric growth laminations remain visible)
- Texture strongly suggests dissolution of outer surface

- Samples taken included:
  - adjacent to the central capillary tube (A and B: interpreted as oldest)
  - layer beneath the outermost surface, removed by milling (C: interpreted as youngest)

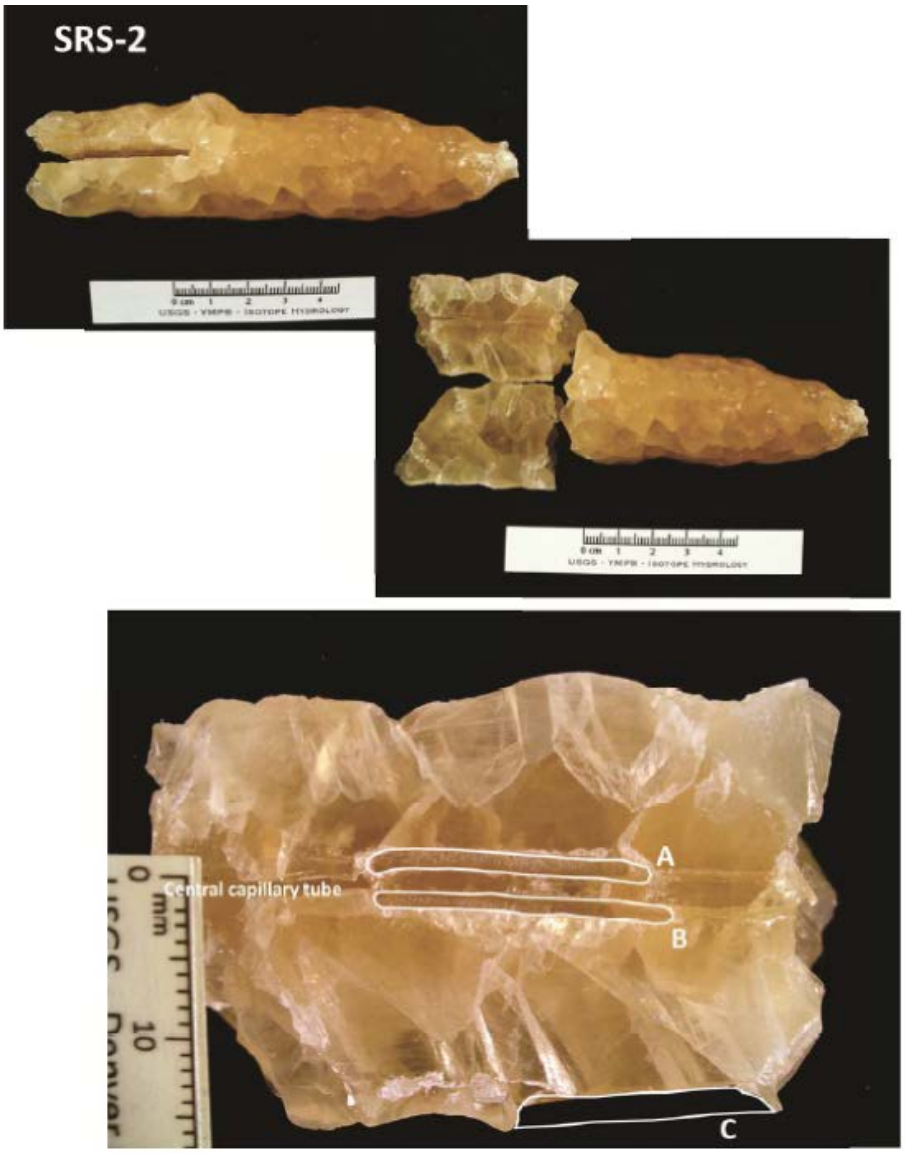

Figure 4-3. Photograph of SRS-2 speleothem showing locations of subsamples excavated from innermost calcite layers on either side of the central capillary tube (SRS-2A, SRS-2B) as well as outermost surface layers (SRS-2C).

Sample SRS 3 (Figure 4-4):

- Coarse grained, acicular calcite flowstone approximately 25 cm thick
- Coarse color banding is present along with fine laminations parallel to flowstone base
- Outer surface contains scattered sugary crystals similar to those forming the substrate of the coating.
- Samples taken included:
  - basal acicular (A and B: interpreted oldest)
  - outermost layer acicular (C: not analyzed)

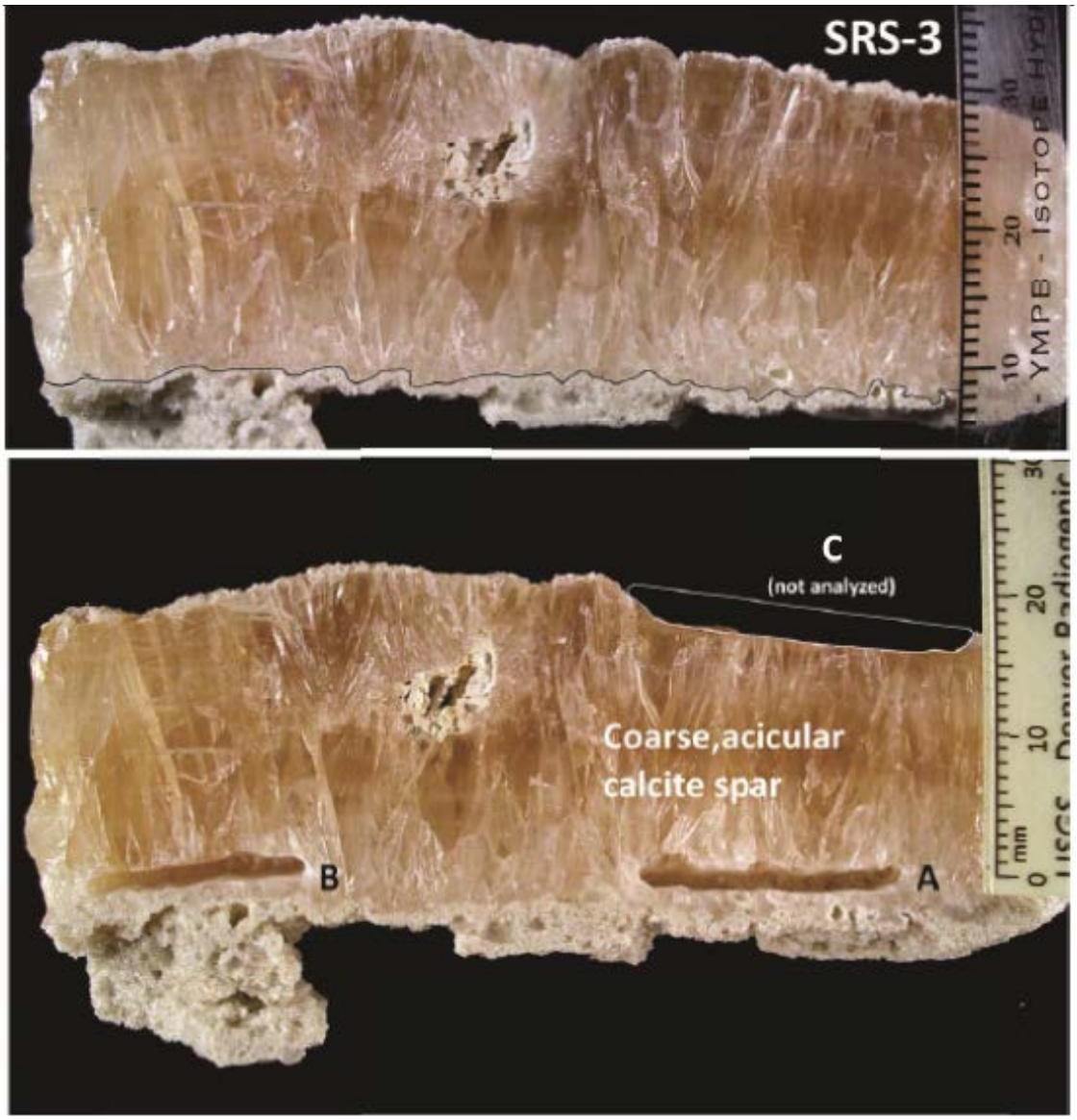

Figure 4-4. Photograph of SRS-3 speleothem showing locations of subsamples excavated from basal calcite layers (SRS-3A, SRS-3B) and outermost layers (SRS-3C) which were not analyzed.

The results of the age dating of the speleothems indicated that the samples were all of a relatively young geologic age (Table 2). While the data indicate that the samples were formed recently, primarily within the last 40,000 thousand years, there were some inconsistencies in the results that need to be identified: samples from the laminated layers of SRS 1 indicated an older

age on the outside layers, when compared to the inner layers, which most likely resulted from uranium leaching after submergence (thorium is highly insoluble, resulting in an age that appears older due to the leached uranium). Specimen SRS 2A was dated at 23,000 years, which was consistent with SRS 1 and SRS 3; however, SRS 2B dated at 3,000 years, which may indicate either deposition of a new material or uranium leaching. Specimen SRS 2C dated at less than 1,000 years. Additionally, the isotopic composition identified with the flowstone samples is indicative of formation within the vadose zone. The ratios of $^{87}Sr/^{86}Sr$ within the samples were also analyzed and are indicative of the formation water source, and yielded a distinct isotope signature between each speleothem, and a constant water source for each individual speleothem (Figure 4-5). These data give further evidence to support the mechanism of distinct water sources (wormholes) feeding into the below ground cavities. The results indicated that the speleothems formed in vadose zones within the caves, most likely during a period of regression; however, the caves are currently located approximately 15 m below the current groundwater table, and the external surfaces of the speleothems exhibit some dissolution features. In summary, the data from the speleothem age dating indicate that the caves were formed more than 20,000 years ago.

Table 2. Speleothem Uranium Thorium Age Dating Results

Sample	Age (thousand years)
SRS 1: Flowstone*	35 to 42
SRS 1C: Laminated layers	29
SRS 1D: Laminated layers	28
SRS 1E	137±3.8
SRS 1E-H: Laminated layers	42-137
SRS 2A	23
SRS 2B	3
SRS 2C	0.490±0.480
SRS 3: Flowstone*	29 to 33

*Flowstone isotopic composition indicates formation in vadose zone

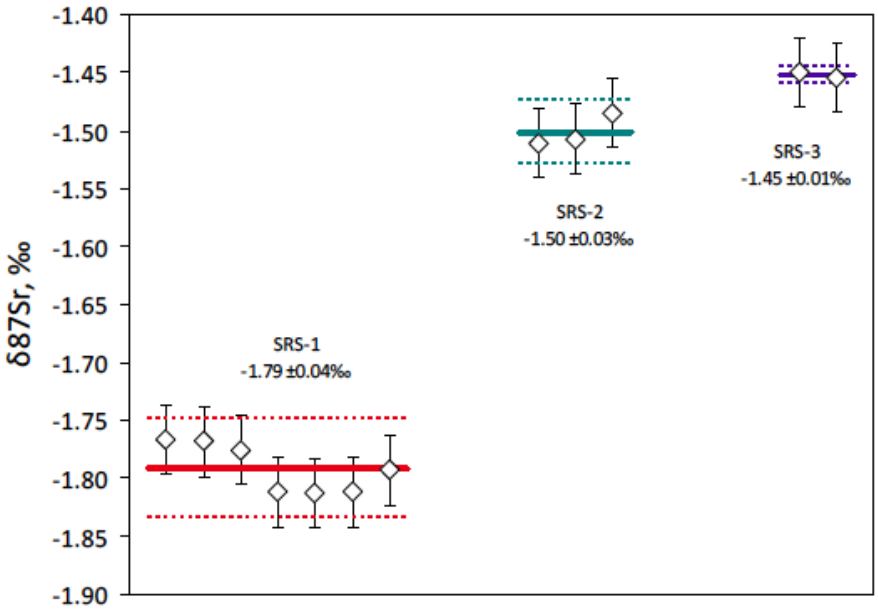

Figure 4-5. Strontium isotope ratios, indicating different water source fed each speleothem.

4.1.4 Stable isotope ratios

Measurement of the stable isotope ratios for the speleothems were performed to give insight into the formation environment of the speleothems, specifically to identify marine versus freshwater formation environments. Isotope ratios for O and C will vary and the ratio of oxygen-18 to oxygen-16 will indicate waters of formation (seawater enriched in ^{18}O, while fresh water enriched in ^{16}O), and the ratio of carbon-13 to carbon-12 will indicate formation in high photosynthetic environments (enriched in ^{13}C) or formation in low or plant free environments (enriched in ^{12}C). Measurement of $\delta^{13}C$ and $\delta^{18}O$ stable isotopes were performed in collaboration with Dr. Kim Cobb and Ms. Stacy Carolin, Georgia Tech (School of Earth and Atmospheric Sciences) (Figure 4-6).

Figure 4-6. Delta V Plus with Kiel Mass Spectrometer (Cobb Lab, EAS).

The stable isotope ratios were determined for Ub and Ubwx samples (approximately 100 mg, powdered). The limestone specimens were dissolved in phosphoric acid and the produced CO_2 gas was freed from impurities after passing through a liquid-nitrogen cooled cryogenic trap. The cleaned gas was directed into the plasma mass spectrometer to determine the abundances and stable isotopic ratios. A total of 8 isotope measurements in a 540 sec time interval were

obtained for each specimen. The results indicated that the Ubwx sample was slightly isotopically lighter (more negative) than the Ub, which indicated that the Ubwx has been exposed to freshwater for a longer duration when compared to Ub (Table 3 and Figure 4-7).

Table 3. Stable Isotope Results for Utley Limestones (in %)

Limestone type	$\delta^{18}O$	$\delta^{13}C$
Ub	**-1.811** **-1.774**	**-2.734** **-2.694**
Ubwx	**-2.228** **-2.191**	**-4.385** **-4.324**

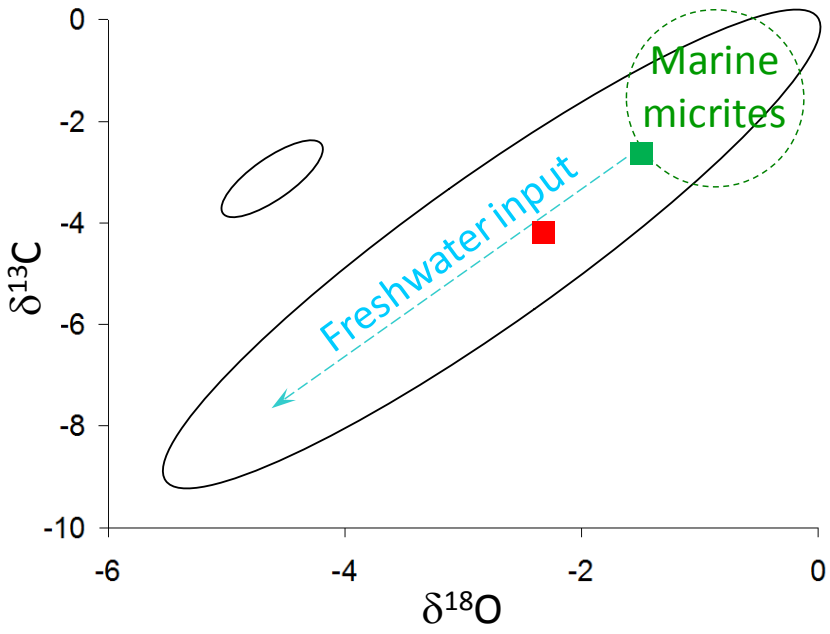

Figure 4-7. Stable isotope results of this study compared to Eocene micrites (Lasemi, 1983). The green square represents Utley limestone (Ub); the red square represents Utley limestone (Ubwx).

4.1.5 Groundwater Analysis

Groundwater was collected from four seepage locations that were observed in the Plant Vogtle excavation. At these locations, one seepage source emanated from Ubwx between Ub contact, another from a Irwinton Sands-Ubwx contact, and the last one from Ubwx only. The level of pH was measured on-site with pH strip indicators, while in the laboratory, total dissolved solids TDS were measured and metal concentrations were determined by ICP-OES (Figure 4-8 through Figure 4-11). Examination of the results of the Vogtle groundwater analysis indicate rock derived waters, but toward the rain water influenced waters when plotted on the Gibbs Plot of Surface Waters, while the SRS samples plot on the rock/rain water boundary (Figure 4-12).

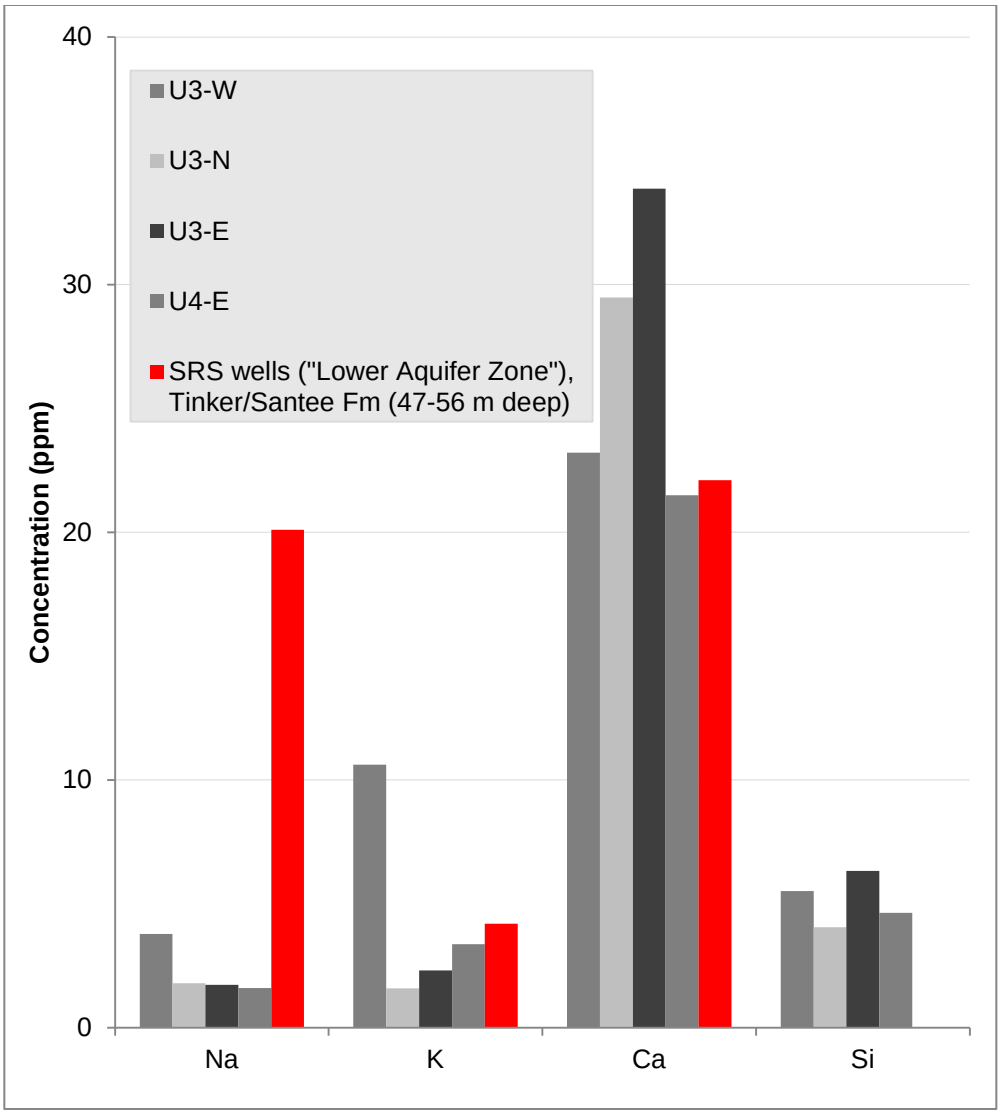

Figure 4-8. Groundwater concentrations from Vogtle samples: Na, K, Ca, and Si with comparison to SRS well data.

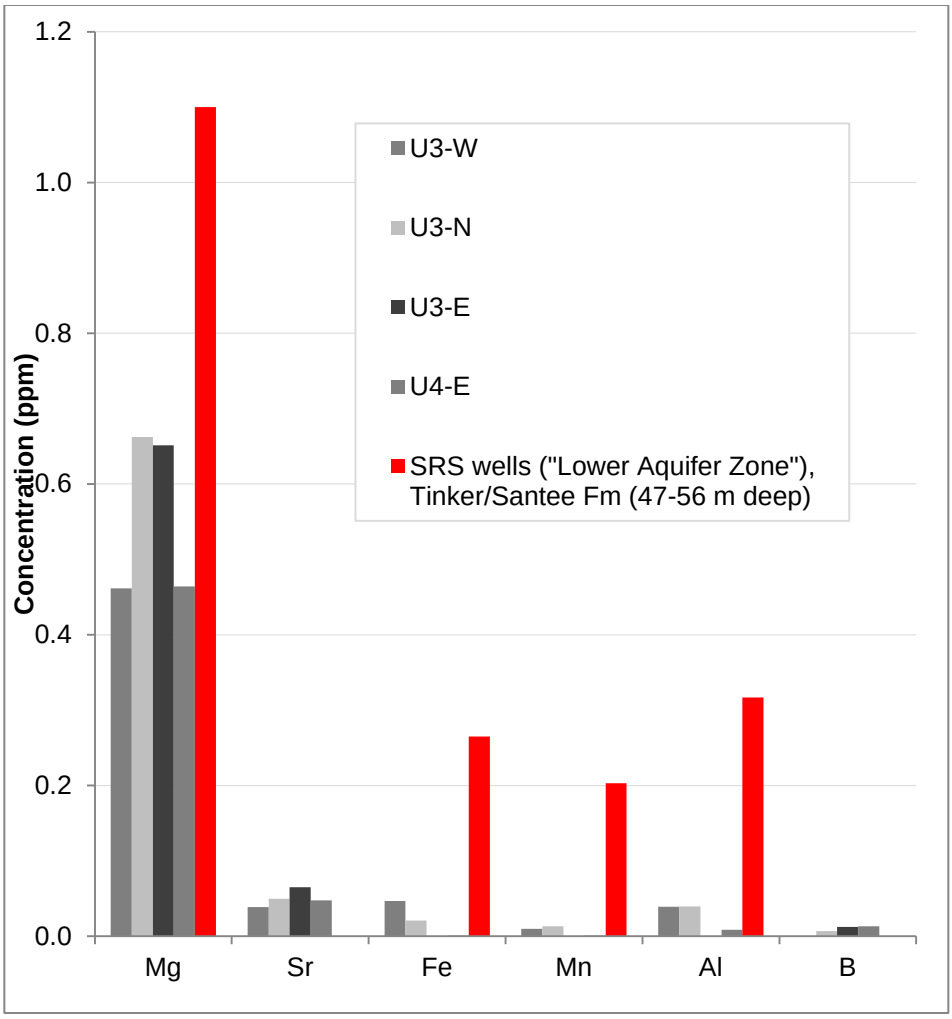

Figure 4-9. Groundwater concentrations from Vogtle samples: Mg, Sr, Fe, Mn, Al, and B with comparison to SRS well data.

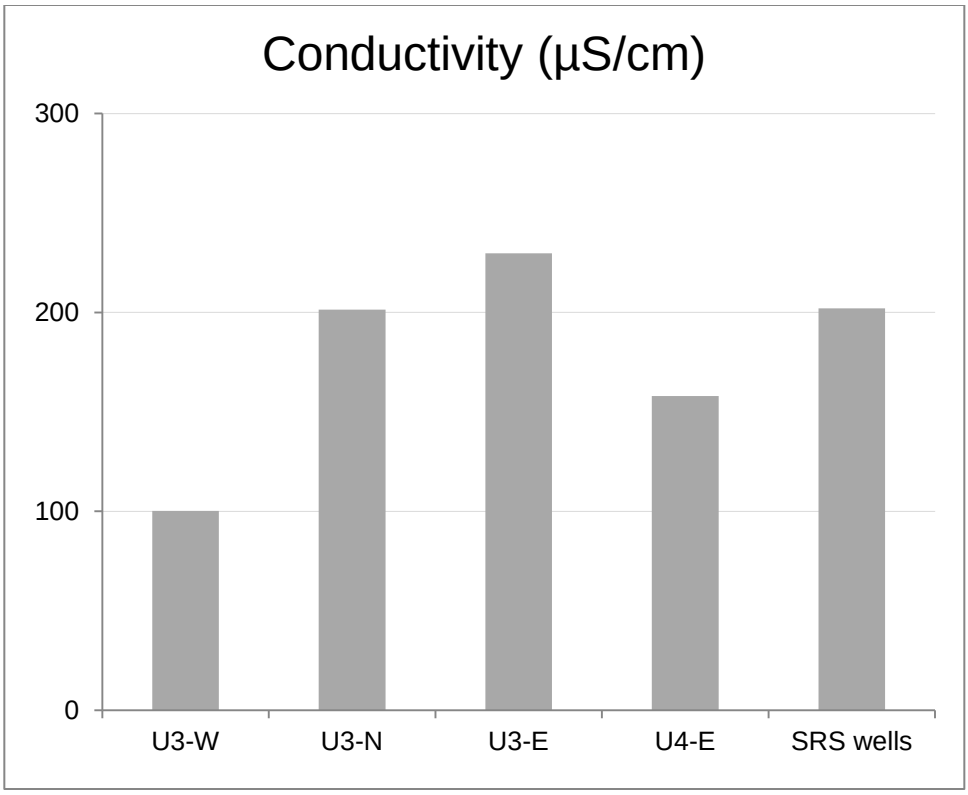

Figure 4-10. Groundwater conductivity at Vogtle with comparison to SRS well data.

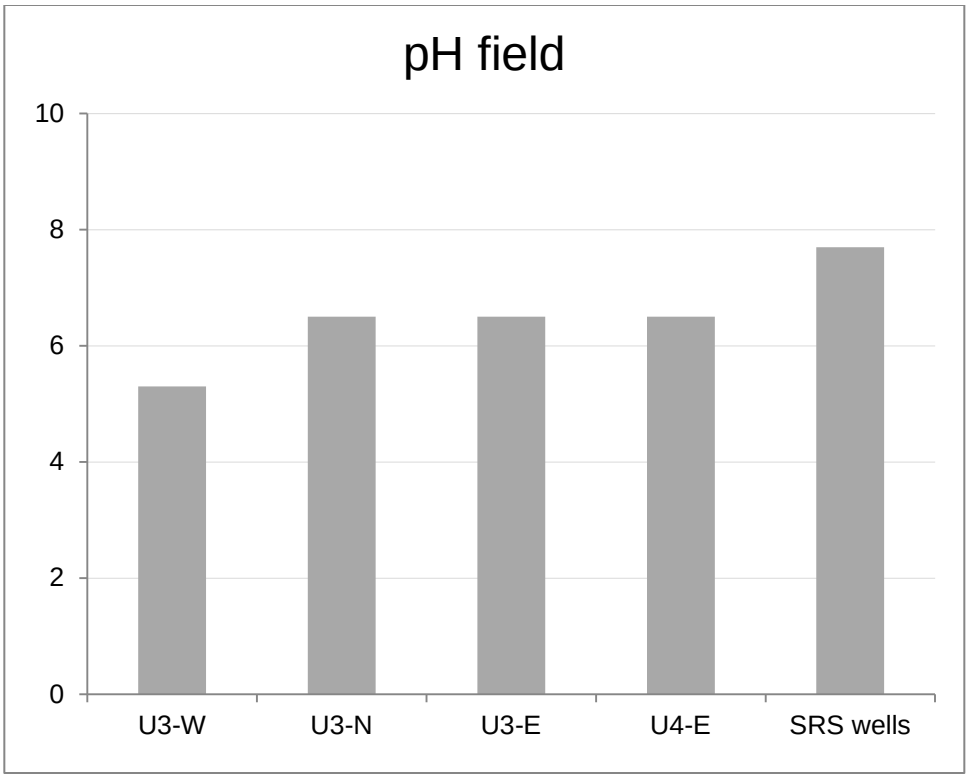

Figure 4-11. pH at Vogtle with comparison to SRS well data.

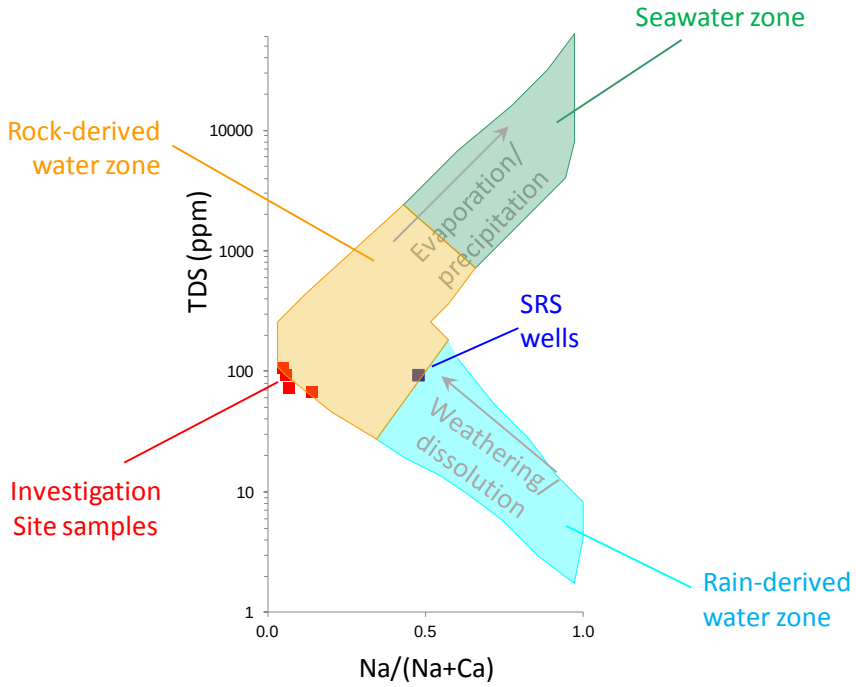

Figure 4-12. Gibbs plot of surface waters (Gibbs, 1970) showing the groundwaters of interest for this study.

Predictions of dissolution of the limestone under geochemical conditions at the SRS were performed using the solubility parameters that were obtained on small limestone blocks (general rate equation approach). Table 4 summarizes the results of the forecast exercise. It appears clear that, unless groundwater conditions change such that at-equilibrium pH is well below normal for calcareous materials (~8.3), major dissolution at the SRS is unlikely. However, major inputs of freshwaters seeping quickly from the surface would need to be prevented from reaching the Santee Formation at the SRS, in order to keep the pH from dropping below neutral.

Table 4. Dissolution Rates Calculated from Kinetic and Groundwater Data (ton = metric tonne)

		Weathered Utley Limestone (Ubwx)		Utley Limestone (Ub)		
Groundwater Source		Saturation degree, Ω	$R_{dissolution}$ (kg/ton-hr)	Saturation degree, Ω	$R_{dissolution}$ (kg/ton-hr)	Notes
Investigation Site		0.01	12.6	0.18-0.27	1.5	pH_{field} = 6.5-7.0
SRS	RAG wells	0.19	10.5	3.4	~0	
	LSW wells	2.5	~0	46.1	~0	
	DCB well	5.0	~0	60.7	~0	

4.2 Summary

Results demonstrate that the weathered and hard limestones had distinct geochemical signatures, with the latter exhibiting higher crystallinity, lower clastic load, and freshwater-influenced composition. Findings also reveal a carbonate diagenesis pathway likely driven by geologic-time seawater/freshwater cycles, microorganism-driven micritization, and freshwater micrite lithification.

Results of the investigation performed to age date the samples indicated that the Utley limestones (Ub and Ubwx) were approximately 35 million years old, which was consistent with the geologic record. The speleothems that formed within the cave structures at Plant Vogtle placed the age of formation of the caves as greater than 40,000 years old. However, the Uc (Putley) dating results indicated a very old specimen, on the order of 100 million years old, indicating the Putley is most likely of detrital origin.

Analysis of the speleothem samples, Ub and Ubwx samples, and groundwater samples collected at Plant Vogtle supported the hypothesis of wormhole formation in the subsurface due to: 1) strontium isotope ratios indicated that each speleothem was fed by a different water source; 2) stabile isotope chemistry indicated that the weathered Ubwx had more exposure to freshwater than the unweatherd Ub; and 3) the Vogtle groundwater analysis indicate a source of rock derived waters, but toward the rain water influenced waters when plotted on the Gibbs Plot of Surface Waters, and the SRS samples plot on the rock/rain water boundary.

4.3 Elastic Properties

A number of cores, 2 in (50.8 mm) in diameter, with lengths varying from about 48 to 110 mm, were drilled and extracted from limestone blocks retrieved from the field. Limestone

densities were >2000 kg/m^3 though variable, depending upon the degree of internal porosity which in turn reflects the degree of local lithifying diagenesis.

Limestone elastic parameters were investigated using non-destructive ultrasonic waves. P-wave and S-wave piezo-electric transducers were coupled with vacuum grease to each limestone core end. The transducers were wired to a signal generator, a signal amplifier/HP-LP filter, and an oscilloscope. The results of P- and S-wave velocities measured across the five limestone specimens are presented in Figure 4-13. These values compare well with published wave velocities in other Eocene-aged limestones from the North Pacific and the Meiji Guyot (Christensen et al., 1973), which range between 2760 and 4225 m/sec in P-wave velocity, and in between 1293 and 2128 m/sec S-wave velocity.

The wave velocity results were then used to calculate mechanical parameters, namely shear modulus, elastic modulus, and Poisson's ratio (see Table 5). Only the 30 kHz input S-wave results were used in the calculations, which was taken as representative of the conditions. Once again, these values compare fairly well with those of the Eocene North Pacific and Meiji Guyot limestones referred above (Christensen et al., 1973) for which G = 9.9 to 3.6 GPa, ν = 0.33 to 0.36, and E = 26.3 to 9.7 GPa. Textbook published data for limestones range as G = 2 to 97 GPa, ν = 0.01 to 0.32, and E = 1.6 to 38 GPa (Santamarina et al., 2001).

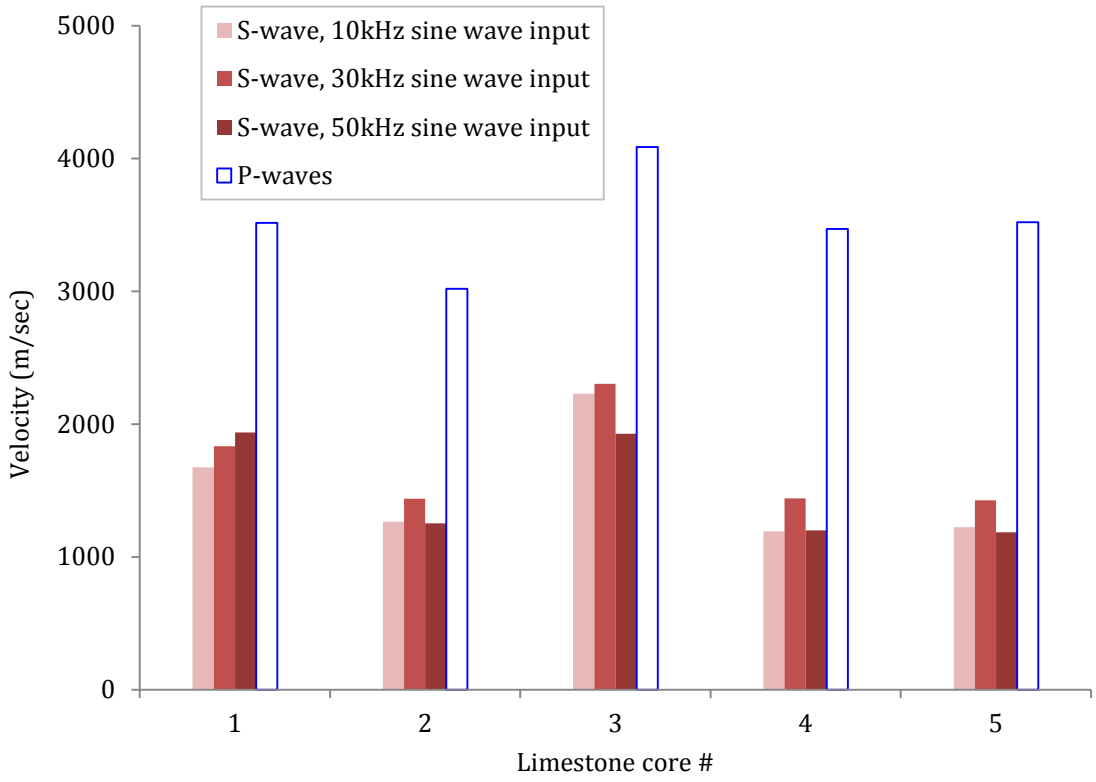

Figure 4-13. Results of ultrasonic wave velocities for the limestone (Ub) specimens

Table 5. Utley limestone (Ub) elastic parameters

Specimen	G (GPa)	ν	E (GPa)
1	7.5	0.31	19.7
2	4.3	0.35	11.7
3	13.5	0.27	34.2
4	5.2	0.40	14.6
5	5.1	0.40	14.3

Tensile strengths of the (Ub) Utley limestone were also studied during this investigation. Brazilian point-load splitting tensile strength tests (ASTM D3967) were performed on 1 inch (25.4 mm) thick disks cut from the limestone. Results are presented in Figure 4-14. These results are comparable to data published for the Late Eocene Ocala Limestone, Florida (Gaswirth et al.,

2006) which range between 3.1 and 6.3 MPa though ranging in porosity from 25 to 16%, respectively.

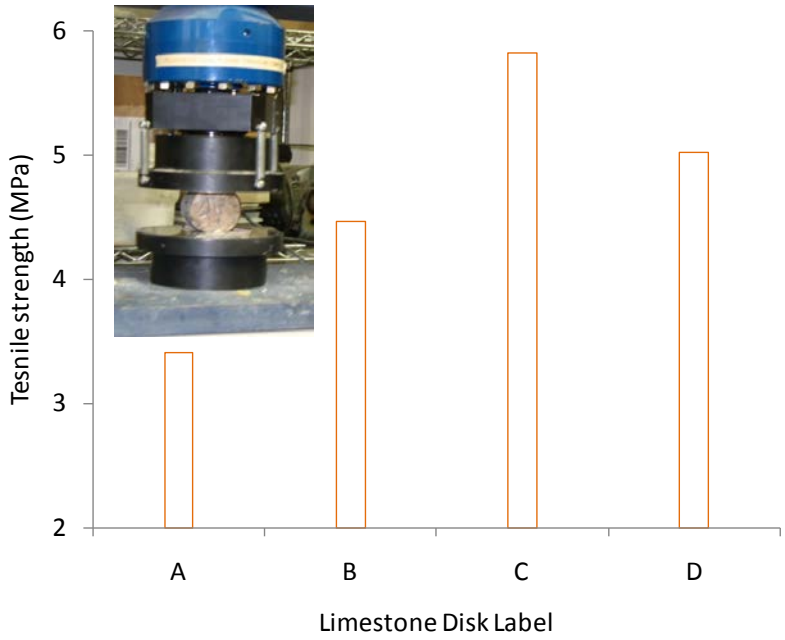

Figure 4-14. Results of tensile strength testing on Utley limestone specimens

5. Soil Properties and Field Testing

5.1 Gap-Graded Soils at SRS

Most of the overburden soils at SRS classify as slightly clayey to clayey sands (SP-SC to SC) based on mechanical analyses by sieves and the hydrometer analyses of the fines content portion. Surprisingly, the sand fraction is uniformly graded in the fine-medium sand size range, however, below the No. 200 sieve, very little silt size grains are found and a predominance of clay or colloidal particles occur. This results in apparent gap-graded sandy soils in the soil column that may be due to extensive weathering. For instance, based on representative samples from Boring B35 at the Salt Waste Processing Facility (SWPF), grain size distribution curves are presented in Figure 5-1 over a full range of depths from 1.2 m to 44.5 m. The soils are noted to have high clay fines contents, appreciable colloids, and plastic fines, as well as high specific surface values. These somewhat unusual gradations may affect penetrometer readings and in-situ test results because of smearing at the steel-soil interface in high plasticity soils, as well as particle breakage and/or crushing when the calcareous component is higher in sandy layers.

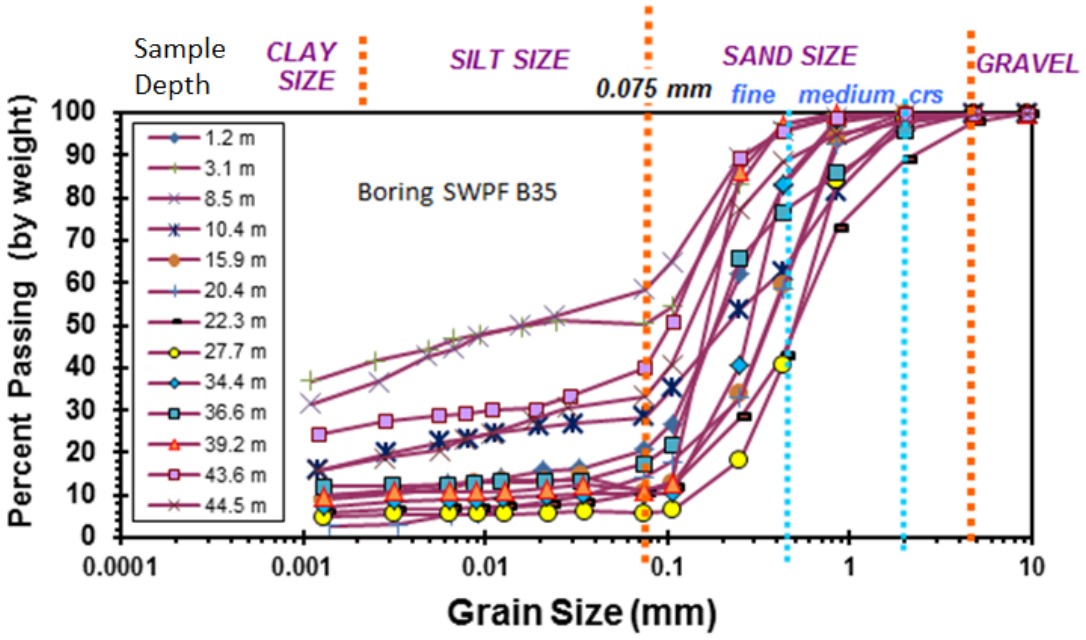

Figure 5-1. Grain size distribution curves for soils at SRS SWPF site (Buechel 2007).

5.2 Shear Wave Velocity Profile

In young uncemented soils, the in-situ shear wave velocity (V_s) generally increases with depth due to its stress-dependent behavior. For instance, Lew and Campbell (1985) observed that V_s increases as a power law with depth for various Quaternary age soils. More recent studies by Brown, Boore, & Stokoe (2002), Andrus et al. (2003, 2007), and Foti (2012) have shown similar trends. On the other hand, the measured V_s profiles at the SRS show the opposite trend with V_s decreasing with depth.

Field geophysical measurements of S-wave velocities were made at many locations within the SRS boundaries. These measurements were made using a variety of geophysical techniques, including crosshole testing (CHT), downhole (DHT), suspension logging (SPL), and surface wave methods (SASW, MASW). Many of the DHT type have been obtained using the

seismic cone penetrometer test (SCPT). A representative trend can be seen in Figure 5-2 that summarizes a total of 87 V_s profiles from SCPT compiled from the SRS APT site. Notably, the V_s measurements decrease with depth at this site in the upper 15 m, followed by a rather constant value of about 350 m/s to depths of around 50 m. The very high shear wave velocities (300 m/s < V_s < 700 m/s) at shallow depths (z < 15 m) are indicative of highly overconsolidated soils, desiccated geomaterials, and/or cemented sands, or likely even a combination of those factors together.

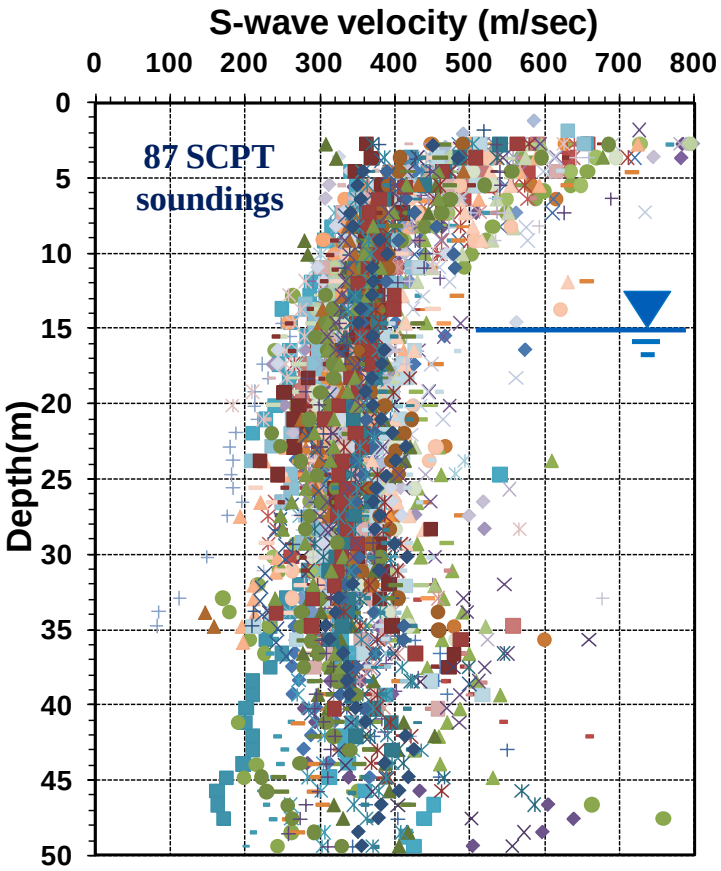

Figure 5-2. Compilation of Shear Wave Velocity from 87 Downhole Test Series at SRS APT

In the past 3 years, a series of Rayleigh wave measurements (SASW) at SRS were made by Dr. Glenn Rix and GT graduate students, and these are compared with the downhole type mean V_s profile in Figure 35a for the upper 70 m of overburden. Overall, the V_s magnitudes seem comparable for both methods, excepting the uppermost 10 m. This upper zone consists of unsaturated sediments of the Altamaha formation and Upland Terrace Deposits. Here, the seasonal variations of capillarity, desiccation, infiltration, and degree of saturation could easily have affected the results depending upon the actual conditions during the specific days of the tests (Ku, Mayne, and Gutierrez 2012). At the Sand Borrow Pit, the V_s magnitudes from SASW are more difficult to compare directly because the surface elevations are different because of 15 m of excavation. Nevertheless, the results appear comparable.

Figure 5-3b provides a summary of the mean shear wave profiles at other SRS area locations (data summarized by Li et al. 2010). Most V_s data were downhole type (i.e., 579 SCPTu, 4 SDMT, and 2 borehole-type DHT), although some are also derived from other techniques (32 crosshole and 11 suspension logger). It is observed that the in-situ V_s profiles show similar trends across the region. Also, shear wave data for the nearby Plant Vogtle nuclear plant are comparable and show similar results (Cooke, Lancaster, & Depree 2007).

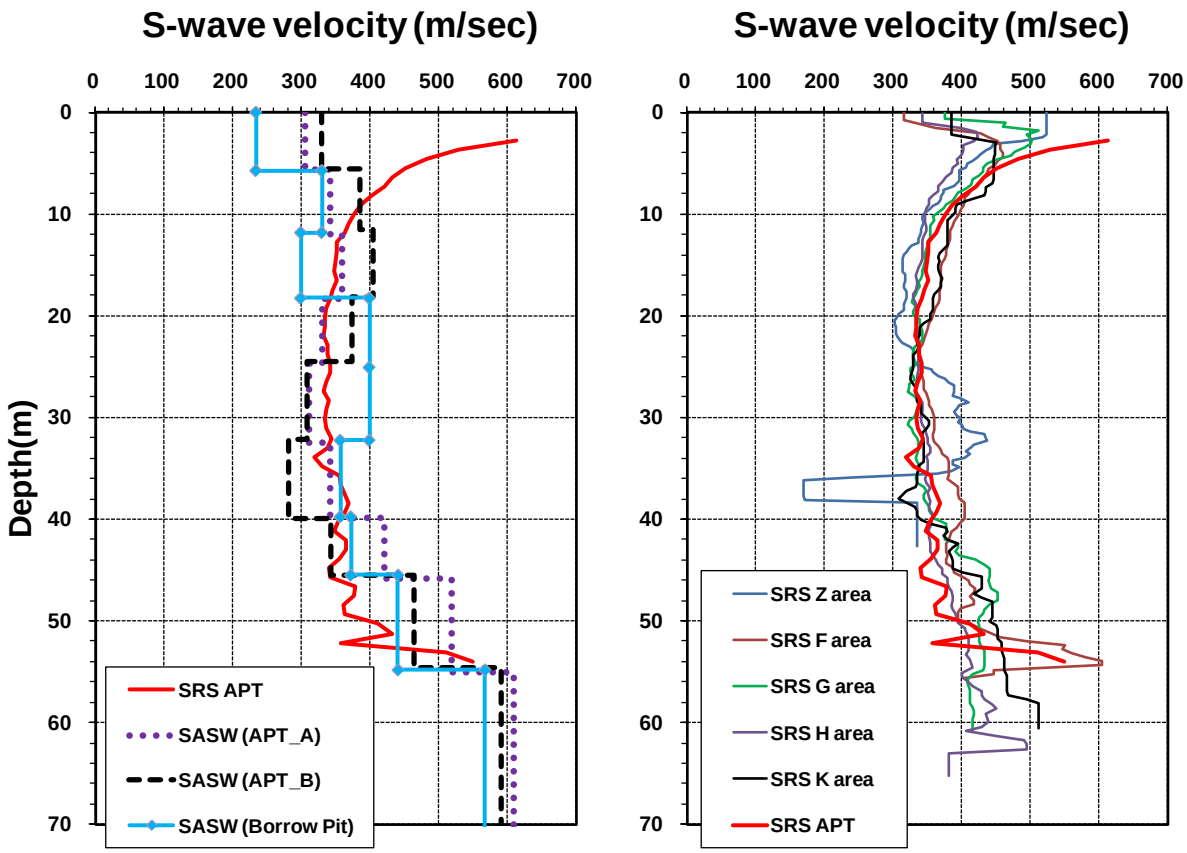

Figure 5-3. Shear wave data from SRS: (a) Comparison of SASW and DHT at the APT site, (b) comparison of average V_s profiles at various SRS areas (adapted after Li et al. 2010).

For several of the comprehensive investigations at SRS, crosshole type V_s and suspension logging V_s measurements were obtained at greater depths in order to provide site-specific stiffness values for analyzing seismic ground hazards and numerical simulations of ground behavior (SRS report 2005). Figure 5-4 compares those deeper V_s data from crosshole testing (CHT) and SASW measurements to 150 m depth range with the shallower DHT type V_s measurements. In the upper 50 meter depth, the crosshole V_s are comparable to the downhole-type V_s. However, the interpreted suspension logging data have coarser resolutions and rather

lower values. In the deeper Eocene sediments such as Blue Bluffs Marl (BBM) - Warley Hill Formation (WHF) from 50 to 70 meter depths, Paleocene deposits from 70 to 100 m, and Cretaceous geomaterials with z > 100 m, the Rayleigh wave measurements show the largest magnitudes of V_s in the profile. One hypothesis for this is perhaps the SASW Rayleigh waves have converted to an HH-type S-wave and that high lateral K_0 stress states exist in the BBM/WHF strata. For instance, at a depth range of 50m to 90 m with V_{sHH} = 600 to 650 m/s and V_{sVH} = 300 to 450 m/s, the ratio of HH/VH waves = 1.5 to 2 suggests K_0 values of between 3 to 4. These very high lateral stress states in the Blue Bluffs Marl can be explained by the high degree of overconsolidation in these hard calcareous clays. Estimated preconsolidation stresses in the Lisbon Formation of the BBM are on the order of 4 MPa at Plant Vogtle (SNOC 2008).

For additional consideration, a series of special rotary type crosshole testing (RCHT) that uses a horizontal source, torsional vane, or rotary hammer can be used to obtain companion sets of HH-waves coupled with downhole VH type shear waves to ascertain and assess the in-situ stress state and lateral stress anisotropy (Ku 2012; Ku & Mayne 2013a, 2013b). By the same methodology, the agreement of the shear wave velocity magnitudes of the CHT, DHT, and SASW surveys suggests that the K_0 values are much lower (K_0 < 0.7) in the depth intervals from 20 to 50 m.

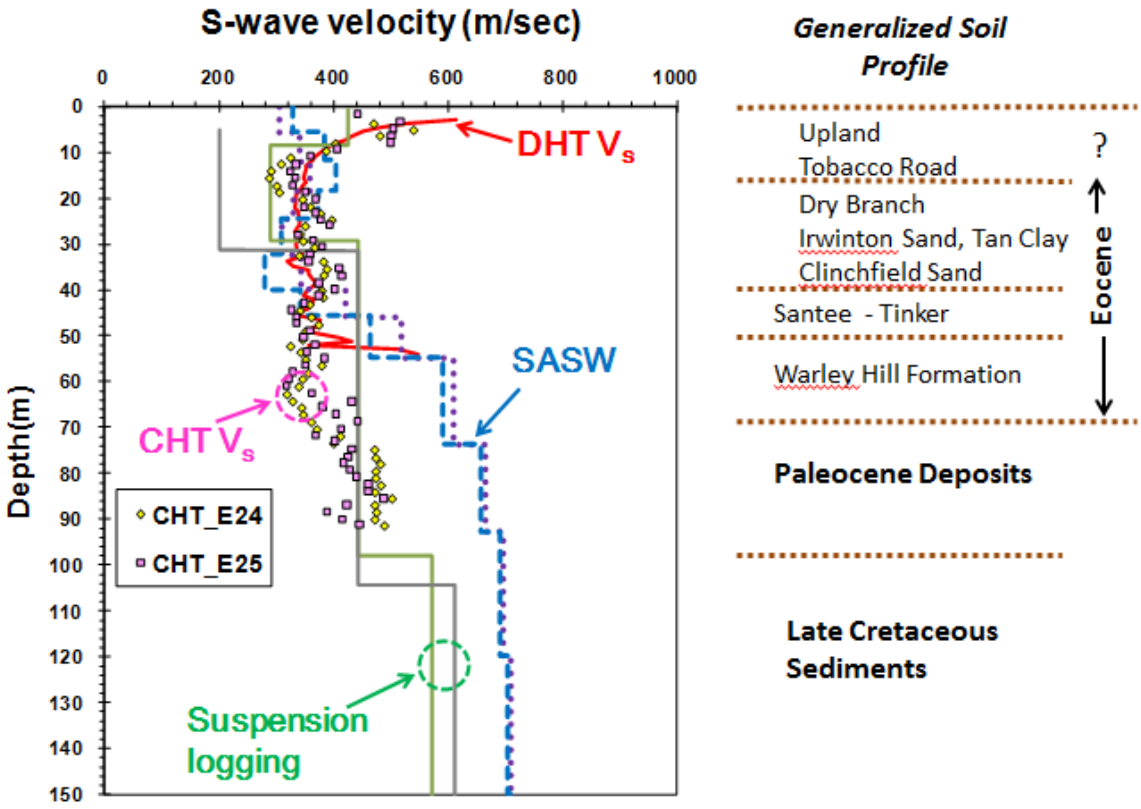

Figure 5-4. Comparison of various types of V_s measurements to 150 meter depths at SRS.

5.3 In-Situ Tests at SRS

In addition to shear wave velocity measurements, the predominant means of site exploration and collection of field geotechnical data at SRS include cone penetrometer testing (CPT) and soil borings with standard penetration testing (SPT). For most of the CPT soundings, seismic piezocone penetrometers were used to obtain downhole type shear waves, thus SCPTu data are available. At some locations, including the recent SWPF, flat plate dilatometer testing (DMT) was also utilized during site investigations. Selected topics concerning the interpretation of in-situ test results are discussed herein, including: (a) soil identification; (b) calcareous soils;

(c) void detection; and (d) stress history evaluation. Additional topics related to in-situ testing are addressed in Ku (2012).

A summary of energy-corrected SPT resistances from the SWPF are given in Figure 5-5 showing considerable variability at any given elevation in the soil profile. Localized lower N_{60} values in the depth zones from 10 to 15 m and 25 to 27 m are indicative of clay layers or high clay fines content. The historic SRS criterion (Aadland et al. 1999) for identification of the void-soft zone with $N_{60} < 5$ bpf is shown as a red vertical line.

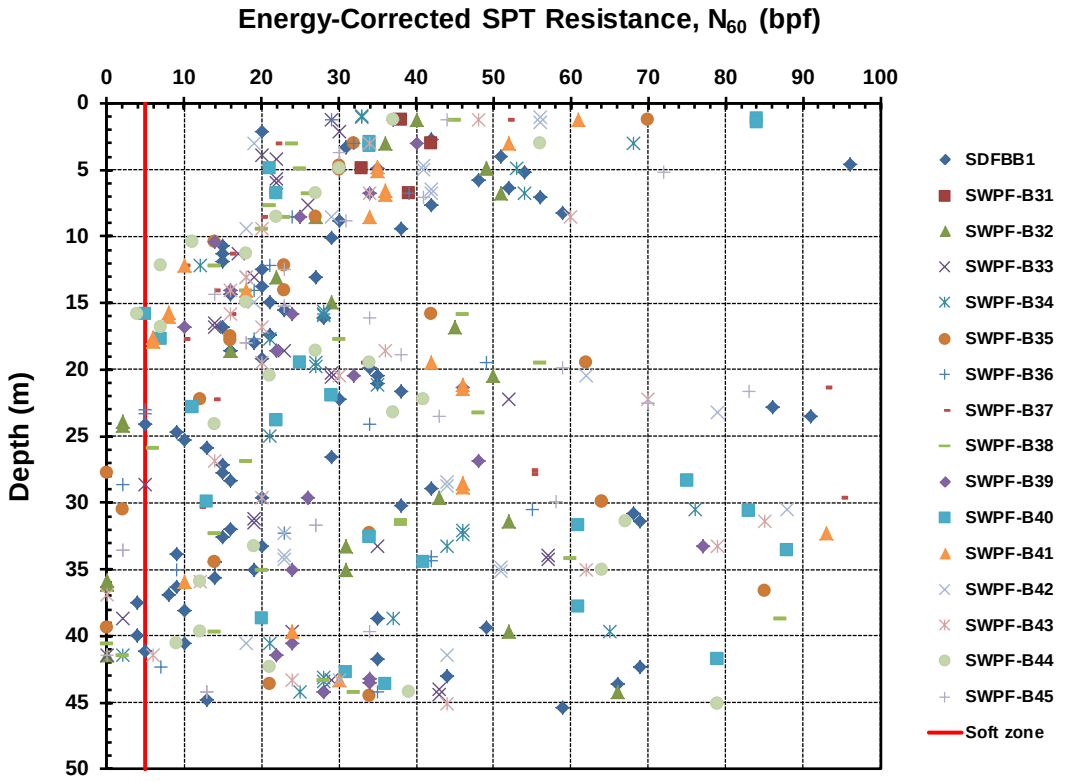

Figure 5-5. Summary of SPT N_{60} values at Salt Waste Processing Facility (data from Buechel 2007).

For the CPT, there are 3 continuous readings obtained with depth for each sounding: cone tip resistance (q_t), sleeve friction (f_s), and penetration porewater pressure (u_2). In Figure 5-6, a summary is presented of the mean CPT readings (plus and minus one standard deviation) with depth from a total 147 soundings at the APT site; results were also compared in terms of elevation (Figure 5-7).

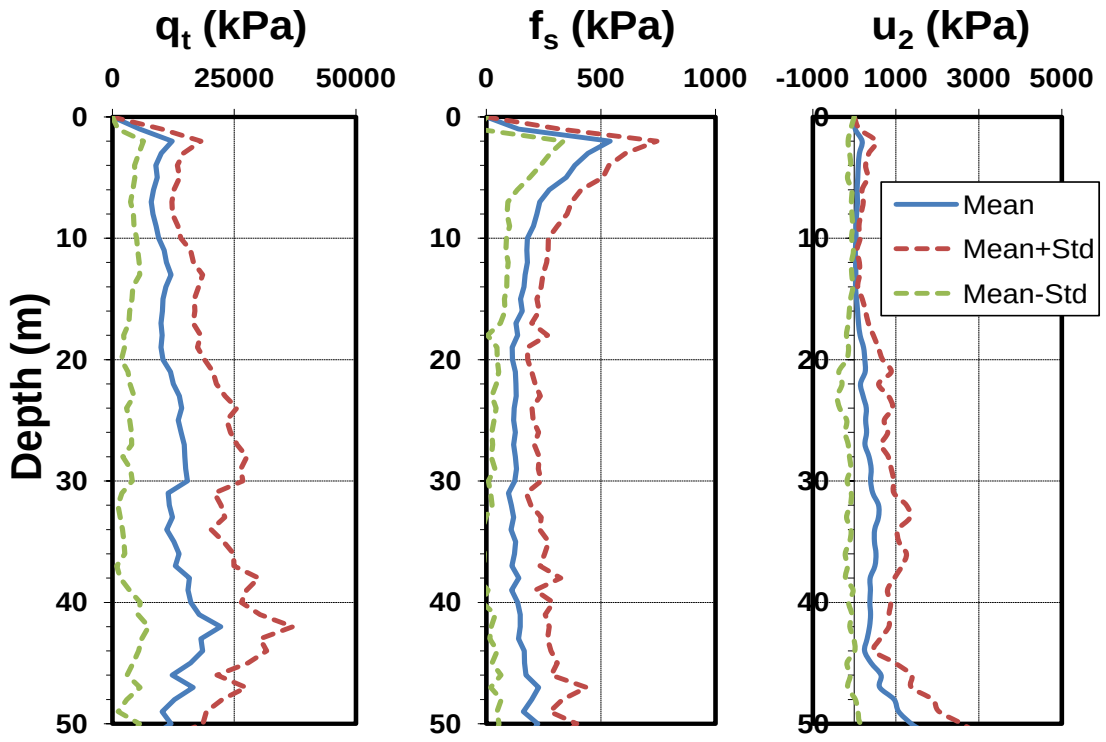

Figure 5-6. Summary of mean readings (± one S.D.) from 147 CPTs at SRS APT site

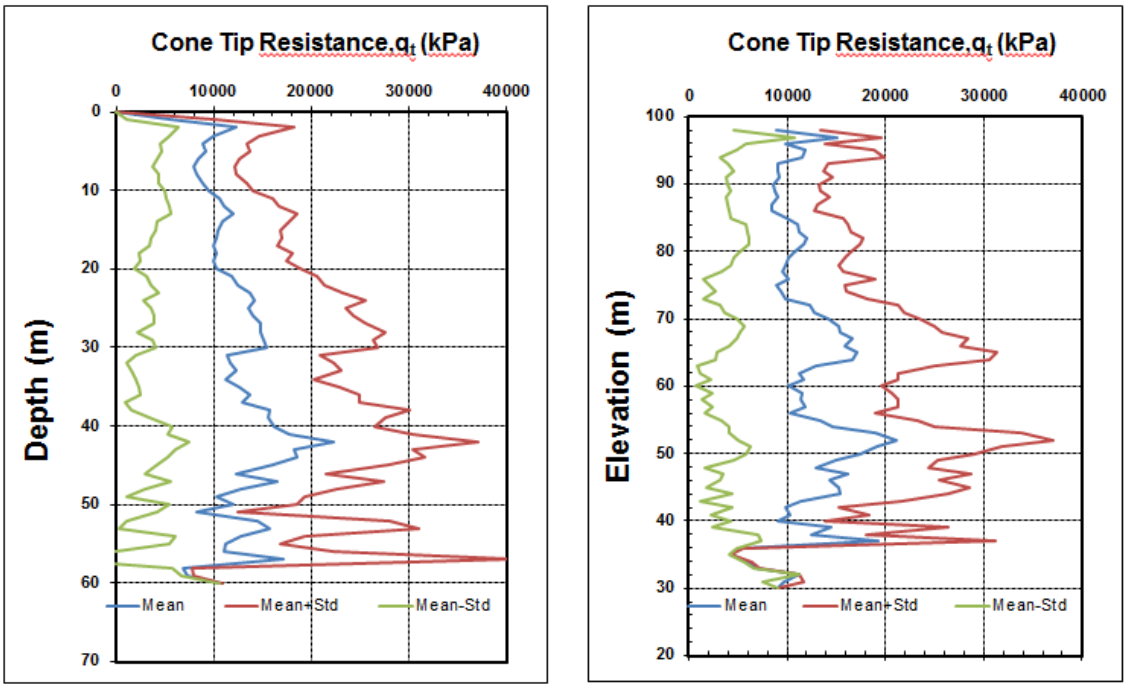

Figure 5-7. Statistics from APT site using data from 147 CPT soundings for cone tip resistance plotted with (a) depth; (b) elevation

5.3.1 Soil Type and Classification

Soil classification is conventionally handled by subjecting recovered samples to a combination of visual-manual identification and ancillary laboratory methods using grain size distributions and/or plasticity index tests, generally per ASTM D 2487 and D 2488 guidelines that detail the Unified Soil Classification System (USCS). Mechanical analyses using sieves are performed on particles with grains > 0.075 mm, while hydrometer tests are used to estimate particle sizes when particles < 0.075 mm. In some instances, undisturbed thin-walled tube samples (ASTM D 1587) are procured during drilling operations, while the vast majority of soil samples are obtained from split barrel (or spoon) samplers per ASTM D 1586. As discussed previously, the sandy soils at SRS appear as gap-graded type geomaterials because of the low silt

fraction and apparent high clay or colloidal components. In fact, the USCS details the clay and/or silt fraction not by the percentage of such particles (as does the European CEN or international ISO standards), but by the plasticity characteristics (LL = liquid limit and PI = plasticity index) on the materials passing a No. 40 sieve. A summary of the percentages of sand, silt, and clay are given from mechanical analyses using a No. 200 sieve (0.075 mm size) and hydrometer tests.

The evaluation of soil classification by direct-push technologies (i.e., CPT and DMT) requires an indirect approach. For the CPT, soil behavior type (SBT) profiles are obtained using a material classification index (I_c), as detailed by Robertson & Wride (1988). Mean CPT readings with depth using the APT soundings are presented in Figure 5-8 for cone tip resistance (q_t), sleeve friction (f_s), and penetration porewater pressure (u_2), respectively. Using the updated procedures established by Robertson (2009), the corresponding I_c profile with depth is presented in Figure 5-8. As noted, the predominant soil types are identified as sandy soil mixtures throughout the profile to approximately 47 m depth. The soil behavior type appears reasonable when compared with sample gradation curves from laboratory tests on soil samples taken from SRS (Figure 5-8), with good agreement. A similar analysis can be obtained using the site-specific material index developed by Syms (2002).

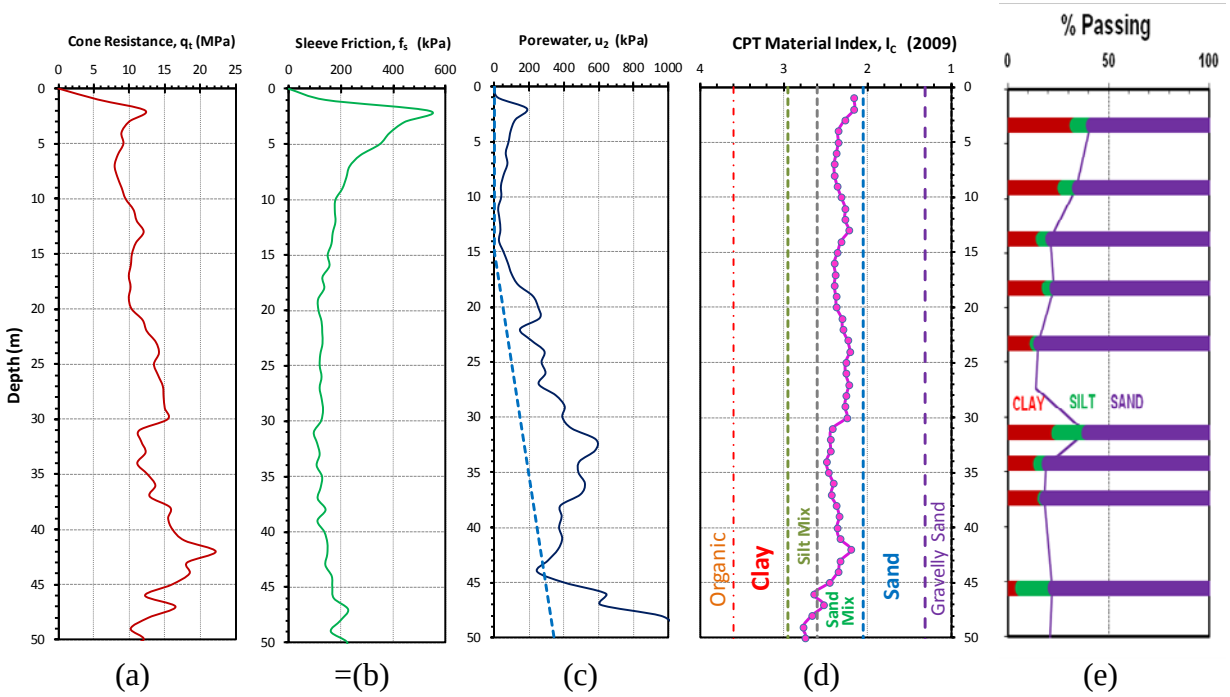

Figure 5-8. Mean CPT results with depth from APT site: (a) cone tip resistance; (b) sleeve friction; (c) porewater pressure; (d) material index of Robertson and Wride (1998); and (e) particle size distribution from laboratory testing on recovered soil samples.

For the DMT, a material index I_D is used to assess soil type (Marchetti, 1980). A total of 13 flat plate dilatometer test (DMT) soundings were obtained at the Salt Waste Processing Facility (SWPF) site. The mean values of contact pressure (P_0) and expansion pressure (P_1) profiles with depth are shown in Figure 5-9. Similar to the CPT analysis, a representative soil type profile on the basis of DMT material index (I_D) is provided in Figure 5-9. Here the I_D profile suggests sandy silt mixtures from 0 to 15 m ($1.2 < I_D < 1.8$) which are underlain by silty sands to about 40 m ($1.8 < I_D < 3.3$). Note that clean sands are identified by $I_D > 3.3$ and that the empirical DMT methodology does not distinguish between silty sand versus clayey sand. The one or two DMT soundings that extended below 40 m show variable profiles and suggest the presence of fine-grained soils (silts to clays) to final termination depths of 48 m.

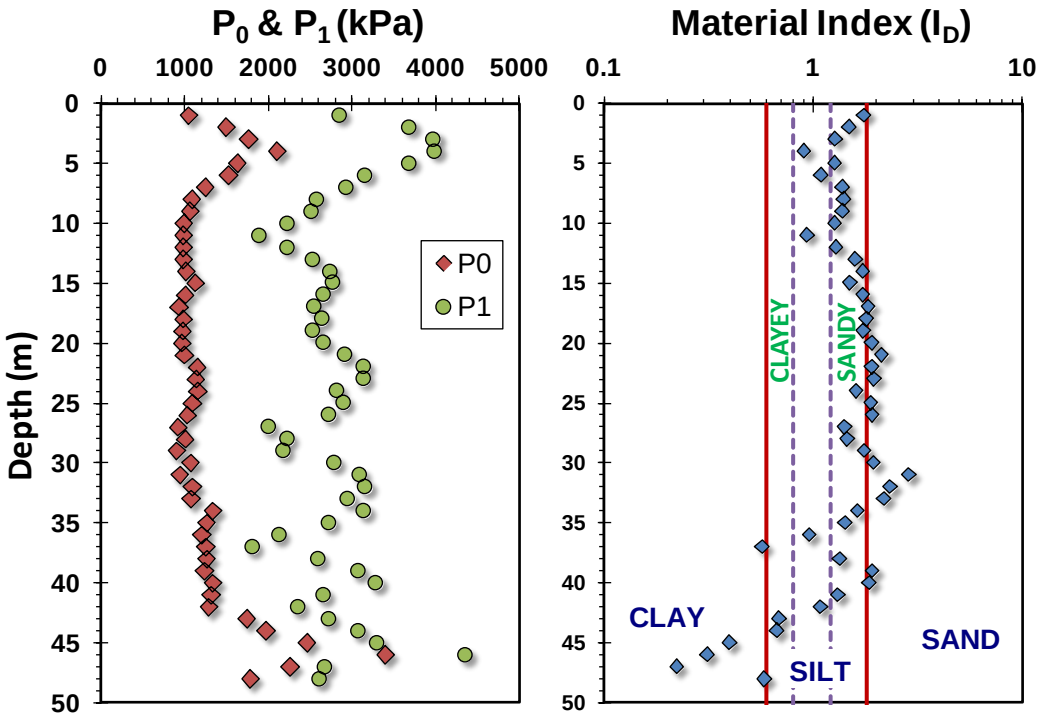

Figure 5-9. DMT profiles at SWPF: (a) mean lift off pressure (P_0) and expansion pressure (P_1) with depth; and (b) representative soil behavior type from DMT material index.

5.3.2 Calcareous Soils

According to downhole geophysical logging data and laboratory results on borehole samples at SRS (Laura Bagwell, SRNL 2008), certain soil layers show a calcareous and carbonate composition. Evidence of calcareous sediments at SRS was verified by both x-ray diffraction and chemical testing (Larrahondo-Cruz 2011). With respect to penetration testing in calcareous sands, it is known that carbonate grains are more easily broken and are relatively crushable. In addition, calcareous sands consist of angular particles, show high void ratios, and rather weak structure, when compared to harder and more resistant quartz and silica sands

(Semple 1988; Lunne et al. 1997). Variable cementation can also be observed in carbonate/calcareous sands. Sample disturbance effects tend to be significant for calcareous soils.

Carbonate sands may be detected by subtle inspection of CPT measurements, but the results are not always definitive nor conclusive. Figure 5-10 shows a comparison of CPT data from calibration chamber tests on 24 different silica-quartz sands versus data from 6 series on calcareous-carbonate sands. Results are presented in terms of stress-normalized cone tip resistances (Mayne 2007). It is observed that the magnitudes of cone resistance in calcareous sands are generally about half the magnitudes of those in siliceous-quartzitic type sands at the same relative density (D_R). If calibrated on a site-specific basis, the presence of calcareous sands can be identified using CPT soil classification charts such as the q_t - FR plot developed by Ebelhar et al. (1988).

Figure 5-11 describes the identification of calcareous sands within the SRS soil column based on a representative CPT sounding of q_t and f_s profiles (#C21) recorded at the SRS K-site. Here, a normalized plot based on the soil behavioral type (SBT) charts of Robertson (2009) has been used to represent the data into groupings of normalized Q and F. While values of Q are comparable for both upper and lower sands, there seems to be an apparent reduction in the normalized friction ratio (F) for the calcareous sands found in the depth range from 23 to 28 m, compared with higher F values in the upper sands that are siliceous. Similar findings have been reported in calcareous sands at Ledge Point north of Perth, Australia (Schneider & Lehane 2010).

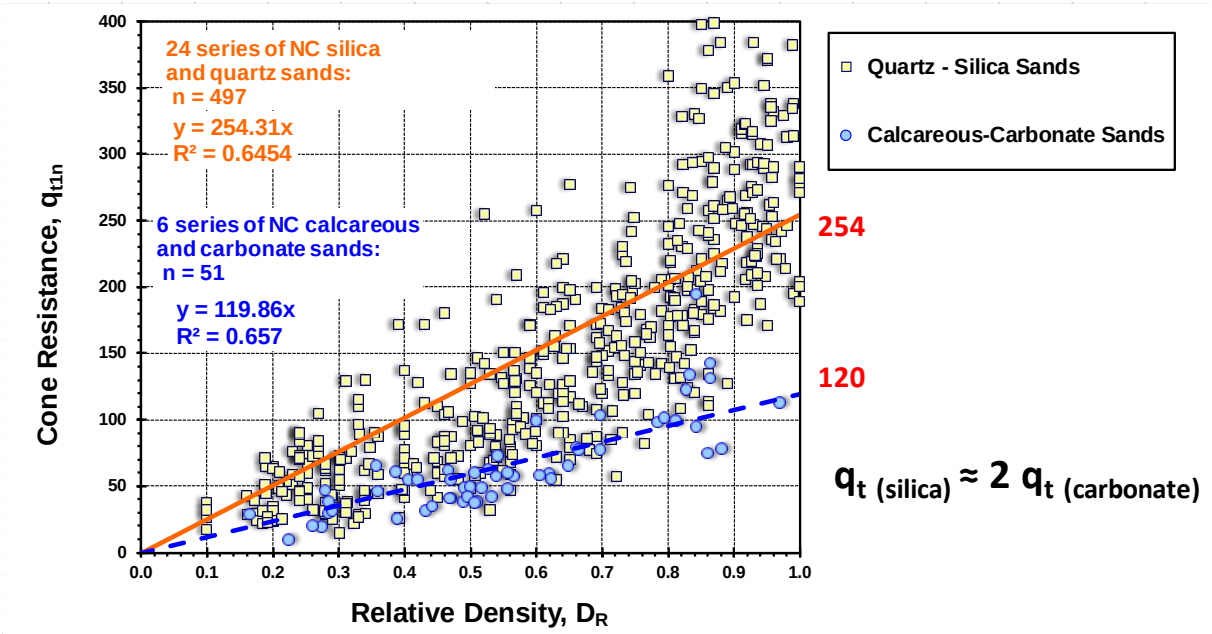

Figure 5-10. Normalized cone resistances at the same relative density from calibration chamber tests: Comparison of siliceous versus calcareous sands.

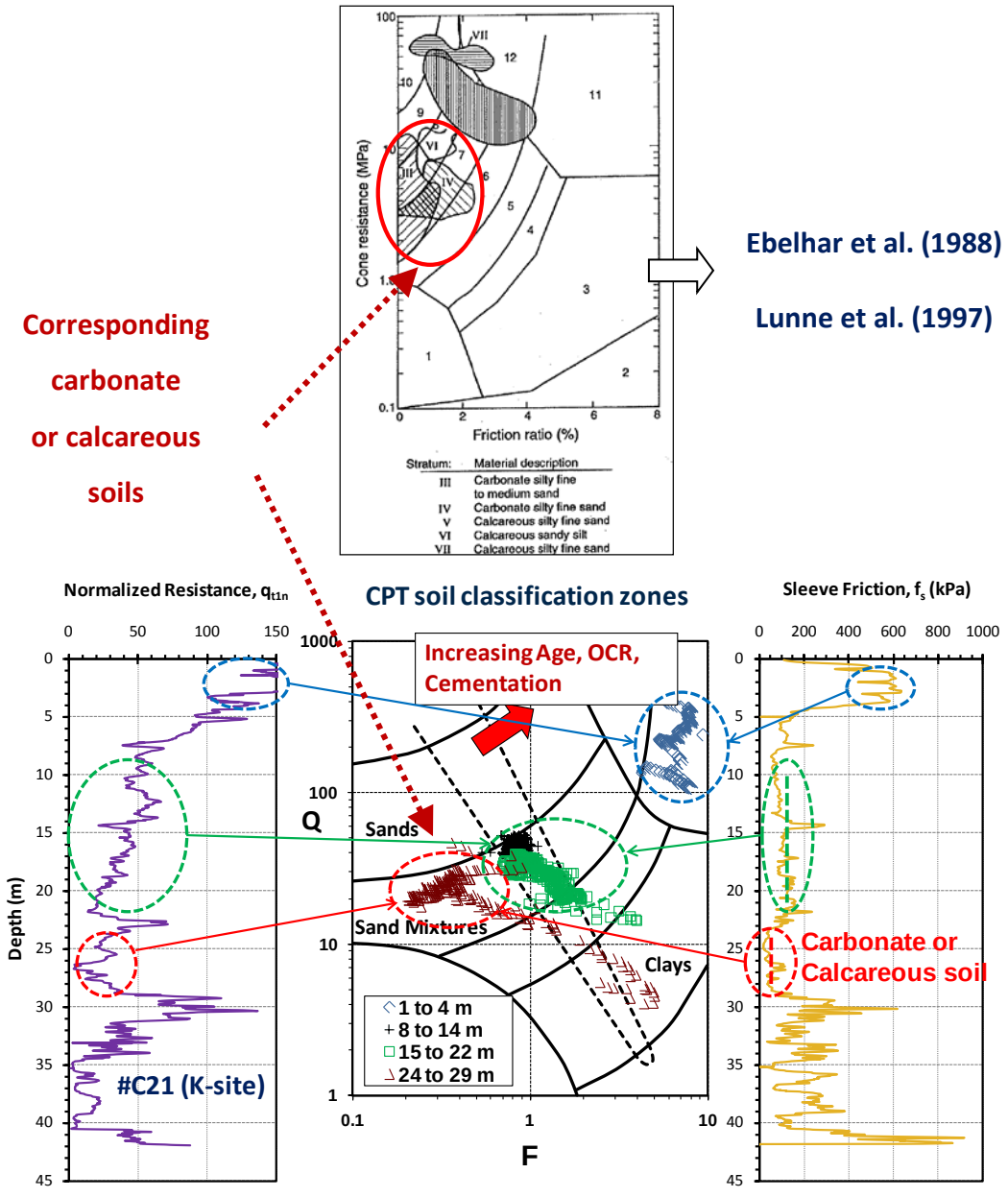

Figure 5-11. Identification of calcareous sands at SRS K-site using method CPT soil classification chart by Ebelhar et al (1988).

5.3.3 Detection of Soft Zones/Voids

According to the summary report by the Washington Savannah River Company (WSRC 2007), the criteria for soft zone identification at SRS are defined as follows:

(1) Criteria based on in-situ penetrometer testing:

(1a) CPT: cone tip resistance (q_t) < 1.5 MPa (15 tsf)

(1b) SPT: blow count (N) ≤ 5 blows/ft

(2) Geologically located in Tinker/Santee formation or lower Dry Branch formation

(3) Continuous vertical thickness ≥ 0.6 m (2 feet), or professional judgment

(4) Consolidation test data: OCR < 1

(5) Atterberg limit data indicating moisture content > liquid limit

Among the above multi-criteria, the possibility of detecting soft zones and/or voids can be further investigated based on CPTu data. A total of 47 piezocone penetration tests (CPTu) were obtained at the SRS K-site by Lankelma Group under contract to DOE/SRS in 2011. Mean values of cone tip resistance (q_t), sleeve friction (f_s), and porewater pressure (u_2) are provided in Figure 5-12 as a summary graph.

As noted, the magnitude of q_t in a soft zone or void is defined as a value less than 1.5 MPa. Generally, for intact clays, the magnitude of penetration porewater pressure (u_2) is approximately half of the q_t magnitude (Mayne et al. 1990). However, if there are significantly large voids in Santee formation, the u_2 may be fully or partially dissipated, perhaps close to hydrostatic (u_0). Hence, the magnitude of u_2 in soft zone including voids is expected to be much less than that observed in a representative clay layer. For instance, Figure 5-13 and Figure 5-14 show tentative detection procedures for soft zones and/or voids. In the corresponding elevation ranges of soft zone – voids, the measured u_2 is considerably less than the upper thin clay layers which also exhibit rather low q_t values. Notably, however, the q_t in these clay layers is around 2.5 to 3 MPa, which is slightly higher than the threshold criterion of 1.5 MPa generally used at

SRS. As 7 possible scenarios have been put forward for the occurrence of voids-soft zones, the possibility of pressurized encapsulated caves and/or artesian conditions may also occur as well.

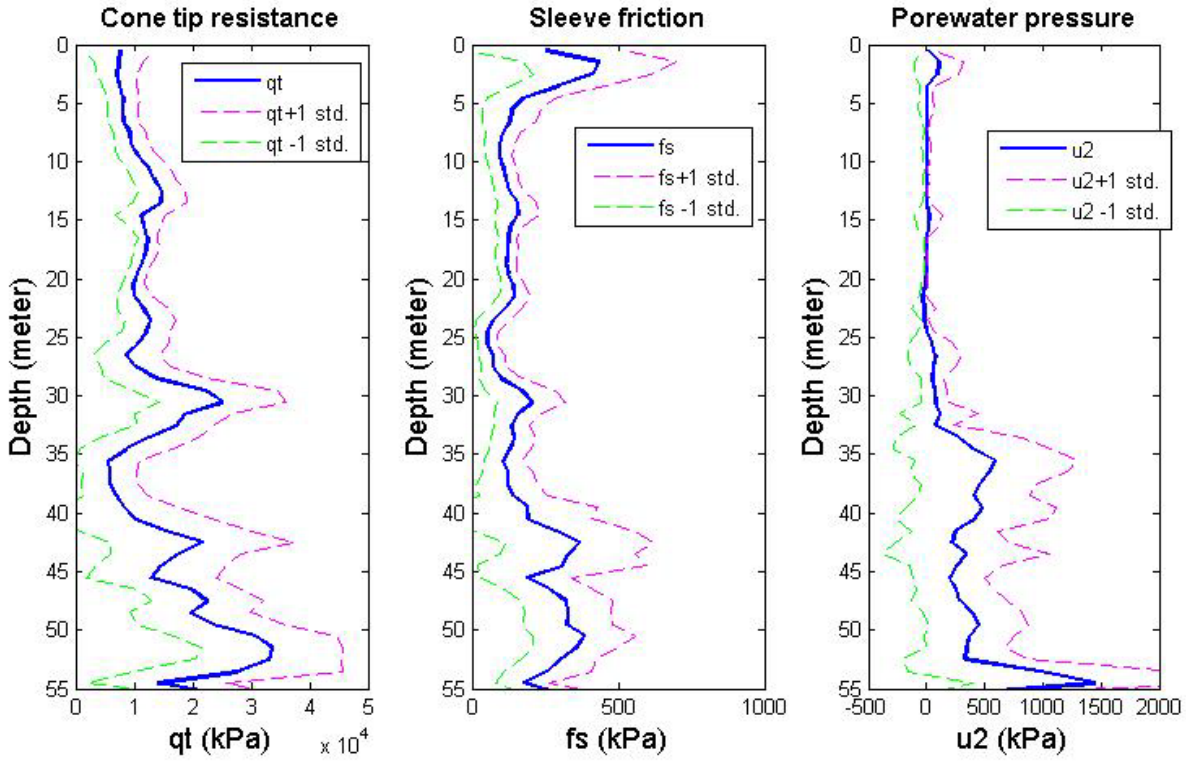

Figure 5-12. Mean CPT profiles from 47 soundings: (a) cone tip resistance, (b) sleeve friction, and (c) porewater pressure at SRS K-site.

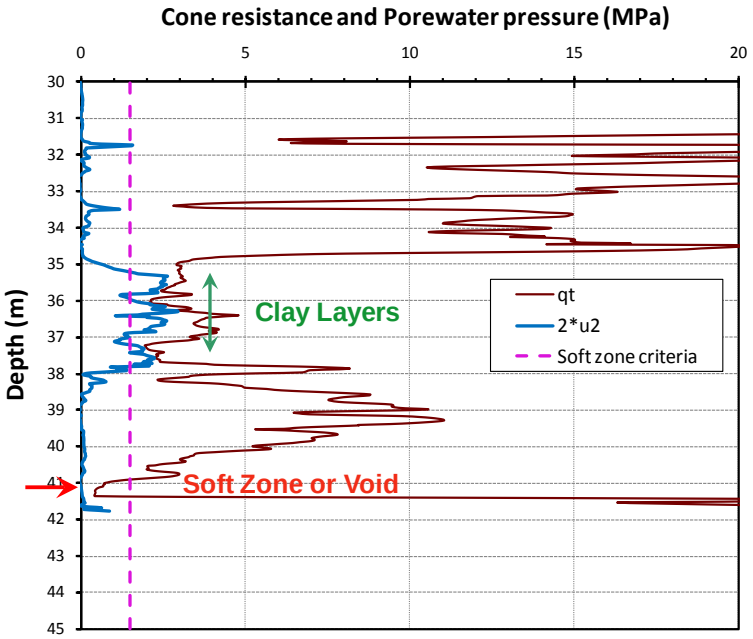

Figure 5-13. Identification of clay layers and detection of the soft zone or void using coupled q_t and u_2 data (Sounding CPT ID:K-PDC-14) at SRS K-site.

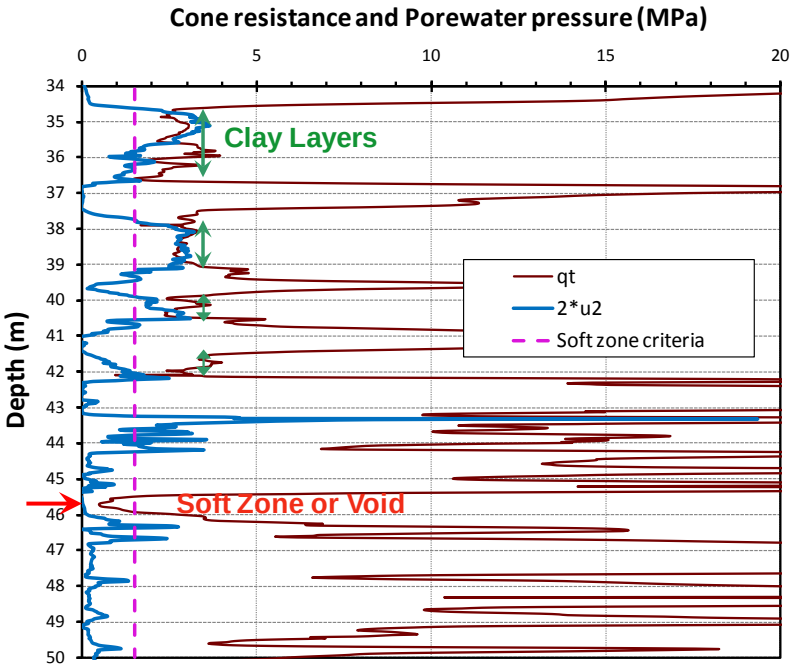

Figure 5-14. Identification of clay layers and detection of soft zone/or void using coupled q_t and u_2 data (CPT ID:K-PDC-25) at SRS K-site.

In the same manner, the CPT data from K-area were reviewed with the aforementioned criteria to detect soft zones and/or voids. Cone penetration profiles are shown in Figure 47. The surface conditions here are nearly level and most cone soundings were advanced more than 40 meters deep. Yellow coloring indicates clays which are evaluated based on CPT soil behavioral classification that occur mainly between 30 and 40 meter depth intervals. Probable soft zones/or voids are marked by red coloring in Figure 5-15. It was also observed (Ku 2012) that the I_c value in detected voids or soft zones was undefined, as due to a calculated negative Q value ($Q < 0$). Among a total of 47 CPT soundings, the detected voids or soft zones having q_t less than 1.5 MPa and low u_2 were found in 24 CPT soundings, or approximately a 50% occurrence rate in K-area. Figure 5-16 shows the implied vertical sizes of the detected soft zones/voids, although field mapping and experience shows the lateral dimensions are usually much greater (Syms 2010).

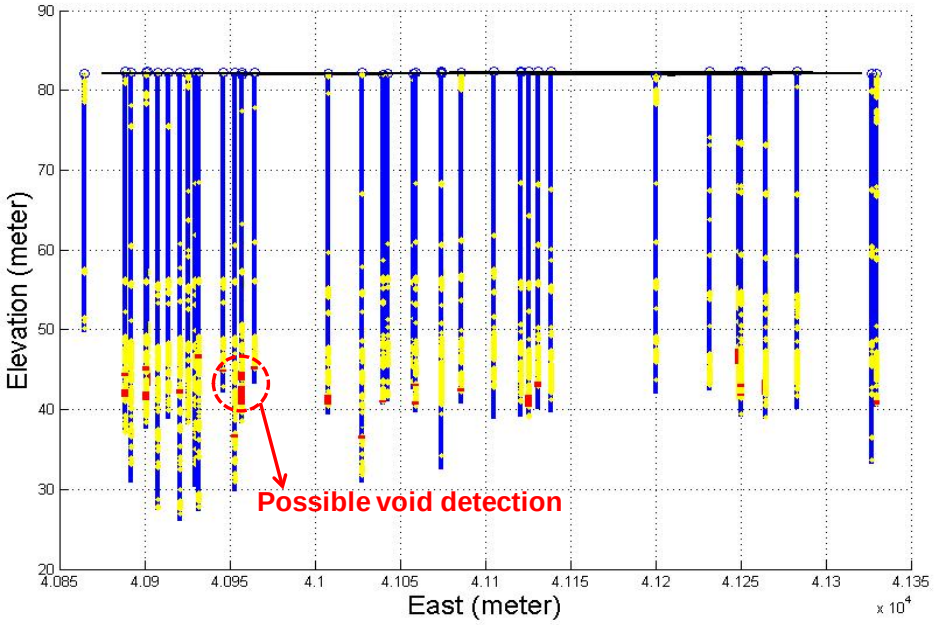

Figure 5-15. CPT profile (East-West direction) with identified clay layers (yellow zone) and probable soft zone/or void (red zone) in K-area.

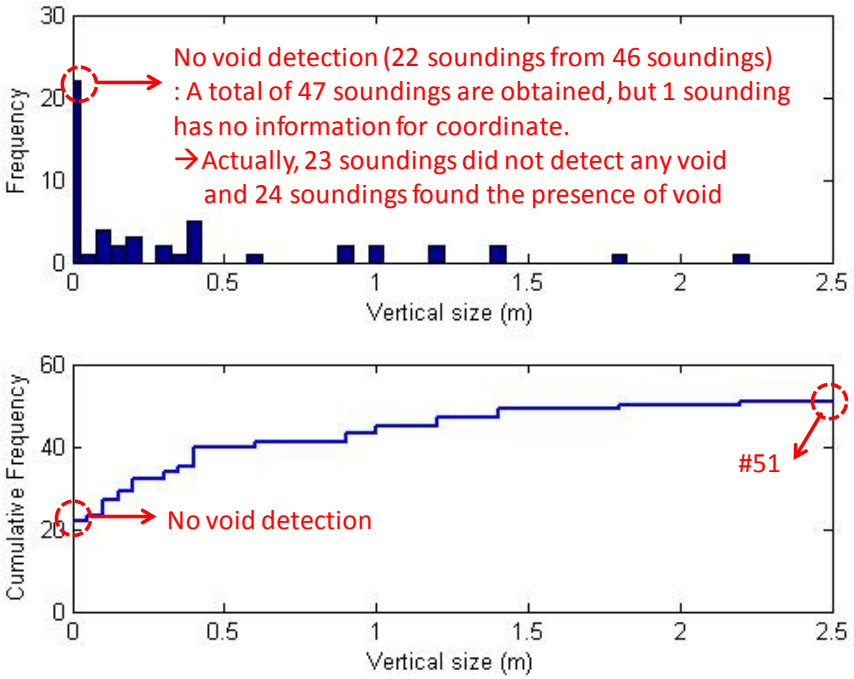

Figure 5-16. Void detection frequency versus CPT-estimated vertical size of detected voids at SRS K-site.

5.4 Geostatic Stress History at SRS

The traditional means to evaluate stress history is via one-dimensional consolidation tests on undisturbed samples. In this regard, the preconsolidation stresses were independently evaluated from the laboratory consolidation test data from the SRS SWPF site (Shannon & Wilson 2007). A total of 41 incremental load (IL) tests and 58 constant-rate-of-strain (CRS) tests were analyzed using several interpretative schemes: (a) Casagrande (1936), (b) Becker et al. (1987), and (c) Boone (2010), as well as other approaches (Ku 2012). To quantify the level of laboratory sample disturbance, a *sample quality index* (SQI) rating system developed by Terzaghi et al. (1996) was adopted herein. The scale for the SQI rating criteria is shown in Table 6 and categorizes specimens from 'A' (excellent) to 'E' (very poor quality), based on the measured volumetric

strain [$\varepsilon_{vol} = \Delta e/(1+e_o)$] needed to re-attain the in-situ effective vertical overburden stress (σ_{vo}') after reloading the sample in a laboratory one-dimensional consolidation test.

Table 6. Scale for *Sample Quality Index* (SQI) for rating degree of sample disturbance from laboratory consolidation data (after Terzaghi et al.,1996)

Volumetric strain ε_{vol} (%)	< 1	1 - 2	2 - 4	4 - 8	> 8
Quality	A Excellent	B Good	C Fair	D Poor	E Very Poor

Note: $\varepsilon_{vol} = 100 \cdot \Delta e/(1+e_o)$ = volumetric strain to recover specimen to its in-situ effective vertical stress, σ_{vo}'

The interpreted yield stresses or preconsolidation stresses (σ_p') from the SWPF consolidation test data are provided in Figure 5-17 based on the common graphical Casagrande procedure. Lab measured values for unit weight, which matched well with the in-test estimated results, were used in the calculations. The generalized soil profile by geologic units at the SWPF area is also presented on the right-hand side of the figure. While sample disturbance appears significant throughout, the estimated values of preconsolidation stresses appear considerably scattered, regardless of depth. Interpretations of σ_p' using alternate graphical methods show similar high variability (Ku 2012).

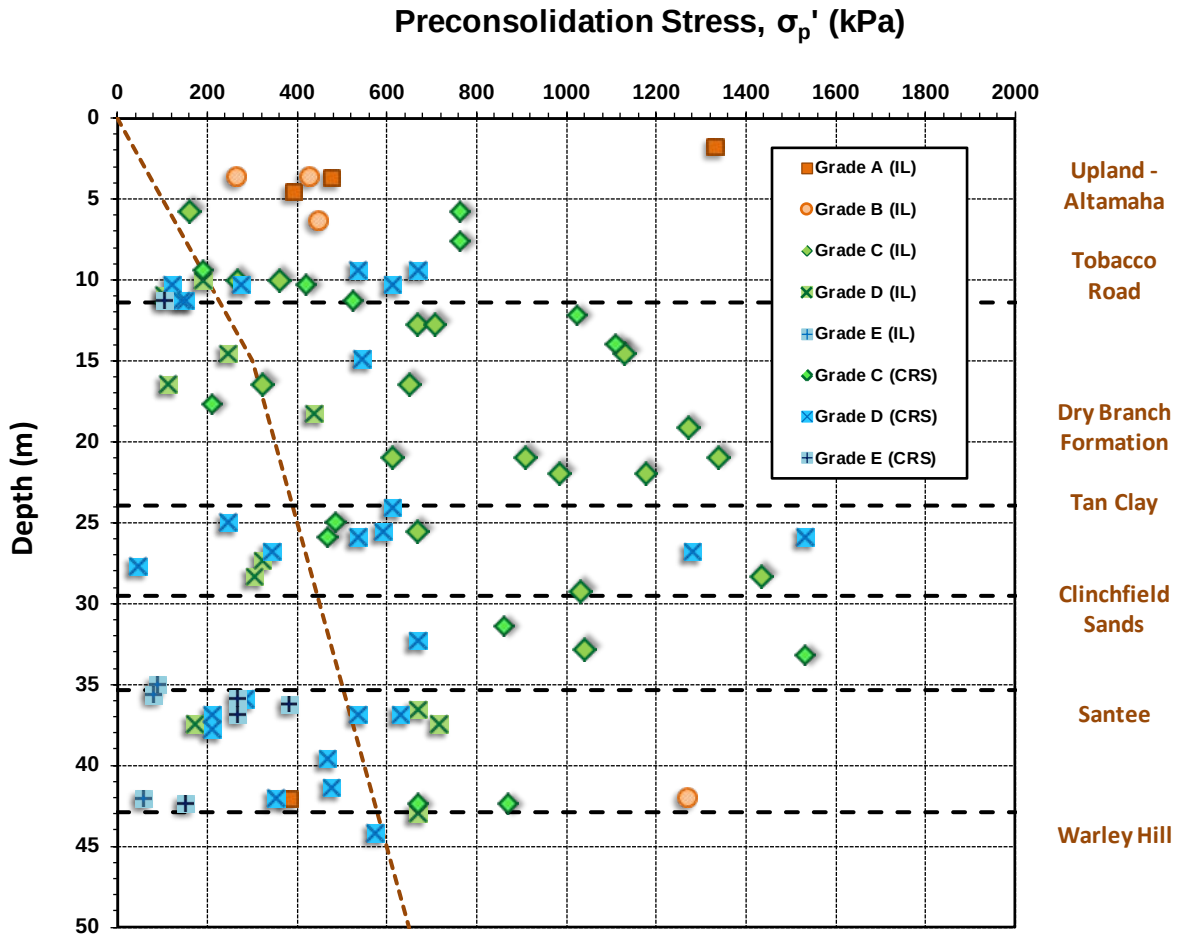

Figure 5-17. Evaluation of preconsolidation stress (σ_p') from laboratory consolidation tests at SWPF using Casagrande interpretation procedure and SQI rating for degree of sample disturbance. Notes: IL = incremental load, CRS = constant rate of strain, Sample quality index, SQI: A = excellent, B = good, C = fair, D = poor, E = very poor.

Overall, considering the very old geologic ages of the SRS deposits (Eocene and Miocene age), the stress history profile estimated from in-situ and laboratory tests appears unusual. It would be expected that such old deposits would have more consistent and less variable preconsolidation stress (σ_p') profiles with depth (varies from 40-1600 kPa). In fact, other well-documented Atlantic Coastal Plain deposits which are also have a calcareous component show

rather consistent σ_p' profiles including: (a) Calvert Formation, Richmond VA (Martin and Drahos 1986); (b) Yorktown Formation, Newport News VA (Mayne 1989); (c) Calvert Cliffs, MD (Unistar Report 2010); and (d) Cooper Marl, Charleston SC (Camp 2004).

Notwithstanding inevitable sample disturbance effects, the very large ranges and scattered variations in preconsolidation stress (and associated OCRs) may have resulted from the noted complex geologic conditions at SRS. As a consequence of the alterations of the Santee causing voids, soft zones, and cave formation by dissolution processes, the geostatic stress state of the overlying overburden may have been altered. A collapsing of the soil columns, coupled with arching and/or faulting, as well as subsidence, may have reduced the magnitude of overburden stresses. If localized portions of the upper soil column are assumed to have collapsed, some regions might be altered to active lateral earth stress states (K_A) while other regions remain at relatively high at-rest lateral stress states (K_0), specifically in the case of highly overconsolidated intact soils. Figure 5-18 describes graphically this possible scenario.

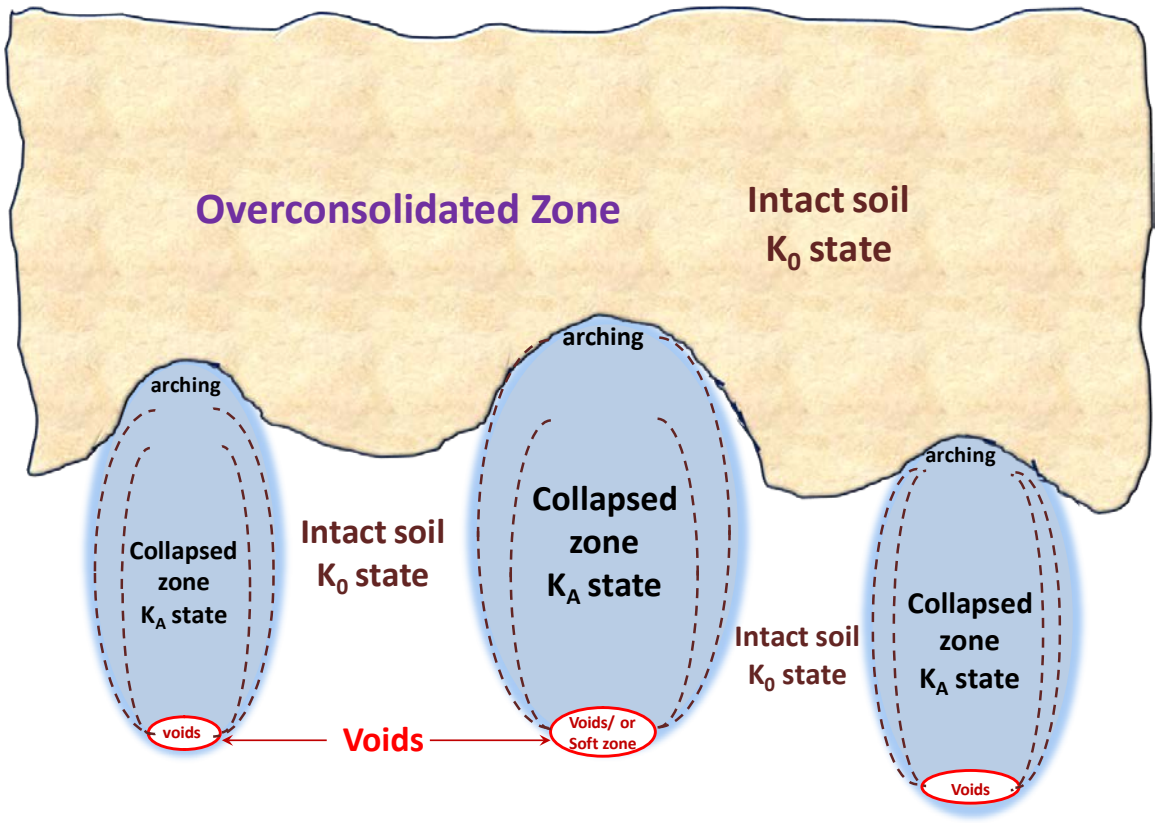

Figure 5-18. Hypothesis of collapsed soil column resulting from voids or soft zones.

This scenario fits with the noted scatter of laboratory consolidation results that implicate stress states ranging from underconsolidated to normally-consolidated to moderately and overconsolidated states, at all elevations (Figure 5-17). This is consistent with profiles of stress history (σ_p') and K_0 evaluations based on 13 DMT soundings from SWPF area, as shown by Figure 5-19 and Figure 5-20, respectively. At some locations of the DMT soundings, unusual stress states are observed, including underconsolidated and/or significantly low lateral stress states < K_A, which are anomalous when compared to nearby DMTs that show OC states and "normal" K_0 states of stress.

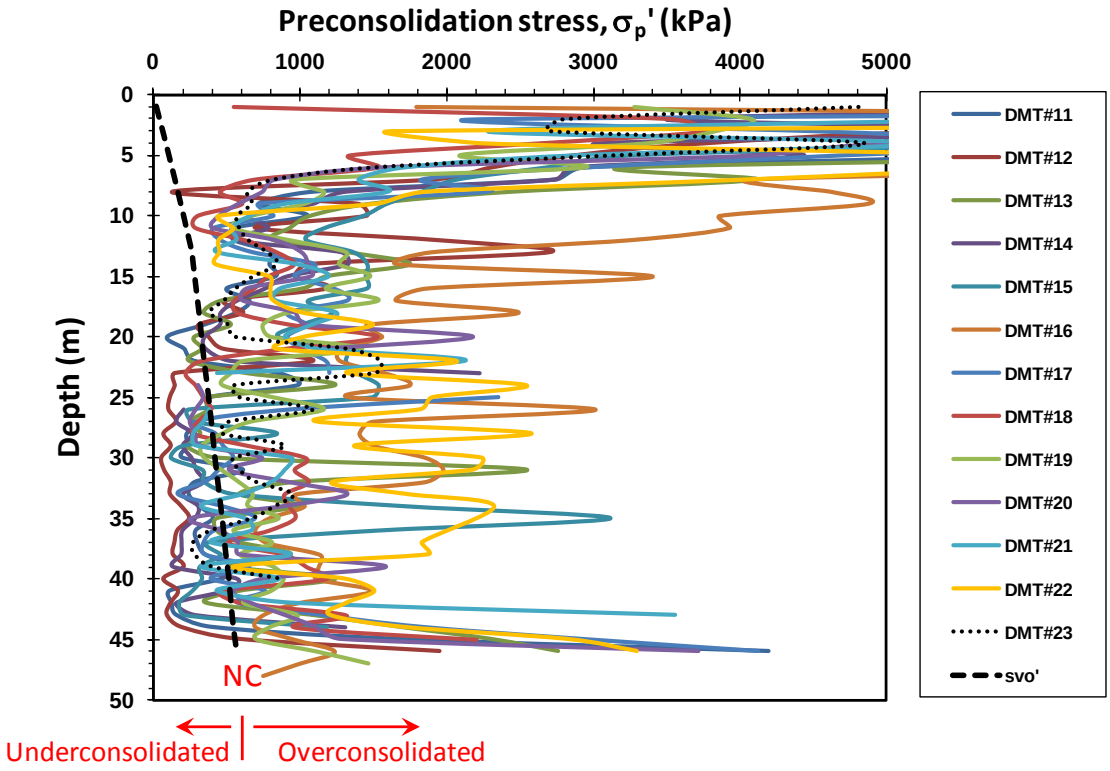

Figure 5-19. Compiled preconsolidation stress assessments using DMT soundings at SWPF area

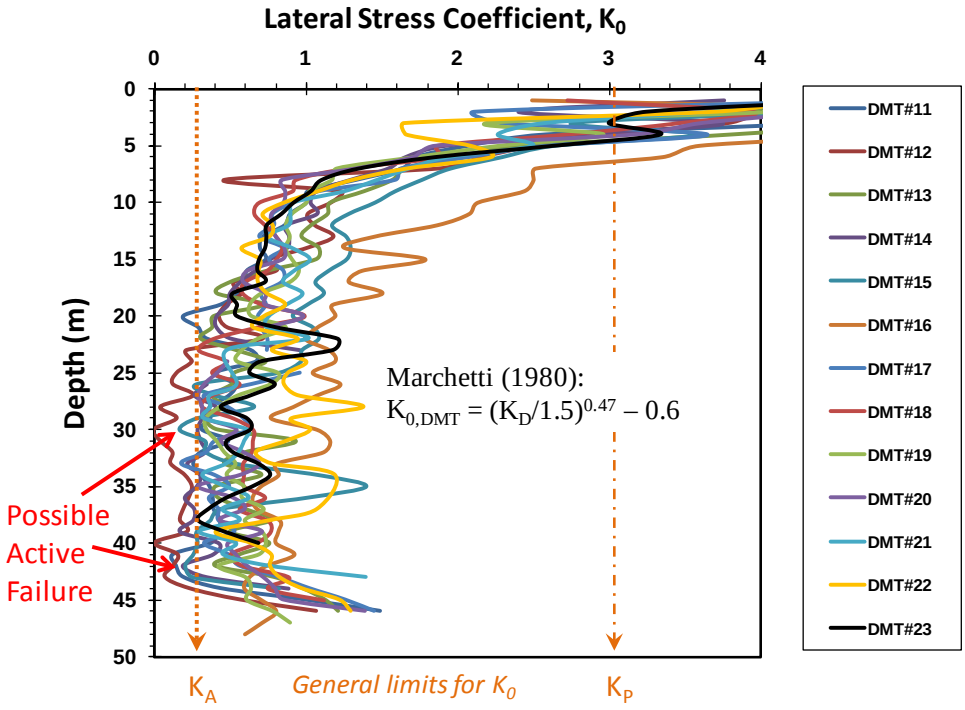

Figure 5-20. Compilation of K_0 assessments using DMT soundings at SRS SWPF.

Results from CPT soundings can also be interpreted to evaluate the stress history of soils (Mayne 2010, 2014). The methodology is based on a combination of two solutions: (a) an analytical cavity expansion-critical state method for undrained CPTu response in clays; and (b) statistical analyses of drained CPT response from over 700 calibration chamber tests on sands. The generalized form was expressed:

$$\sigma_p' = 0.33\,(q_t - \sigma_{vo})^{m'}\,(\sigma_{atm}/100)^{1-m'}$$

where the exponent m' varies with the CPT material index, I_c:

$$m' = 1 - \frac{0.28}{1+(I_c/2.65)^{25}}$$

Using CPT data from the K-area show similarly high variability in overconsolidation ratios (OCR = σ_p'/σ_{vo}') with depth at SRS in Figure 5-21. The large contrast in stress history evaluations over relatively short distances at any given elevation suggests significant heterogeneity and differences in geostatic stress regime.

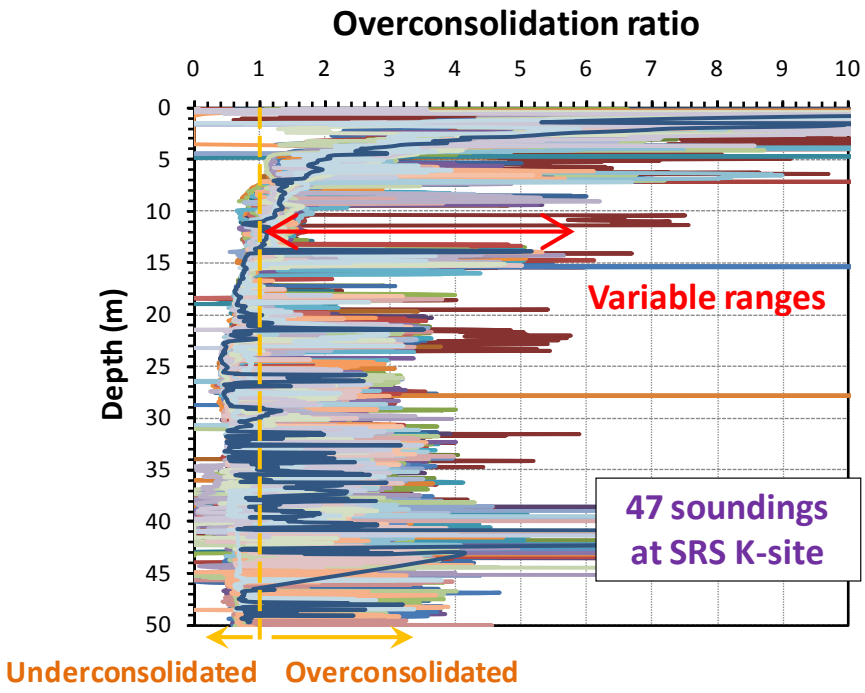

Figure 5-21. Compiled overconsolidation ratios evaluated from CPTs at K-area.

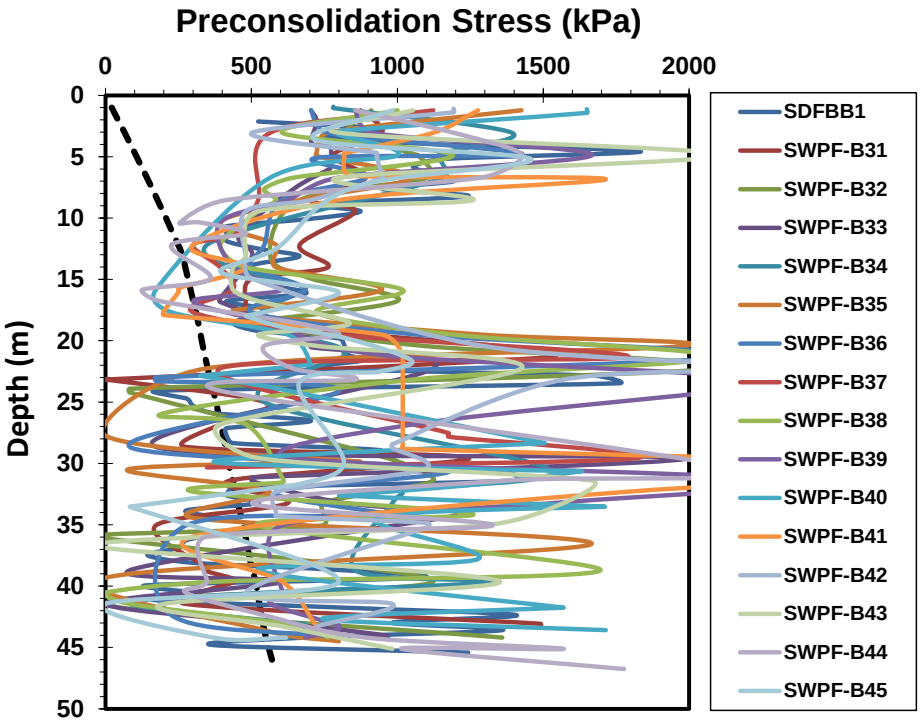

Figure 5-22. Estimated yield stress profile from SPT N_{60} values at SWPF area.

The energy-corrected SPT resistance may also be utilized to assess stress history in soils (Mayne 2007a):

$$\sigma_p' = 0.47 \cdot \sigma_{atm} \cdot (N_{60})^k$$

where the exponent k varies with mean grain size of the soil. In the hierarchy, the exponent k takes on values of 1 (clays), 0.8 (silts), and 0.6 (clean quartz-silica sands). For SRS, the N_{60} data from the SWPF area were employed to evaluate the preconsolidation stress profile, as presented in Figure 5-22. The results are generally compatible with the aforementioned arguments that the observed σ_p' variations at SRS may be due to alternating zones of intact soil columns that are peppered with collapsed zones due to the dissolutioning in the Santee at deep depths of 40 ± m.

The aforementioned hypothesis of soil column collapse is rather unusual in soil deposits, yet found widespread in karstic limestone terrain (Sowers 1996). Dissolutioning of calcareous and carbonatic components due to groundwater flow, infiltration, and changes in the phreatic surface are well-appreciated in the geologic and geotechnical studies of limestone terrain. Resedimentation in the form of stalactites and stalagmites as calcite precipitates is a common manifestation in such geologic formations as karst. In the case of the more rare "karstic soil" that is found at SRS, the remaining "pillars" or columns of original ground formed by the geomaterial matrix still reside within the subsurface environment. However, the "normal" sinkhole features that would eventually be realized are, in fact, filled with soil debris and detritus from the upper collapsed soil layers, thus buried and not readily available for visual examination or therefore not fully appreciated. Such buried remnants might be depicted in a number of karstic scenarios, as summarized by Sowers (1996) and presented in Figure 5-23.

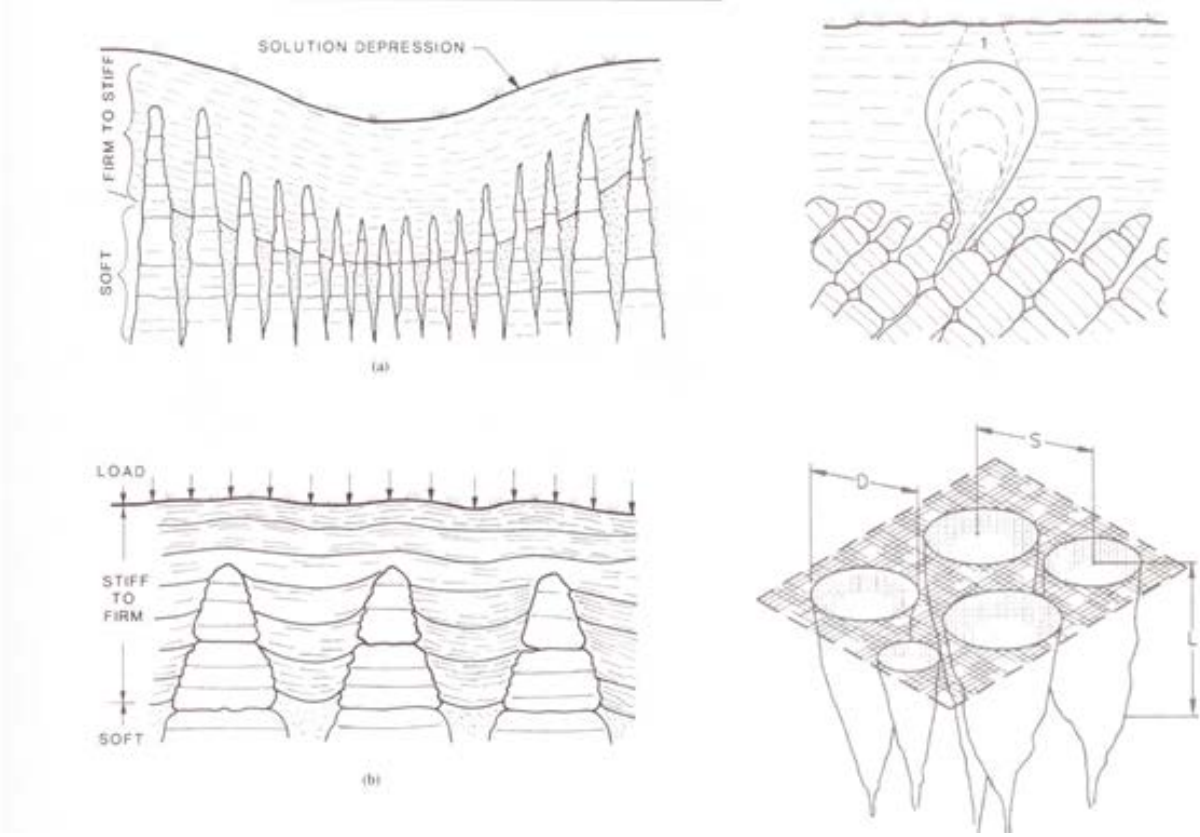

Figure 5-23. Examples of karstic features in fully matured limestone terrain (Sowers 1996).

6. Mineral Dissolution In Sediments - A Particle-Level Study: Micromechanics Analyses

6.1. Introduction

6.1.1 Relevance

Sediments experience mineral dissolution, precipitation and transformation in most natural settings and engineered processes. Furthermore, there are often dissolution-like phenomena that affect ground behavior such as solifluction, organic matter decomposition, thawing, and gas hydrate dissociation (Figure 6-1).

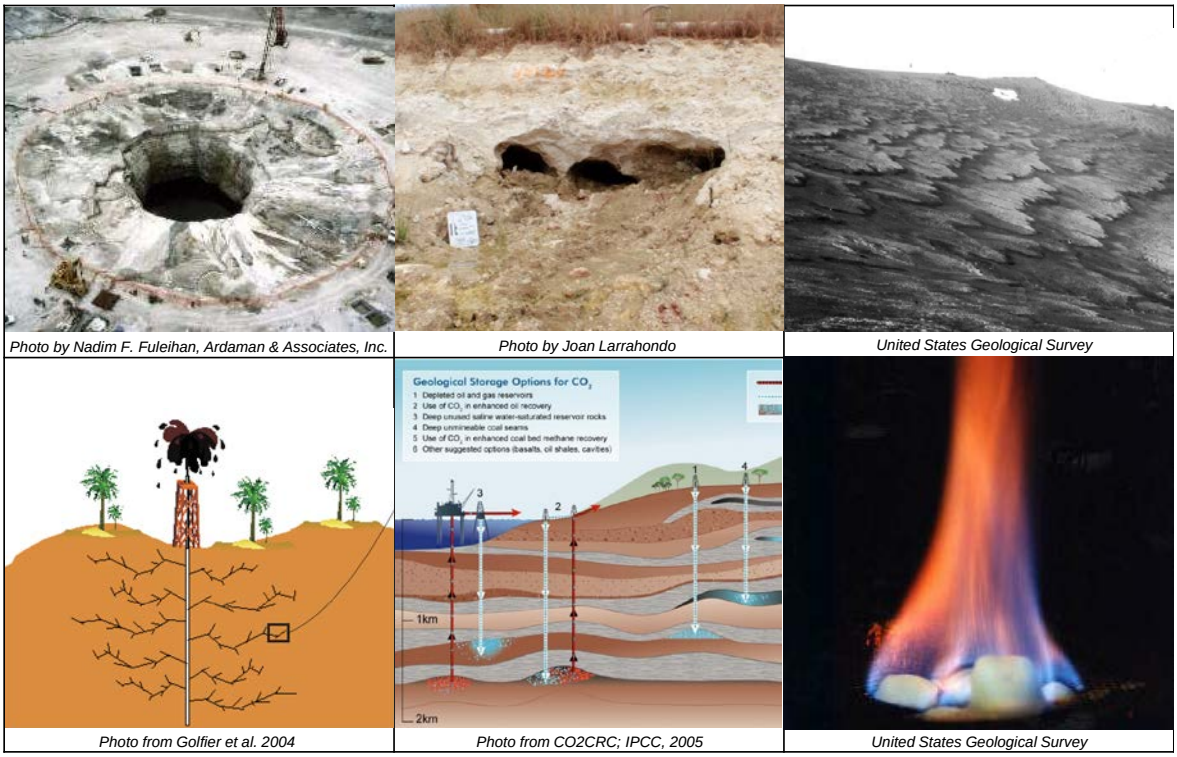

Photo by Nadim F. Fuleihan, Ardaman & Associates, Inc. | *Photo by Joan Larrahondo* | *United States Geological Survey*

Photo from Golfier et al. 2004 | *Photo from CO2CRC; IPCC, 2005* | *United States Geological Survey*

Figure 6-1. Introduction-Relevance – Dissolution affects a wide range of geotechnical situations, including minerals, ice and hydrate.

The consequences of dissolution are often overlooked in geoengineering. However, an increasing body of evidence shows that dissolution can have a profound effect on the performance of engineered systems (including fly ash and mine tailing ponds), and geotechnical components in the field of energy geotechnology (such as nuclear waste repositories, CO2 geostorage and methane hydrate). A thorough understanding of the consequences of mineral dissolution on sediment behavior and system response is needed.

In this section, we investigate the effect of mineral dissolution on sediment behavior using particle-scale numerical simulations. The choice of the discrete element method highlights the inherently particle-scale nature of dissolution.

6.1.2. Numerical Method

Dissolution is performed in a numerical 2D- and/or 3D-cell with zero-lateral strain side-walls using the Discrete Element Method (Itasca Program - PFC-3D). Spherical particles with uniform grain size distribution are packed by randomly placing smaller grains in the cube and gradually expanding them under zero gravity and zero interparticle friction to attain the target porosity and a homogeneous granular medium. Then, friction and gravity are turned on, and the specimen is incrementally loaded in the vertical direction under zero lateral strain conditions.

Dissolution under constant servo-controlled vertical stress and zero lateral strain $\varepsilon_h=0$ is simulated by gradually reducing the radius of selected particles while ensuring numerically stable conditions throughout the dissolution processes.

6.2. Dissolution Modes

Dissolution has different pore-scale manifestations:

- *homogeneous dissolution*: a sediment made of two minerals A&B experiences the selective dissolution of grains made of mineral A while grains made of mineral B must rearrange to sustain the applied loads
- *pressure solution*: grains dissolve preferentially at contacts were stresses are higher
- *localized dissolution*: dissolution localizes along pipes in high advection regimes

The implications of these dissolution modes are reported herein. Simulations in this section are conducted for parameters listed in the following table.

Table 7. Model Parameters

	Properties	Values
Ball	Initial radius of balls	Uniform size distribution (R_{min}=1mm, R_{max}=1.5mm)
	Number of balls	9167
	Mass density of balls	2650 kg/m^3
	Hertzian contact model	Shear modulus = 2.9×10^9 Pa
		Poisson's ratio = 0.3
	Inter-particle friction	0.5
Boundary conditions	Initial cell size	(Height × Width × Length) 5cm × 5cm × 5cm
	Vertical load	100 kPa (during dissolution)
	Zero lateral strain	
	Particle-to-wall friction	0

6.2.1. Homogeneous Dissolution

Changes in K_0 ***- Effect of granular interlocking.*** Spherical particles rotate more freely than non-spherical particles found in real sediments where interlocking inhibits rotation. While particle rotation has a limited effect on elastic properties, it alters shear resistance and volume change. In this study, we hinder rotation on preselected particles HR as a numerical proxy for angularity.

Results in Figure 6-2 show that the value of k_0 (vertical axis) tends to decrease during mineral dissolution (horizontal axis), and that more angular/interlocked particles (as captured by hindered rotation HR) will experience a more pronounced drop in lateral effective stress. The stress anisotropy reaches a minimum value and eventually regains horizontal stress due to internal shear.

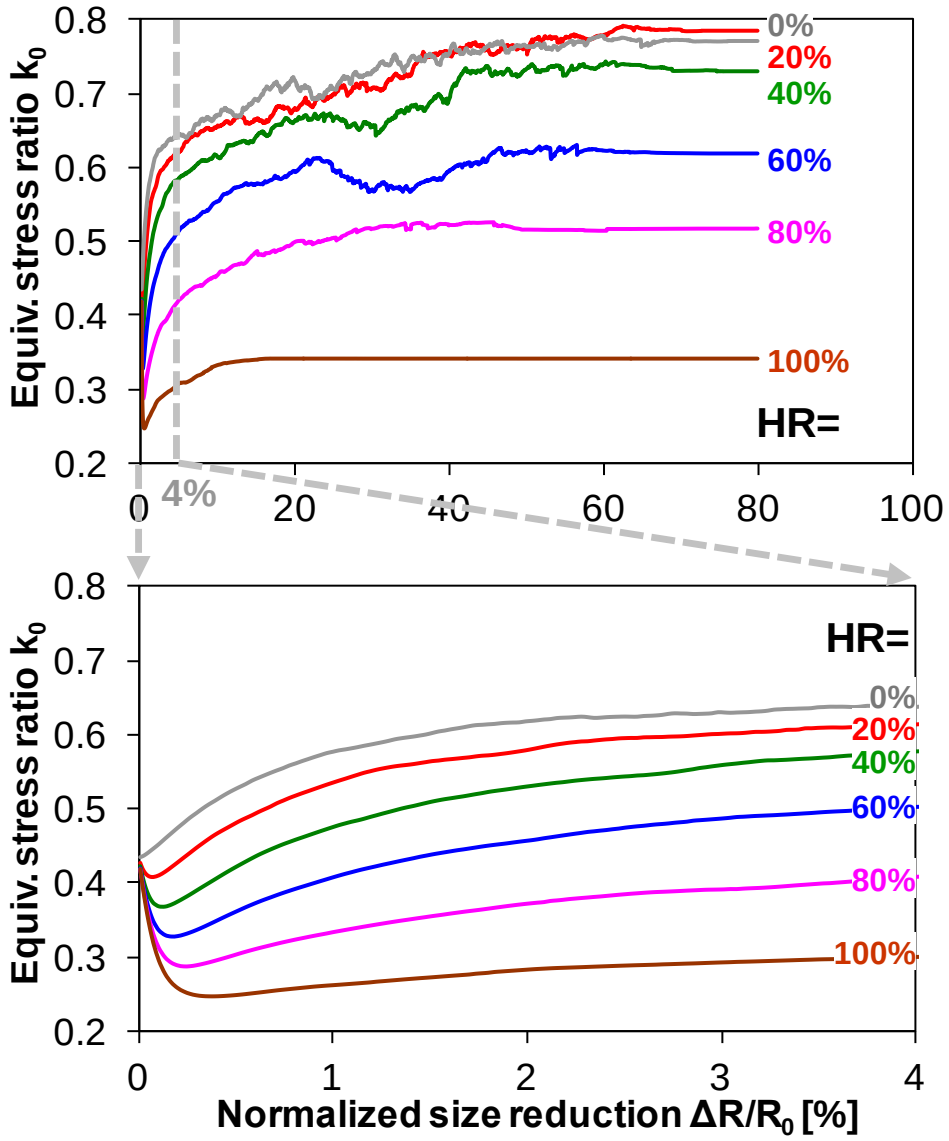

Figure 6-2. Effect of granular interlocking HR on the evolution of the lateral stress k_0 during dissolution

Contact force histogram. Histograms of contact forces before and after dissolution are compared in Figure 6-3 for quasi-horizontal (±30° from horizontal axis) and quasi-vertical (±30° from vertical axis) contact forces. The total number of contacts decreases and higher normal contact forces develop both in the vertical and horizontal directions; in the meantime, the number of

contacts with lower contact forces decreases after dissolution. (Note that the vertical axis is in logarithmic scale. The order of magnitude for the mean force is $d^2\sigma \approx 0.2N$).

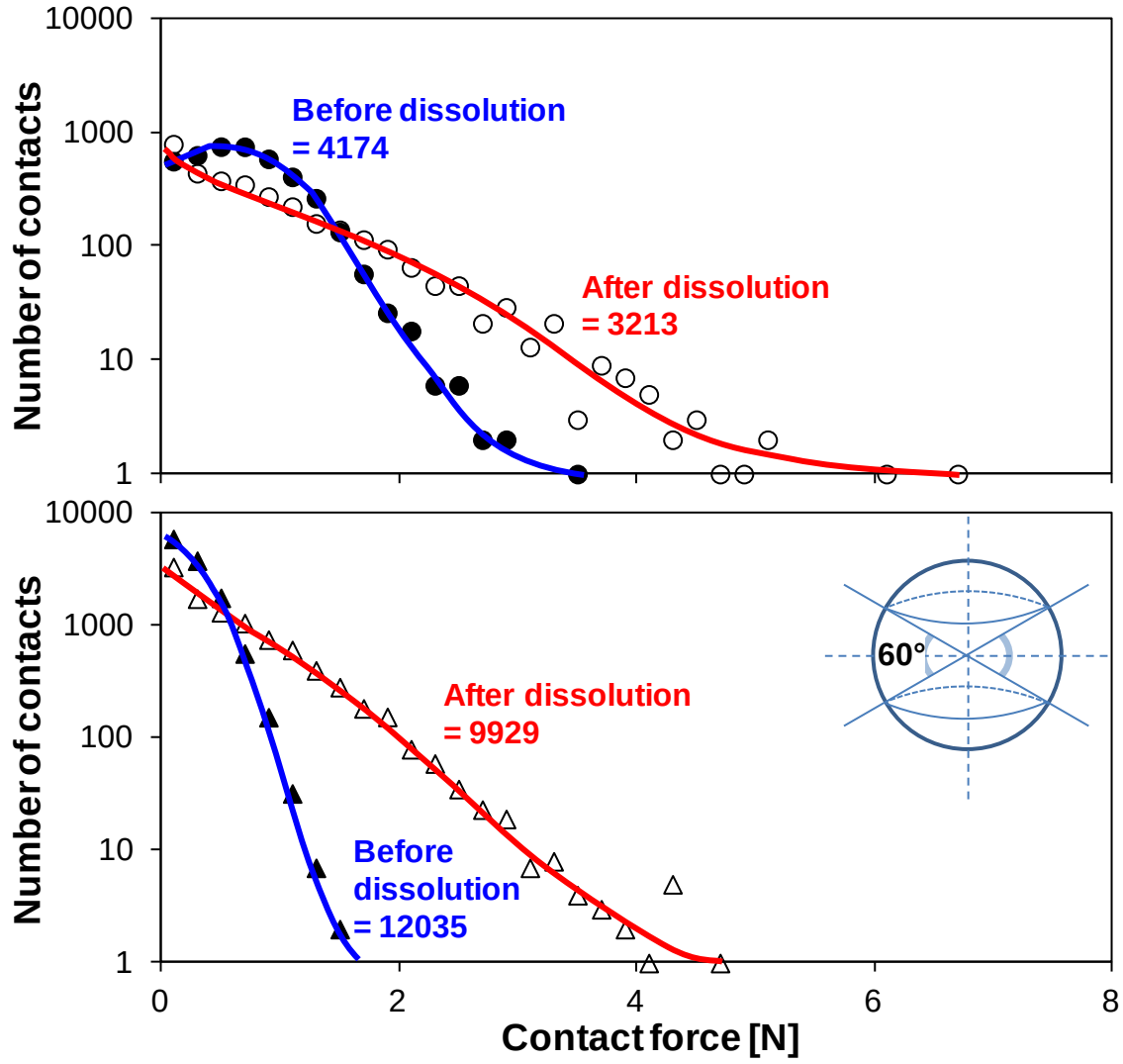

Figure 6-3. Contact force histogram for (a) quasi vertical and (b) quasi horizontal normal contact forces before and after dissolution

Micromechanical parameters. Figure 6-4 shows polar plots of micromechanical parameters for three specimens made of rounded particles without hindered rotation: more contacts develop in

the horizontal direction, and normal contact force anisotropy and the mean tangential contact forces decrease after dissolution; these trends become more prominent as the fraction of soluble particles SF increases.

	Before dissolution	At the end of dissolution	
		SF=2%	SF=10%
Contact density	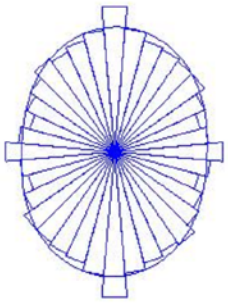	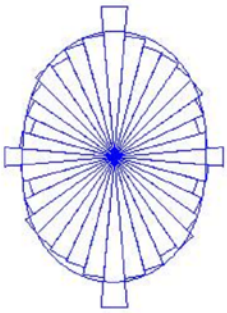	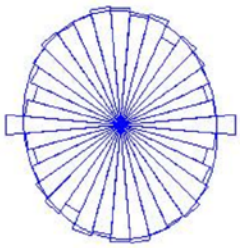
Mean normal contact force (Scale=1)	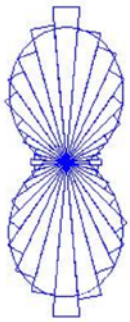	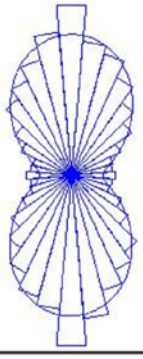	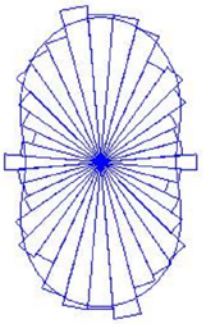
Average tangential contact force (Scale=0.16)	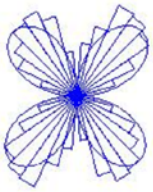		
Stress ratio k	0.43	0.50	0.75

Figure 6-4. Polar plots of the evolution of micromechanical parameters during dissolution. Results are shown for two mass fractions of soluble particles SF. The scale of tangential contact forces is magnified by a factor of 1/0.16 in comparison to the normal contact forces.

Local porosity and force chains. Careful inspection of the granular assemblies after dissolution reveals that large remnant voids are aligned near major contact force chains after dissolution, i.e., force arches develop near the dissolving particles. These voids contribute to the post-dissolution contractive behavior. The 2D cross correlation analysis between an image of large voids and an image of contact force chains confirms that large voids are most developed about one particle diameter away (and typically below) major force chains (Figure 6-5).

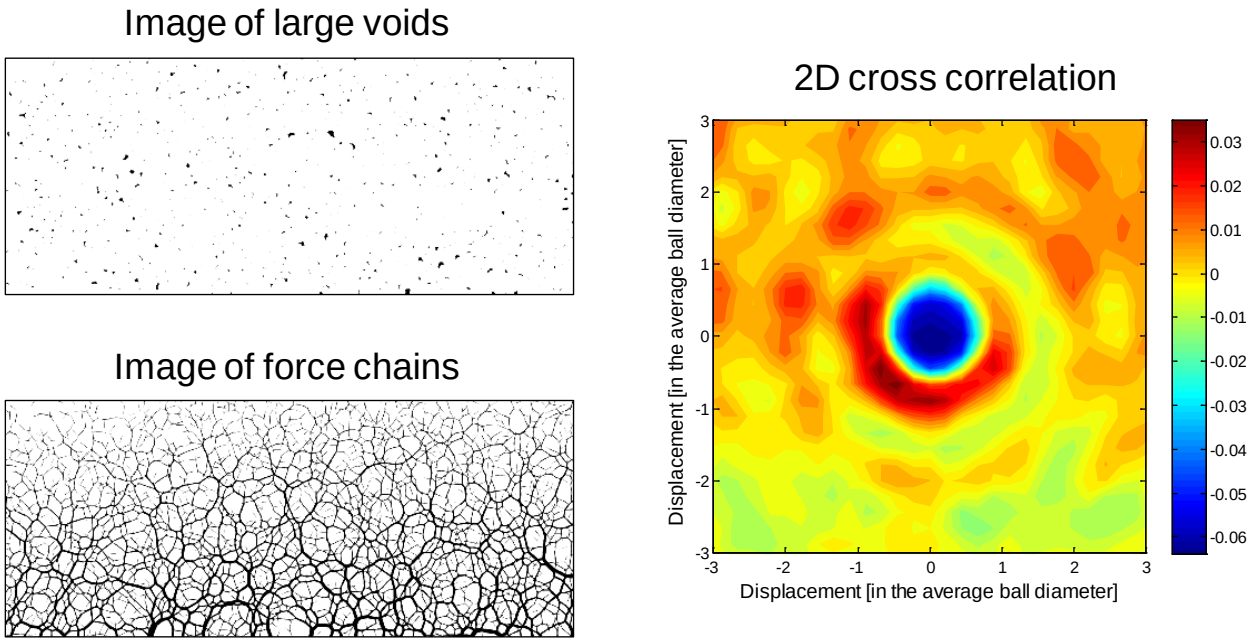

Figure 6-5. Local porosity and force chains. (a) image of large voids -- grains and small voids are made transparent, (b) image of force chains, (c) 2D cross correlation between large voids and chains.

Porosity change vs. mass loss. Mass loss at constant total volume allows us to estimate an upper bound for the gain in porosity Δn that a sediment with initial porosity n_0 could experience during dissolution within rigid boundaries:

$$\Delta n = (1 - n_0) SF$$

The evolution in porosity measured in numerical simulations vs. mass loss $\Delta M/M_0 \leq SF$ superimpose with the line for dissolution at constant volume (equation above) for sediments with low fraction of soluble particles SF (Figure 6-6), suggesting the development of internal arching with minimal fabric change to effectively accommodate mass loss with minimum vertical displacement (Note: these results apply to constant vertical stress - global volume contraction depends on the applied stress). Arch formation depends on factors such as interparticle friction and particle angularity. Indeed, sediments with higher hindered rotation HR=80% tend to experience mineral dissolution at constant volume i.e., accompanied by the increase in porosity Δn, even for relatively high fractions of soluble particles SF (Figure 6-6).

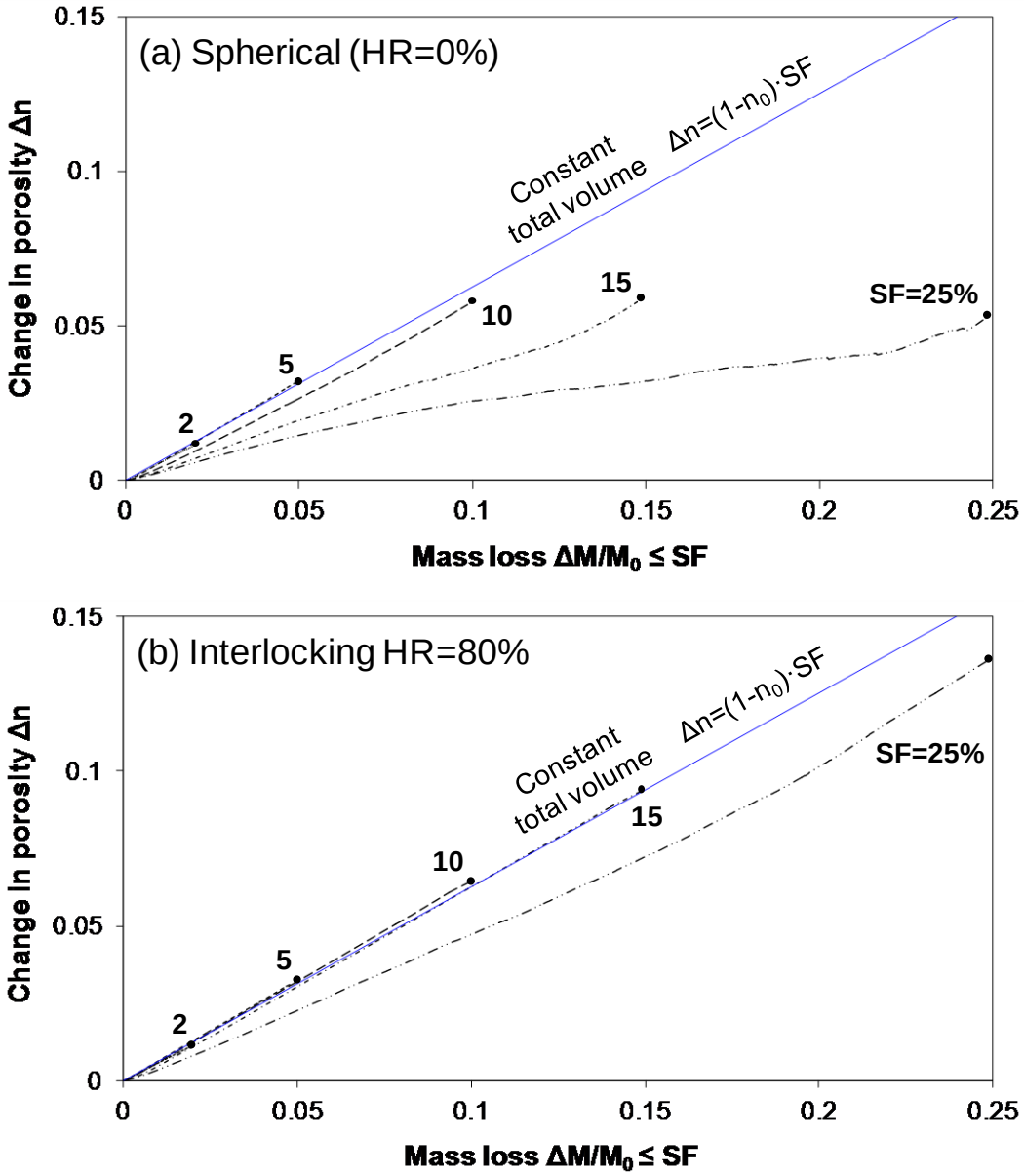

Figure 6-6. Porosity change vs. mass loss at constant vertical stress for different fractions of soluble particles; (a) smooth grains and (b) interlocked grains.

6.2.2. Pressure Solution

Pressure solution is simulated through multiple particle size reduction steps, each followed by an equilibration stage. Each sphere (3D) or disk (2D) is shrank by reducing its radius proportionally to the total contact force ΣFN acting on the particle. In the absence of physic-chemical data, we explore two dissolution rate functions to accommodate possible conditions: linear $dR/dt=\alpha(\Sigma F_N)$ and quadratic $dR/dt=\alpha(\Sigma F_N)^2$.

Shear strain localization. Before dissolution, contact forces align preferentially in the vertical principal stress direction, and evenly distributed force chains are observed throughout; this situation changes severely during pressure solution. Figure 6-7 shows contact force chains and strain fields after pressure solution (Note: strain fields are computed as the gradient of accumulated displacements from the beginning of dissolution. Before dissolution: contact forces are homogeneous, displacement vectors are zero and the strain field is zero everywhere). Shear bands developed spontaneously, for both linear and quadratic dissolution rates, and in packings made of either free-rotating particles (HR=0%) or interlocked particles (hindered rotation HR=80%). When there is a free upper boundary, shear localization is more pronounced at depth and diffuses towards the free surface as pressure solution is contact-force dependent. Shear bands form at steeper angles in packings with interlocked particles, in agreement with the higher global friction angle for granular materials with interlocking. Shear bands are 12~15 particles thick and marked force chains form inside shear bands. These strong force chains form and buckle as force-dependent dissolution progresses, and the evolution of dissolution is faster in bands than in wedges.

Why do shear band forms? During the early stage of pressure solution, the sediment evolves towards a dense granular structure that will tend to dilate upon shear due to its high coordination and low porosity; in the meantime, the horizontal stress decreases. Eventually, the vertical-to-horizontal stress ratio σ_v/σ_h reaches the Coulomb failure condition and sediment experiences internal shear. Due to its dilative tendency and post peak strain softening behavior, shear localizes along shear bands. The local coordination number decreases and porosity increases inside the shear band, in the same way as in shear bands that form in conventional triaxial loading conditions. Higher contact forces within the shear band promote dissolution and sustain further shear between wedges along shear bands.

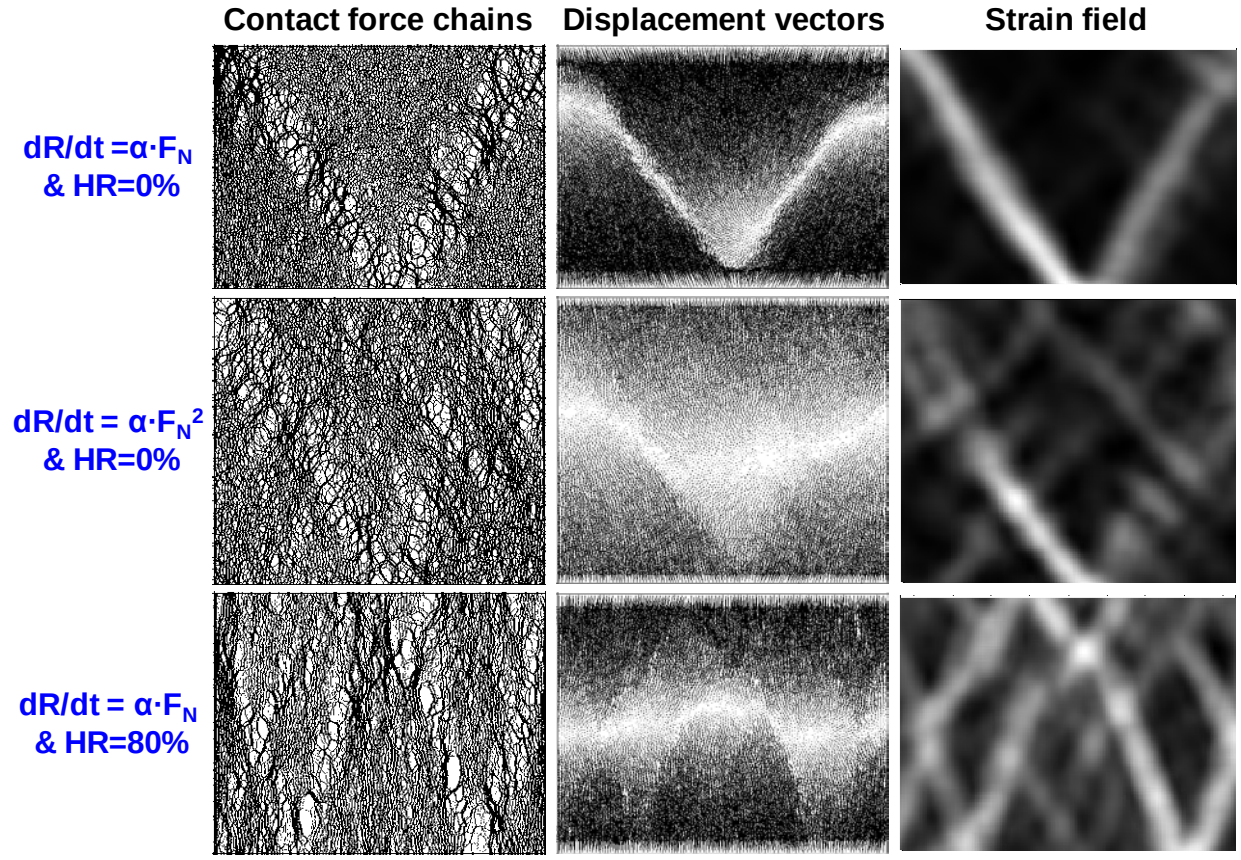

Figure 6-7. Pressure solution: The emergence of shear strain localization

Histogram of contact forces and grain size. The grain size distribution is uniform before pressure solution in all cases. The size distribution shifts to smaller sizes and evolves towards a unimodal distribution during pressure solution (Figure 6-8).

The change in grain size is coupled with changes in contact forces. Pressure-dependent dissolution promotes global contact force homogenization (Figure 6-8). Once the shear localization is triggered, force homogenization continues within wedges, but high forces develop within shear bands. The increase in coordination number and the homogenization of contact forces during pressure solution can be interpreted in terms of “dissolving” springs in parallel: “force” dependent dissolution causes heavily loaded particles (or springs) to shorten first and shed force to other particles (springs) that come into contact.

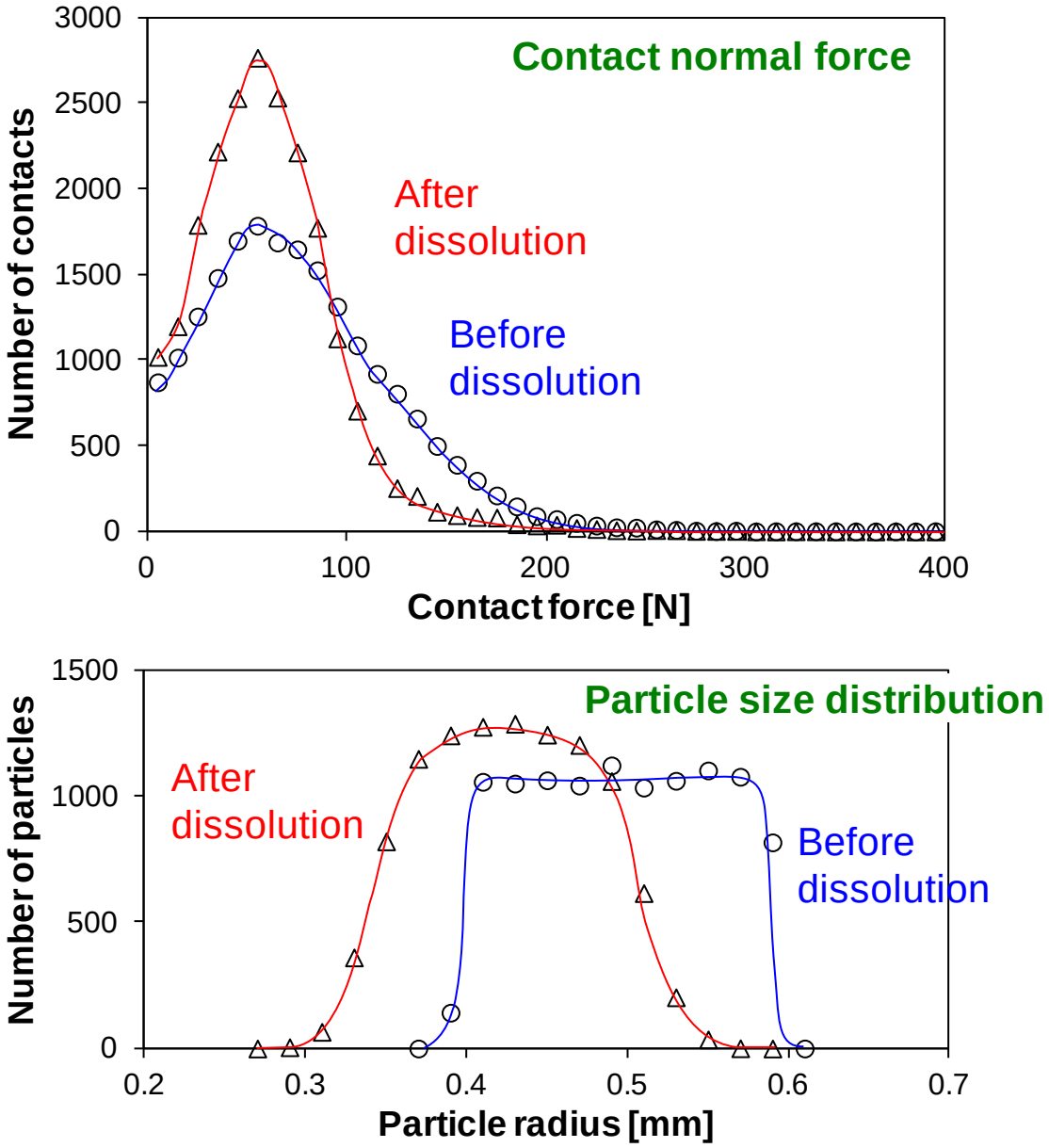

Figure 6-8. Pressure solution: contact force and grain size (2D confined, dR/dt=a•FN, HR=0%).

For these 2D simulations the contact force is for unit length of the “cylindrical particles”, i.e., N per m.

6.2.3. Localized Dissolution

Exploratory experimental study. A quartzitic-carbonate sandy sediment from the SRS (Atlantic coastal plains in Georgia - D_{10}=0.25mm; D_{50}=0.8mm; all the sediment passes sieve #10 and is retained on sieve #100. Composition: 52% calcite, 47% quartz, and trace of clay minerals) was compacted in a zero-lateral strain cell (initial porosity n=0.7; stainless steel cell, ID=100mm; 60mm sediment height) and subjected to a 400kPa vertical stress. After saturation, the specimen was subjected to fluid flow using 25 pore volumes of 1 molar solution of acetic acid CH_3COOH injected through the bottom porous stone at a constant hydraulic gradient i=35 (No fines removal was observed). Finally, the sediment was dried, extruded from the cell, and subjected to slicing and visual inspection. Evidence of localized dissolution in the form of pipes filled with quartzitic grains but without any carbonates left is readily confirmed by visual inspection during gradual shaving of sediment layers (Figure 6-9): pipes are the dark color patches that are surrounded by the light colored sediment (Note: XRD results show that the mineralogy of the background medium consists of both quartz and calcite, but that only quartz remains in pipes i.e., there has been a ~52% mass loss in pipes).

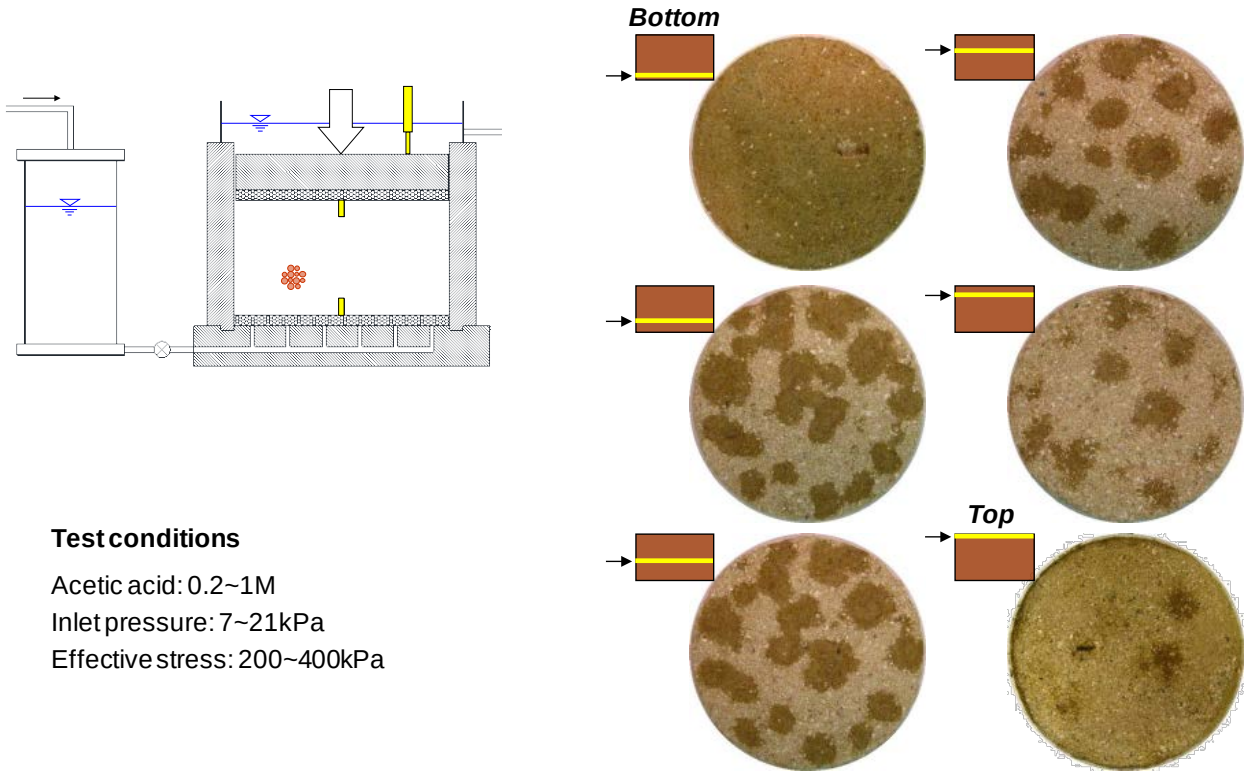

Figure 6-9. Localized dissolution – Experimental results. (a) device; (b) post-dissolution inspection

Vertical Pipes - Force chain and stress evolution. The discrete element code PFC is used to study the geo-mechanical implications of localized dissolution both in 2D and 3D conditions. The vertical stress is kept constant during dissolution. The position and size of vertical pipes are predefined in the sediment.

Force chains are strong in the vertical direction before dissolution, in agreement with principal stress directions. After dissolution, marked force chains remain preferentially vertical away from pipes, yet, they are preferentially horizontal within pipes (Figure 6-10). In fact, horizontal contact forces inside pipes prevent the buckling of granular columns in the

surrounding sediment. As dissolution continues, surrounding soils slide towards the looser pipes, and structural differences between the two zones become less prominent.

Vertical forces increase rapidly in the host medium when dissolution starts in pipes, as vertical load is shed to the host medium (Figure 6-10). Equivalent stresses are calculated within pipes and in the host medium. Global vertical equilibrium with the applied vertical stress 100kPa is verified in all cases. In the horizontal direction, horizontal stresses in pipes and host are almost identical ($\sigma_{h|pipe} \approx \sigma_{h|host}$) to satisfy equilibrium. In terms of equivalent stresses, principal stresses rotate in pipes during dissolution. The peak equivalent global stress ratios reach the Coulomb failure condition in both the pipes and the host medium.

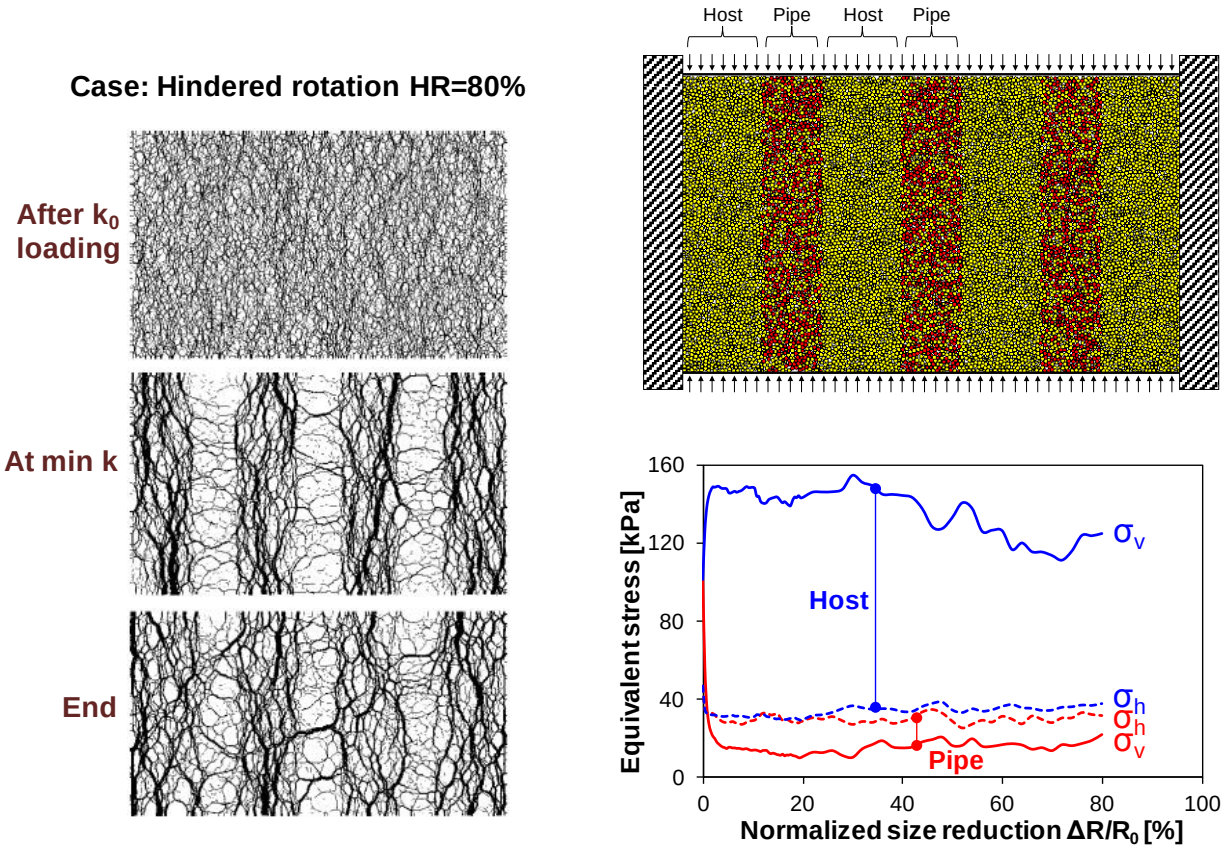

Figure 6-10. Localized dissolution: Evolution of force chains and equivalent stress

Deep horizontal pipes. The stress gradient along the inclusion height is negligible when the depth z to inclusion size D ratio is large, say z/D>10. The representative volume tested in these simulations is subjected to constant vertical stress and zero-lateral strain boundary conditions: strictly speaking, this implies horizontally repetitive conditions. Three different contractible zone sizes are tested: the case of D/L=0.2 corresponds to sparsely populated deep inclusions, while the case of D/L=0.6 corresponds to interacting near-neighbor cavities (see circles sketched on Figure 2.10). Finally, the percentage of particles within the contractible zone that experience size reduction is either SF=50% or 100%. The dissolution of particles in the contractible zone is performed by simultaneously reducing the radius of all SF soluble particles. Slow size reduction is enforced to prevent numerical instability and dynamic effects.

The vertical contraction δ is normalized by the initial REV size L. The δ/L ratio increases with the contractible zone size D/L (Figure 6-11). The normalized vertical displacement decreases and porosity increases for higher sediment friction angles (i.e., interlocking in terms of hindered rotation HR). In general, the equivalent global stress ratio k_0 increases with dissolution to eventually reach a steady value that can be as high as $k_0 \approx 0.7$ to 0.8 (higher for lower interlocking HR). An early drop in k_0 is measured for packings with high interlocking (e.g., HR=80%) and large contractible zone (e.g, D/L>0.4) (Figure 6-11). Fluctuations in the equivalent global stress ratio k_0 trends hint to successive internal slippages.

Grains adjacent to the contractible zone flow towards the shrinking volume as particles dissolve (Figure 2.10) and no cavity remains after dissolution in agreement with the cohesionless nature of the sediment. Horizontal displacements prevail along the side of the contractible zone and are mostly responsible for filling the contractible space; vertical displacement is more dominant above and below the zone.

Even minute radius reductions mobilize internal friction/interlocking of surrounding grains and unload initial force chains across the contractible zone. Forces arch around the contractible zone as a consequence of interparticle friction and rotational frustration, and there are only small transverse forces inside the contracted zone that prevent chain buckling. Force arching is more pronounced and a larger “effective void” forms in sediments with higher friction angle.

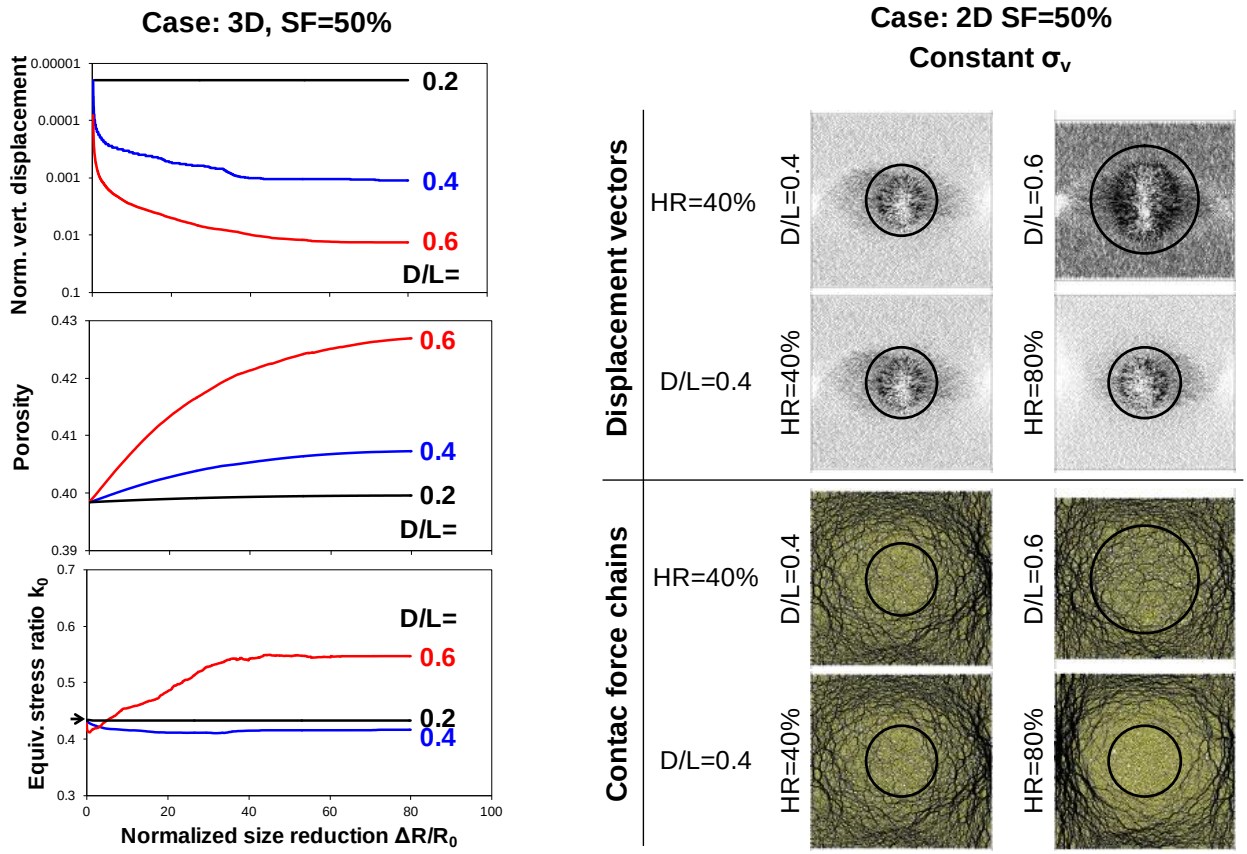

Figure 6-11. Localized dissolution at depth and parallel to the surface.

6.2.4. Conclusions

Dissolution can take place with different grain-scale characteristics. We explored homogeneous dissolution (multi-mineral sediments), pressure solution, and localized dissolution (typically in high fluid flow regimes). We can conclude that:

- Homogeneous dissolution leads to global contraction, changes in fabric (similar to a honeycomb structure), and increase in internal porosity towards a terminal density characteristic to dissolution. In contrast, pressure solution leads to densification (even in the absence of reprecipitation) at least during the early stages of pressure solution.
- Higher interparticle friction and granular interlocking hinders global contraction and leads to a higher increase in porosity
- In all dissolution modes conducted under constant vertical load and zero lateral strain, the horizontal stress drops, often as low as to K_A (particularly in high friction/interlocking sediments). There is principal stress rotation in the stress field within vertically forming pipes
- Shear localization naturally emerges in pressure solution.

6.3. Post-Dissolution Stress-Strain Behavior

How does a sediment respond to loading after it has experienced dissolution? Different soluble fractions SF are simulated, where SF is defined as the mass of soluble particles with respect to the total mass. Soluble particles are randomly assigned in the preformed granular packing (Figure 6-12). Then, dissolution under constant servo-controlled vertical stress and zero lateral strain $\varepsilon_h=0$ is simulated by gradually reducing the radius of all the soluble particles at the same rate (Note: model parameters in Table 7). After dissolution, the specimen is either loaded at zero-lateral strain to assess k_0 compressibility, or subjected to simple shear to evaluate shear resistance and volume change.

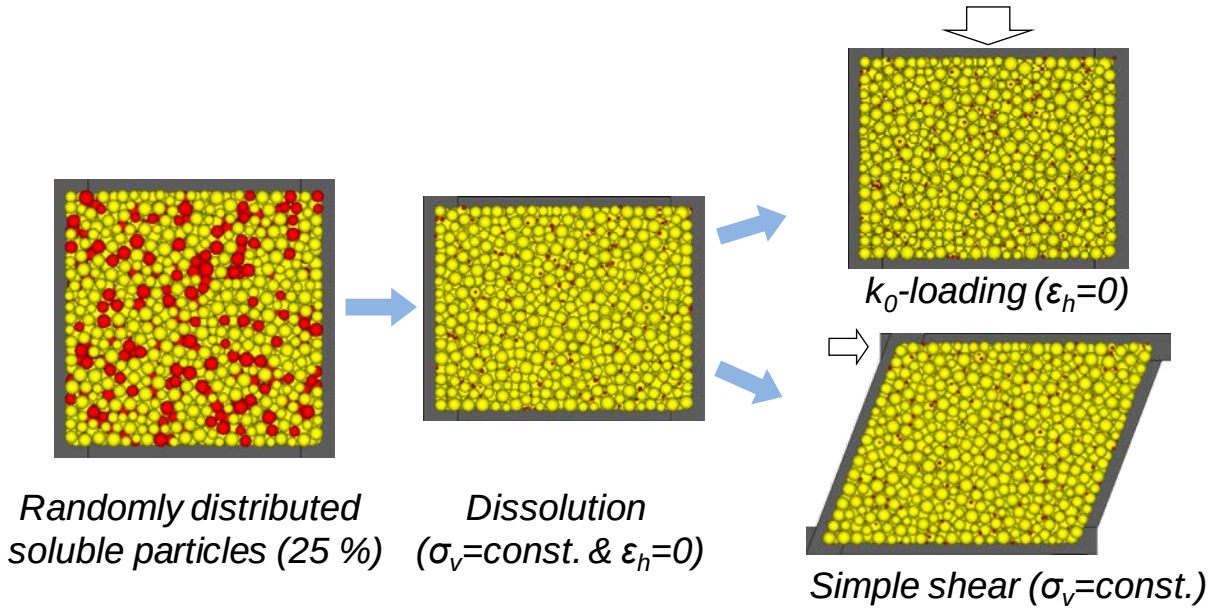

Figure 6-12. DEM Simulation study

Post-dissolution K_0 ***vertical loading.*** The post-dissolution sediment response to vertical loading under zero lateral strain $\varepsilon_h=0$ is investigated to assess changes in compressibility. Results show that the vertical displacement is higher for specimens that experienced more extensive dissolution (Figure 6-13). Porosity decreases with increasing vertical stress, although the magnitude of volume contraction for an order of magnitude increase in stress is relatively small compared to the gain in porosity during dissolution. The internal sediment structure is relatively unaffected by post-dissolution k_0-loading (for an order of magnitude increase in stress). And, the equivalent global stress ratio k_0 decreases upon loading (Figure 6-13).

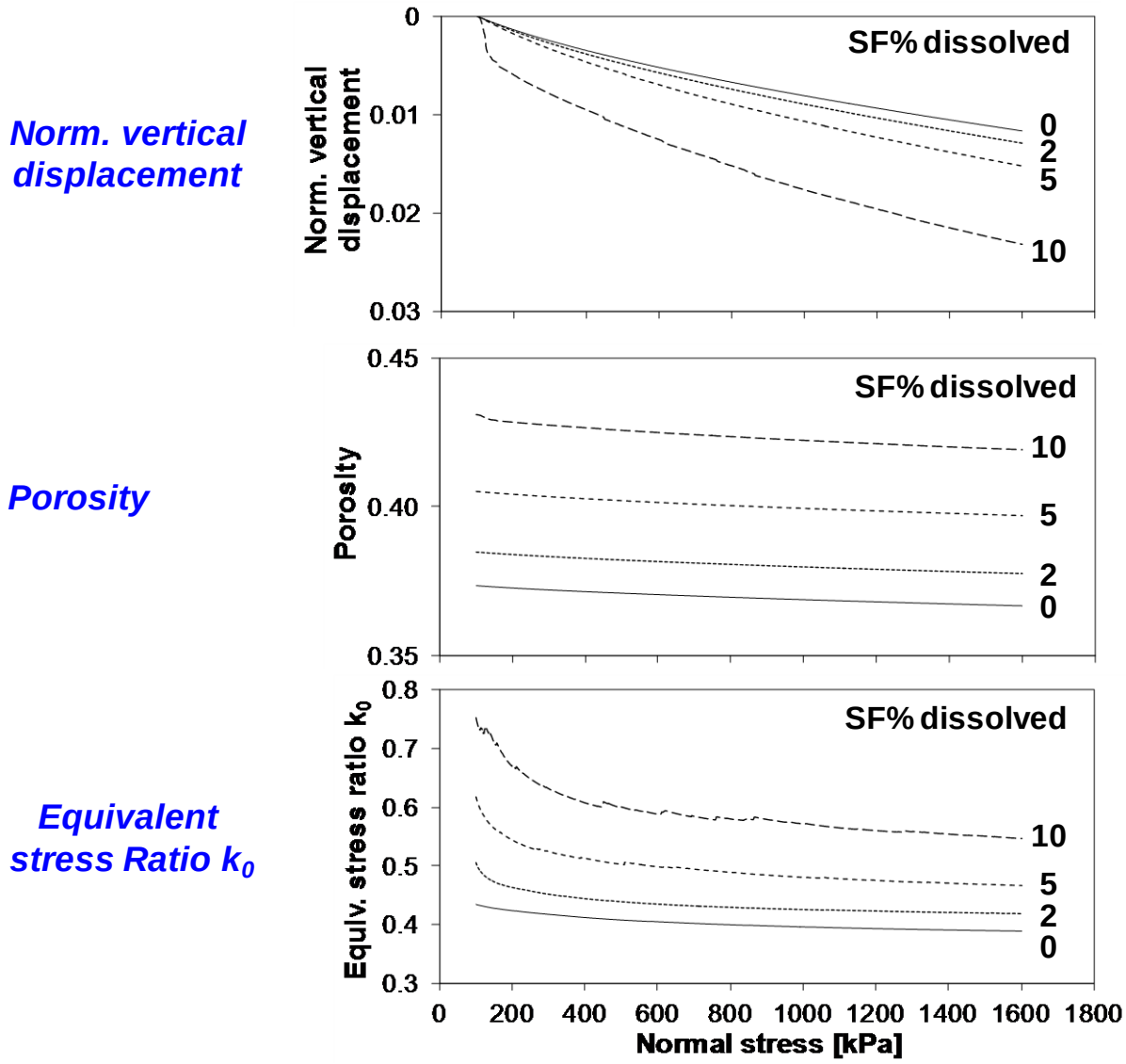

Figure 6-13. Post-dissolution vertical load

Post-dissolution shear loading. The same post-dissolution sediments tested above are subjected to simple shear under constant vertical stress σ_v=100 kPa. Numerical results show a pronounced decrease in shear stiffness with the increase in soluble fraction SF (Figure 6-14). The dilative tendency decreases as the soluble fraction SF increases; eventually the sediment becomes

contractive (when SF≥10% in this case). Void ratio and shear resistance tend to a common "critical state" for all specimens at large strains (Figure 6-14).

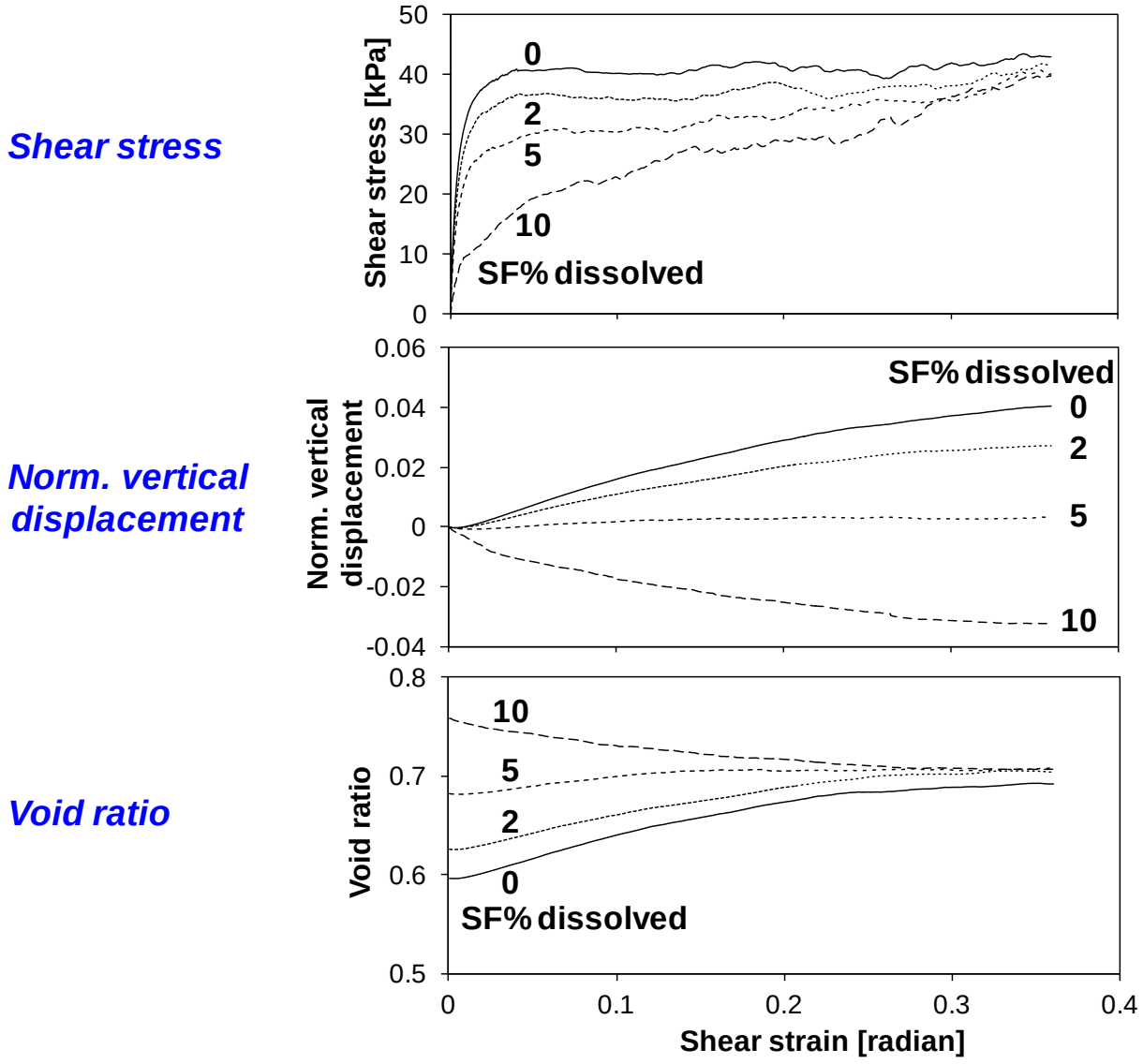

Figure 6-14. Post-dissolution shear load

Conclusions. The loss of solid mass has important particle-scale and macroscale implications upon loading. Numerical results obtained in this study show that:

- Sediments are more compressible after dissolution. The increase in compressibility correlates with the extent of dissolution the sediment has experienced.
- Post-dissolution simple shear loading encounters lower shear stiffness and higher contractive tendency in sediments that have experienced more pronounced dissolution. Therefore, water saturated post dissolution sediments will be more vulnerable to excess pore pressure generation when sheared under undrainded conditions.
- Regardless of the extent of dissolution (and in the absence of reprecipitation or changes in particle shape), specimens evolve to the same critical state strength and void ratios at large shear strains.

Overall, the post dissolution stress-strain behavior will be a function of the mass loss, the dissolution mode and the degree of friction/interlocking within the sediment.

6.4. Engineering Implications

The engineering implications of mineral dissolution at depth are explored for site characterization using penetration devices, slope stability, and shallow foundations.

6.4.1. Site Characterization - CPT

Materials. The sediment used for these tests is a mixture of quartzitic sand mixed with dissolvable salt grains. Details follow:

	Insoluble grains	Dissolvable grains
Materials	Ottawa F-110 sand	Table salt
D_{50}	0.12	0.3
G_S	2.65	2.165
e_{min}	0.535	0.45
e_{max}	0.848	0.78
Roundness	0.7	Cubical
Sphericity	0.7	

Chamber and cone. Calibration chambers have been extensively used to establish relationships between cone resistance and soil properties. Because of boundary effects, the difference between chamber and field cone resistance values decreases as the ratio of chamber to cone diameter increases. The zero-lateral strain calibration chamber used for this study is spring-loaded to impose a constant vertical stiffness condition analogous to field situations (ID=191mm, see Figure 6-15). The spring length (152mm) and stiffness (58N/mm) are selected to accommodate significant deformations with minor changes in vertical stress for a target vertical effective stress of 100 kPa. The bottom plate is densely grooved to ensure one-dimensional fluid flow.

The small-diameter electrical cone (OD=7.8mm) satisfies a 24-to-1 chamber-to-cone diameter ratio to minimize boundary effects. The cone tip (apex angle 60°) is mounted onto a force-sensing stud to effectively determine the tip resistance (force transducer range: 0 to 1200 N). The cone side resistance is mechanically removed by using an outer sleeve so that the tip resistance can be independently measured.

Figure 6-15. Chamber and instrumented small-scale cone used in this study

Settlement during dissolution. The sediment settles as it dissolves at constant vertical stress (Figure 6-16). Clearly, sediments that experience more extensive dissolution settle more (soluble fraction SF=20% compared to SF=5%). Furthermore, specimens with lower initial density experience larger settlement for the same fraction of soluble particles. These observations hint to internal changes in void ratio.

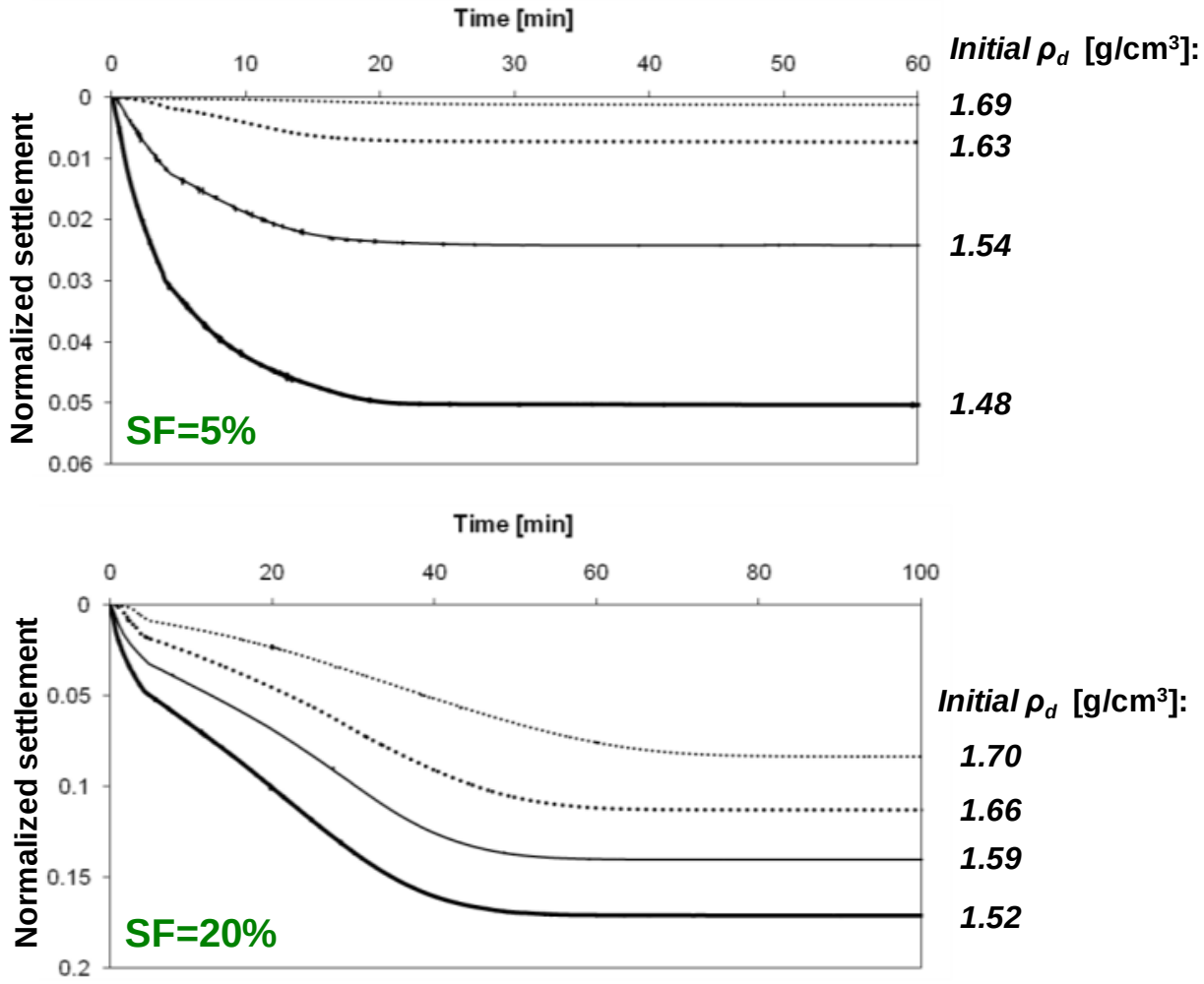

Figure 6-16. Settlement during dissolution for different initial densities and mass fraction of soluble particles SF

Void ratio changes upon dissolution. Changes in void ratio and dry density after dissolution are plotted in Figure 6-17. The void ratio increases and the dry density decreases after dissolution. Denser sediments experience a more pronounced change in density, and the increase in void ratio is higher in mixtures with higher fraction of soluble grains. However, post-dissolution void ratios do not exceed the maximum void ratio e_{max} for this sand (Note: the sand-salt mixture is a binary mixture with two different particle sizes; thus the mixture can have a smaller e_{min} than that of the sand-only sediment as seen in Figure 6-17). At a very high salt fraction (e.g. SF=20%), the sand void ratios after dissolution are independent of the initial density or void ratio (Figure 6-17). This is the “terminal void ratio” for dissolution under zero lateral strain: the post-dissolution void ratio cannot be higher than this terminal void ratio regardless of the initial soluble fraction.

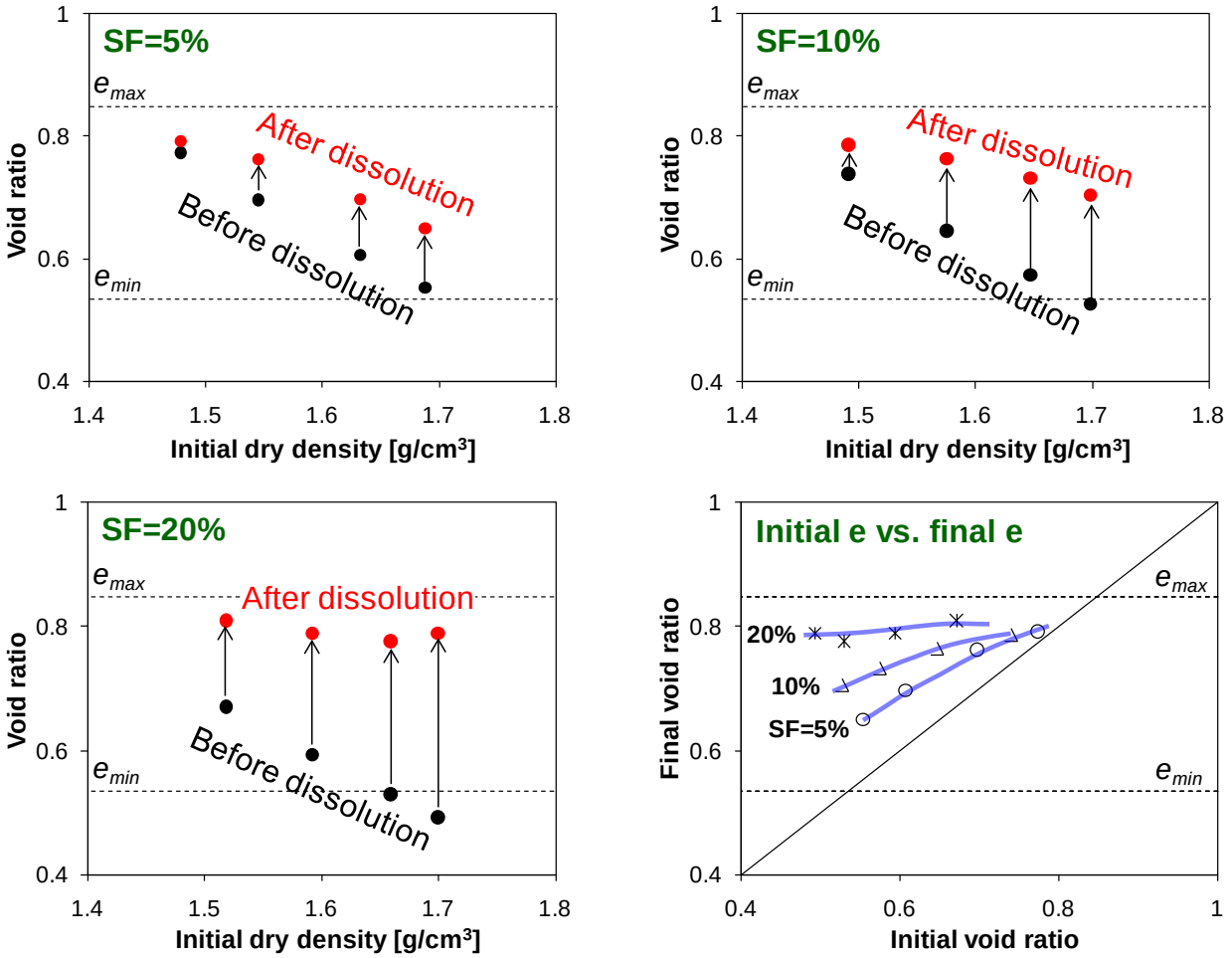

Figure 6-17. Void ratio changes upon dissolution. The dotted lines show the values for e_{max} and e_{min} for the tested Ottawa sand.

Penetration profiles. Figure 6-18 shows the cone tip resistance profiles for all 18 specimens. (Note: the initial high gradient at shallow depth z<30mm results from upper boundary effects around the central orifice). In general, the tip resistance decreases after dissolution (Figure 6-18 - various panes). The tip resistance increases with sediment density (Figure 6-18 – each pane). The drop in tip resistance increases with the extent of dissolution, and it is most pronounced when comparing the penetration resistance in initially dense soils to the penetration resistance in the

same soil after dissolution. No appreciable changes in tip resistance are observed after dissolution in initially loose sediments.

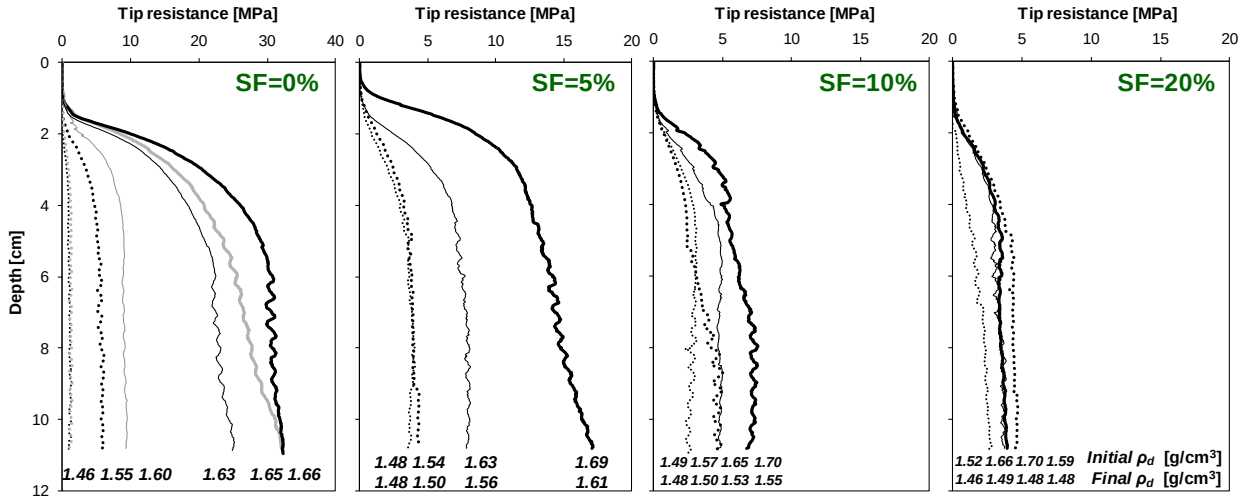

Figure 6-18. Penetration profiles for different initial densities and mass fraction of soluble particles SF

Void ratio vs. tip resistance and settlement. The mean values of penetration resistance in the steady lower 2/3's of the profile are plotted together in Figure 6-19. A single trend is observed when the tip resistance is plotted vs. void ratio at the time of penetration. This suggests that penetration resistance is primarily a measure of density at the time of penetration.

Previously proposed equations for penetration resistance q_t as a function of relative density D_R superimpose with the experimental data shown in Figure 6-19 and confirm the prevalent effect of void ratio on penetration resistance.

Jamiolkowski et al. 2001 $$D_R = 100 \cdot \left[0.268 \cdot \ln\left(\frac{q_t / \sigma_{atm}}{\sqrt{\sigma_{vo}' / \sigma_{atm}}} \right) - 0.675 \right]$$

The single trend between cone resistance and void ratio at the time of penetration indicate that cone resistance is insensitive to other dissolution effects such as changes in soil fabric and in horizontal stress. In part, this confirms that initial fabric does not significantly affect large-strain shear strength. High post-dissolution void ratios minimize the effect of horizontal stress on post-dissolution cone resistance, even as the horizontal stress may change between k_0=0.3 and k_0=0.65 during dissolution (this range applies to normally consolidated soils; changes depend on initial soluble fraction and grain size reduction.

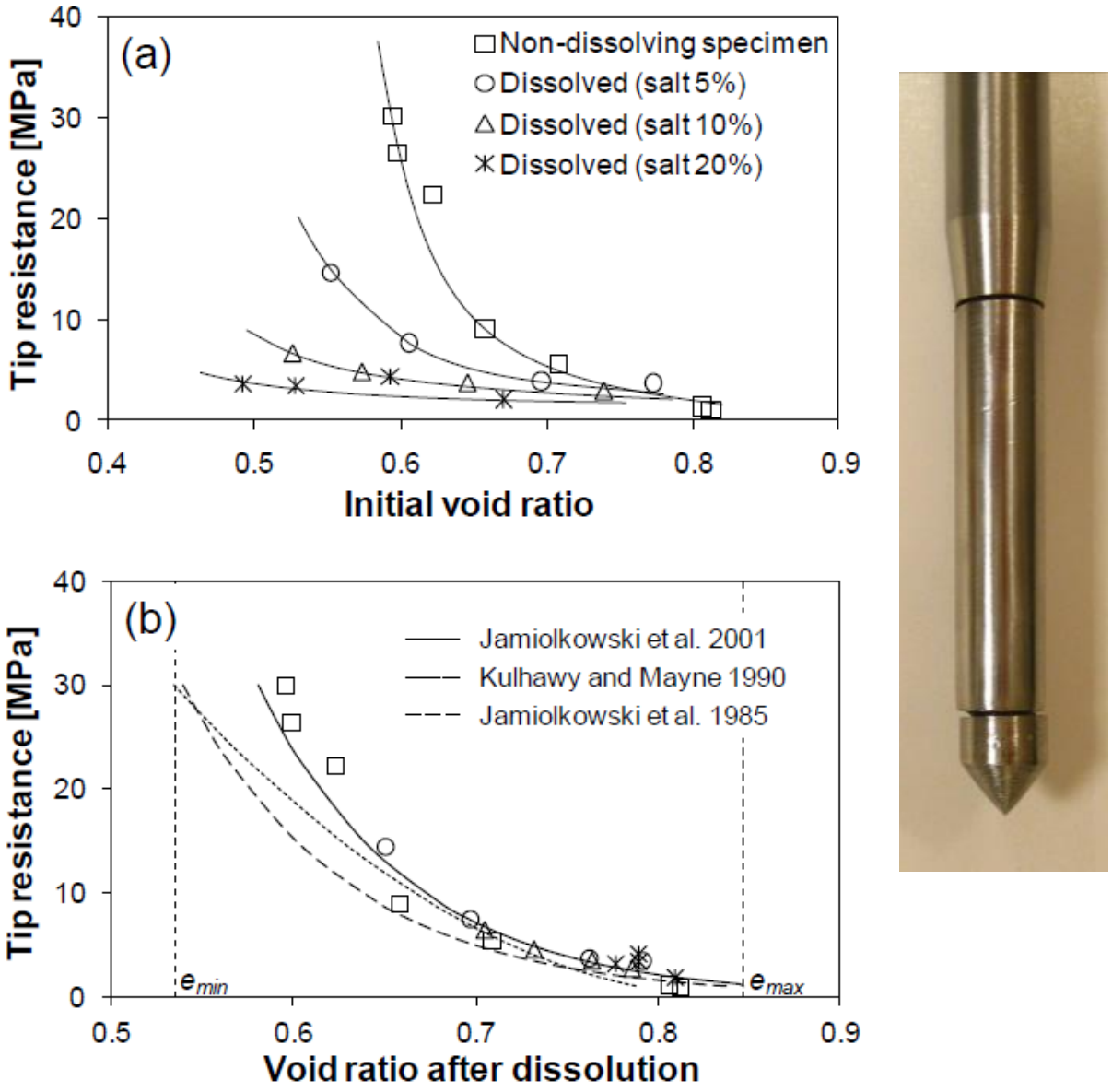

Figure 6-19. Void ratio vs. tip resistance and settlement – All test results

Conclusions: Site characterization. These experimental results allow us to conclude that

- Void ratio increases due to homogeneous mineral dissolution (as shown in Section 2). The change in void ratio is more pronounced in initially dense sediments. There is a terminal density or void ratio for dissolution, and the void ratio after dissolution will not exceed this terminal void ratio regardless of the extent of dissolution. For the conditions of this study, the

terminal void ratio for dissolution corresponds to a relative density of Dr ≈15% and it is attained when dissolution exceeds a mass fraction loss of SF>10% (probably closer to 20%).

- Mineral dissolution decreases the cone tip resistance. The drop in tip resistance increases with the extent of dissolution, is most pronounced in dense sands, and it is minimal for initially loose sands.
- There is a single trend in penetration resistance vs. the void ratio at the time of penetration. Fabric and changes in lateral stress that accompany mineral dissolution do not seem to affect this trend.

Once again, these observations are relevant to the homogenous dissolution of randomly distributed dissolvable grains.

6.4.2. Slope Stability

The potential for slope instability due to solid phase loss is explored in this section. The research approach combines experiments and discrete element simulations.

Experimental Study. A small scale 1g-laboratory experiment was designed to explore the consequences of dissolution on slope stability under realistic saturated conditions, where dissolution usually occurs. The experimental study was implemented in a thin tank made of two parallel acrylic plates (width 18mm, separated by 13mm gap - Figure 6-20). The thick acrylic walls were firmly fixed to the spacer along all edges to minimize the horizontal deformation of walls (maximum δh=0.06mm). Three inlet ports at the bottom were covered with a flow diffuser that runs all along beneath the sediment to promote 1D flow.

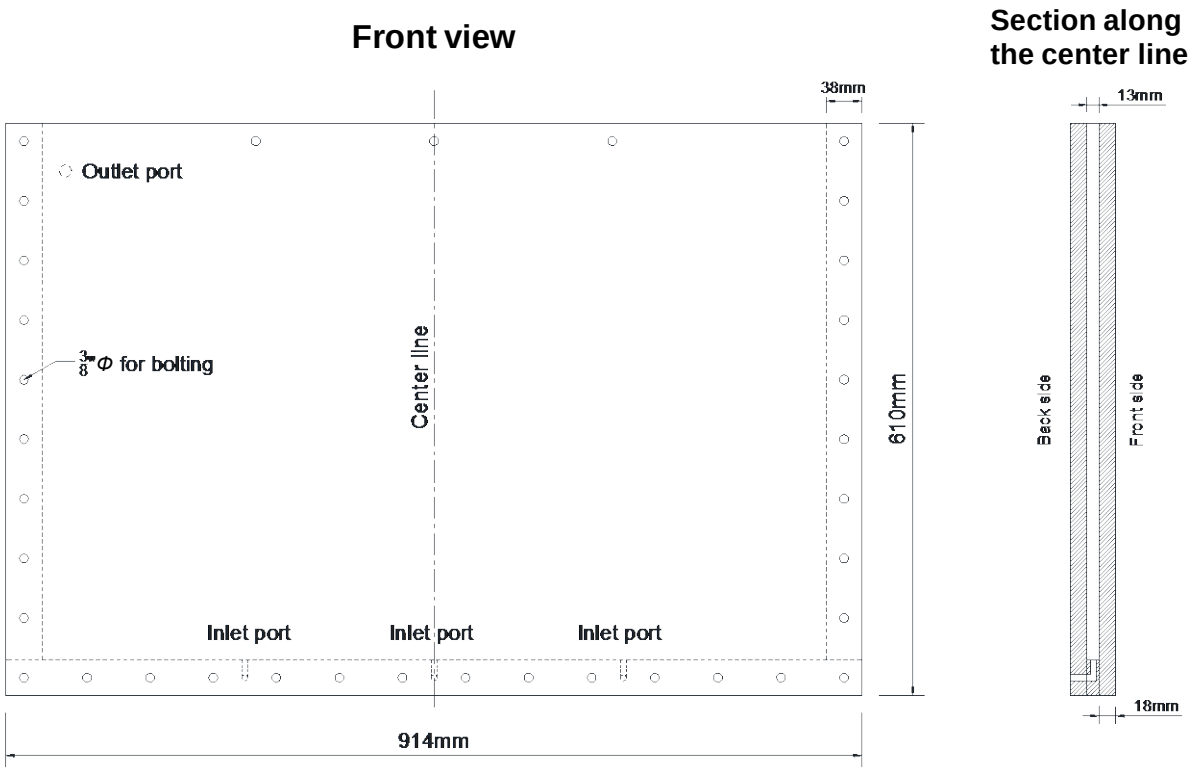

Figure 6-20. Transparent 2D tank for the study of dissolution effects on slope stability

The sediment is a mixture of 90% sand (insoluble grains) and SF=10% salt (soluble grains). Sand and salt are dry mixed, and pluviated into the tank to form the slope at an initial angle of 30°. The model is slowly flooded with a saturated NaCl brine solution injected from the bottom (5 hrs). Gradual dissolution is controlled by progressively lowering the salt concentration in the injected fluid (duration: 3 days). The deformation of the slope is recorded using time-lapse photography with a 5 min time interval.

Results in Figure 6-21 show displacement vectors between photographs gathered before dissolution and at the end of dissolution. Global vertical displacements prevail, the magnitude of displacement increases almost linearly with elevation, and horizontal displacements are more prominent near the slope surface.

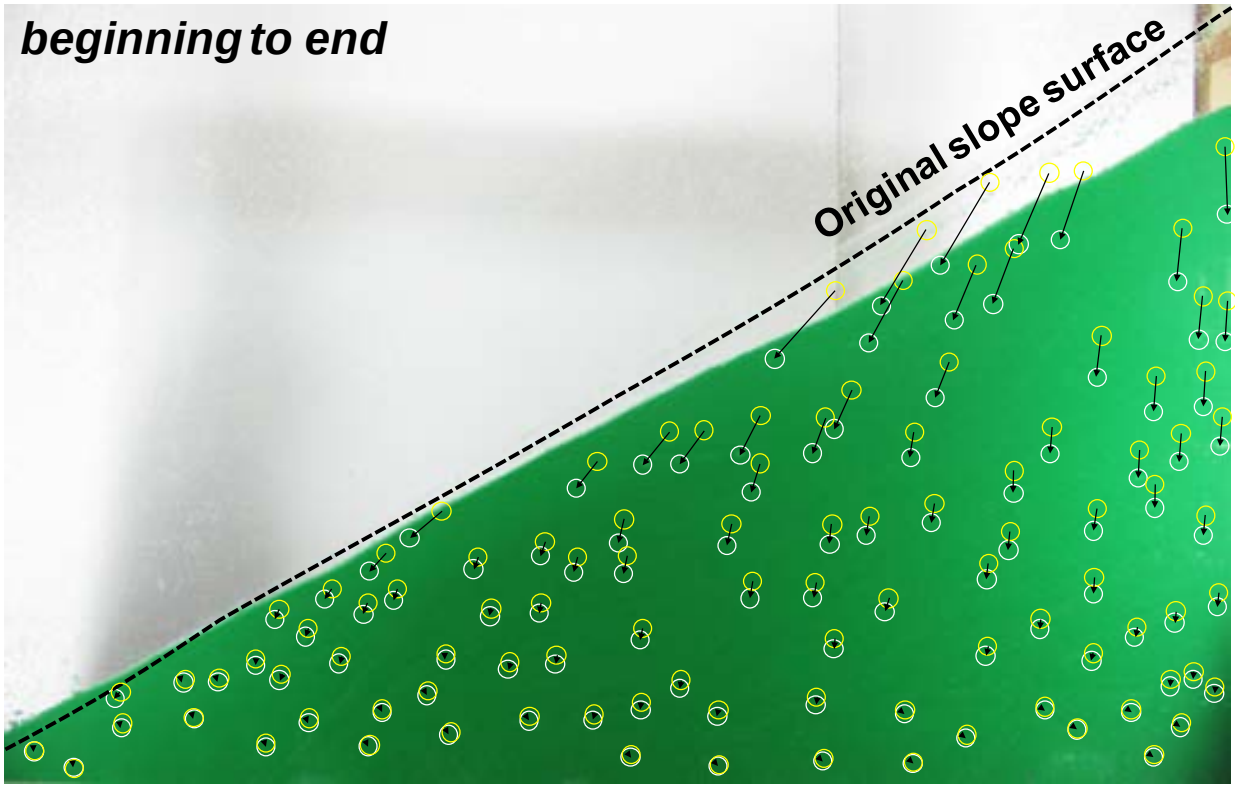

Figure 6-21. Experimental results – Overall displacements

A sudden displacement is detectable when all recorded images are projected in movie-form. The two consecutive images that capture this sudden displacement are compared in Figure 6-22: displacement vectors suggest the development of a shallow failure that occurred within the 5 min picture interval. The maximum possible time for this local failure is the time interval between photographs Δt=5 min; given a drainage length similar to the slide depth d=10 cm, then the coefficient of consolidation for drained conditions should be higher than $c_v > d^2/\Delta t$= 0.333 cm^2/sec, which corresponds to fine sands. Therefore, there is high probability that this local failure took place under undrained conditions assuming that the duration was less than 5 min. The possible sequence of events could involve: dissolution, internal stress states approaches

failure (see previous sections), increased porosity, granular skeleton collapse, excess pore pressure generation, decreased shear strength and failure.

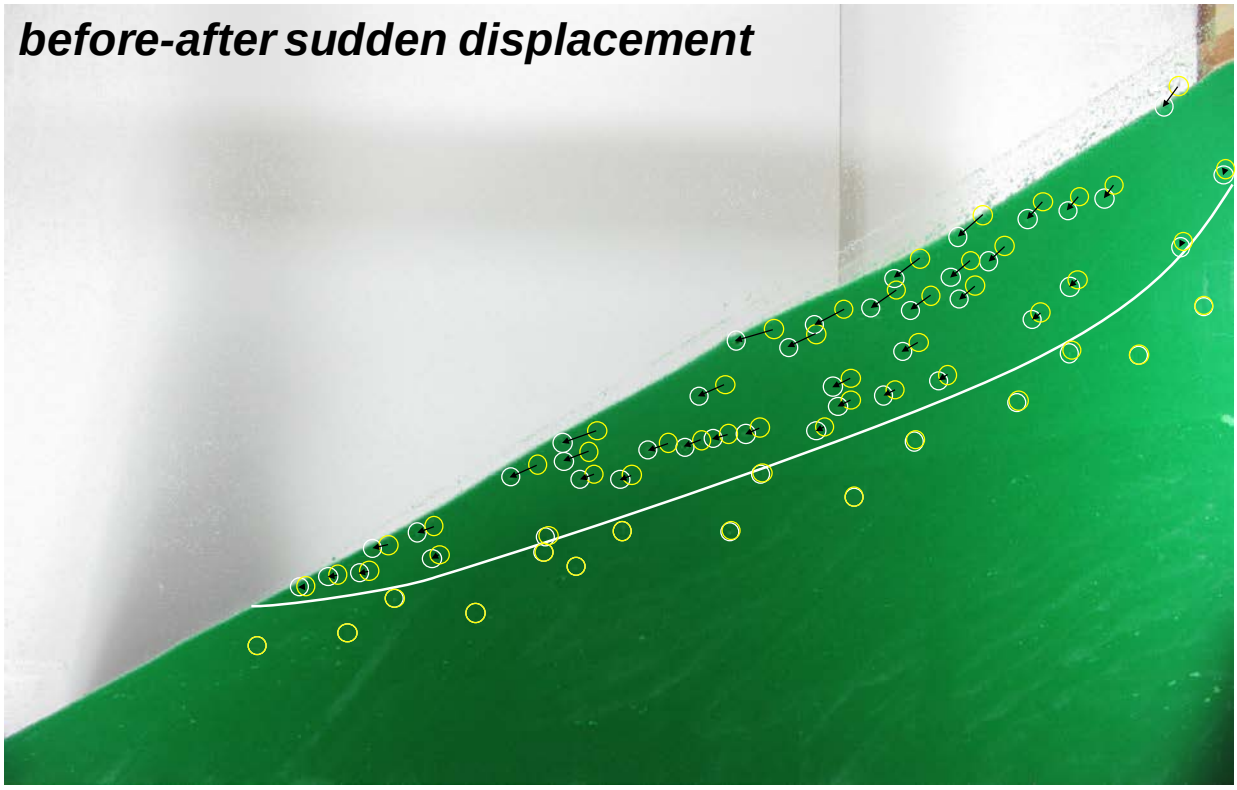

Figure 6-22. Experimental results – Positions before and after a sudden localized displacement

Numerical Study. The consequences of dissolution in sloping ground is further investigated using 2D-DEM simulations (PFC 2D – Itasca). Conditions are “drained” throughout the test, there is no friction between the sediment and the vertical lateral walls (i.e., slice of a long slope), and the friction coefficient is 0.5 between the sediment and the base. We simulate interlocking due to grain angularity by hindering the rotation of a preselected percentage of particles, HR=0%, 40%, and 80%. Soluble particles are homogeneously distributed and account for SF=25% of all particles. Dissolution is simulated by slowly and simultaneously reducing the size of all soluble particles.

Three initial slope angles are considered β=20°, 30°, and 40°. Figure 6-23 shows the initial geometry for a β_o=20° slope angle. The numerically determined angle of repose β_{repose} increases with the percentage of particles with hindered rotation: β_{repose} =20° for HR=0%, β_{repose} =35° for HR=40%, β_{repose} =51° for HR=80%. Therefore, only the slope with β_o=20° is stable when HR=0%, β_o=20° and 30° are stable slopes for HR=40%, and the three slopes β_o=20°, 30°, and 40° are stable when HR=80%.

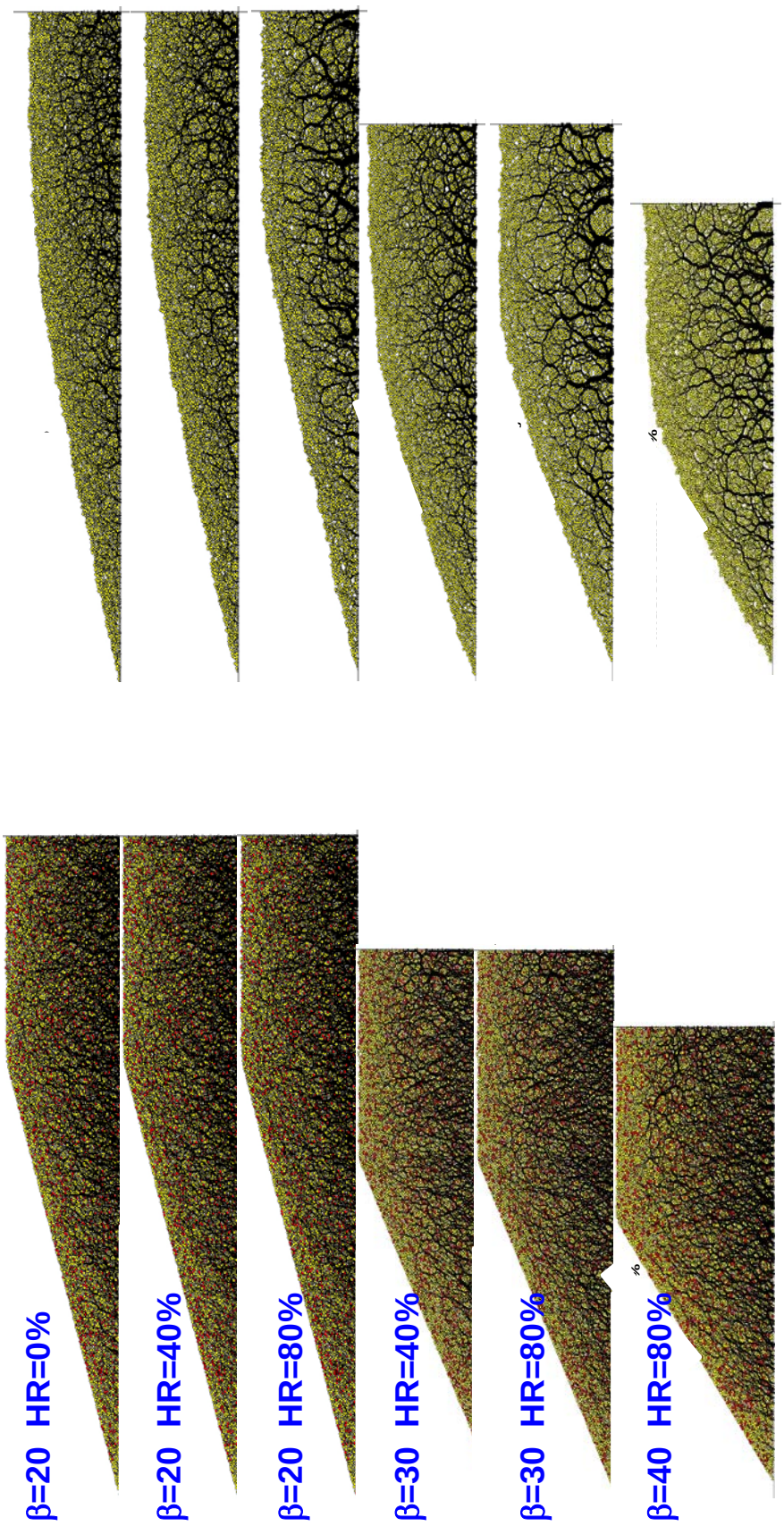

Figure 6-23. Force chains before and after dissolution for different initial slope angles and interlocking

123

Force chains plots before and after dissolution show that a honeycomb-shaped topology characterizes the fabric after dissolution (Figure 6-23). Load-carrying granular arches develop around dissolving particles and the local porosity increases (Notice that voids are next to strong chains). The honeycomb-shaped force chains are more prominent in sediments with greater interlocking, i.e., higher rotationally hindered particles HR. The final overall porosity increased in all cases. This distinct post-dissolution internal fabric anticipates a different sediment response upon further loading. In particular, the inherent shear loading the slope imposes on the sediment may trigger static liquefaction and flow given the higher contractive tendency in soils that experienced dissolution.

In agreement with experimental results, vertical settlement is the prevailing global deformation pattern (Figure 6-24). Sediments with higher soluble fraction SF and lower internal friction/interlocking HR experience more settlement. The horizontal components extracted from displacement vectors show that horizontal displacements are largest near the slope free surface and decrease away from the slope surface without a sharp transition

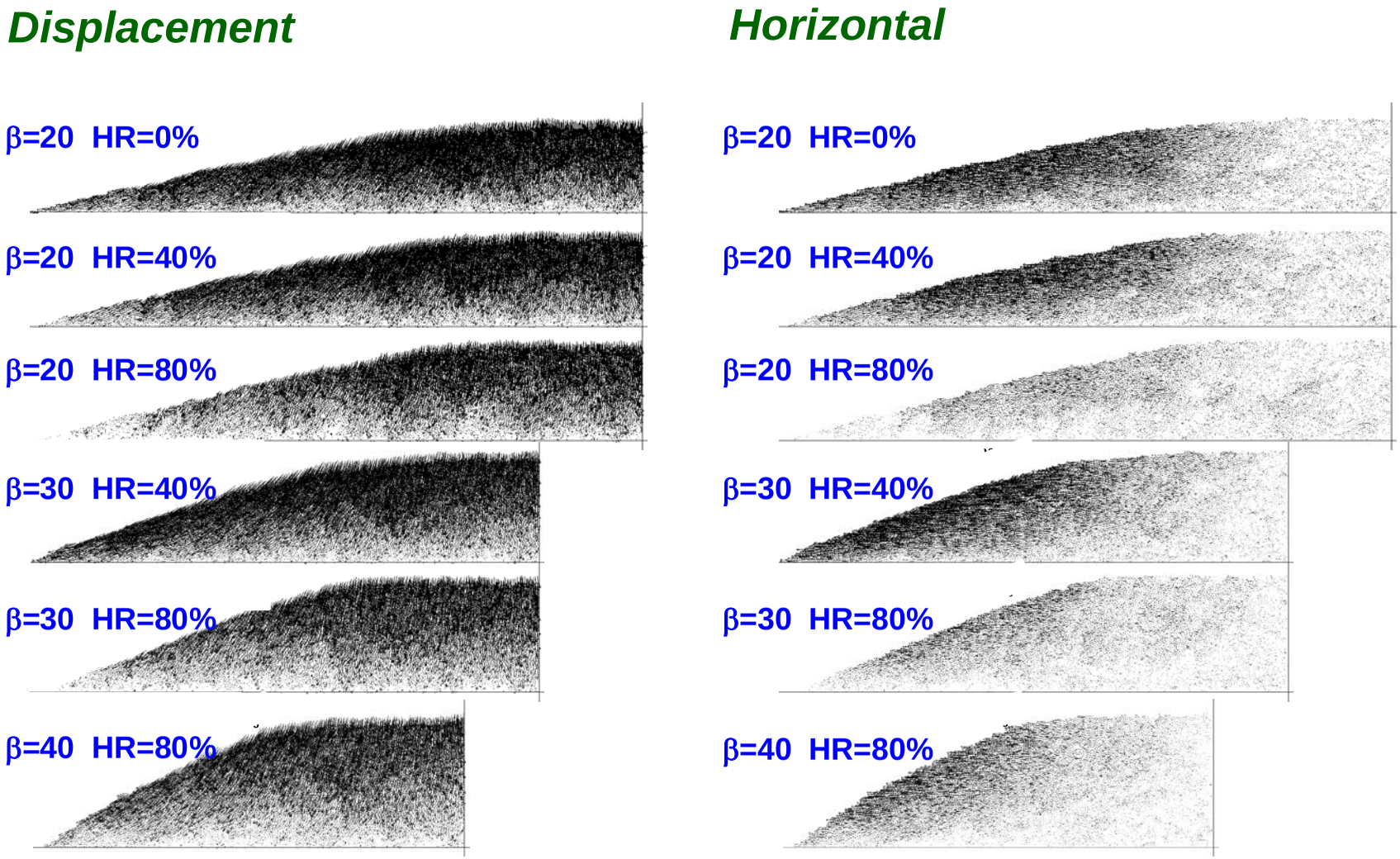

Figure 6-24. Displacement vectors for different initial slope angles and interlocking

Slope angles become smaller as dissolution progresses in all cases (Figure 6-25). Slope flattening is more pronounced in sediments with lower friction angle. The data are normalized by the angle of repose in each case. A single trend $\beta_{final}/\beta_{repose}= 0.8(\beta_0/\beta_{repose})$ is observed when the lost solid fraction is SF=25%.

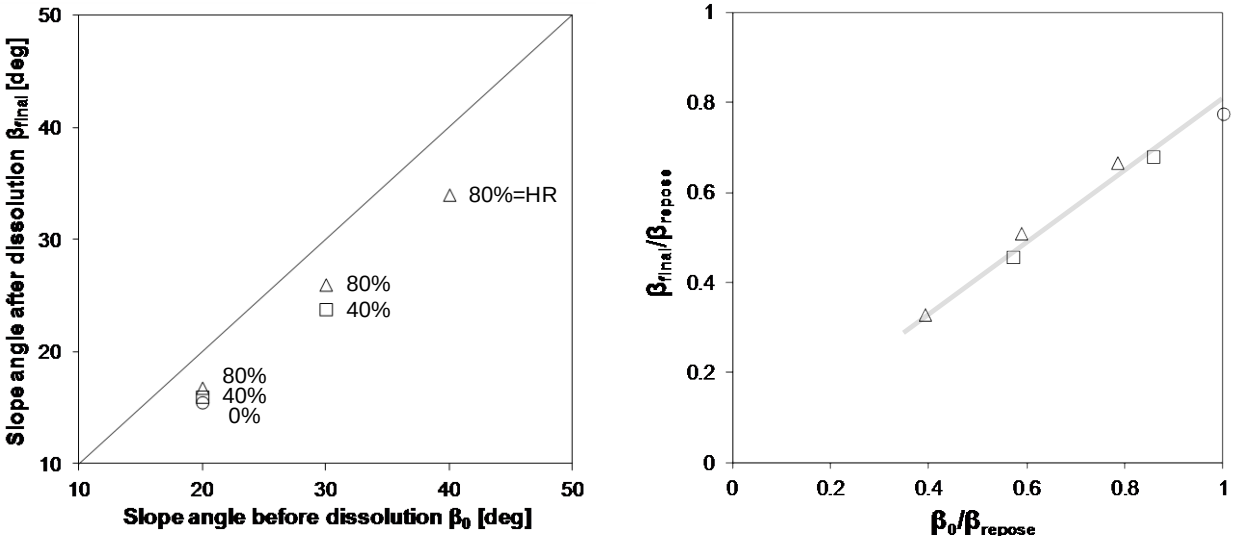

Figure 6-25. Initial slope angle vs. the final slope angle

Conclusions: Slope Stability

- Dissolution leads to significant slope movement. Global vertical settlements are the prevailing deformation pattern. Lateral movements are prominent near the slope free surface. Higher granular interlocking and lower initial slope angle lead to lower dissolution-induced later displacements.
- Slopes become flatter after dissolution; the reduction in slope angle is more pronounced in sediments with lower friction and higher initial slope angle.
- There is no shear localization or catastrophic failure during dissolution under drained condition. However, sudden undrained shear failure may take place during dissolution. A possible sequence of events could involve: dissolution and increase in porosity, internal stress

approaches failure, structural collapse and pore pressure generation leading to static liquefaction.

- Upon dissolution, load-carrying grain arches develop around dissolving particles, and a honeycomb-shaped contact force chain characterizes the high-porosity fabric after dissolution. This distinct internal fabric will have a different sediment response upon further loading; in particular, the inherent shear load bias in slopes may trigger liquefaction and flow.

6.4.3. Surface Settlement & Shallow Foundations

A firm foundation can be compromised by dissolution-induced volume contraction in the underlying soil. This section documents the study of grain dissolution effects on the load-settlement behavior of a free surface and on shallow foundations. We use a two-dimensional discrete element code (PFC-2D) to simulate subsurface volume contraction by removing an inclusion size D within a laterally confined sediment. Sediments are either loosely or densely packed, and particle angularity is modeled by hindering rotation HR. The inclusion depth z to diameter D ratio is varied between z/D=2 and 9.

Free surface. Grains flow to fill the cavity once the inclusion is removed, in agreement with the cohesionless nature of the sediment. As grain interlocking increases, the displacement field is limited to a smaller-angled fan and lower displacement magnitude take place. As grains flow downwards, emergent “porosity waves” propagate upward towards the free surface; these phenomena result as a combination of gravity and friction.

Grain flow is accompanied by contact force arch formation and collapse (Figure 6-26). Contact forces concentrate along the sides of the lost region and are most prominent in sediments

with higher friction angle. Grains in the re-filled cavity have small contact forces. Hence, there is a “ghost effective void” that is larger than the original inclusion size. While grains inside the effective void carry almost no vertical forces, they do contribute to prevent the buckling of granular arches around the effective void. Porosity is high inside the effective void especially in sediments with high interlocking (i.e., high hindered rotation HR), because friction hinders particle arrangement as grains flow to fill the void. The global contact force network elongates towards the free surface especially in sediments with higher interlocking.

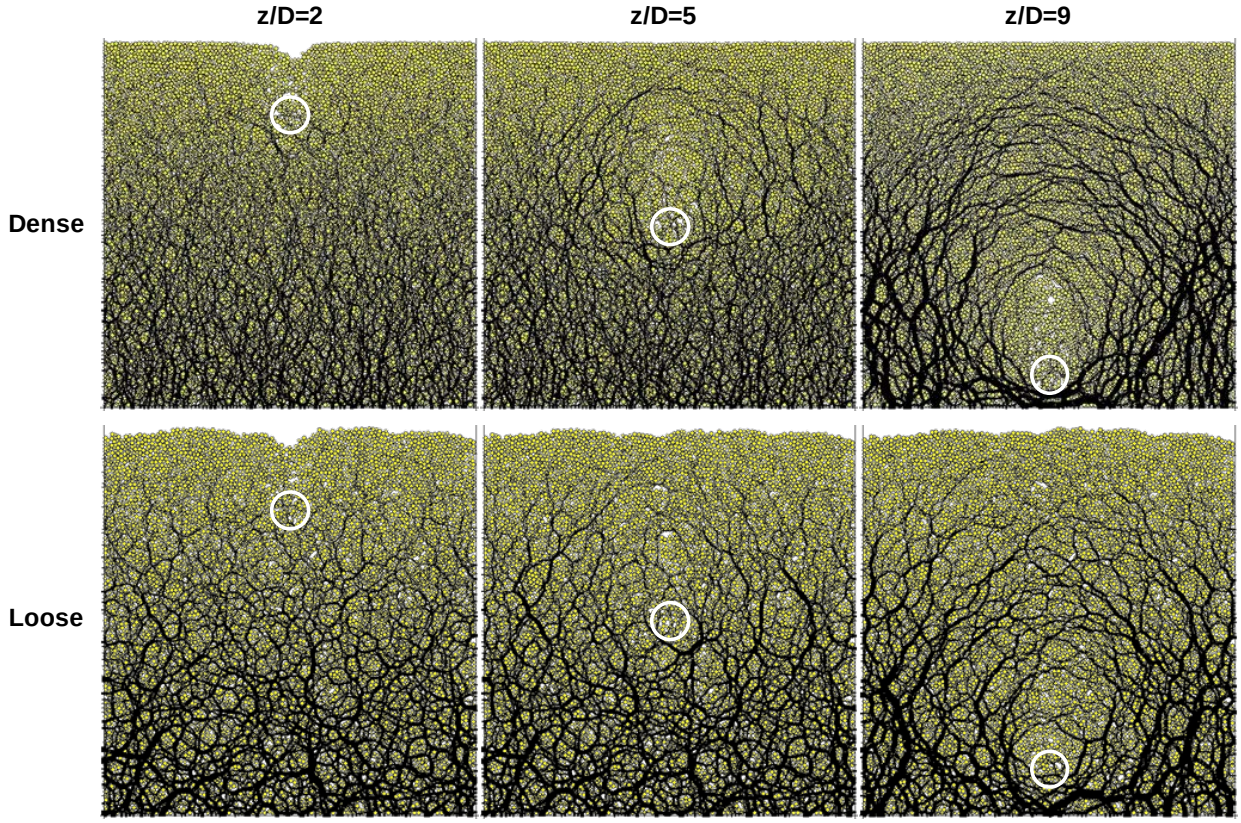

Figure 6-26. Shallow cavity contraction: post-dissolution force chains (HR=40%)

A Gaussian function can be fitted to the observed surface settlement profiles, in agreement with large-scale field observations (Figure 6-27). The maximum surface settlement d_{max} (1)

decreases with the depth-size ratio z/D, (2) it is relatively unaffected by interlocking or packing density for shallow inclusions z/D~2, (3) however, denser or more interlocked sediments lead to lower peak settlement d_{max} when inclusions are deep z/D>5. The affected "characteristic width" of the surface settlement profile" W is the standard deviation in the fitted Gaussian function. DEM results show that the effective width W increases with z/D and it decreases with friction/interlocking (Figure 6-27).

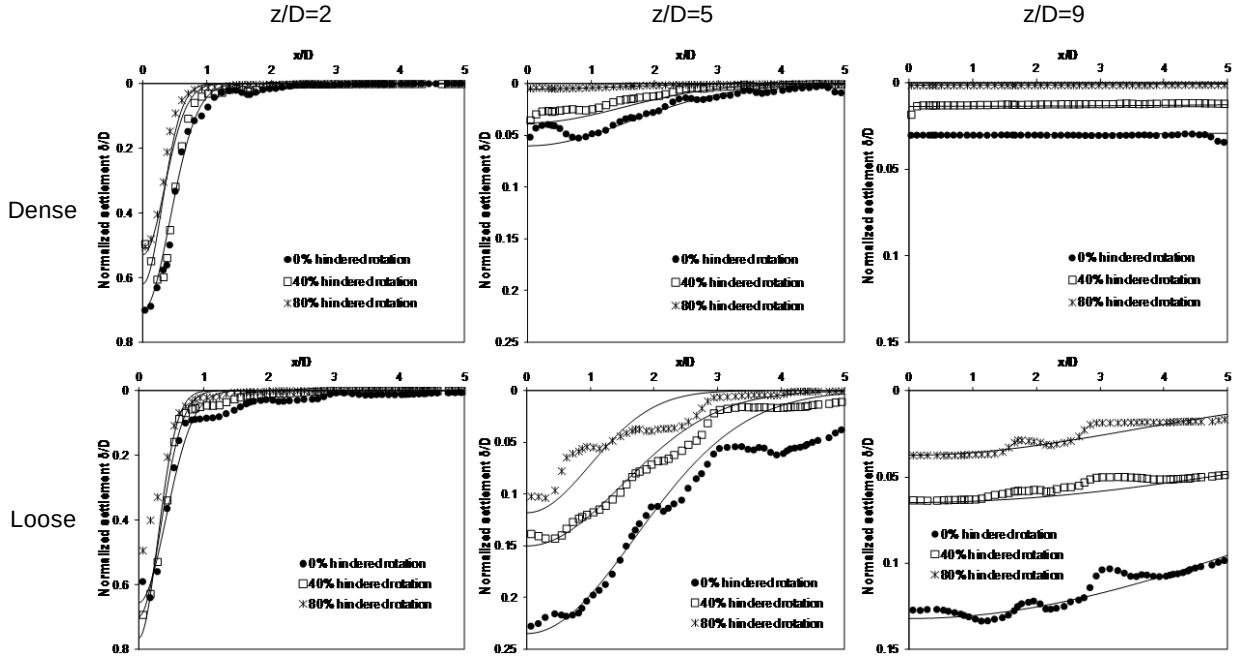

Figure 6-27. Surface settlement profiles

It is often assumed that the volume per unit length or the area of surface settlement AS in the field is equal to the volume of ground loss AV around the tunnel. Our simulation results show that the ratio is AS/AV<1 for dense dilative sediments, and that it decreases with z/D and interlocking (Figure 6-28); in these cases, there is clear gain in porosity above the ground loss region. On the other hand, contractive sediments with low friction can cause surface settlement

volumes higher than the extracted volume AS/AV and contraction increases with the normalized inclusion depth z/D.

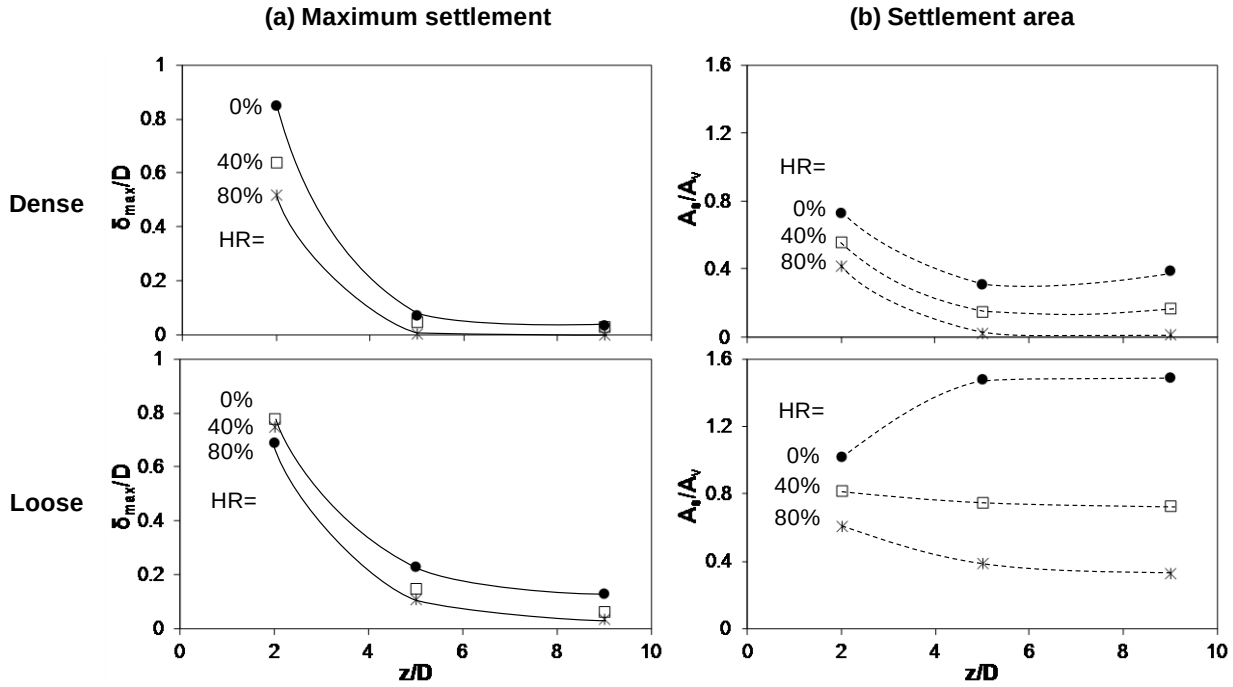

Figure 6-28. Maximum settlement and settlement area

Footing. Figure 6-29 shows the test geometry and boundary conditions for a shallow footing. Load-settlement simulations are done in stress-controlled mode: the load is applied in small steps, and settlements follow. Dissolution under zero lateral strain $\varepsilon_h=0$ is simulated by gradually reducing the radius of all the soluble particles at the same rate.

Simulations are performed for three load-dissolution histories: (1) virgin sediments loaded to failure, (2) load-settlement tests on sediments after dissolution, and (3) load to a factor of safety FS~2.5 followed by grain dissolution under constant vertical load (Figure 6-29). The load-settlement response on post-dissolution sediments show lower stiffness than on soil prior to dissolution. While the asymptotic “ultimate capacity” may be similar, loading after dissolution

requires much larger settlements to reach capacity than loading before dissolution. Dissolution under an existing foundation load significantly enhances settlements (Figure 6-30); in fact, the footing settlements are much greater than those the footing experienced for the same load when dissolution took place before loading.

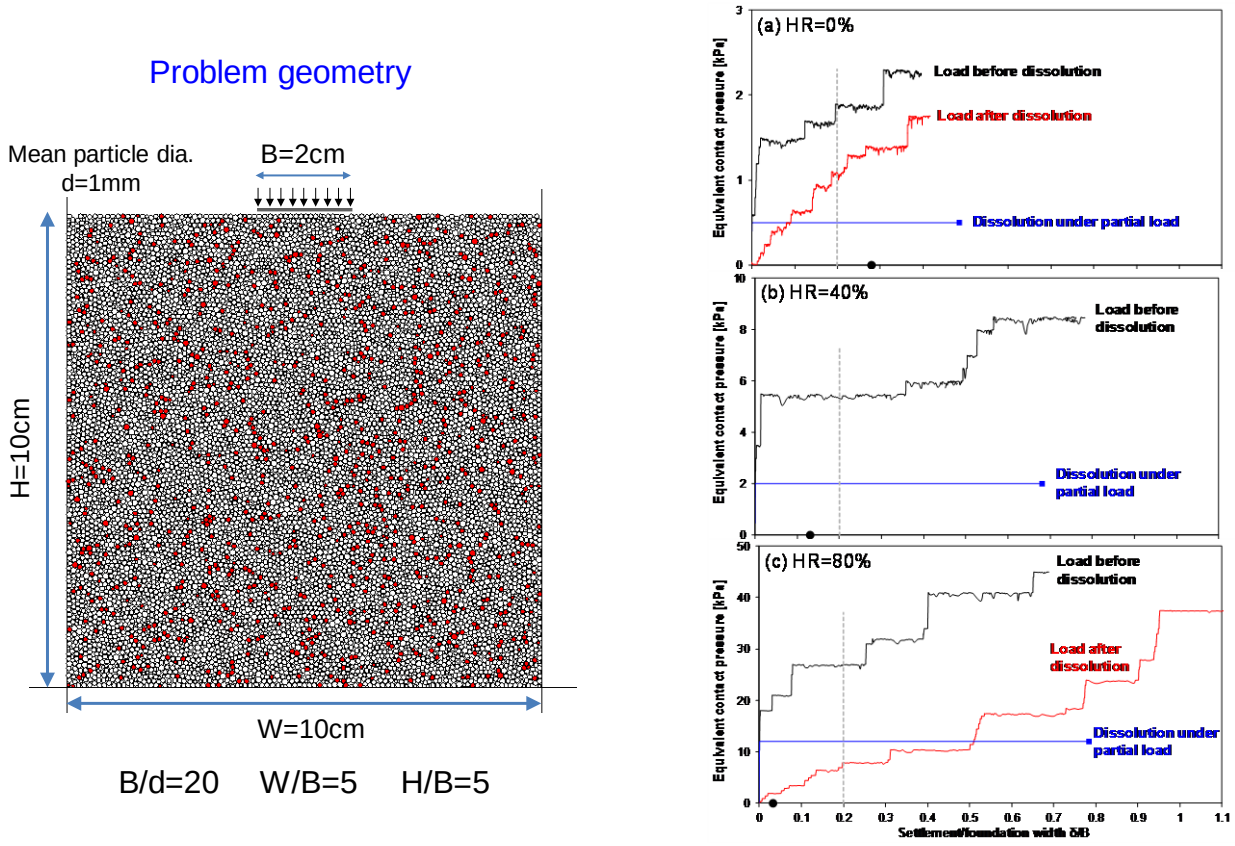

Figure 6-29. Footing: stress vs. settlement for two load-dissolution histories

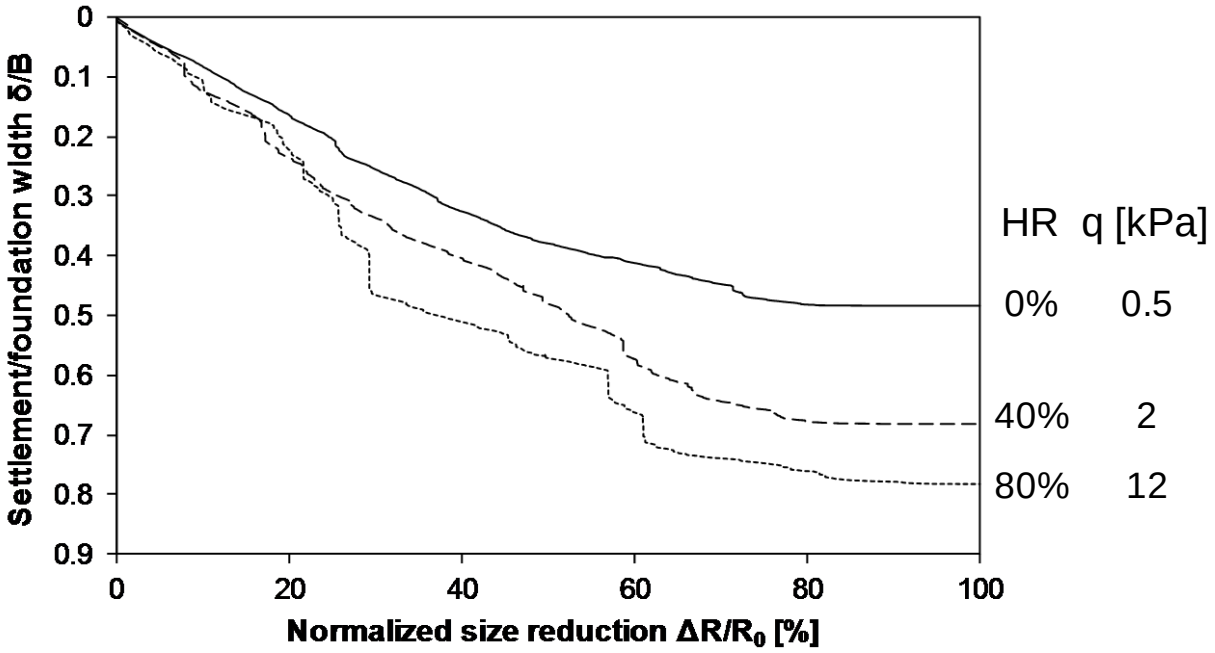

Figure 6-30. Dissolution under constant footing loading

Figure 6-31 shows grain displacement vectors for the three load-dissolution histories, for the case of no hindered rotation HR=0%. Displacements during pre- and post-dissolution loading are concentrated near the footing. Particle movements are high in dissolution under a constant load, affect deeper particles and cause significant upward flow at the sides. The internal fabric in post-dissolution sediments consists of a high-porosity honeycomb-shaped fabric that exhibits low stiffness and high compressibility.

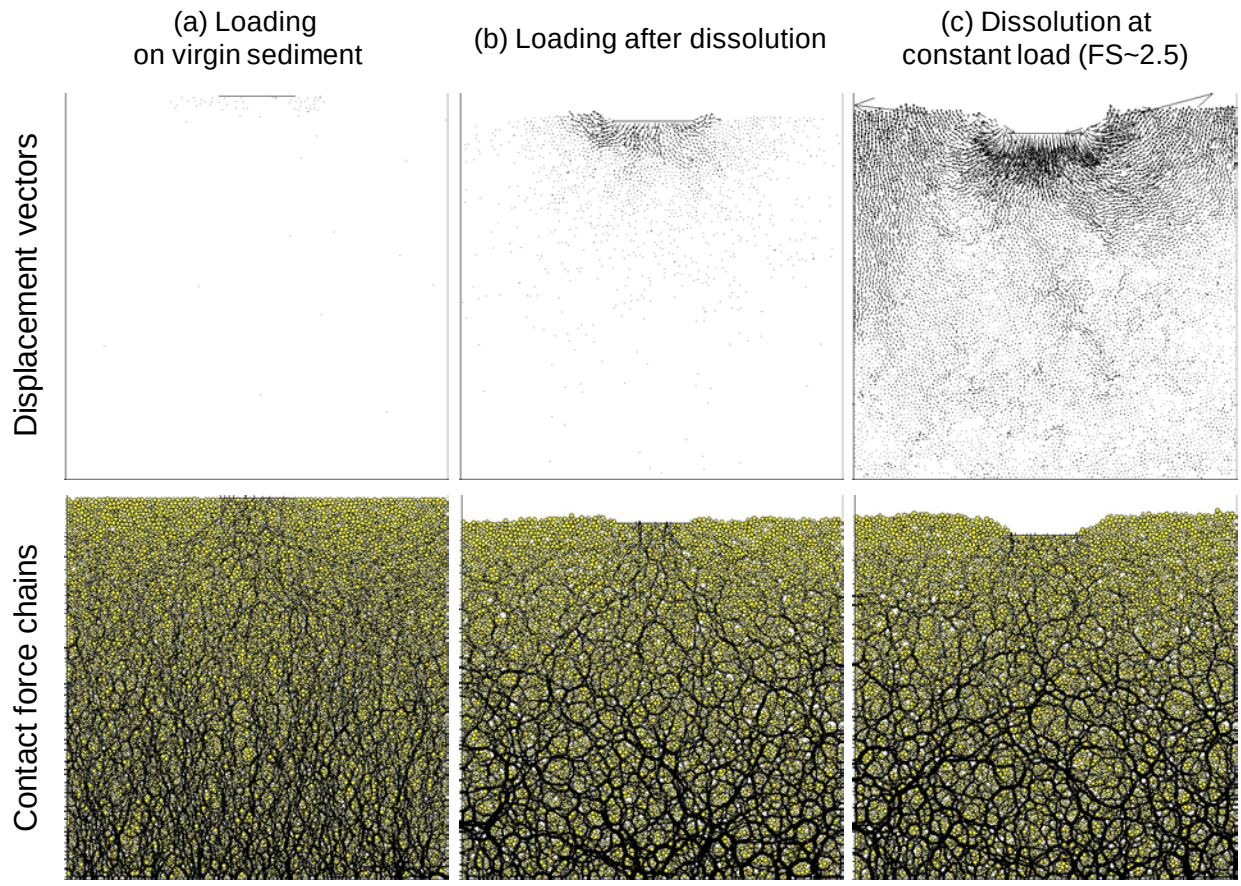

Figure 6-31. Grain displacements and contact force chains

Conclusions: Surface settlement. The load-settlement behavior of footings changes due to dissolution. The pre-dissolution sediment can pick up significant stress at relatively small settlement. On the other hand, post-dissolution sediments require higher settlements to mobilize resistance and to reach a bearing capacity. Grain interlocking significantly increases the overall load capacity on sediments either before or after dissolution. Settlement during dissolution under constant footing load is higher than when a foundation load is applied after dissolution.

6.5. Conclusions

This research investigated the effect of dissolution on sediment behavior, through experimental and numerical methods. We chose to use a discrete element method as a numerical simulator to capture the inherent particle-scale phenomena. The main conclusions from this study follow.

Dissolution: New Phenomena

- There are several modes of dissolution: homogenous dissolution (single mineral or randomly distributed soluble particles), pressure-dependent dissolution, and localized dissolution (high advection regimes with limited diffusion).
- Dissolution causes global contraction.
- The internal pore volume increases towards a "terminal void ratio" in the case of homogeneous dissolution. Pressure solution promotes densification during early stages of dissolution, even in the absence of reprecipitation.
- High friction/interlocking hinders global contraction but leads to a higher increase in porosity.
- A new internal fabric develops where honeycomb force chains are spatially correlated with higher local voids.
- Horizontal stress may drop to K_A in high friction/interlocking sediments
- Shear localization naturally emerges in pressure solution
- Hydro-chemical coupling can lead to dissolution localization (pipes or wormholes) as the result of the positive feedback that involves changes in porosity and reactive transport. Marked force chains are preferentially vertical away from pipes, yet, they are preferentially horizontal within pipes. Horizontal contact forces inside pipes prevent the buckling of granular columns in the stable zones.

Post Dissolution Stress-Strain Behavior.

- Post-dissolution sediments are more compressible than the original sediments. The increase in compressibility correlates with the extent of dissolution the sediment has experienced.

- Post-dissolution simple shear loading encounters lower shear stiffness and higher contractive tendency in sediments that have experienced more pronounced dissolution. Therefore, post dissolution sediments will be more vulnerable to liquefaction when sheared under undrained condition.

Engineering implications.

- Characterization: the cone tip resistance decreases due to dissolution, and it is a function of the final void ratio only.
- Slopes experience global vertical settlement and lateral displacement takes place near the slope. Lateral displacements increase with slope angle and the extent of dissolution, and are hindered by friction and interlocking. No sudden drained failures are caused, yet static liquefaction possibly may take place in saturated conditions following a structural collapse of the internal fabric during dissolution.
- Footings need larger settlement to mobilize capacity when sediments have experienced dissolution. Higher total settlements are recorded for footings on ground that is subjected to dissolution after the footing has been loaded, than when footings are loaded on ground that has experienced dissolution before the application of the footing load.

7. The Effect of Subsurface Mass Loss on the Response of Shallow Foundations

7.1. Introduction

7.1.1. Context

Subsurface volume loss results from natural processes (dissolution, piping erosion and grain migration) and manmade processes (e.g., mining, tunneling, energy geo-storage system, CO2 injection driven dissolution, and resource recovery such as dissociation of methane hydrates).

The sediments of Atlantic Coastal Plain in the vicinity of the Savannah River Site (SRS) consist of quartz sand, clay, limestone, and conglomerate ranging in age from late Cretaceous to Holocene. Multiple site investigation studies have shown a complex stratigraphy that resulted from marine and the fresh-water depositional environments, including the presence of dissolved cavities and soft zones (WSRC, 1999; see also Kochanov, 1999). The geological formation history and subsurface stratigraphy are reported in Section 4.

Subsurface volume loss leads to complex stress and displacement fields which depend on stratigraphy, mechanical parameters (density, stiffness, cementation, diagenesis and preconsolidation), hydro-geological conditions, the extent of removed mass, depth, and load-dissolution histories (i.e., whether load is applied before or after dissolution). General conclusions may not be provided for such a complex system and simple analytical solutions fail to capture emerging effects and governing parameters. Consequently, numerical simulations are needed to study the implications of soft zone formation in the subsurface.

Dissolution cavities and soft zones in the subsurface at the Savannah River Site (SRS) raise concerns about their potential impact on near surface infrastructure. Macroscale analyses conducted in this part of the study require the development of a robust methodology to reproduce localized stress relaxation associated with dissolution and soft zone formation, the selection of adequate constitutive models, and proper calibration using laboratory and field data. A case history at the SRS was used for site-specific validation and subsurface model calibration followed by comprehensive simulations of hypothetical cases relevant to the SRS. Variables used in this report are identified in Figure 7-1.

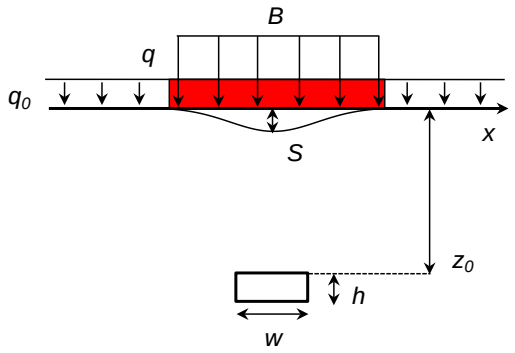

B [m]	Footing size
S [m]	Surface settlement
z_0 [m]	Soft zone depth
x [m]	Distance from the centerline
h [m]	Soft zone height
w [m]	Soft zone width
q_0 [kPa]	Surcharge loading
q [kPa]	Building loading
$q_{applied}$ [kPa]	Applied loading ($q - q_0$)

Figure 7-1. Notation used in this study

7.1.2. Preliminary Observations on the Choice of Constitutive Model

The selection of constitutive models has been a recursive process in this research. Our criteria for model selection have been driven by the need for:

- a simple model capable of capturing a wide range of stress paths
- a small number of physically meaningful parameters
- model parameters which must be able to be reliably estimated from characterization studies

Elastic, elasto-plastic with Drucker-Prager yield criterion (the conical yield surface provides more stable numerical simulations in complex stress paths than the hexagonal yield surface that characterizes the Mohr-Coulomb criterion), and Modified Cam Clay models were used throughout this study. Predicted stress-strain responses in each case are shown in Figure 7-2, Figure 7-3, and Figure 7-4. Most simulations were repeated with both plastic models. Selected runs most relevant to this study are presented in each case.

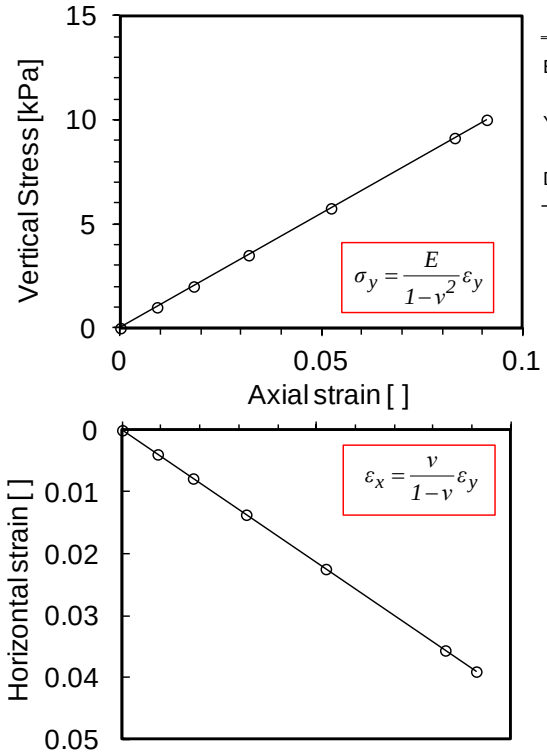

Element type	Plane Strain
Young's modulus E [MPa]	300
Drained Poisson's ratio υ	0.3

Figure 7-2. Elastic model

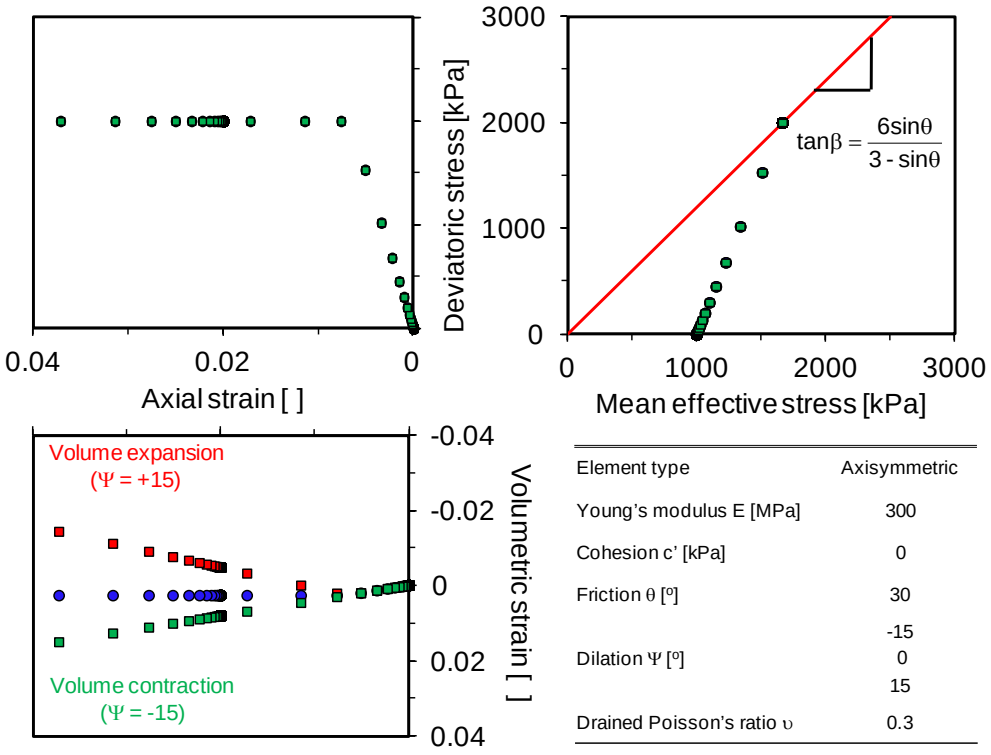

Element type	Axisymmetric
Young's modulus E [MPa]	300
Cohesion c' [kPa]	0
Friction θ [º]	30
Dilation Ψ [º]	-15 0 15
Drained Poisson's ratio υ	0.3

Figure 7-3. Elasto-plastic model (Note that strain hardening takes place in plane strain)

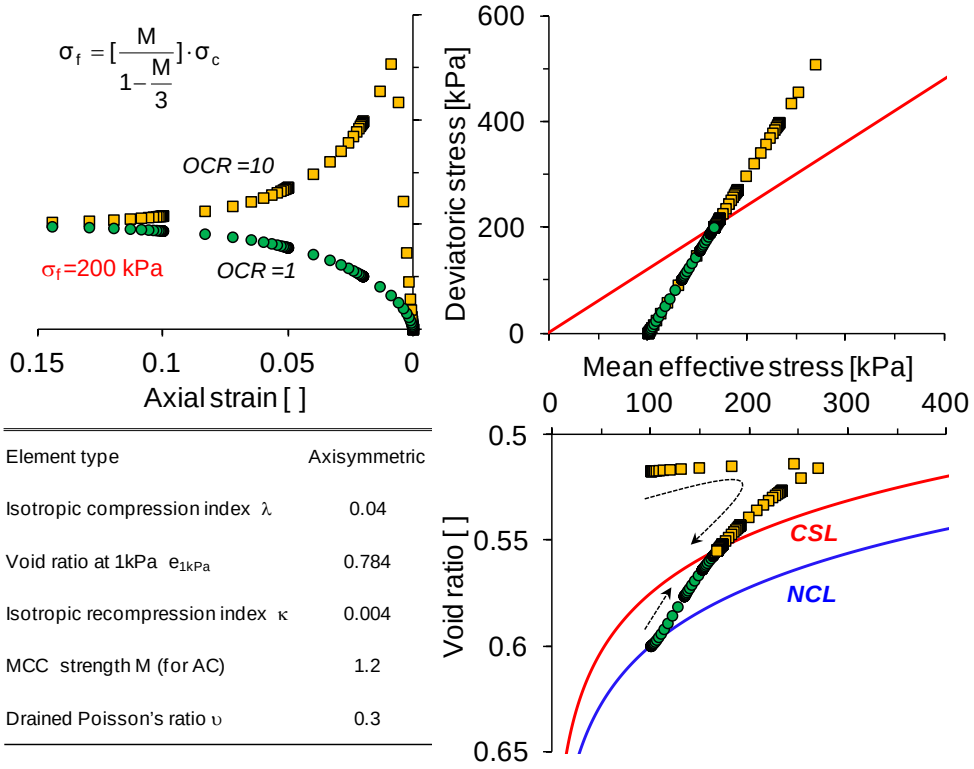

Element type	Axisymmetric
Isotropic compression index λ	0.04
Void ratio at 1kPa e_{1kPa}	0.784
Isotropic recompression index κ	0.004
MCC strength M (for AC)	1.2
Drained Poisson's ratio υ	0.3

Figure 7-4. Modified Cam clay model

The selection of a constitutive model and modeling strategy is intimately related to the nature of the problem and it is constrained by available information. In particular, our modeling approach recognizes:

- The stress field is very sensitive to model and model parameters in kinematically coupled conditions (Figure 7-5); this is not necessarily the case in large shallow foundation problems.
- Algorithms must be verifiable at all stages against closed-form solutions for similar conditions (Figure 7-6).
- Complex models imply a large number of parameters; this favors the ability of predicting past data, but hinders the robust predictability of future performance (Figure 7-7). We will place preference for simple, robust models that can be calibrated with available data.
- Field performance data is typically smooth, hence, information-limited. For example, settlement results shown in Figure 7-8 can be closely fitted with a 3rd order polynomial; this means that regardless of the number of measurement points gathered throughout the foundation and the construction history, these settlement data provides 4 “pieces of information” only (for comparison, x-y data fitted with a straight line y=a+bx provides only 2 pieces of information: a and b). We are guided by Ockham’s criterion throughout this research.

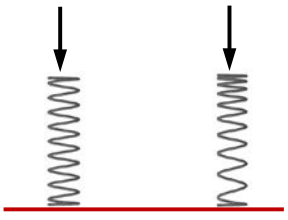

Model-**in**dependent force

Model-dependent deformation

(e.g., closed-form solution)

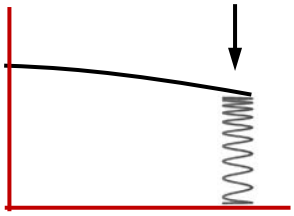

Kinematically coupled

Model-dependent force

Model-dependent deformation

(e.g., finite element analysis)

Figure 7-5. Geotechnical problems: Constitutive models

Boussinesq

$$\Delta\sigma_v = \frac{q}{\pi}\left[\beta + \sin\beta\cos(\beta + 2\alpha)\right]$$

$$\Delta\sigma_h = \frac{q}{\pi}\left[\beta - \sin\beta\cos(\beta + 2\alpha)\right]$$

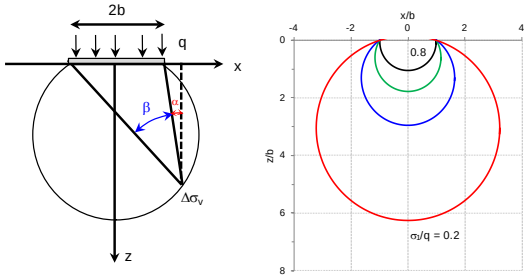

Kirsch

$$\sigma_r = p_i\frac{a^2}{r^2} + \frac{\sigma_{v\infty}}{2}\left(1 - \frac{a^2}{r^2}\right) + \frac{\sigma_{v\infty}}{2}\left(1 + \frac{3a^4}{r^4} - \frac{4a^2}{r^2}\right)\cos 2\theta$$

$$\sigma_\theta = -p_i\frac{a^2}{r^2} + \frac{\sigma_{v\infty}}{2}\left(1 + \frac{a^2}{r^2}\right) - \frac{\sigma_{v\infty}}{2}\left(1 + \frac{3a^4}{r^4}\right)\cos 2\theta$$

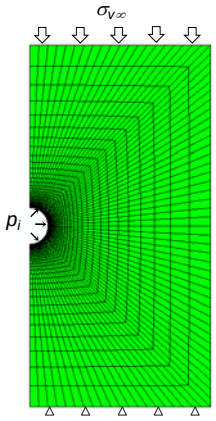

Figure 7-6. Geotechnical problems: Constitutive models

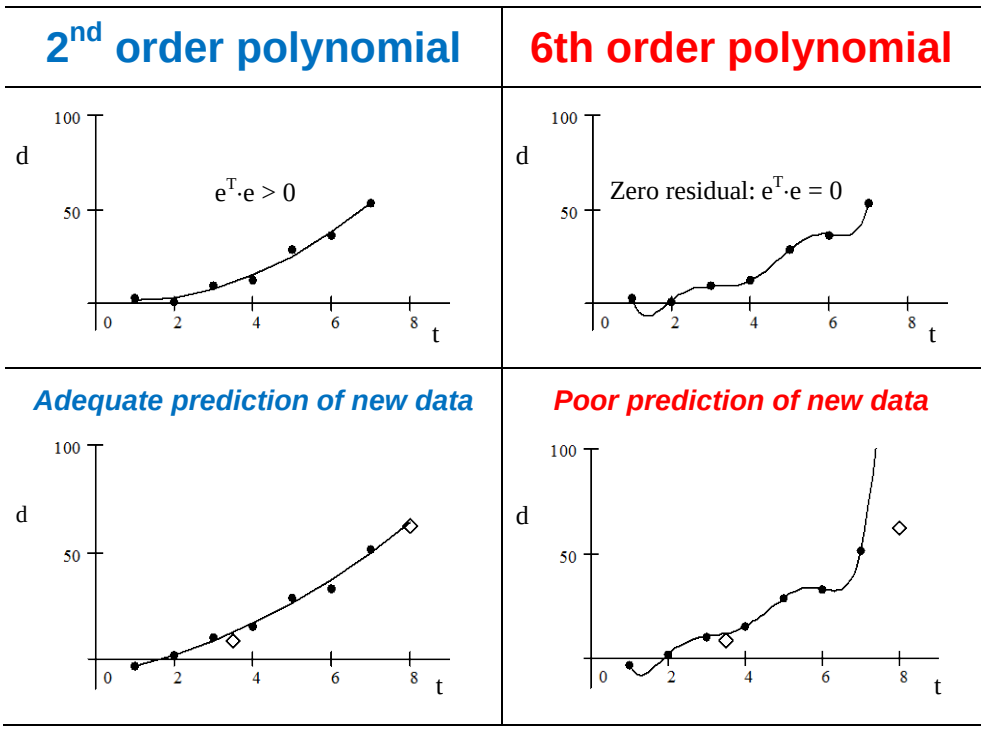

Figure 7-7. How much information is in the data?

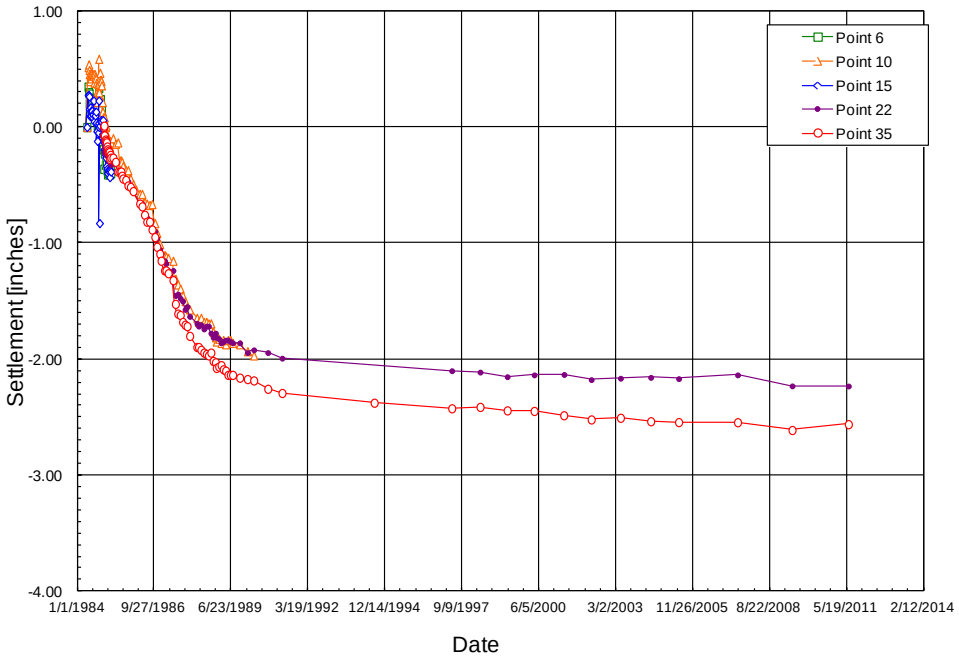

Figure 7-8. How much information is in these field settlement data? (data from SRNS, 2011)

7.2. Settlement Due To Soft Zones

7.2.1. Introduction

Strains and displacement fields are induced by localized mass loss within sediments. Various semi-empirical solutions have been proposed to predict surface settlements and subsurface deformations. However, the complexity of subsurface geological conditions often require more complex analyses and numerical simulations so that governing parameters can be properly captured to obtain credible results.

This section reviews previous studies and presents the stress relaxation module developed within the finite element program ABAQUS. A comprehensive parametric study is performed to explore the effect of various parameters for different subsurface conditions (soft zone depth z_0, number of nearby cavities, constant volume shear friction angle ϕ_{cs}, preconsolidation, and internal stress reduction). The extensive dataset generated from the numerical study is captured in a summary of simple trends that can be readily used for engineering applications.

7.2.2. Previous Studies

Closed-form solutions assume perfect plasticity to predict collapse (kinematically and statically admissible conditions - Atkinson and Potts 1977b), and elasticity to estimate stress fields (Kirsch, 1898; Terzaghi and Richart, 1952; Fares, 1987; Verruijt and Booker, 1996; Bobet, 2001). Numerical simulations have explored a wider range of conditions (Mair et al., 1981; Rodrıguez-Roa, 2000; Rodrıguez-Roa, 2002; Franzius and Potts, 2005; Chen et al., 2012) in particular, simulations show that ground movement is significantly affected by stress anisotropy (Guedes and Santos Pereira, 2000). Small scale (Atkinson et al., 1975; Atkinson and Potts,

1977a; Ahmed and Iskander, 2011_ENREF_1) centrifuge model tests (Atkinson and Potts, 1977b; Mair et al., 1981; Jacobsz et al., 2004; Marshall et al., 2012), and field studies have provided extensive surface and subsurface settlement profiles associated to mining and tunneling operations (Peck, 1969; Schmidt, 1969; Clough and Schmidt, 1981; O' Reilly and New, 1982; Mair et al., 1993; Mair, 2008). Displacement fields are regular-smooth in homogeneous media and can be expressed using a few characteristic parameters, as described next.

Surface Settlement. Settlement profiles with limited ground distortions are well matched by the Gaussian function, in terms of two degrees of freedom: the maximum settlement over the centerline S_{max} and the transverse distance from the centerline to the inflection point x_{infl} (Peck, 1969; Schmidt, 1969; Clough and Schmidt, 1981; Cording, 1991). Modifications to the Gaussian trend (Jacobsz et al., 2004) and other published functions with higher degrees of freedom (Celestino et al., 2000; Vorster et al., 2005) are summarized in Figure 7-9.

Model parameters	Equation	Reference
S_{max}, x_{infl}	$S(x) = S_{max} \cdot e^{-\frac{1}{2}\left(\frac{x}{x_{infl}}\right)^2}$	Peck (1969)
S_{max}, x_{infl}	$S(x) = S_{max} \cdot e^{-\frac{1}{3}\left(\frac{x}{x_{infl}}\right)^{1.5}}$	Jacobsz *et al.* (2004)
S_{max}, x_{infl}, β Note: $\alpha = f(\beta)$	$S(x) = S_{max} \cdot \frac{1}{1+\alpha\left(\frac{x}{x_{infl}}\right)^{\beta}}$	Celestino *et al.* (2000)
S_{max}, x_{infl}, β Note: $\alpha = f(\beta)$	$S(x) = S_{max} \cdot \frac{\alpha}{(\alpha-1)+e^{\beta\left(\frac{x}{x_{infl}}\right)^2}}$	Vorster *et al.* (2005)

Figure 7-9. Surface settlement - Empirical equations

Maximum Settlement S_{max}. The maximum settlement S_{max} is related to the mass loss, its depth and geometry, and the contractive-or-dilative tendency of the soil. Assuming neither dilation nor contraction, the value S_{max} can be obtained from the volume loss V_L and the distance to the inflection point x_{infl} by integrating the Gaussian settlement profile_ENREF_4

$$S_{max} = \frac{V_L}{\sqrt{2\pi}\, x_{inf\,l}}$$

Distance to Inflection Point x_{infl}. Published statistical regressions based on field data proved estimates of the distance from the centerline to the inflection point x_{infl} (Figure 7-10 – Peck,

1969; Schmidt, 1969; Atkinson and Potts, 1977a; Clough and Schmidt, 1981; Mair et al., 1981; O' Reilly and New, 1982; Mair et al., 1993; Moh et al., 1996). Equations relate the value x_{infl} to the soft zone depth z_0, and size R.

Subsurface Displacements. Subsurface displacements follow a Gaussian function as well. The distance to subsurface inflection points x_{infl} at depth z can be estimated with equations summarized in Figure 7-10 (Mair et al., 1993; Moh et al., 1996).

(a) *Ground surface*

Equations		Parameters	References
$\frac{x_{infl}}{R} = \left(\frac{z_0}{2R}\right)^n$		z_0, n, R	Peck (1969) Schmidt (1969) Clough and Schmidt (1981)
$x_{infl} = 0.25(z_0 + R)$	Loose sand	z_0, R	Atkinson and Potts (1977)
$x_{infl} = 0.25(1.5z_0 + R)$	Dense sand and OC clay	z_0, R	
$x_{infl} = 0.28z_0 - 0.12$	Sands	z_0	O'Reilly and New (1982)
$x_{infl} = 0.43z_0 + 1.1$	Stiff clay	z_0	
$x_{infl} = 0.5z_0$		z_0	Mair (1993)

(b) *Subsurface*

$x_{infl}(z) = 0.175z_0 + 0.325(z_0 - z)$	K, z_0,z	Mair (1993)
$x_{infl}(z) = R \cdot \left(\frac{z}{2R}\right)^{0.8} \cdot \left(\frac{z_0 - z}{z_0}\right)^n$	R,z, z_0, n	Moh, Z. C. *et al*. (1996)

Figure 7-10. Inflection point

7.2.3. Numerical Simulation – Two dimensional - Code Verification

Dissolution pipes are inherently long. Therefore, numerical simulations can be reduced to two dimensional 2D configurations.

Soft zone formation simulation. The stress relaxation module developed in ABAQUS for this study is based on the internal stress reduction method. The numerical procedure is as follows:

1) The soft zone geometry is pre-defined
2) The initial internal stress inside the soft zone is equivalent to the value of geostatic k_0-stress
3) The internal stress is gradually reduced at the same rate everywhere on the soft zone walls

The main advantage of this approach is the ability to have complete knowledge of the state of stress within the soft zone until numerical instability takes place. The internal stress reduction (ISR) can be expressed

$$ISR_i = \frac{\sigma_{initial} - \sigma_i}{\sigma_{initial}}$$

where $\sigma_{initial}$ is the initially stress around the soft zone and σ_i is the internal stress at the *i* th step.

Code verification. The code is verified for plane-strain conditions. The closed-form Kirsch solution applies to a circular cavity of radius a and internal stress p_i in homogeneous isotropic, linear elastic medium subjected to far-field stresses. The stress distribution around the cavity is (Kirsch, 1898)

$$\sigma_r = p_i \frac{a^2}{r^2} + \frac{\sigma_{v\infty} + \sigma_{h\infty}}{2}\left(1 - \frac{a^2}{r^2}\right) + \frac{\sigma_{v\infty} - \sigma_{h\infty}}{2}\left(1 + \frac{3a^4}{r^4} - \frac{4a^2}{r^2}\right)cos\,2\theta$$

$$\sigma_\theta = -p_i \frac{a^2}{r^2} + \frac{\sigma_{v\infty} + \sigma_{h\infty}}{2}\left(1 + \frac{a^2}{r^2}\right) - \frac{\sigma_{v\infty} - \sigma_{h\infty}}{2}\left(1 + \frac{3a^4}{r^4}\right)cos\,2\theta$$

where the radial σ_r and circumferential σ_θ stresses at distance r and at an angle θ are a function of far-field stresses $\sigma_{v\infty}$ and $\sigma_{h\infty}$.

An initial pressure $p_{int} = 5\sigma_{v\infty}$ is applied first and the internal pressure is gradually reduced. A perfect match between the analytical and numerical predictions requires proper mesh refinement near the cavity and implies higher computational costs (see also Potts, 2003; Rajendran, 2010_ENREF_39). Figure 7-11 shows the high agreement attained between the closed-form and numerical simulation for the stress relaxation module when a high resolution mesh is used around the cavity.

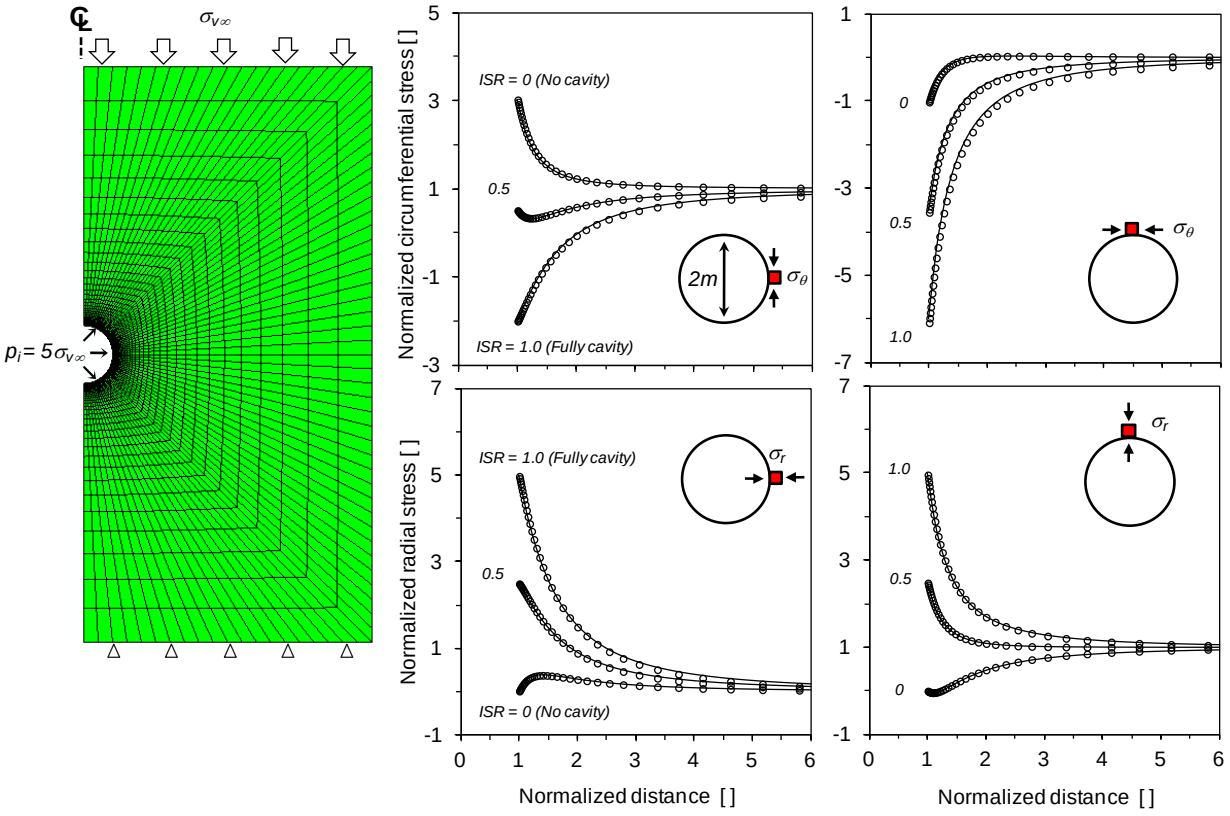

Figure 7-11. Stress relaxation module - Code verification (Solid lines indicate the close-form solution; points are numerically computed values)

7.2.4. Parametric study – Methodology and General Trends

Constitutive model and material parameters. Cavities are of rectangular cross section. The homogeneous soil mass is modeled as a Modified Cam Clay material to capture the pressure-dependent soil strength and volume change upon shear (Roscoe and Burland, 1968_ENREF_42). Material properties are summarized in Figure 7-12. The initial void ratio is calculated from constitutive parameters, the preconsolidation pressure p_c' and the current geostatic pressure p'.

Unit weight γ [kN/m^3]	17
Isotropic compression index λ	0.1
Isotropic recompression index κ	0.01
Critical state friction angle (in AC)	Variable
Drained Poisson's ratio υ	0.3
Void ratio at 1kPa e_{1kPa}	1.28
Void ratio e_0	Variable
Earth pressure k_0	Variable

Figure 7-12. Material properties – Modified cam clay ($\kappa = 0.1 \cdot \lambda$; AC implies axial compression)

This comprehensive parametric study explores the effect of soft zone depth z_0, number of nearby soft zones, critical state friction angle ϕ_{cs}, preconsolidation, and internal stress reduction ISR within the soft zone (variables are summarized in Figure 7-13). Different levels of internal stress reduction ISR capture different degrees of dissolution. The internal stress reduction ISR is

limited by numerical instabilities and mesh distortion (the determinant of the Jacobian matrix approaches zero and the stiffness integral cannot be solved). In the absence of any cohesive strength, most simulations presented herein reach numerical instability between ISR~0.8 and 0.95 (Note: there is cohesion in situ, otherwise, there would be no open cavities larger than $3 \cdot D_{50}$ to $5 \cdot D_{50}$ where D_{50} is the median grain size). Preloading effects are simulated by changing the k_0 ratio for a given critical friction angle M. Then, the initial overconsolidation ratio OCR is (Borja and Lee, 1990)

$$OCR = \frac{p_y'}{p_0'} = \frac{p_y'}{p' + \frac{q^2}{M^2 p'}}$$

where p_y' is the size of the yield surface and p_0' is the equivalent preconsolidation pressure corresponding to the current stress state p'. Cavities are assumed of rectangular shape in agreement with layered stratigraphies observed at SRS, and to facilitate the soft zone simulation. A study of soft zone geometry showed that geometry affects stress conditions at the soft zone springline more than near the crown (Greenspan, 1944_ENREF_22), and that deviations from circularity exacerbate stress concentrations that lead to numerical instabilities at lower internal stress reduction ISR values.

z_0/h	5	10	25	50
# Soft zones	1	3	5	
ϕ_{cs} [^{0}]	30	35	40	
OCR	1.3		4.0	
ISR	0 – 0.7			

< *Soft zone dimensions* >

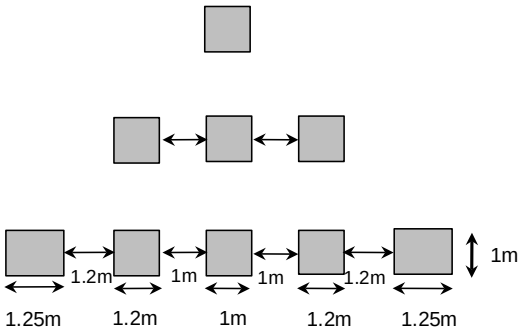

Note:

1. ISR is Internal stress reduction
2. ϕ_{cs} implies the constant volume friction angle
3. The symmetry condition is considered

Figure 7-13. Parametric study

Plane strain cases are simulated using eight-node biquadratic reduced integration elements (geometry and boundary conditions are shown in Figure 7-14). The domain size, boundary conditions and mesh refinement affect the computed surface settlement profile and computational demand (Burd et al., 1994; Pang et al., 2005; Potts, 2003). The absence of lateral boundary effects on the worst case tested in this section is demonstrated in Figure 7-15: the far-field surface settlement is close to zero and horizontal stresses are identical before and after the stress relaxation.

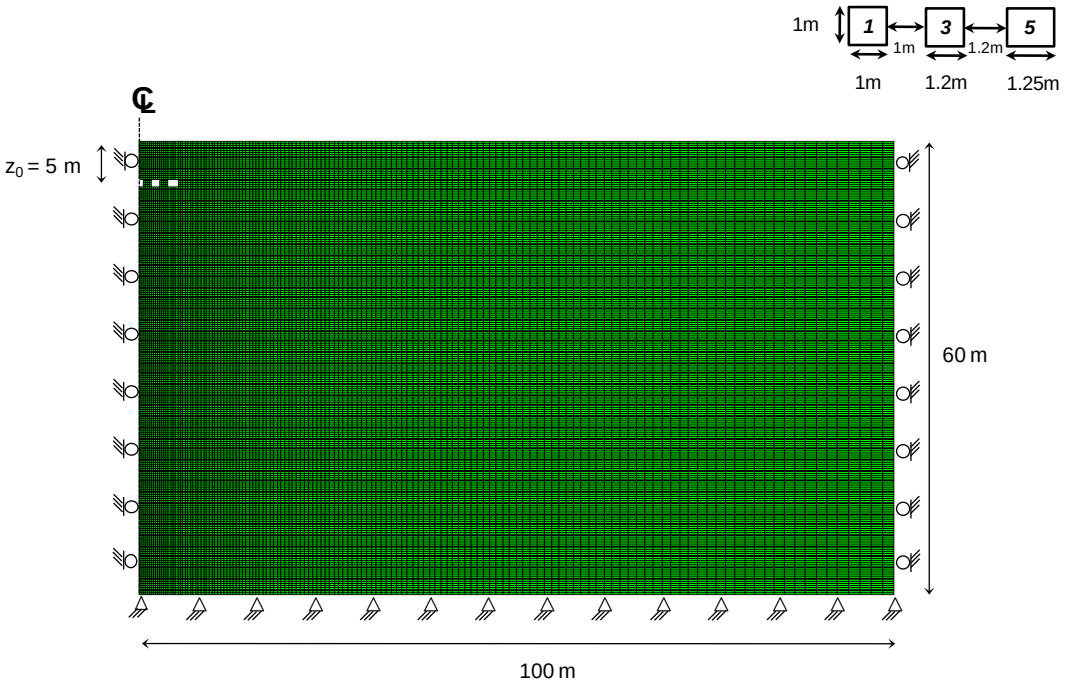

Figure 7-14. Geometry - Boundary conditions

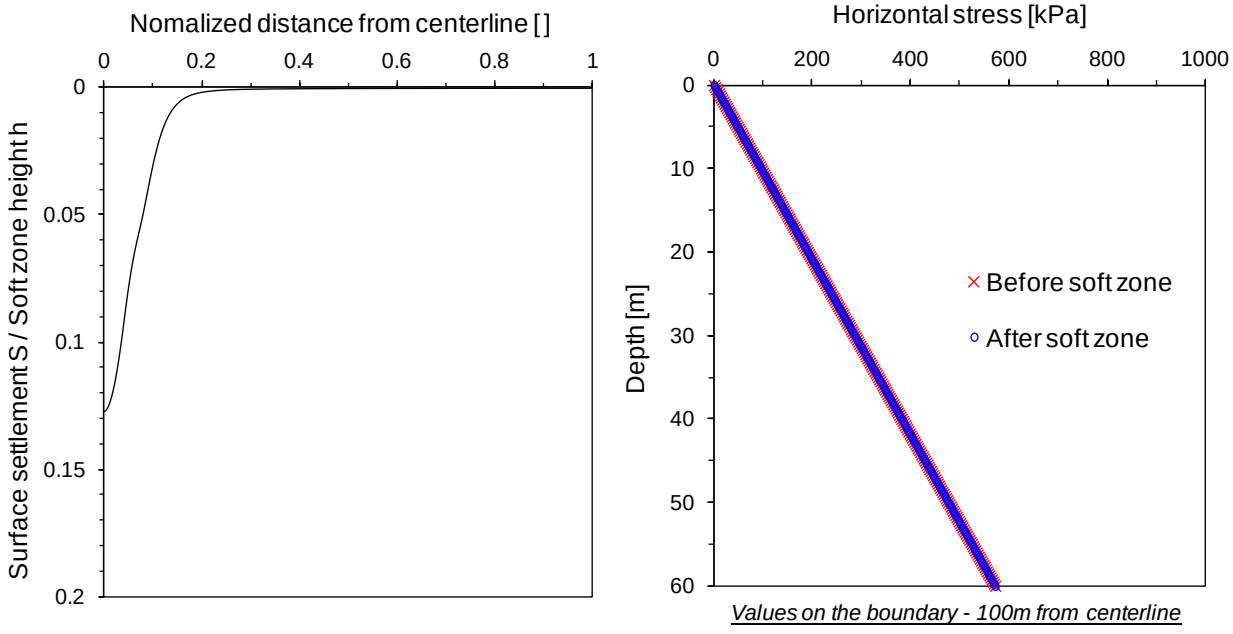

Figure 7-15. Boundary effect (Case: $z_0/h = 5$; $\phi cs = 30^o$; Five soft zones)

Governing dimensionless ratio. The normalization of results into dimensionless ratios facilitates the comparison of parametric studies and the identification of salient trends. Given the non-linear nature of the material behavior, we conducted all simulations in a dimensional regime, however, we explore prevailing trends in terms of normalized results using key dimensionless parameters.

Post-Processing. Given the regularity and smoothness of numerically computed displacement fields, each settlement profile at depth-z is fitted with a Gaussian function; the inferred distance to the inflection point x_{inf} and the maximum settlement S_{max}. The post-processing module developed in Matlab computes the error e_i between the predicted and numerically computed settlement at node i

$$e_i = S_i^{<Num>} - S_i^{<Anal>}$$

and identifies the set $(x_{inf}, S_{max})_z$ that minimizes the square error norm

$$L_2 = \sqrt{\underline{e}^T \cdot \underline{e}}$$

General trends. As the soft zone depth increases in high friction and/or OC sediments, the displacement field evolves towards narrow troughs that may even become carrot-shaped (Figure 7-16 and Figure 7-17). Deeper cavities and higher preconsolidation ratios result in lower surface and subsurface settlements. Furthermore, Figure 7-18 shows fitted surface settlement profiles (z=0) for two distinct cases, and slices of the error surface presenting the invertibility of the inflection point. The Gausian model fits the surface settlement better for small stress reductions of the soft zone inside (lower residual). However, the higher stress reduction increases the resolvability of the inflection (narrower error surface).

Summary trends for all fitted surface profiles show that the maximum surface settlement increases with higher internal stress reduction, shallower cavities, lower friction angle (higher frictional strength hinders the propagation of plastic deformations towards the ground surface), and in lightly overconsolidated rather than highly overconsolidated sediments (Figure 7-19). The maximum subsurface settlement S/z_0 is only slightly larger near the soft zone than at the ground surface in all cases regardless of soft zone location, soil friction angle, and degree of preconsolidation (Figure 7-20).

The inflection point is a function of the soft zone depth (Figure 7-21): shallower cavities favor vertical displacement vectors and narrower settlement troughs, i.e., lower values of the inflection point. Inflection point trends with depth collapse into a quasi-single trend when the sediment is overconsolidated.

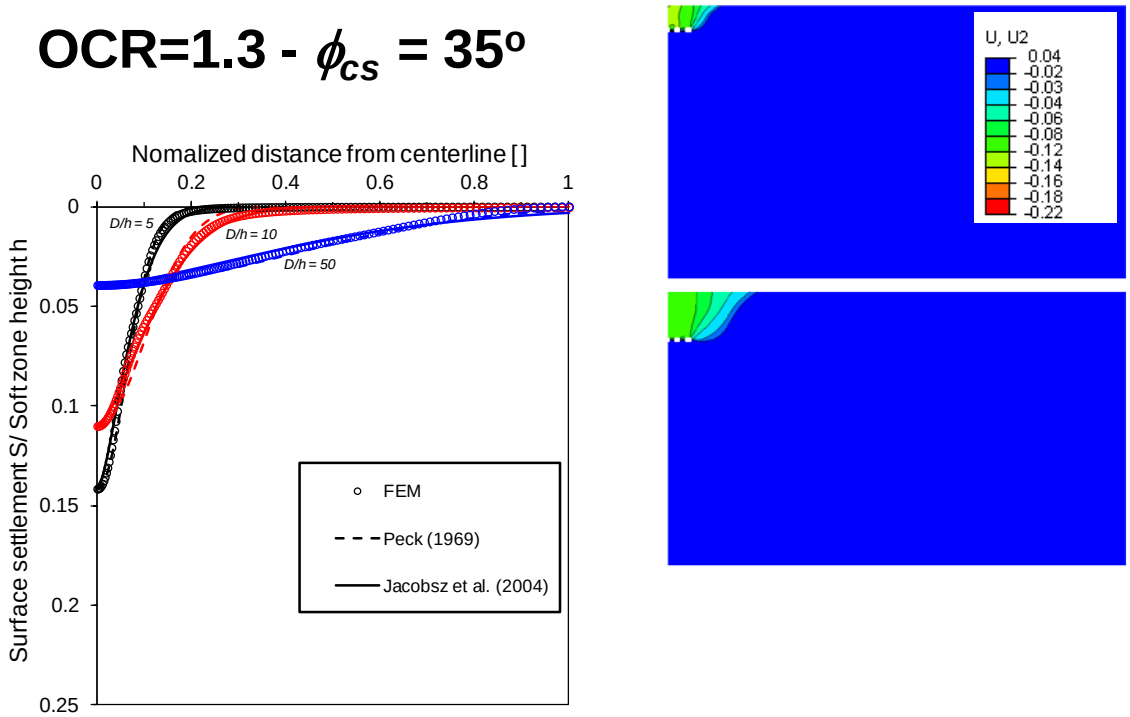

Figure 7-16. Normalized settlements and displacement fields – Quasi NC sediment

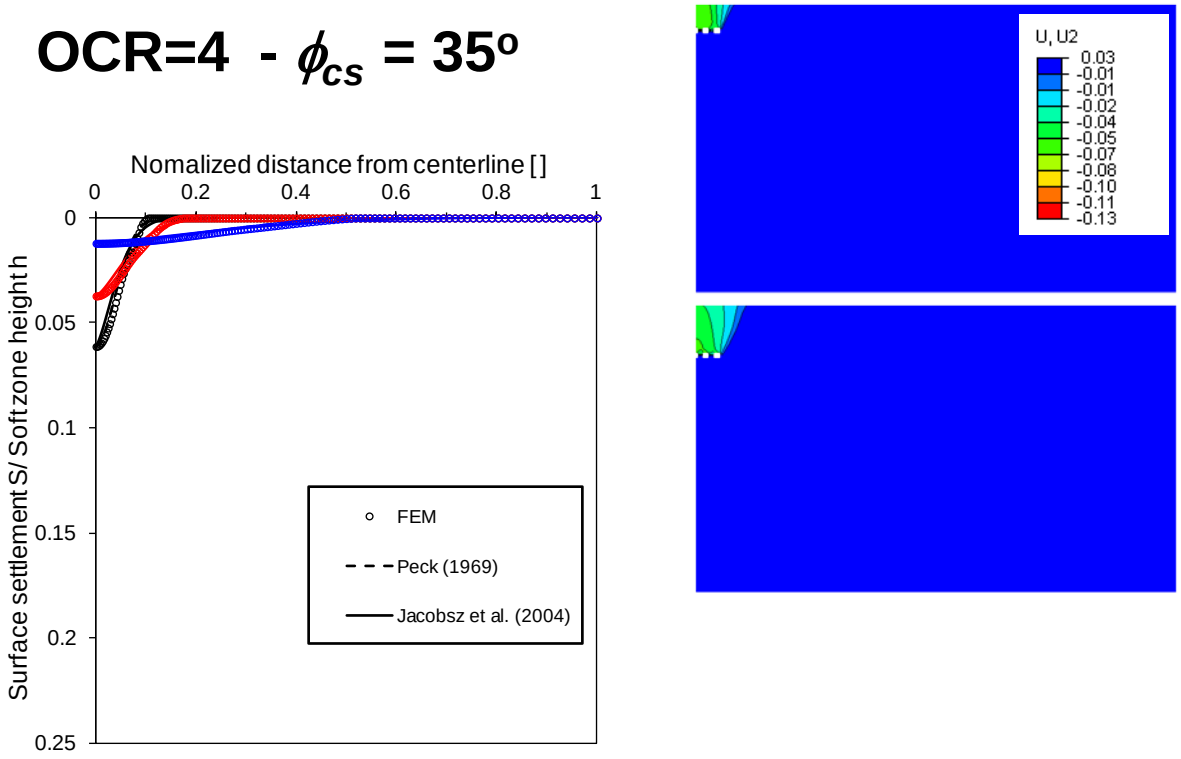

Figure 7-17. Normalized settlements and displacement fields – OC sediment

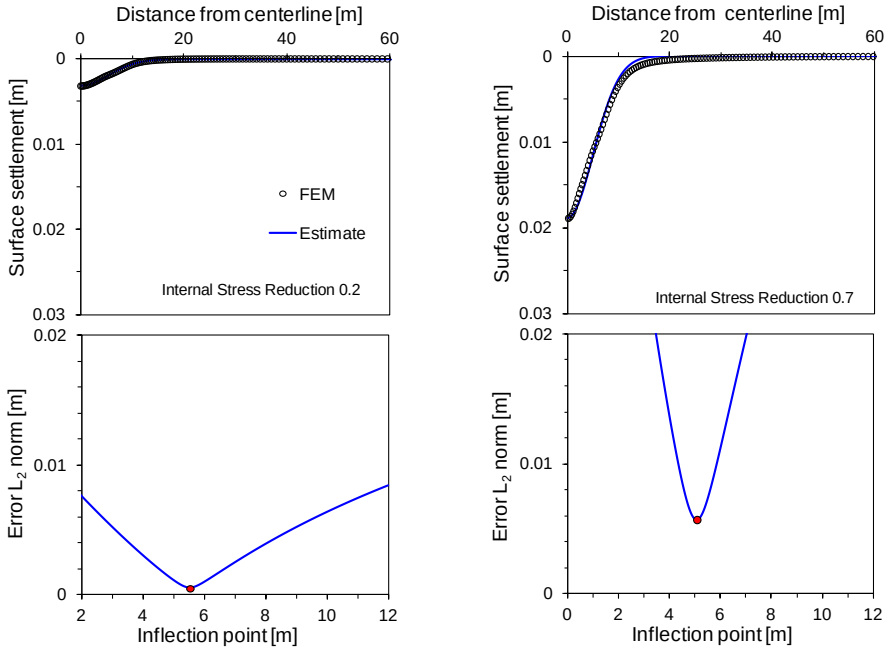

Figure 7-18. Surface settlements - Gaussian function

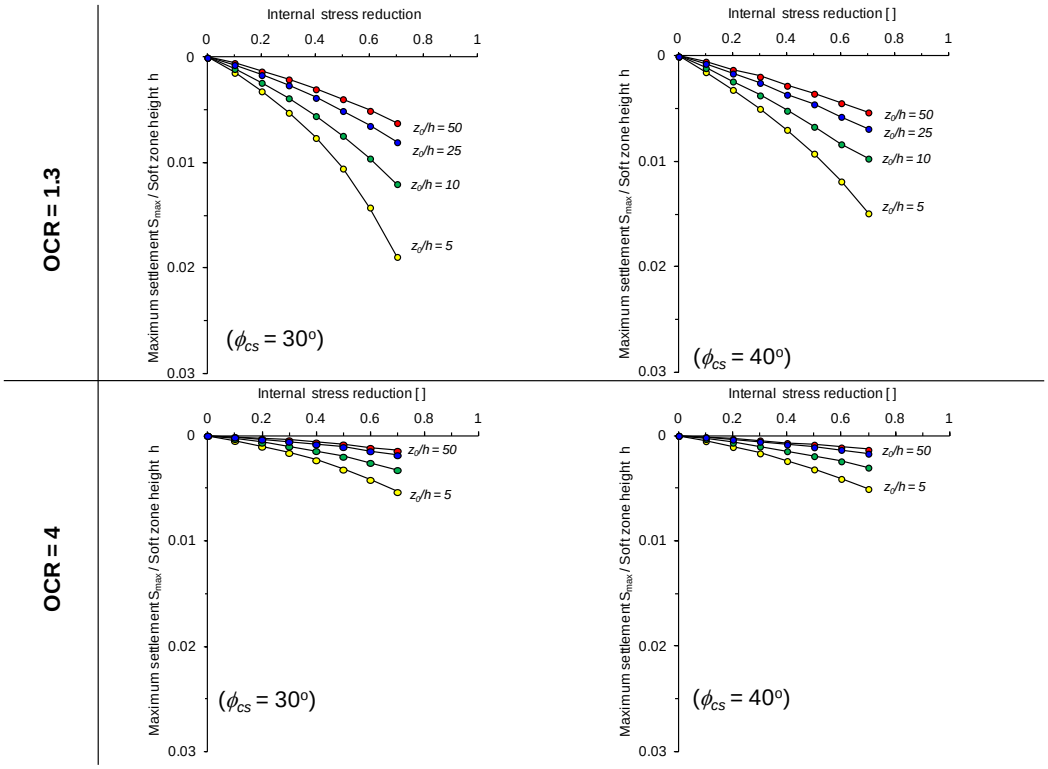

Figure 7-19. Maximum Surface settlement S_{max} (One soft zone)

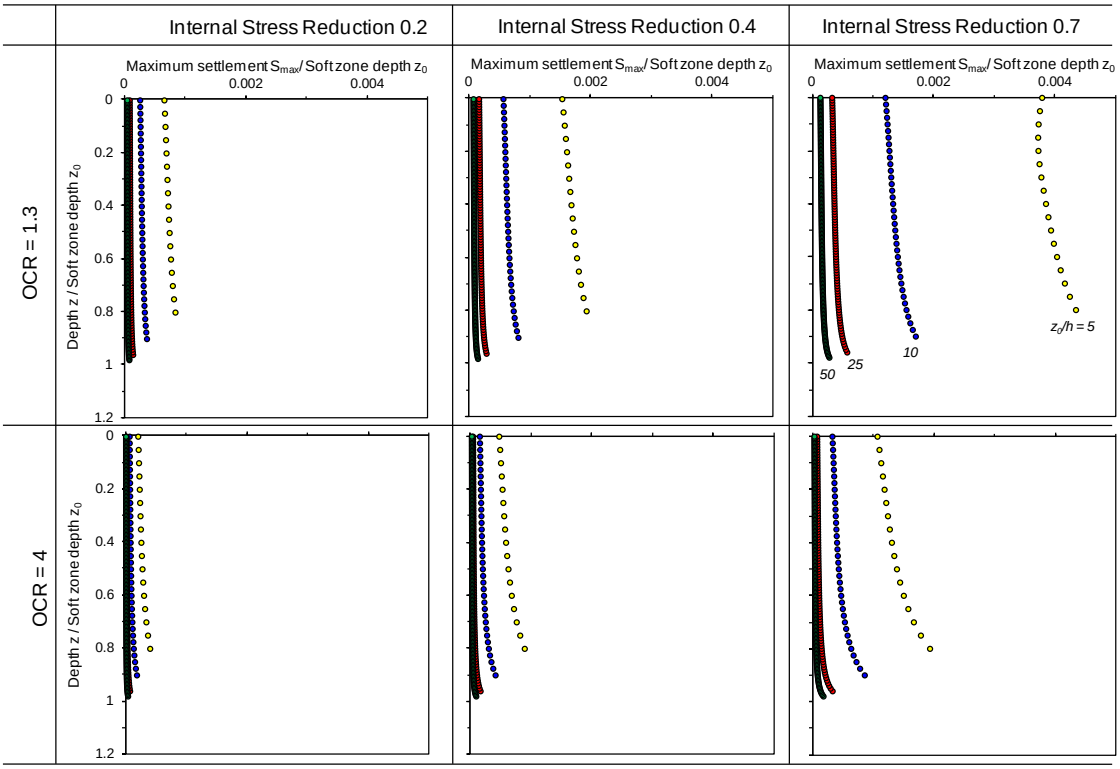

Figure 7-20. Subsurface settlement profiles (One soft zone; $\phi = 30^0$)

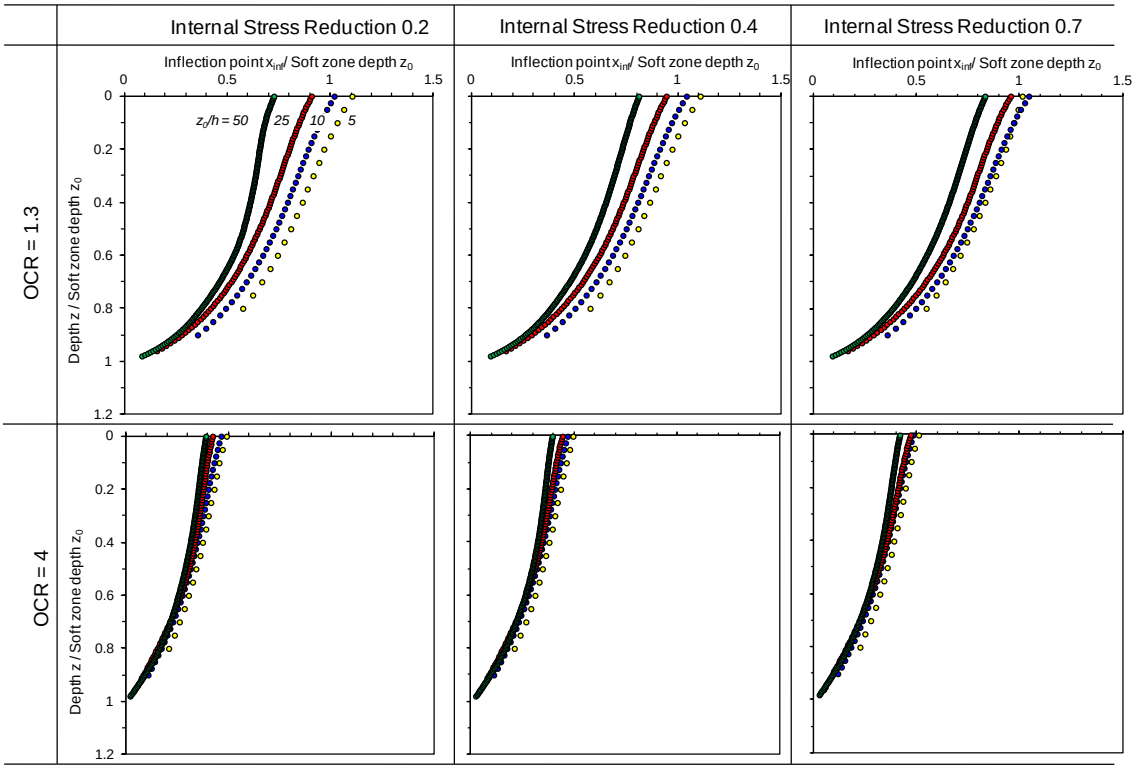

Figure 7-21. Subsurface inflection point (One soft zone; $\phi = 30^0$)

7.2.5. Analyses and Discussions

Surface settlement area compared to soft zone size. Figure 7-22 shows the area of the surface settlement profile normalized by the area that the *soft zone contracted* as a function of soft zone depth, overconsolidation and friction angle. The ground volume loss is calculated by numerical integration of the surface settlement. The area ratio decreases for deeper cavities, higher friction angle, and higher preconsolidation. We highlight that surface settlements correspond to an internal stress reduction ISR=70%, and that the soft zone has not fully vanished.

Applicability of Superposition Principle. The validity of the superposition principle is explored by comparing the sum of surface settlement areas caused by each single soft zone acting separately to that caused by all cavities concurrently formed in the sediment. Results in Figure 7-22 show that linear superposition over predicts surface settlements by a large amount in both low and high OCR sediments compared to the situation when all cavities form simultaneously in the non-linear system.

Inflection Point Trends - Underlying Mechanism. The position of the inflection point with depth migrates towards the centerline during soft zone formation (Figure 7-21 and Figure 7-23). Internal stress reduction prompts early elastic deformation, followed by yielding, stress redistribution and arching; eventually, the plastic zone propagates upward toward the surface. Consequently, inflection point trends are narrower and closer to the centerline at higher ISR.

Comparisons of Inflection Point. The numerically computed trend for inflection points with depth are compared against the empirical equation proposed by Mair et al (1993). Results presented in Figure 7-23 show that the empirical equation applies to overconsolidated sediments, and underestimates the width of the surface and subsurface settlement trough in low OCR sediments. Once again, we highlight the importance of the sediment stress history on displacement fields caused by subsurface soft zone formation.

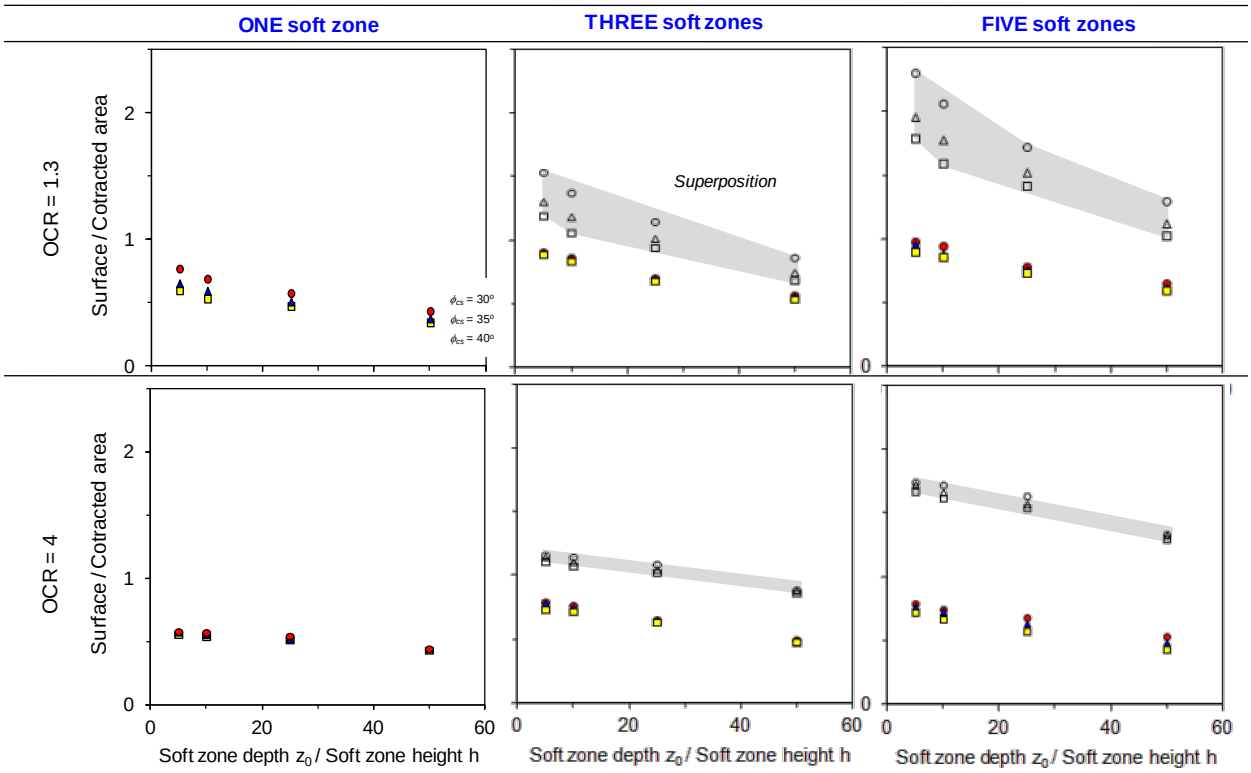

Figure 7-22. Applicability of superposition principle

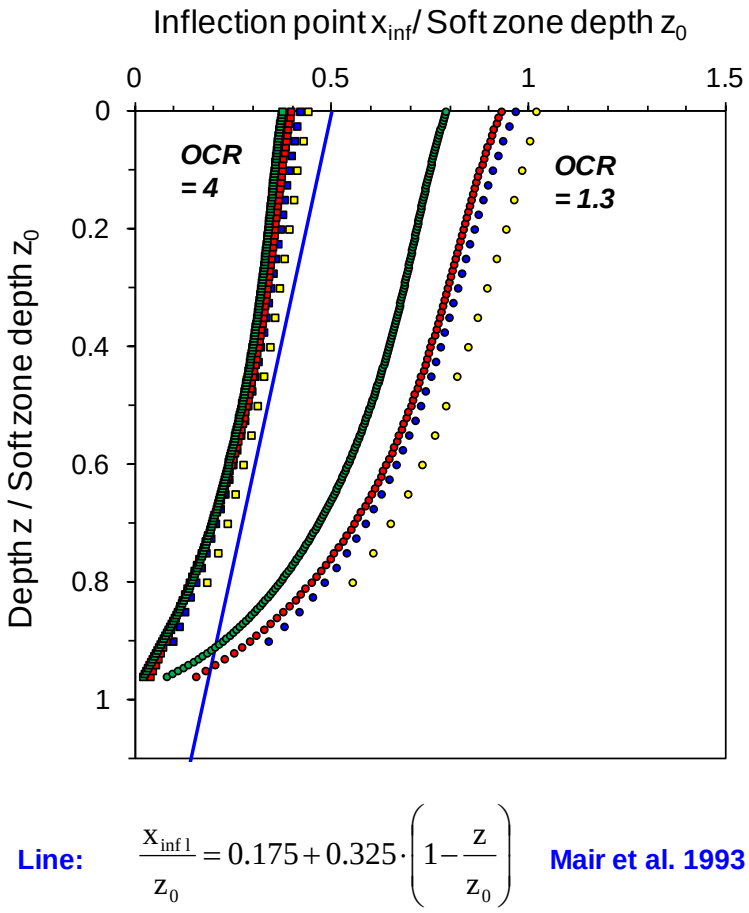

Figure 7-23. Position of inflection point vs. depth (ISR = 0.7; $\phi = 30^0$)

7.2.6. Conclusions

Subsurface volume loss takes place in many geotechnical situations, and it is inherently accompanied by stress relaxation and displacements that may reach the surface.

- Subsurface volume loss and soft zone formation can be numerically simulated by gradually reducing the anisotropic insitu state of stress in the predefined soft zone.
- Smaller and deeper cavities, higher friction angles and higher preconsolidation ratio lead to smaller settlements at all depths.
- Surface and subsurface settlements are quite regular and can be adequately fitted with a two parameter Gaussian function in the absence of pronounced distortions (e.g., shear

localizations).

- The maximum settlement decreases towards the surface (but only slightly). The position of inflections points widens towards the surface, inflection point trends with depth are narrower for higher OCR sediments (in fact, carrot-shaped displacement fields can develop for deep cavities in highly dilative media), and inflection points move towards the centerline during soft zone formation.
- Linear superposition of surface settlements caused by neighboring cavities overestimates deformations in low and high OCR sediments
- Published guidelines for the position of the inflection point fail to recognize the profound effect of overconsolidation.

Note that the medium has been assumed to have no cohesion in all cases analyzed. The addition of cohesion could dramatically diminish the impact of soft zones / soft zone formation on displacement fields.

7.3. Effect Of Localized Dissolution On Shallow Foundations

7.3.1. Introduction

Shallow foundations are typically designed to satisfy bearing capacity and settlement criteria compatible with structural tolerance_ENREF_19. Relatively simple computational schemes are available for simple subsurface conditions, such as elastic solutions for settlement and plasticity solutions for bearing capacity. The N_γ coefficient in bearing capacity equations significantly depends upon geometric assumptions made in kinematically admissible solutions and other effects such as the role of the sediment self-weight effect on shear strength and wedge geometry (e.g., Prandtl log spiral; Terzaghi, 1943_ENREF_49; Meyerhof, 1963; Vesic, 1973; Chen, 1975). Numerical simulations underscore the variation in bearing capacity coefficient N_γ (Griffiths, 1982; Frydman and Burd, 1997; Hjiaj et al., 2005; Loukidis and Salgado, 2009).

The situation is aggravated when shallow foundations rest on sediments that have experienced mineral dissolution before the footing load, or that may experience subsurface dissolution during the life of the structure. Previous studies used analytical, numerical and experimental methods to evaluate the bearing capacity of a strip footing above a soft zone (Baus and Wang, 1983; Badie and Wang, 1984; Wang and Badie, 1985; Wang and Hsieh, 1987; Azam et al., 1991; Hsieh, 1991; Crapps, 2010). These studies showed that cavities deeper than a critical depth have a negligible effect on bearing capacity, and that the effect of cavities shallower than the critical depth depends on the relative size and depth of the foundation and the soft zone. However, general guidelines are still limited and incomplete.

A numerical study conducted to explore the effect of subsurface volume contraction on shallow foundations is reported herein using material characteristics that are relevant to the

Savannah River Site. The parametric study considers footing size B, soft zone location D, dilation angle ψ, and load-dissolution history (stress relaxation-before-footing and footing-before-stress relaxation).

7.3.2. Preliminary Simulations: Mesh Design and Code Verification

Mesh Refinement. The numerically computed bearing capacity factor N_γ is significantly affected by mesh size (Griffiths, 1982; Manoharan and Dasgupta, 1995; Woodward and Griffiths, 1998; Day and Potts, 2000). In a preliminary study, we compared numerically computed bearing capacity factors with analytical expressions widely used in design. A parametric study was conducted to address the trade-off between mesh size, computational accuracy and cost. In particular, high mesh refinement was imposed near footings and cavities.

Footing Model. Different footing widths are simulated by varying the number of nodes subjected to controlled displacement. Smooth and rough, flexible and rigid footings are numerically modeled for this study (details in Figure 7-24). The rough and rigid footing, is simulated by deformation-controlled vertical node displacement, and facilitates the determination of the bearing capacity. The resistance mobilized at a given vertical displacement is the integral of average vertical component of stress acting on the first row of Gaussian integration points below the displaced nodes. The mesh geometry is selected so that predicted bearing capacity values are mesh independent (Woodward and Griffiths, 1998).

Numerical Environment. The commercial finite element software ABAQUS is used for these 2D plane-strain simulations. The medium is represented using eight-node biquadratic reduced integration elements (CPE8R). Lateral boundaries are located far from the footing edge so that there are no boundary effects on deformations and bearing resistance; vertical displacement is allowed on side boundaries, the bottom boundary is pinned, and the top surface is free (Figure 7-25). The simulated space is 40m high and 80m wide. The soil is homogeneous and it is modeled using an elastic perfectly plastic constitutive model with a Drucker-Prager failure criterion (Drucker and Prager, 1952; material properties are summarized in Figure 7-24).

Boundary Effects. Results in Figure 7-26 show that the far-field surface settlement is almost zero, and the horizontal stresses on the vertical lateral boundaries subjected to zero lateral strain conditions are identical before and after stress relaxation, and footing loading. Therefore, the modeled domain avoids boundary effects

Preliminary Results - Verification. The variation of the numerically computed $N\gamma$ value with friction angle is plotted together with analytically predicted $N\gamma$ values using classical bearing capacity equations in Figure 7-27. The Prandtl solution overestimates $N\gamma$, while the modified Terzaghi's solution leads to conservative estimates where a reduced friction angle $\tan\phi^* = 2/3 \tan\phi$ is used in computations (Note: values for the modified Terzaghi's solution are obtained with a reduced friction angle ϕ^* so that $\tan\phi^* = 2/3 \tan\phi$ - refer to Das, 1999). The value of $N\gamma$ depends on dilation (see also Frydman and Burd, 1997), and the effect of dilation is most pronounced for sediments with higher constant volume friction angles. The Hansen (1970)

solution overestimated values but it is close to the computed Nγ obtained for dilation equal to friction ψ=ϕ i.e., associated flow rule (see also Potts, 2003). Results in Figure 7-27 highlight the sensitivity of bearing capacity to friction angle and the spread between analytical predictions.

	Footing type	Conditions
Footing characteristics	Smooth (δ =0)	Nodes are free to move horizontally
	Rough ($\delta \geq \phi$)	Constrained horizontal displacement
	Flexible	Load-control (Uniform load)
	Rigid	Displacement-control (Uniform displacement)

Material Properties Drucker-Prager	Unit weight γ [kN/m^3]	17
	Young's modulus E [MPa]	300
	Cohesion c [kPa]	0
	Friction ϕ [º]	30
	Dilation Ψ [º]	0 and 30
	Drained Poisson's ratio υ	0.3

Figure 7-24. Simulations

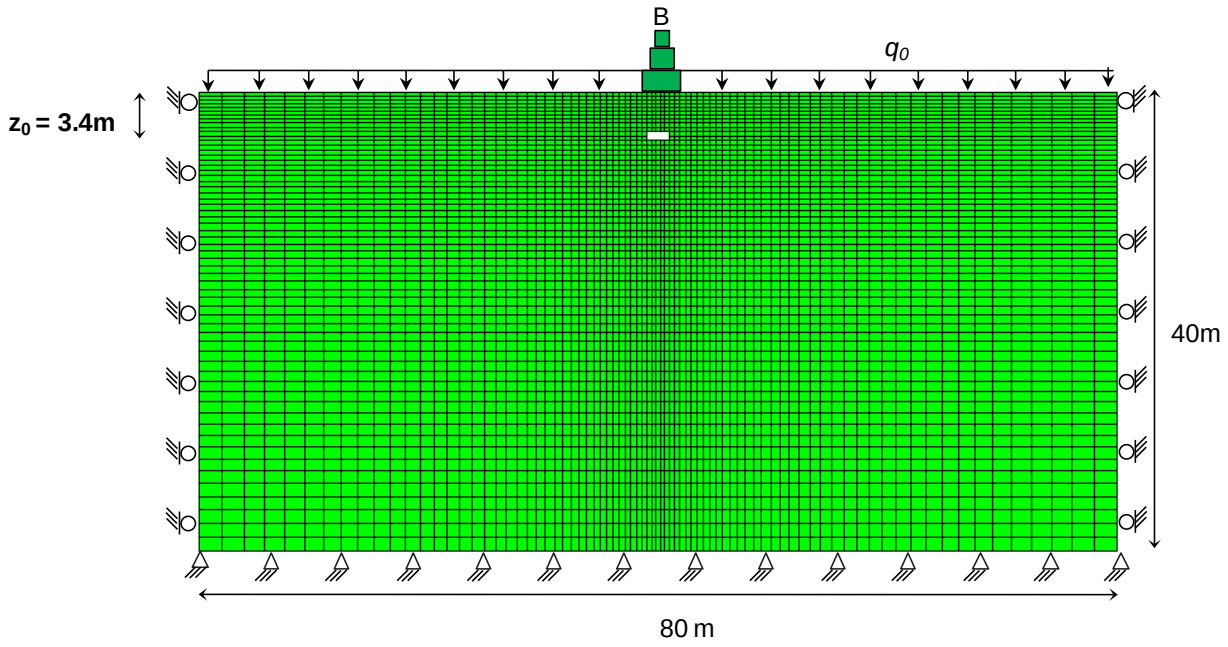

Figure 7-25. Mesh adopted for this analysis; element type - CPE8R (8-node biquadratic plane strain quadrilateral, reduced integration)

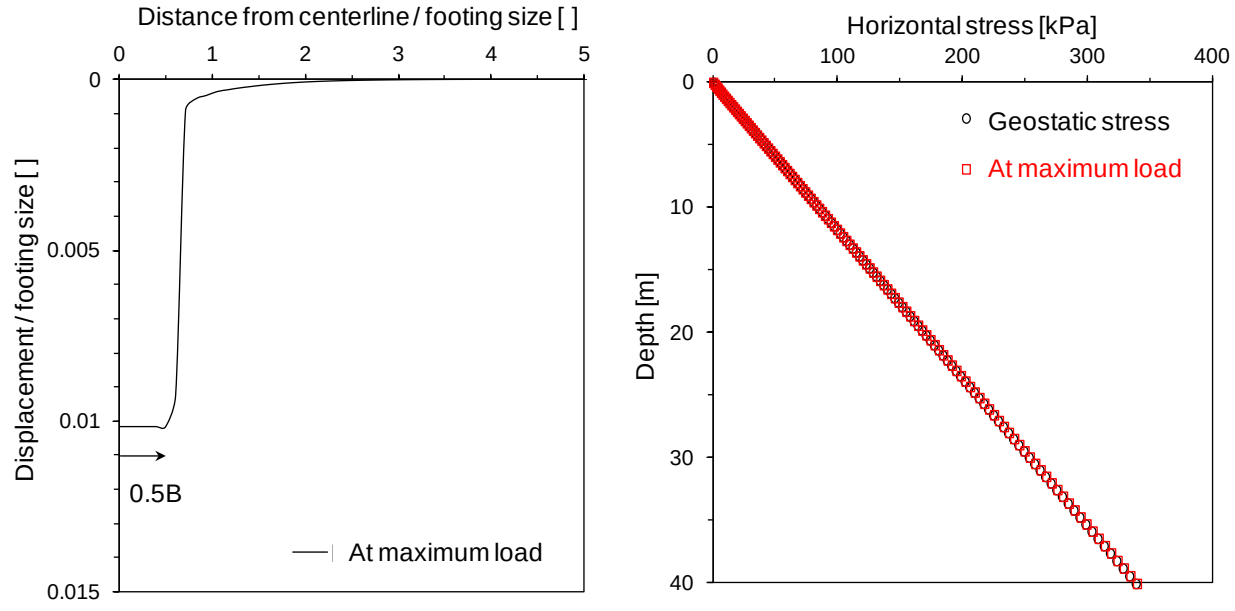

Figure 7-26. Boundary effect; Case: B = 2.0m; z_0 = 3.4m; ϕ_{cs} = 30°; ψ = 0; ISR = 0.5

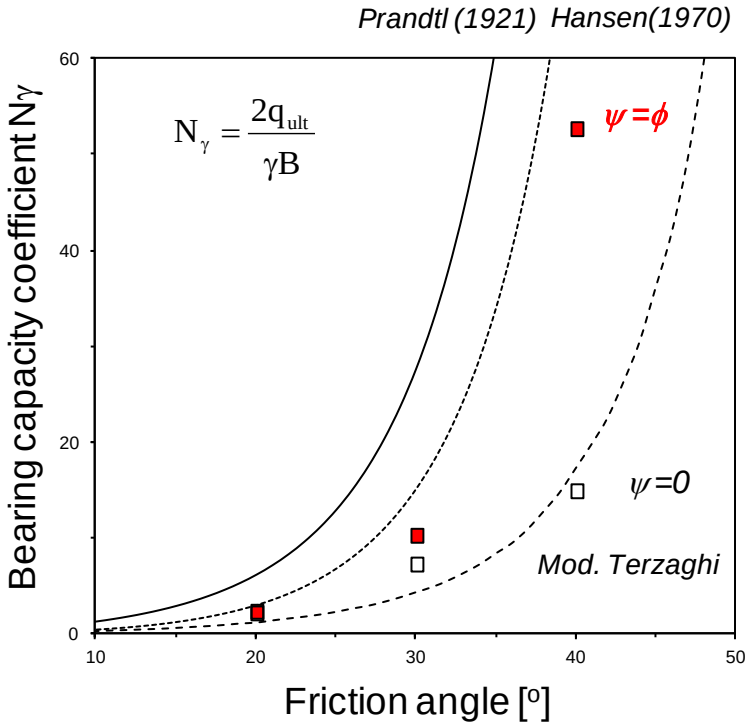

Figure 7-27. Bearing capacity coefficient Nγ (γ ≠ 0, c = 0, and q0 = 0)

7.3.3. Parametric Study – Results

Scope. The parametric study explores the effect of footing size B, soft zone depth z_0, dilation angle ψ, internal stress reduction ISR, and the soft zone formation vs. loading history, i.e., stress relaxation-before-footing and footing-before-stress relaxation on the foundation bearing capacity. A surcharge load q_0 = 17 kPa is applied on the surface to simulate a nominal burial depth, and the selected soft zone is ~1.0m high and 2.0m wide in all cases. Different levels of internal stress reduction ISR capture different degrees of dissolution. The scope of the parametric study is summarized in Figure 7-28.

Footing size B [m]	Zone depth z_0 [m]	Dilation Ψ [°]	Possible Stress Relaxation Histories	
			Load After Stress Relaxation	Load Before Stress Relaxation
1.2	3.4 7.7 11.4	0 ϕ	1) Reduce internal stress 2) Displace over B 3) Determine bearing capacity 4) Repeat for ISR= 0,0.1,0.2,0.4,0.5	1) Load footing to a FS=3 2) Form soft zone by gradual ISR 3) Monitor footing settlement 4) Repeat for all cases
2.0	3.4 7.7 11.4	0 ϕ		
3.8	3.4 7.7 11.4	0 ϕ		

Figure 7-28. Parametric study (Surcharge: q_o=17 kPa; Soft zone: w ≈ 2m - h ≈ 1m)

The stress relaxation module based on the internal stress reduction ISR method is employed in these simulations. The internal stress reduction inside the soft zone is limited by numerical instability and mesh deformation (when the determinant of the Jacobian matrix approaches zero, the stiffness integral cannot be solved). In general, we exceed ISR~0.5 (the deformed configuration around the soft zone is shown in Figure 7-29).

Results. Load-displacement curves are shown in Figure 7-29 and Figure 7-30. The applied load is normalized by the bearing capacity in the absence of cavities. Shallow cavities interact with the footing, the ultimate bearing capacity is significantly decreased proportionally to the internal stress reduction in the soft zone, but dilation diminishes the effect of cavities beneath the footing (z_0/B=1.7 - Figure 7-29). The foundation response is almost insensitive to the presence of deep

cavities (z_0/B=5.7 - Figure 7-30). The load-displacement shows a more brittle response in dilative sediments (Note: elastic properties are kept the same for all simulations).

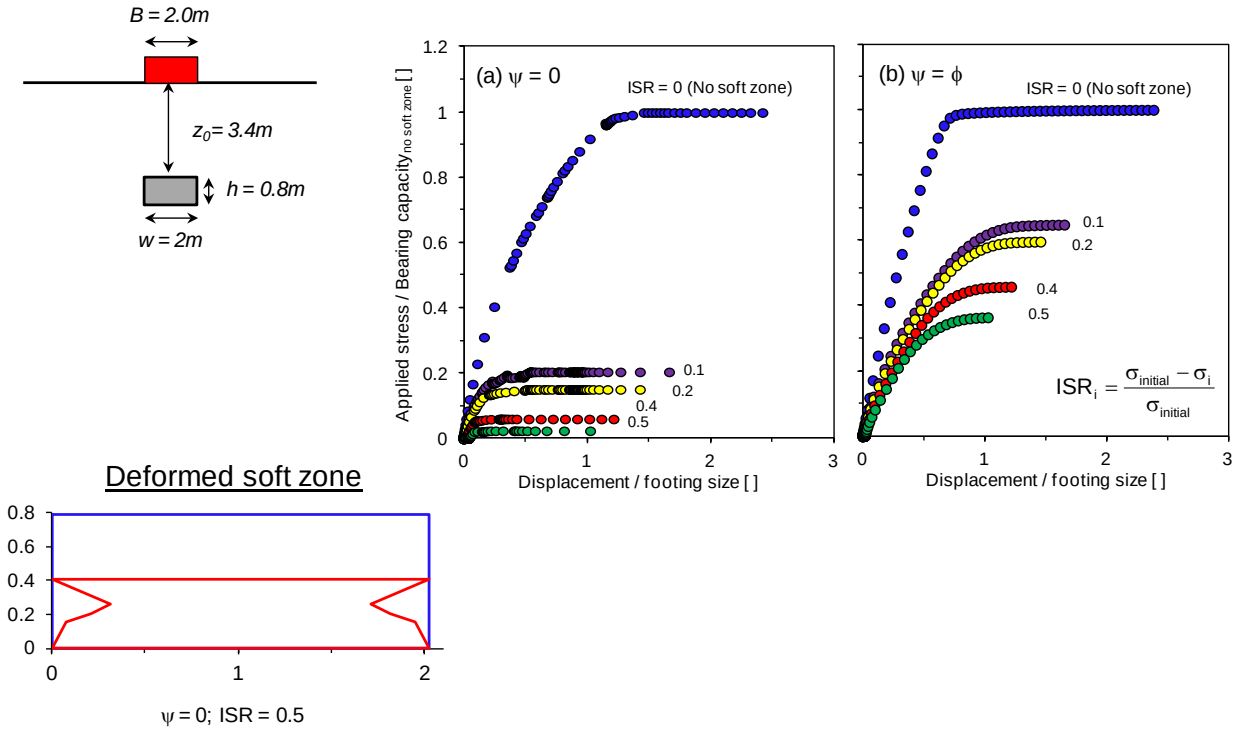

Figure 7-29. Load-displacement - Soft zone formation (z_0/B=1.7)

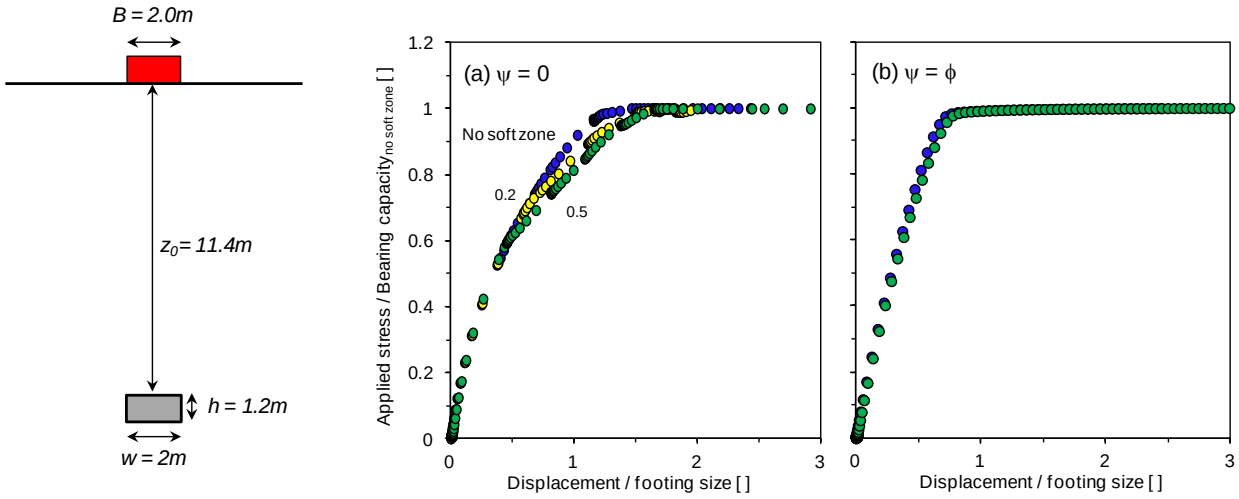

Figure 7-30. Load-displacement - Soft zone formation (z_0/B=5.7)

Computed bearing capacity values are summarized in Figure 7-31 in terms of the bearing capacity in the presence of the soft zone normalized by the footing bearing capacity in the absence of any soft zone. The loss in bearing capacity is worst when the footing size is equal to the soft zone width B=w and ψ=0 (NOTE: in the absence of cavities, the bearing capacity increases with footing width). Deeper cavities have diminishing effects on bearing capacity. For dilation equal to the friction angle ψ=ϕ (normality), the reduction in bearing capacity is gradual with ISR, and proportional to the footing size because dilatancy hinders the propagation of plastic deformations underneath the footing from the soft zone to the top. The transition from shallow to deep anomaly depends on z_0/B (about 3-to4), but this value is affected by anomaly size B/w, dilatancy ψ, and internal stress reduction ISR.

Consider next the settlement experienced by all footings subjected to an initial load equal to 1/3 the bearing capacity in the medium without soft zone (FS=3). After loading, the soft zone is gradually formed by internal stress reduction from the initial equilibrium condition in the sediment subjected to gravity and footing load (load-before-stress relaxation). The surface settlement that the footing experiences during the soft zone formation process is normalized by the surface settlement produced by the applied load. Results are summarized in Figure 7-32. Shallow cavities increase surface settlement, particularly when the footing width B is equal to the soft zone width w in a medium with dilatancy ψ=0. Dilation markedly reduces surface settlements. Numerically instability occurs as the settlement increases rapidly with the reduction of internal stress in the soft zone. Once again, the transition from deep to shallow behavior varies with anomaly size B/w, dilatancy ψ, and internal stress reduction ISR.

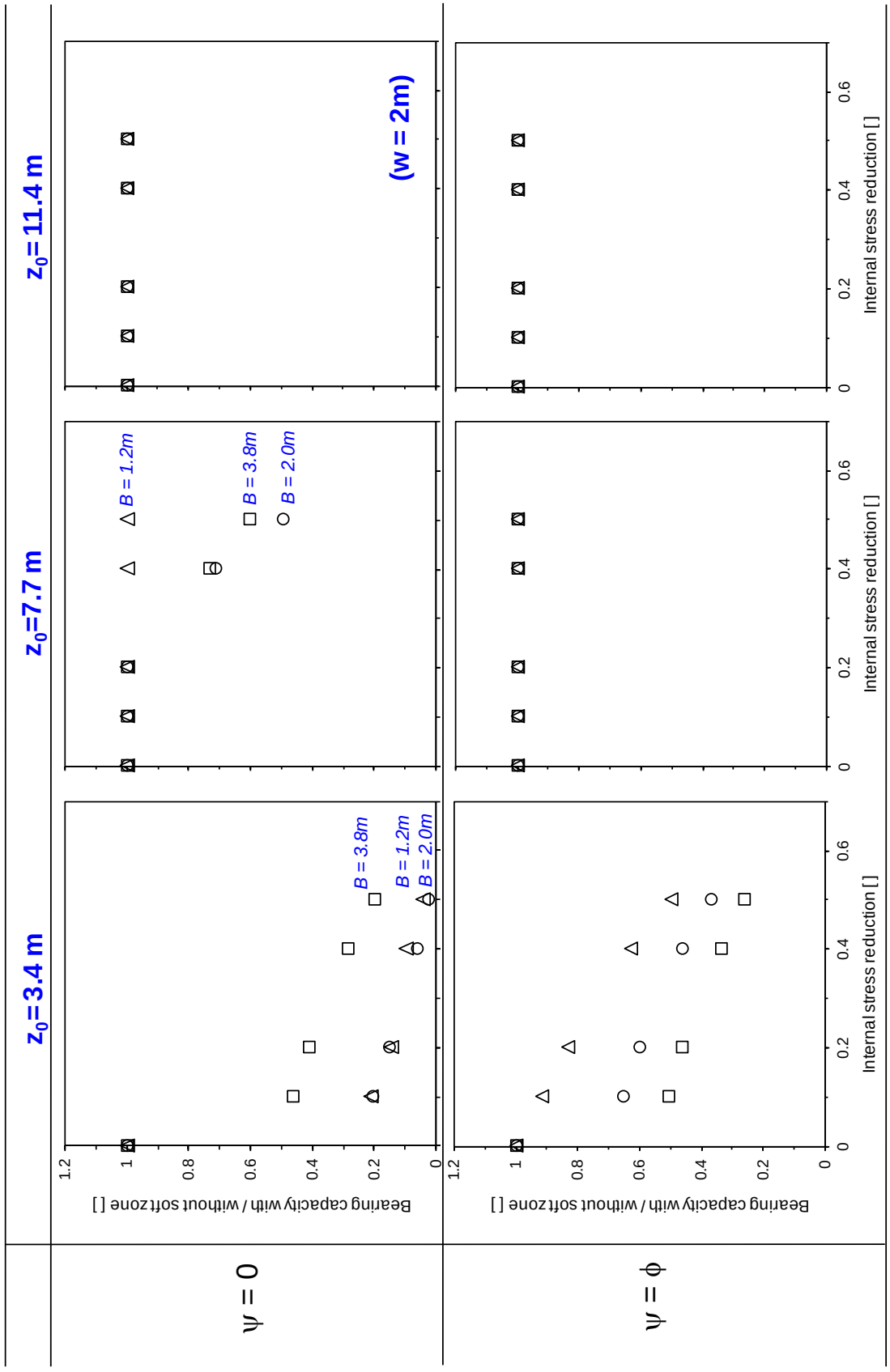

Figure 7-31. Load-after-stress relaxation: bearing capacity (w = 2m)

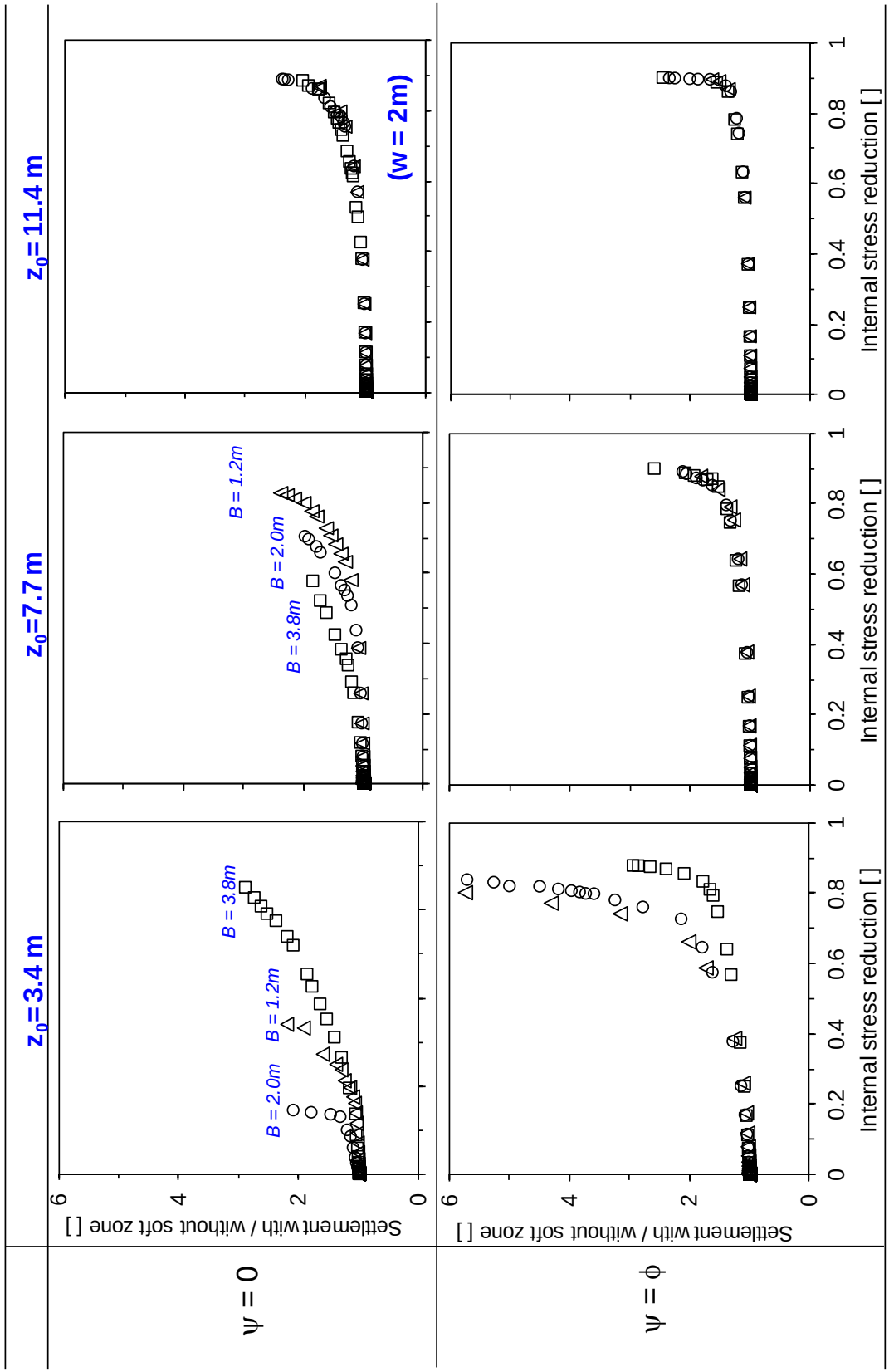

Figure 7-32. Stress relaxation-after-load: settlement @ FS=3 (w = 2m)

7.3.4. Discussion

Failure modes. Bearing capacity failure can involve general shear failure, local shear failure, and punching shear failure (Vesic, 1973). In particular, the punching shear failure mode involves primarily vertical displacements, and the soil outside the loaded region remains relatively immobile during the failure. Figure 7-33 and Figure 7-34 show displacement fields beneath footings near failure. The failure mode in the absence of cavities exhibits general shear failure characteristics. The presence of shallow cavities "attracts" the displacement field and the failure mode resembles the punching mode. The displacement field resembles a funnel when the depth-to-width z0/B is low; however, quasi vertical or even carrot shaped displacements can develop in deep cavities and dilatant soils.

Friction angle. Friction angle plays a controlling role on deformations, strength and failure mode for footings placed on sediments with subsurface cavities. Yet, there is large uncertainty on the selection of friction angle (Cho et al., 2006; Santamarina and Shin, 2009); for example: the friction angle in lateral compression can be $\phi_{LC} \approx 1.5\phi_{AC}$ (due to flow conditions during yield), dilatancy is stress dependent, and post-peak strain softening leads to progressive failure (see for example Rowe and Peaker, 1965).

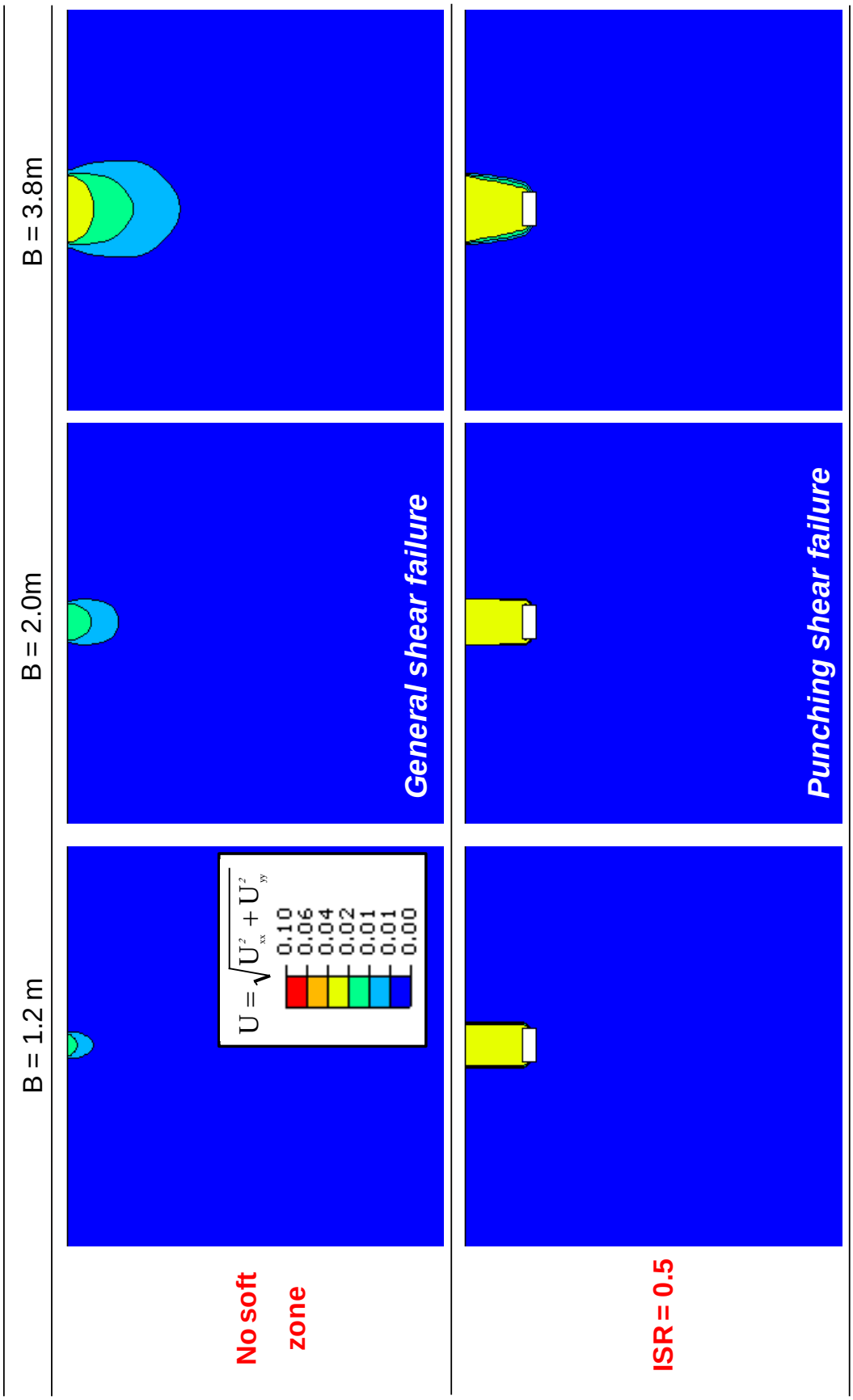

Figure 7-33. Displacement field ($\psi = 0$; $z_0 = 3.4$m; $w = 2.0$m)

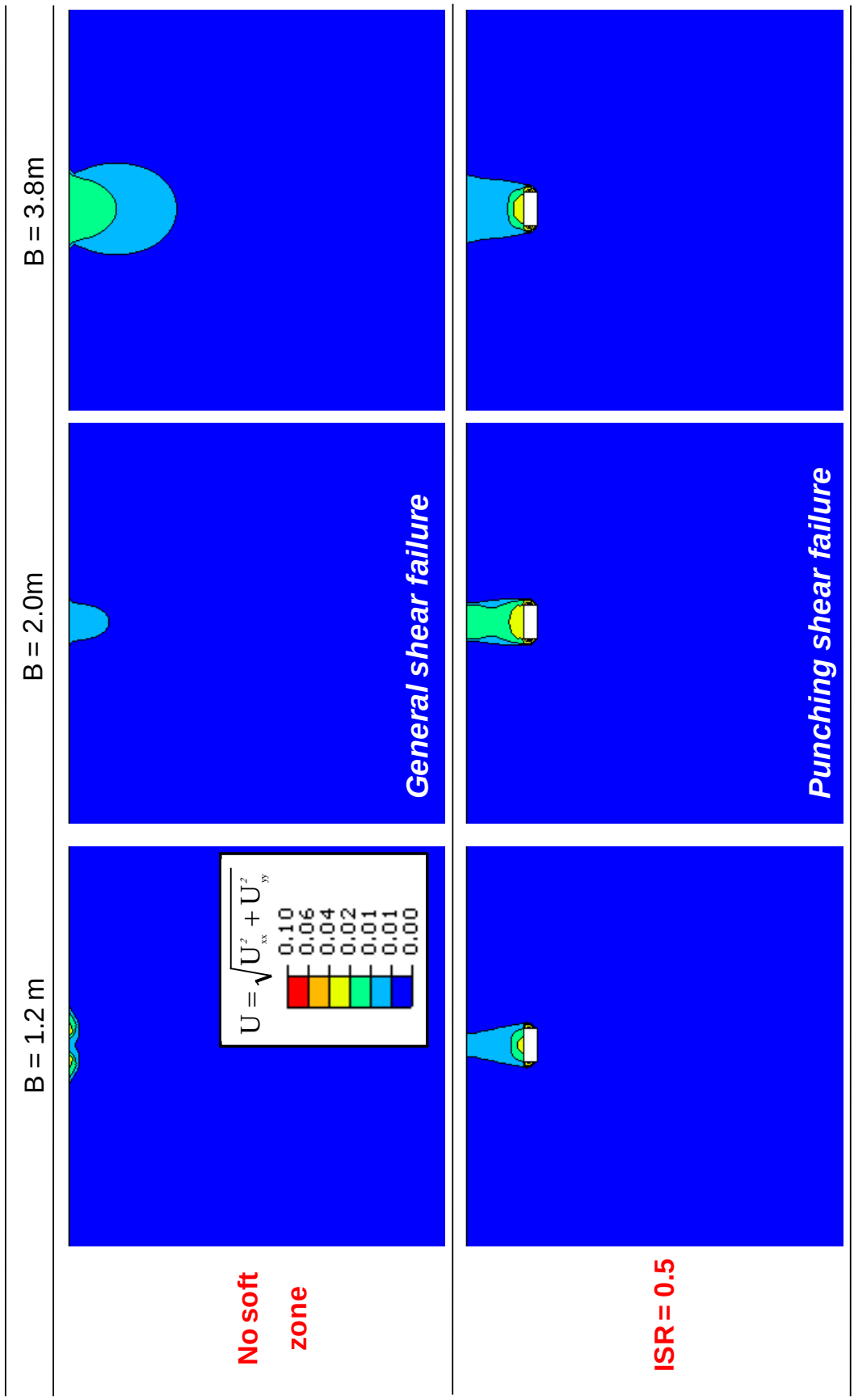

Figure 7-34. Displacement field ($\psi = \phi$; z_0 = 3.4m; w = 2.0m)

7.3.5. Conclusions

A comprehensive numerical study was implemented to identify and quantify the effect of cavities on the response of shallow foundations. Results show that:

- Careful mesh refinement is required to avoid numerical effects.
- Shallow cavities interact with the footing, lower the bearing capacity, increase settlements, and promote local-punching failures.
- When the footing size is much wider than the soft zone size B>>w, failure remains global (and embodies the soft zone); global shear failures also develop when B<<w and z_0>w. Hence, the worst condition corresponds to B~w; in this case, the system is prone to punching shear failure.
- The critical depth that separates shallow from deep cavities depends on soft zone depth to footing width z_0/B, anomaly size B/w, dilatancy ψ, and the internal stress reduction ISR in the soft zone or cavity. As a guiding rule, the critical depth is about z_0/B~3-to-4 when B/w~1 (the most critical case)
- Dilatancy increases bearing capacity, promotes more brittle load-settlement response, hinders settlements even in the presence of anomalies, and leads to narrower subsurface settlement troughs.

Note that the medium was modeled with no cohesion. Yet, open cavities observed at the Vogtle excavation confirm marked cementation in the layer above the crown, otherwise, grains would flow and fill any developing soft zone as dissolution takes place and no explicit soft zone larger than a few grain diameters could form (see micromechanical results in Section 6). Increased strength on the layer above the soft zone by the addition of cohesion would lead to open cavities, yet, these cohesive layers would dramatically diminish the impact of soft zone/cavity formation on displacement fields above the soft zone/cavity; indeed, the soft zone/cavity would remain “hidden” by the strong layers.

7.4. SRS Case - Selection Of Material Properties

The rest of this report deals with the specific case of dissolution cavities in the subsurface at the Savannah River Site (SRS) and their potential impact on near surface infrastructure. A comprehensive study of the formation history is documented in Section 2. The selection of material properties needed for numerical simulations is documented in this section. The selection of material properties benefited from extensive studies conducted at SRS in the past (Burns and Roe Enterprises, 2001; WSRC, 2007), complementary experimental studies conducted in standard and large diameter oedometer tests (within Shelby tubes with shear wave monitoring – reported in progress reports), and extensive compilations of published data in the literature. A summary of selected properties follows.

7.4.1. Unit Weight

Figure 7-35 shows unit weights inferred from SCPT and laboratory-measured unit weights gathered from undisturbed specimens. It is important to highlight that the total weight decreases with depth, contrary to standard trends in sedimentary systems. This reversed trend is consistent with dissolution activity during the formation history of these sediments

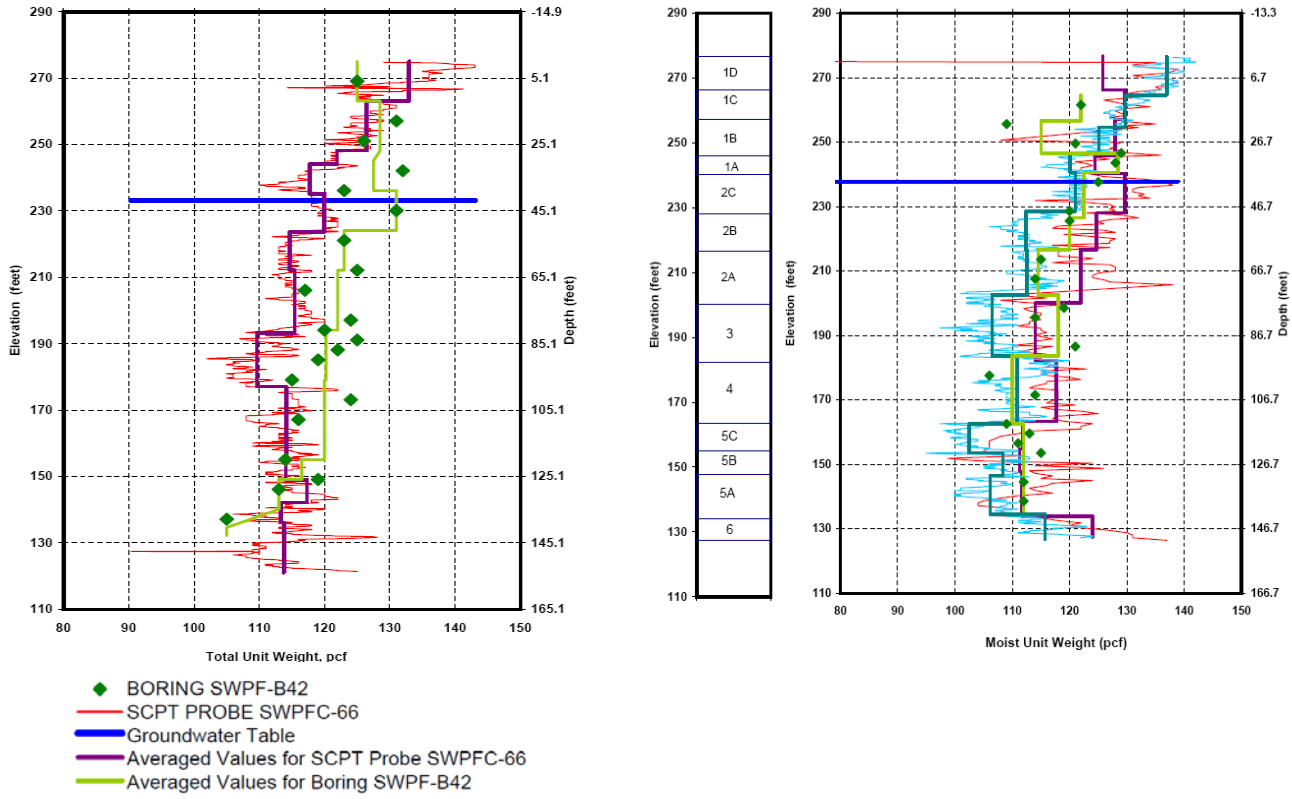

Figure 7-35. Unit weight (WSRC, 2007)

7.4.2. Small Strain Stiffness and Compressibility

The small strain stiffness profile with depth is inferred from shear wave velocity data. Figure 7-36 shows measured shear wave velocity profiles gathered at SRS. Contrary to the stress-dependent stiffness observed in uncemented sediments (Herzian contact behavior), these profiles show an almost constant stiffness with depth. Stress-dependent velocity in uncemented soils is demonstrated in Figure 7-37; for comparison, stress-independent travel times are observed for lightly cemented soils regardless of the state of stress (Figure 7-38). Light cementation is very sensitive to sampling induced strains

(Figure 7-39). Published data gathered in the field and after sampling are compiled in Figure 7-40.

These results confirm the sensitivity of small strain stiffness to sampling. We can conclude that SRS sediments are lightly cemented and could experience pronounced stiffness reduction upon sampling.

Do odometer data provide relevant compressibility for SRS samples? Besides sampling disturbance discussed above, two other effects were explored in this study (see also Santagata and Germaine, 2002; Ladd and DeGroot, 2003; Lunne and Long, 2006):

- extrusion from Shelby tube: it was investigated by testing within the Shelby tube (Figure 7-41)
- cap seating effects: a simple analysis demonstrates that soft boundary layers have a pronounced effect on the compressibility determined for these oedometer specimens, particularly when they are stiff, as it is the case of cemented SRS sediments (Figure 7-42).

A preliminary back analysis of measured field settlements at SRS (details in the following section) confirmed the pronounced effects of sampling, extrusion and seating effects. In fact, the compression ratio that adequately predicted measured settlements is lower than any value measured at the site using “undisturbed specimens”. Indeed, Figure 7-43 shows ranges and mean values for $C_r/(1+e)$ and $C_c/(1+e)$ ratios measured for the different layers at the SRS; for comparison, the yellow band shows the range of compression ratios that are back-calculated to match measured settlements.

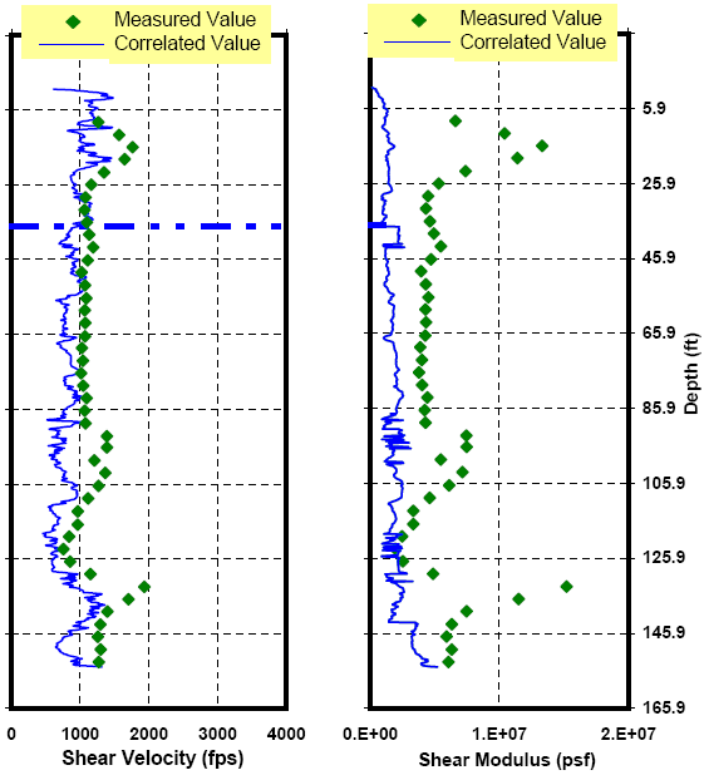

Figure 7-36. Stiffness-stress in situ (WSRC, 2007)

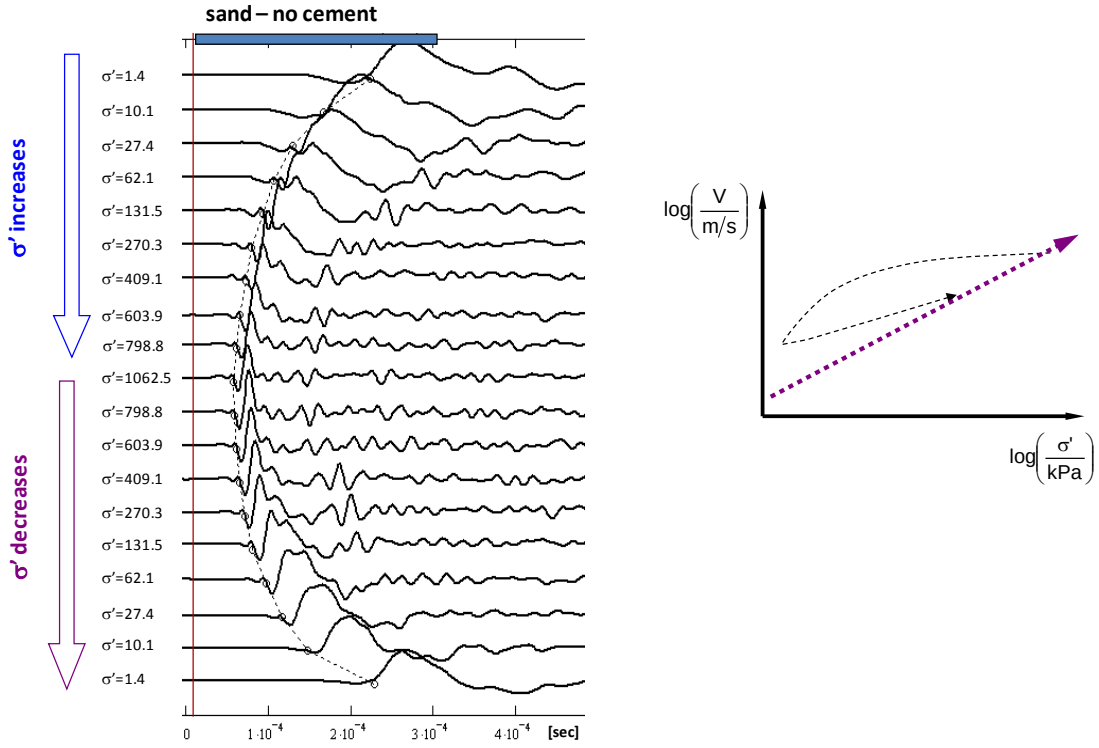

Figure 7-37. Stiffness-stress: uncemented soil (Yun and Santamarina, 2005)

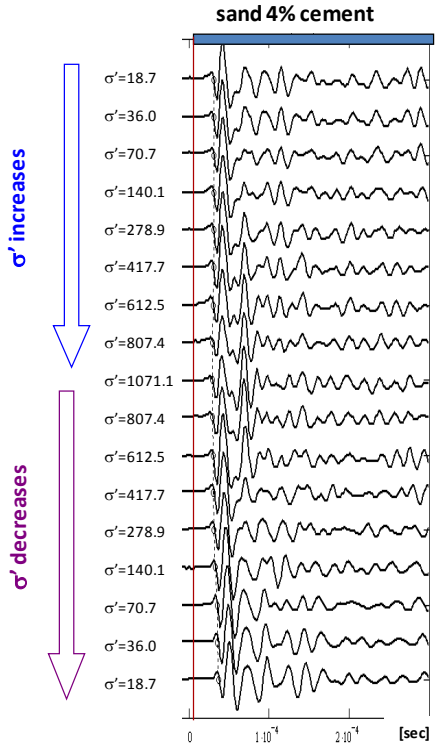

Figure 7-38. Stiffness-stress: cemented soil (Yun and Santamarina, 2005)

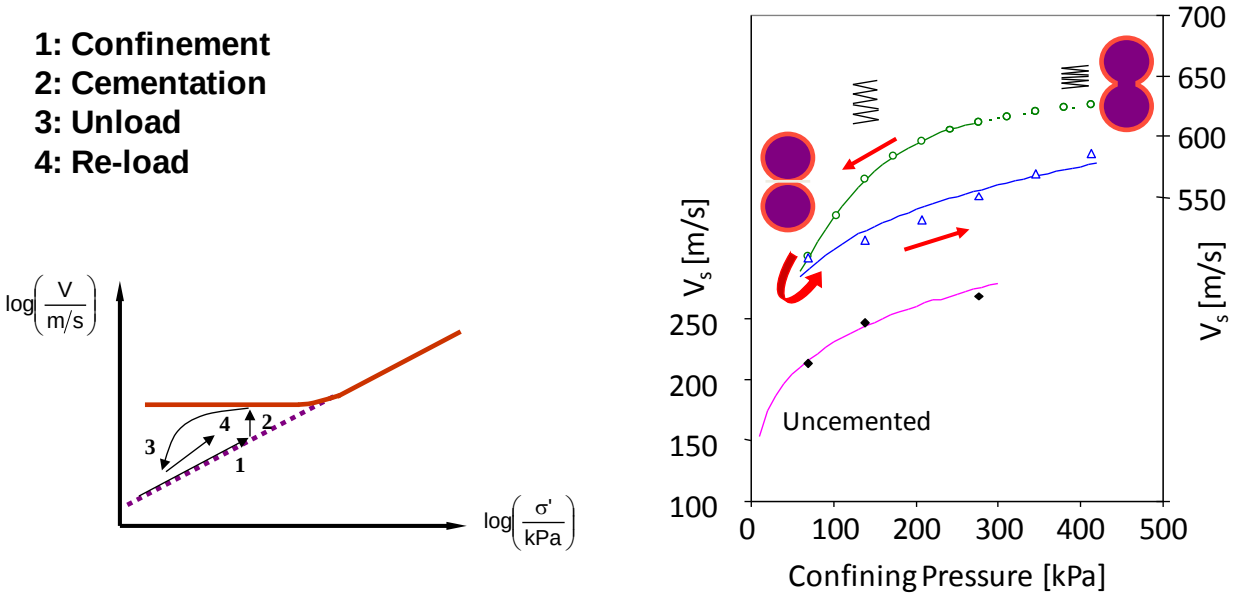

Figure 7-39. Sampling effect: cemented sandy soils (Fernandez and Santamarina, 2001)

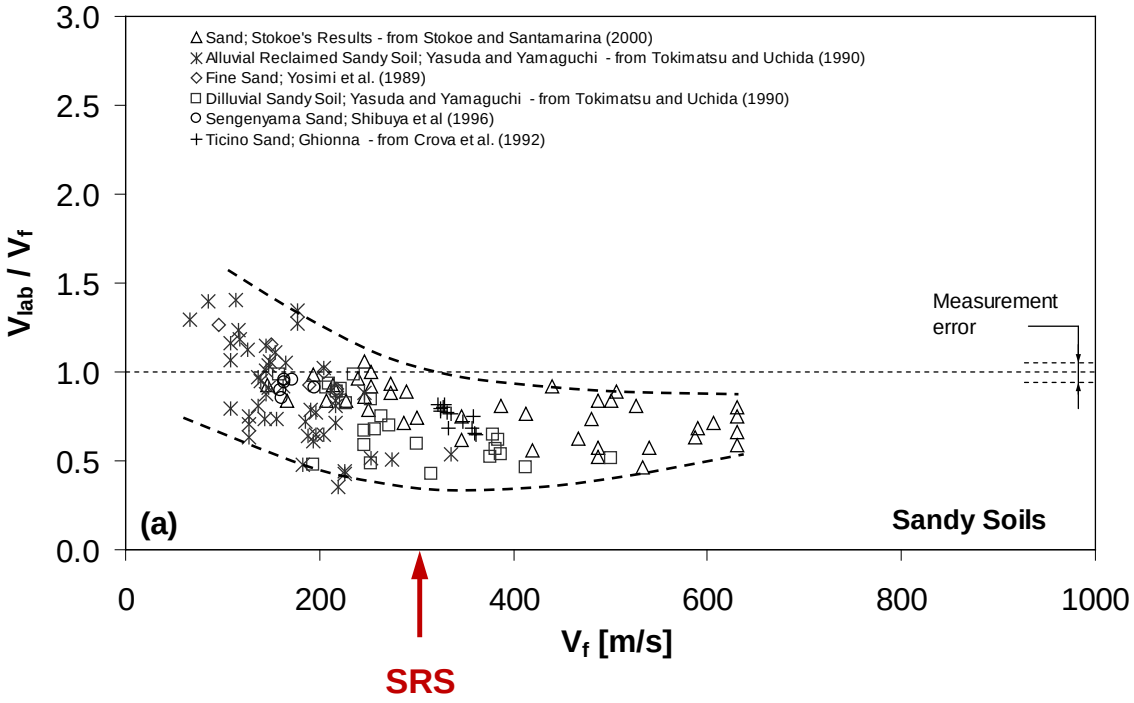

Figure 7-40. Sampling effect: sandy soils (Rinaldi and Santamarina, 2008)

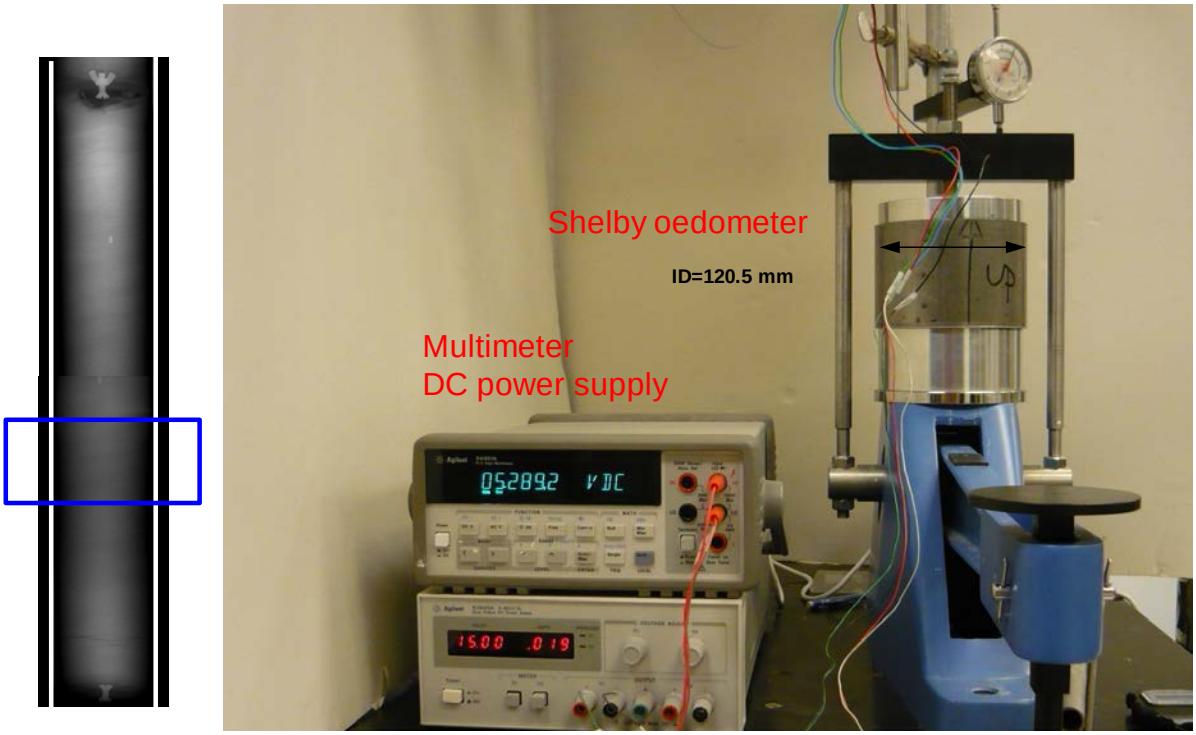

Figure 7-41. "In-Shelby" consolidation test

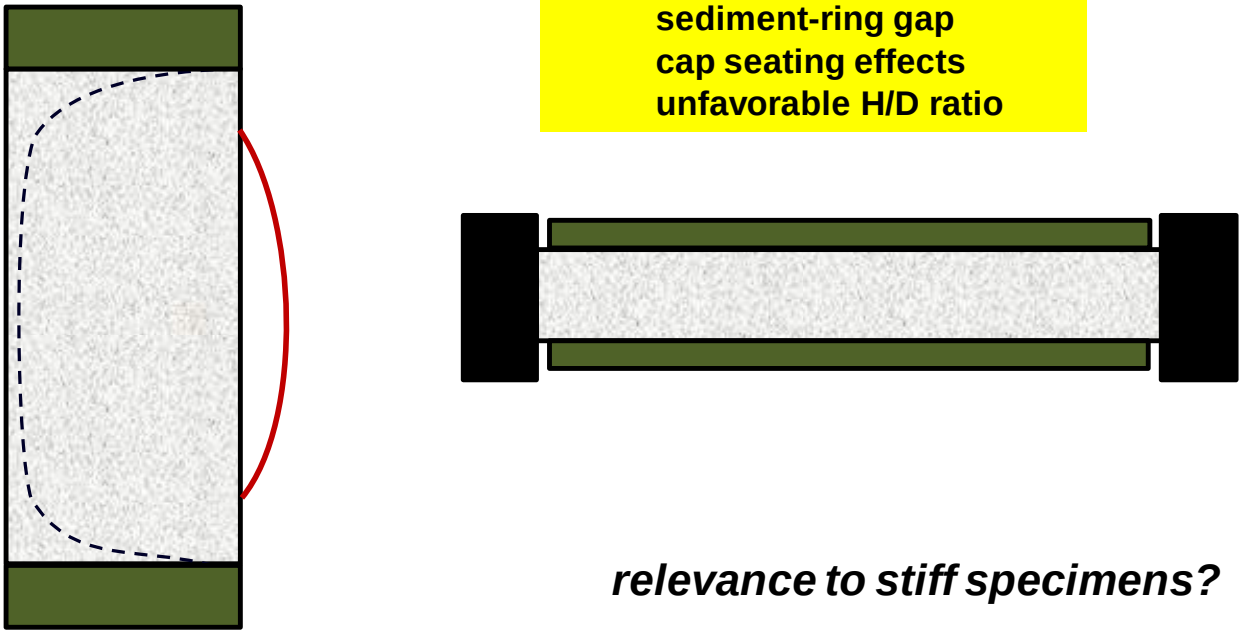

Figure 7-42. Cap seating effects

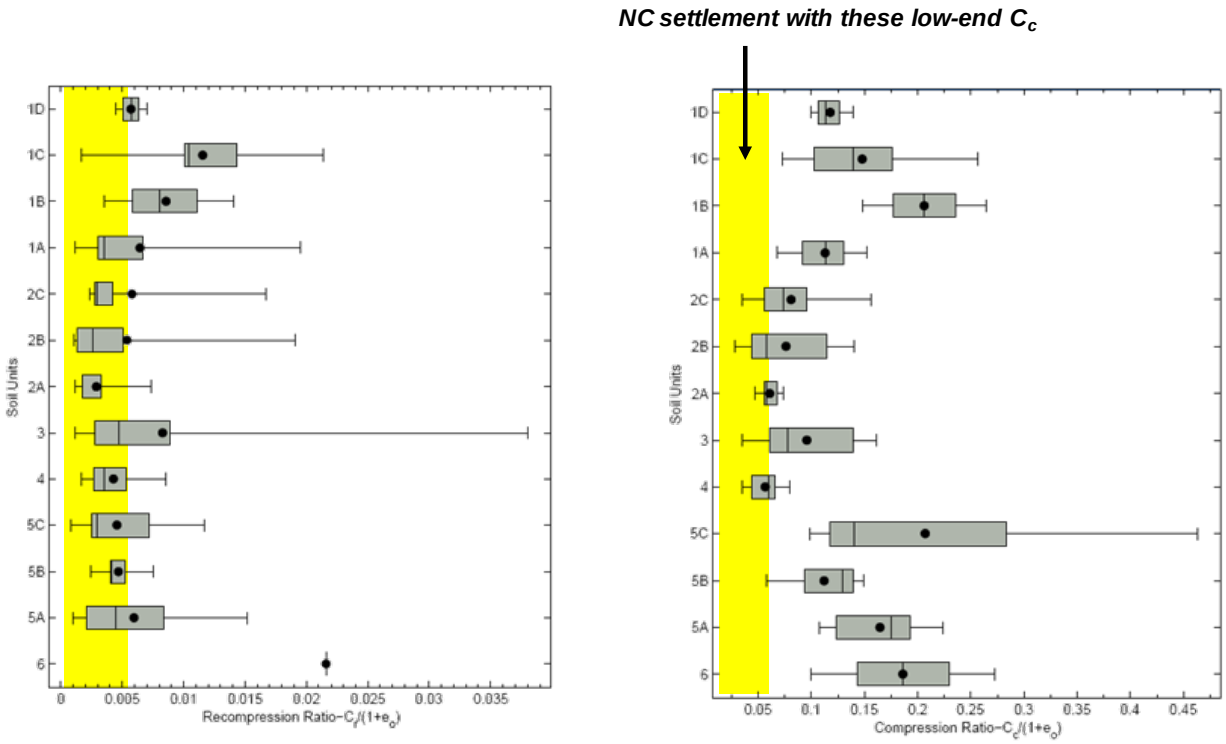

Figure 7-43. Ranges and mean values for recompression and compression ratio (Yellow bands are selected for preliminary back analysis in Figure 5.6; WSRC, 2007)

7.4.3. Strength: Friction angle

As noted earlier, there is pronounced uncertainty in the selection of the friction angle, due to (Figure 7-44 – refer to Section 3 - Cho et al., 2006; Santamarina and Shin, 2009). Stress path dependent friction angle (intermediate stress and b-value): Figure 4.10 shows differences in friction angle ϕ when flow at yield is 1D→2D as in the external angle of repose in a cone, which is similar to AC-loading ($\phi_{AC} = \phi_{EXT}$), and when flow is 2D→1D as in the internal angle of repose in a conical void, which is similar to LC-loading ($\phi_{AE} = \phi_{INT}$).

- Different points beneath a footing experience different flow conditions (b-value)
- Confinement-dependent dilation.

- Post-peak strain softening leads to progressive failure (see for example Rowe and Peaker, 1965) and the effective friction angle decreases as failure progresses

Implications on bearing capacity can be striking, as can be inferred by comparing bearing capacity coefficients for ϕ_{AC} and for $\phi_{AE} \approx 1.5\phi_{AC}$, say 30° and 45° respectively (Figure 7-44).

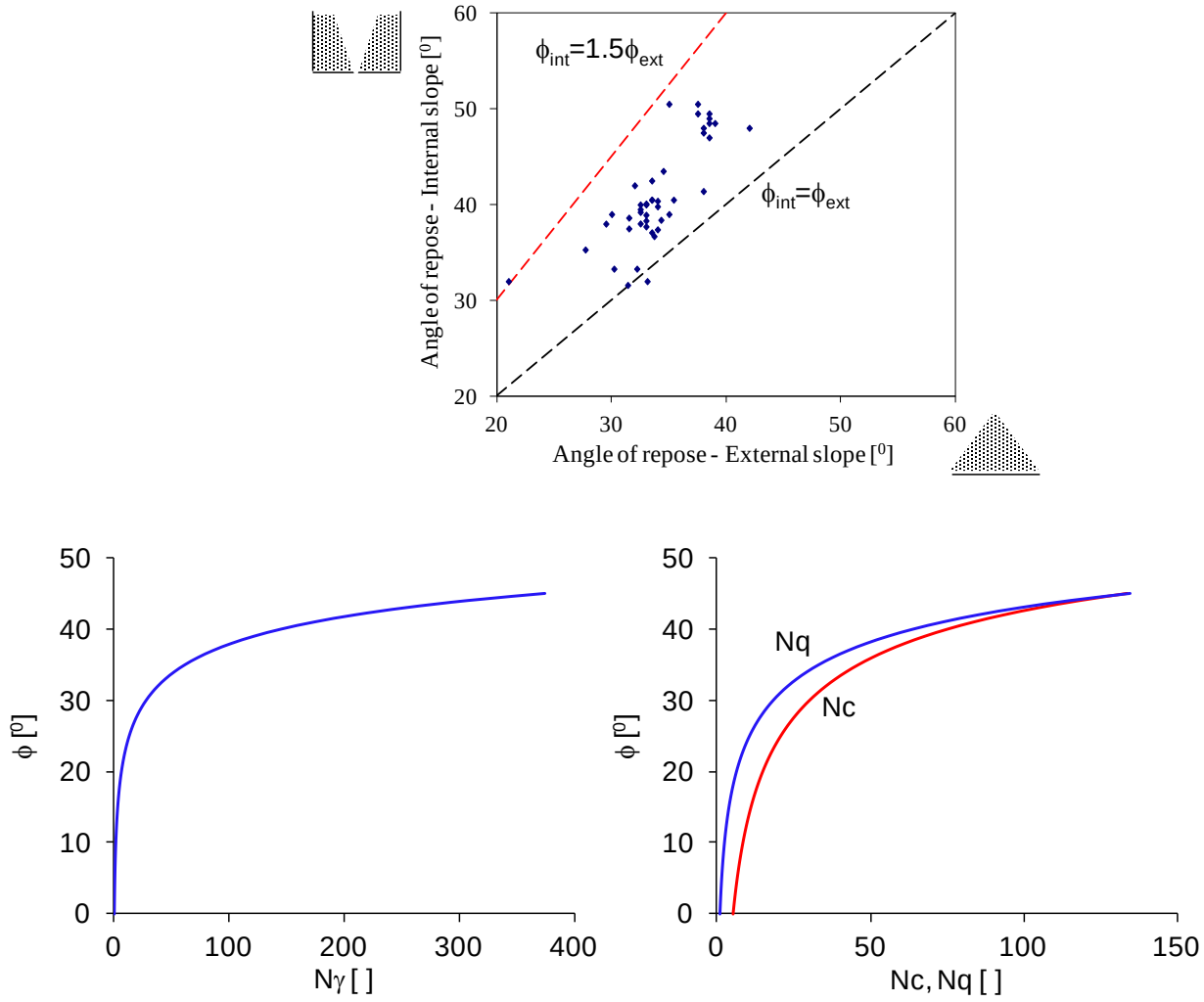

Figure 7-44. Uncertainty of the soil friction and its implication on bearing capacity

7.4.4. Initial K_0 condition

The value of k0 plays a secondary role in the estimation of footing settlements, but it does affect displacement fields induced by soft zone formation. The initial value of K_0 is unknown. If the sediment is overconsolidated by preloading then K_0 =1.0 is an adequate first estimate for this formation (say, OCR~4 - Mayne and Kulhawy, 1982). If the formation is lightly cemented, K_0 could vary in a wide range depending on the stress-cementation history. Finally, the value of K_0 in layers that have experienced dissolution could have decreased to the minimum value of $K_0 = K_A$ at some point in the formation history (Shin and Santamarina, 2009). A value of K_0 =1.0 is adopted for the simulation.

7.4.5. Design parameters – Preliminary values

Material properties for elasto-plastic and Modified Cam Clay models were selected following guidelines identified above and the selected parameters are summarized in Figure 7-45. The maximum soil stiffness E_{max} is determined from small-strain geophysical field data.

The stiffening effect of cementation is inherently taken into consideration when stiffness is computed from shear wave velocity. However, no cohesion or dilation is considered for the strength of any of the layers: this is the “worst-case condition” (from a material parameters point of view) as very advanced softening of soft zones can be modelled without forming cavities underneath cemented layers. The presence of cemented layers would “hide” cavities and soft zones from the shallower layers.

Parameter	Source	Upland Unit	Tobacco Road	Dry Branch	Santee	Warley Hill
Depth [m]		0 - 8	8 -13	13-40	40-48	48-200
Effective unit weight γ [kN/m^3]		20	10	10	10	10
Isotropic compression index λ	*min < back-calculated < max*	0.01	0.02	0.03	0.04	0.005
Void ratio at 1kPa e_{1kPa}	*Appendix (related to λ)*	0.56	0.63	0.71	0.78	0.52
Isotropic recompression index κ	*Assumed (λ/10)*	0.001	0.002	0.003	0.004	0.0005
OCR	*Assumed*	4	4	4	4	4
Shear velocity V_s [m/s]	*Shannon and Wilson (2007)*	350	300	300	250	500
Small-strain Poisson's ratio υ	*Assumed*	0.15	0.15	0.15	0.15	0.15
Young's modulus E_{max} [MPa]	*from Vs*	*574*	*422*	*422*	*293*	*1173*
Drained Poisson's ratio υ	*Assumed*	0.2	0.2	0.2	0.2	0.2
Friction ϕ [^{o}]	*Shannon and Wilson (2007)*	37	35	34	24	43
MCC strength M (for AC)	*from ϕ*	1.51	1.42	1.38	0.94	1.77

Cohesion Intercept MC	*Assumed*	0	0	0	0	0
Dilation Ψ [^{o}]	*Assumed*	0	0	0	0	0
Earth pressure K_o	*Assumed*	1.0	1.0	1.0	1.0	1.0

Figure 7-45. Selected material properties

7.5. SRS Case History – Back Analysis

7.5.1. Introduction

Numerical methods are increasingly used for design and construction decisions. Still, predicted and anticipated settlements show pronounced differences. In most cases, these differences are not due to model choices or boundary conditions but reflect inadequate material parameters, in part due to limited understanding of the geological formation history. The availability of field data gathered for a nearby built structure or during construction provides invaluable information for model calibration/adaptation.

The calibration of constitutive models for soils poses significant challenges due to their inherent nonlinear (Hertzian) and nonelastic behavior (Mindlin) and stress dependent stiffness, strength and dilatancy. Model calibration can be implemented through a formal inversion analysis that seeks to minimize the difference between field measurement and numerically computed results (Kavanagh, 1973; Gioda, 1980a; Gioda and Maier, 1980b; Cividini et al., 1981; Sakurai and Takeuchi, 1983; Gioda and Sakurai, 1987; Hollowell et al., 1988; Gioda and Locatelli, 1999; Calvello and Finno, 2004; Finno and Calvello, 2005; Alonso et al., 2010; Hashash et al., 2010). Guidelines and inversion algorithms can be found in Santamarina and Fratta (2005). Typically, such calibration exercises make extensive use of displacement measurements as they are economically and reliably gathered at multiple surface and subsurface locations.

This section documents a simple but robust back analysis procedure developed to calibrate our numerical model to the SRS field conditions. We apply the methodology to monitoring data

gathered during the construction of the Defense Waste Processing Facility. The calibrated model is used to estimate additional settlements due to the pre-existing cavities, new cavities and a seismic event during the design life of the facility.

7.5.2. The Case History

Defense Waste Processing Facility. This structure was constructed on the S-Area of the SRS Site (SRNS, 2011). The building was supported on a mat foundation (~110 m long, ~38 m wide, and ~1.5 m thick). The average distributed design load is 220kPa. A settlement monitoring program was implemented from the beginning of the excavation of the building site. It was divided into four stages:

- Stage A: excavation
- Stage B: construction of the mat foundation
- Stage C: structural and other loads
- Stage D: post-completion

Figure 7-46 shows the major defense waste processing facility buildings on the left. The figure on the right shows the geometry of the mat foundation and the location of monitoring monuments for building 221-S; the loading history is shown in Figure 7-47. Figure 7-48 shows settlement-vs-time data gathered midway along the footing. The loading and settlement histories are combined into settlement-load plots in Figure 7-49: results show a relatively linear trend. This suggests the possible estimation of an equivalent global stiffness using the elastic solution: indeed, data replotted in Figure 7-50 suggest a first order estimate of the global stiffness is about E=150 MPa for settlements greater than about 0.025m.

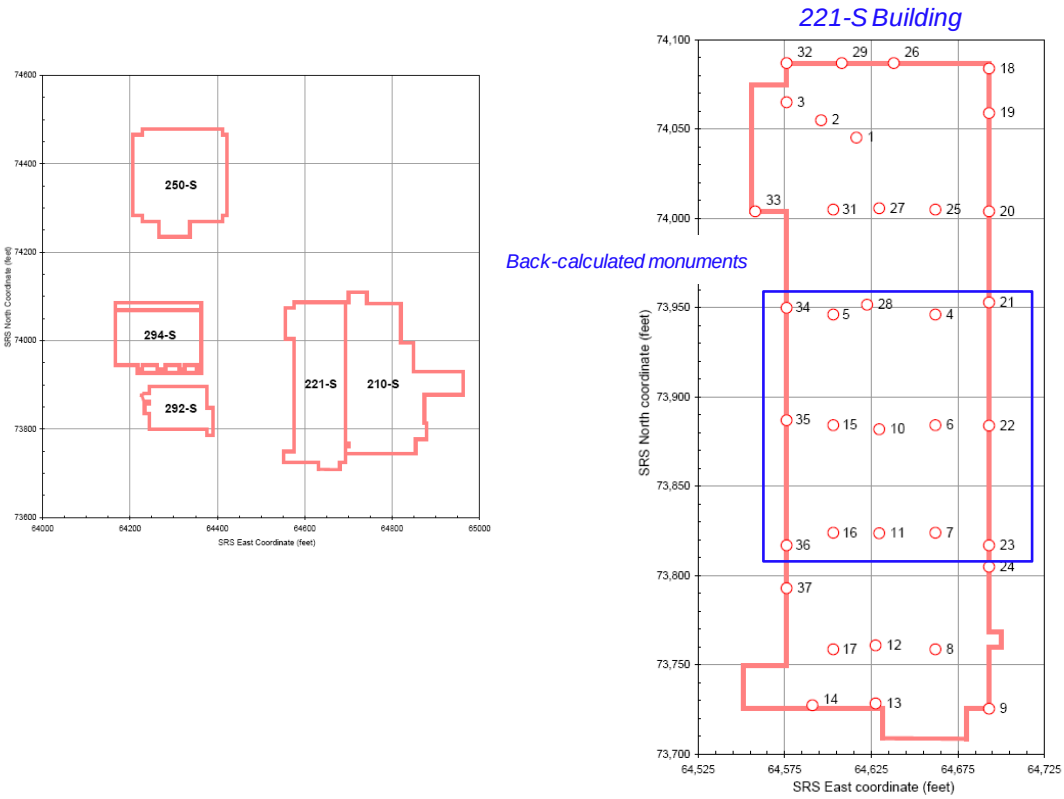

Figure 7-46. Mat foundation - Monitoring stations

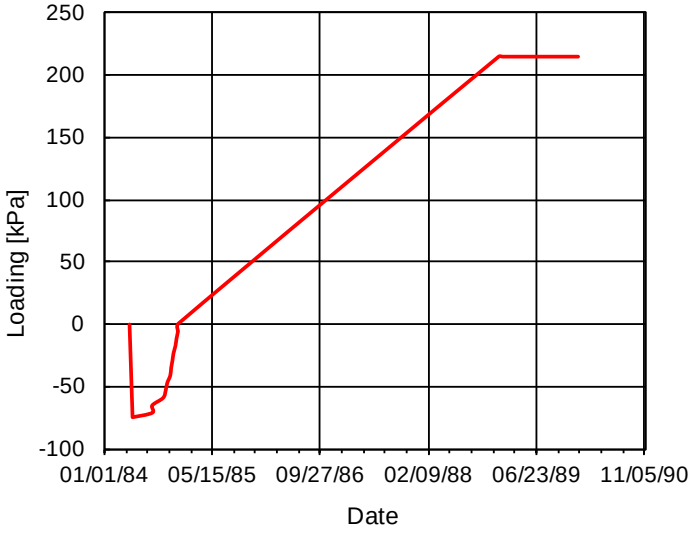

Figure 7-47. Loading history

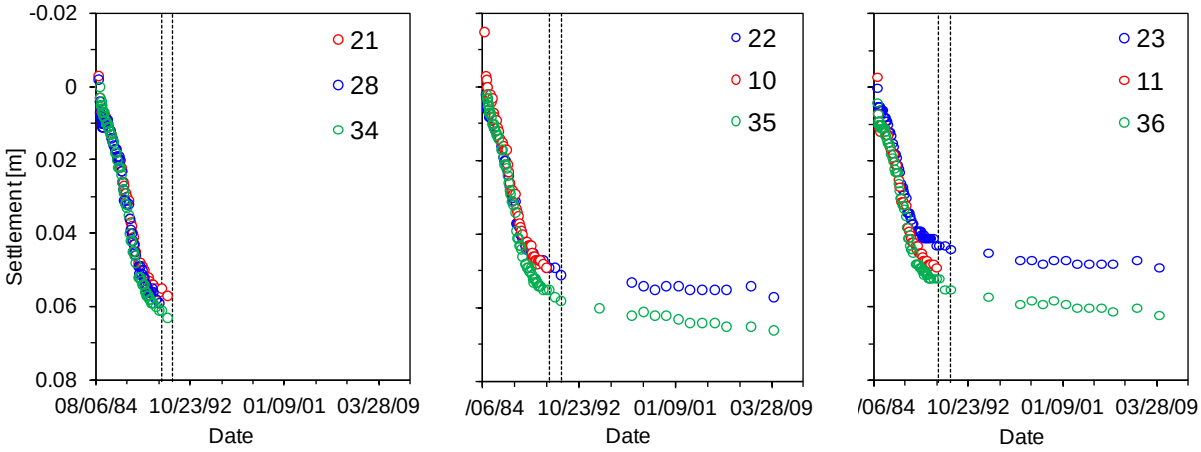

Figure 7-48. Settlement-vs-time

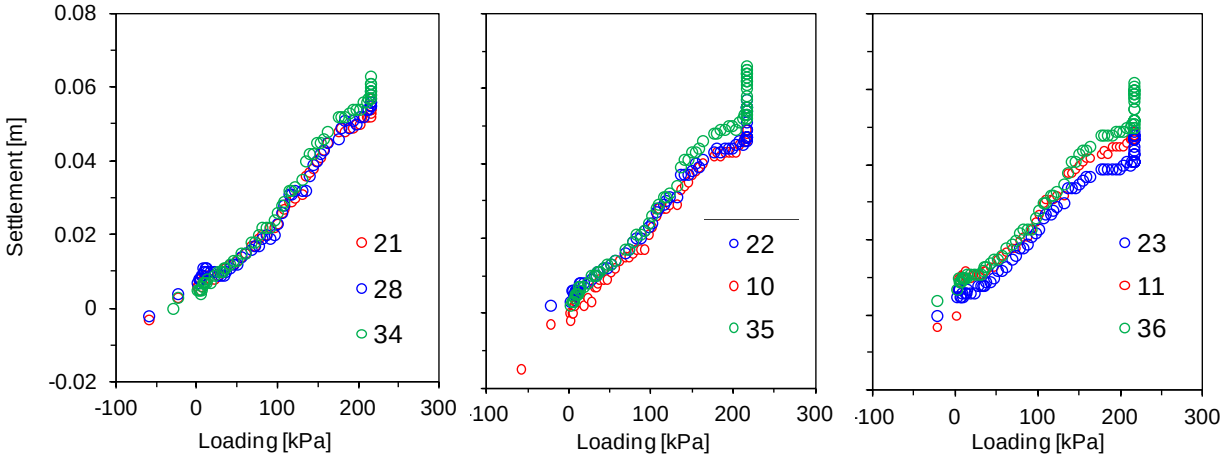

Figure 7-49. Settlement-vs-load

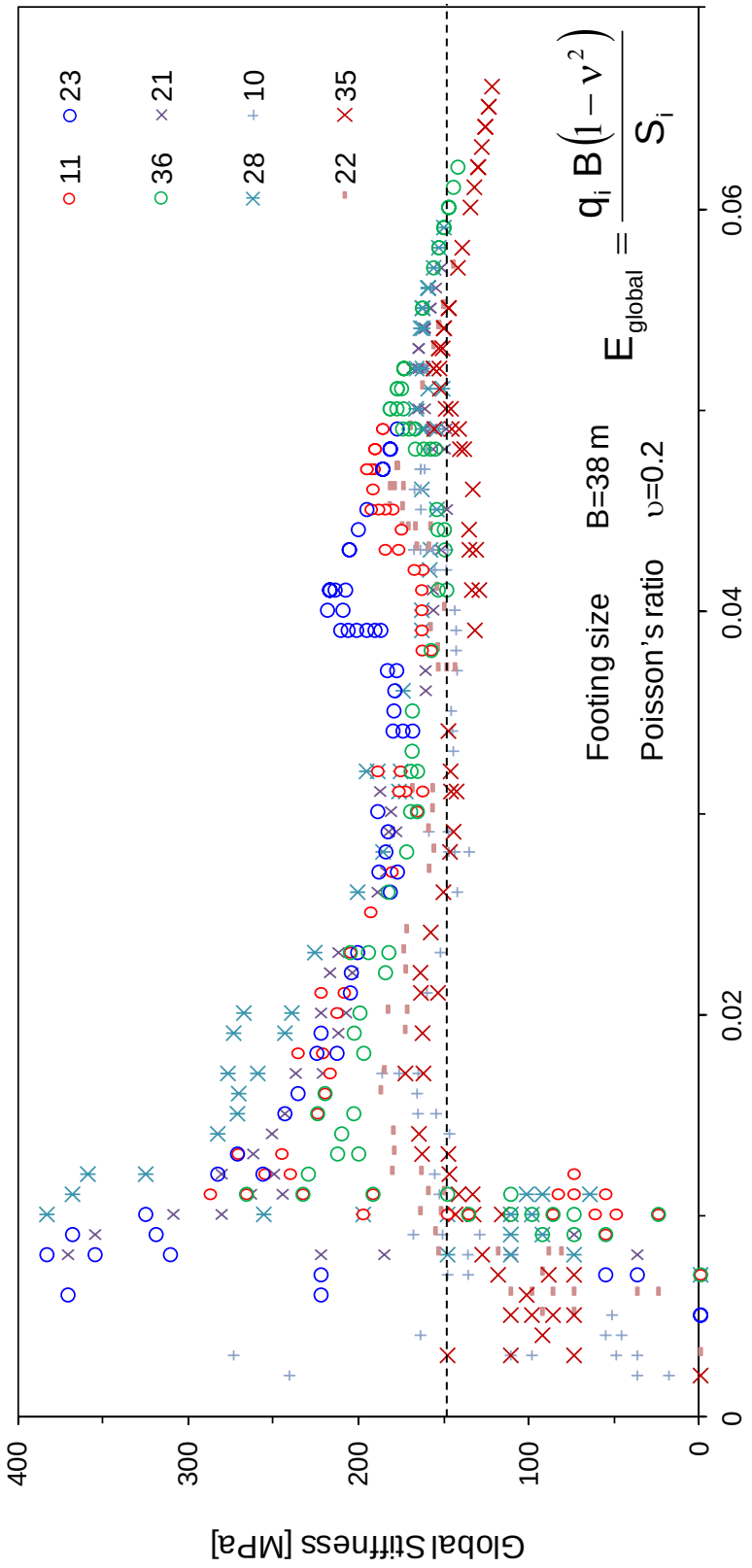

Figure 7-50. Back-calculated global modulus (Dotted line indicates the first order estimate of the global stiffness for settlements greater than about 0.025m)

Preliminary Analysis. A 2D analysis conducted using Modified Cam Clay and verified with standard 1D consolidation using the same parameters show that (Figure 5.6):

- the 2D and 1D analyses conducted assuming OC conditions provide almost identical results
- in order to match the measured surface settlements, the selected consolidation parameters are in the lower end of values reported from laboratory studies (as noted in reference to Figure 7-43).
- for the given geometry (B=34 m, layered stratigraphy, most compressible layers in upper <50 m), the 1D analysis provides an excellent approximation to the 2D results.
- as a corollary, parameter selection is much more important than the decision to capture this case history using a 1D or 2D representation.

The 6cm mean settlement implies an "average strain" lower than $<10^{-3}$ within the depth of influence of the mat foundation. This relatively small strain requires high quality specimens and detailed test procedures to minimize the impact of core-chamber gap and seating effects on thin oedometer specimens. An alternative approach based on field data is explored next.

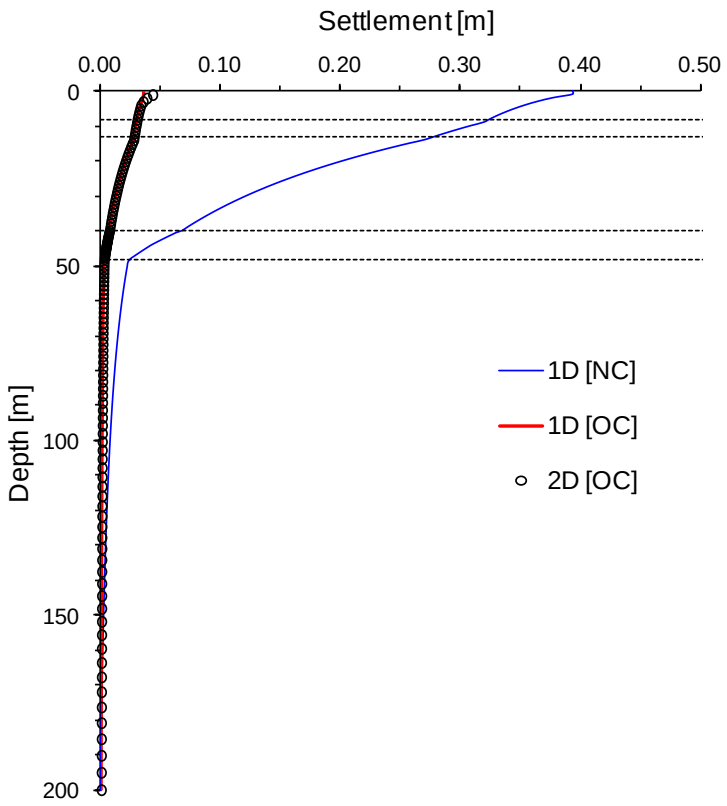

Figure 7-51. Settlement calculation - Oedometer data

Numerical Simulation. The commercial software ABAQUS is used for the simulations. The medium is discretized into plane-strain, eight-node biquadratic reduced integration elements. The lower boundary and lateral boundaries are located far from the footing to minimize boundary effects (model: 200 m high and 300 m wide - due to symmetry, the effective width is 600 m). Vertical displacement is allowed on side boundaries, the bottom boundary is pinned, and the top surface is free (Figure 7-52). Five distinct strata are modeled. A surcharge load of q_0=10kPa is applied everywhere to reflect a nominal burial depth in standard construction practice.

Lateral boundary effects were assessed for the selected domain using cases that include various soft zone-loading histories. Results in Figure 7-53 confirm that there are no boundary effects in these simulations: the far-field surface settlement is almost null in all cases and the

geostatic horizontal stresses against far field zero-lateral strain boundaries remain constant through loading-dissolution histories.

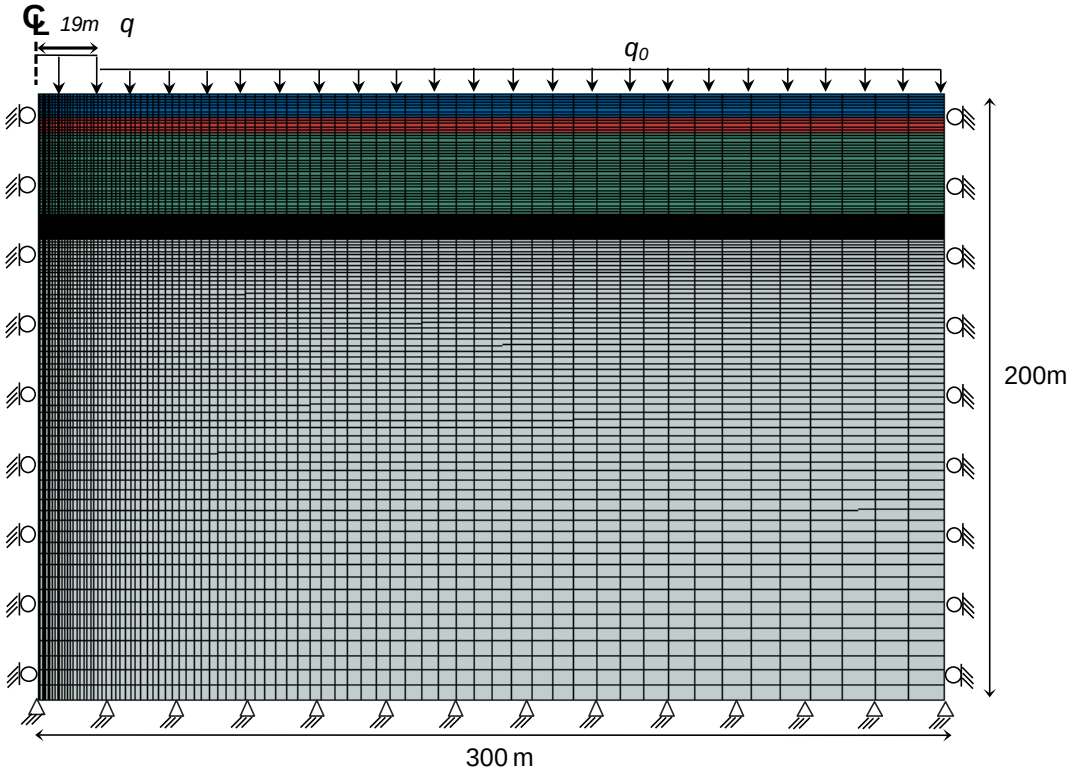

Figure 7-52. Geometry - Boundary conditions

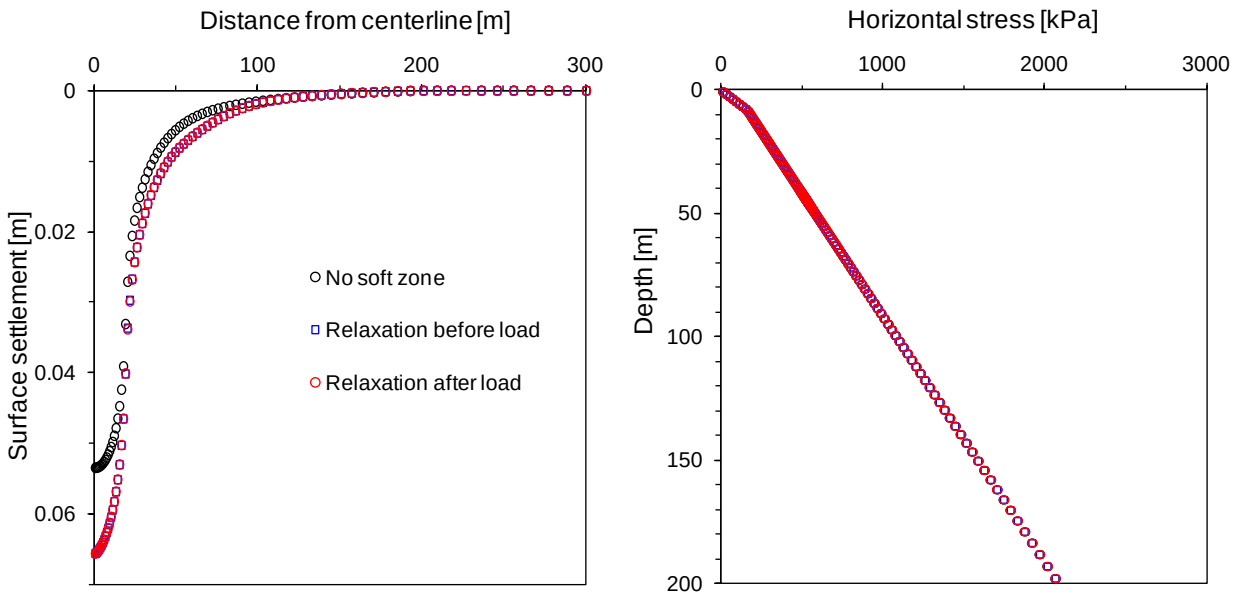

Figure 7-53. Boundary effect (Case3; ISR ≈ 0.95)

7.5.3. Model Calibration by Back Analysis

The alternative approach selected for back analysis is based on a secant formulation using the elastic perfectly plastic Drucker-Prager material model to represent all strata. This is a simple and robust approach, in line with Ockham's criterion.

Load-settlement results are shown in Figure 7-54. The predicted failure load is about 10 times higher than the applied load (in agreement with the small strains anticipated above).

Stiffness Reduction. The basic hyperbolic model (Kondner, 1963; Duncan and Chang, 1970) is adopted to evaluate the reduction of stiffness with strain in a robust manner (Figure 7-55). The secant stiffness E_{sec} that corresponds to strain ε is related to the maximum stiffness E_{max} estimated from in situ measurements of wave propagation,

$$\Pi = \frac{E_{sec}}{E_{max}} = \frac{1}{1+\frac{\varepsilon}{\varepsilon_{ref}}}$$ *Modulus reduction factor*

where the reference strain $\varepsilon_{ref}=\sigma_{ult}/E_{max}$ is computed using the Coulomb frictional strength at the corresponding state of stress σ_{ult} and the value of E_{max}.

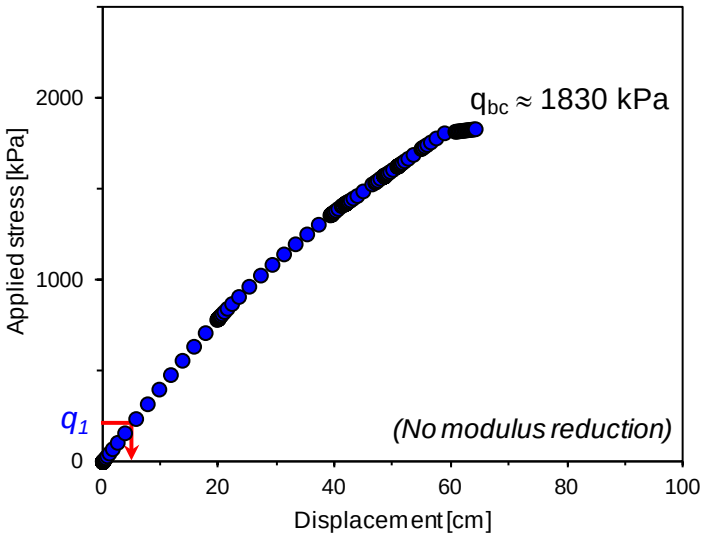

Figure 7-54. Load-displacement (No soft zone)

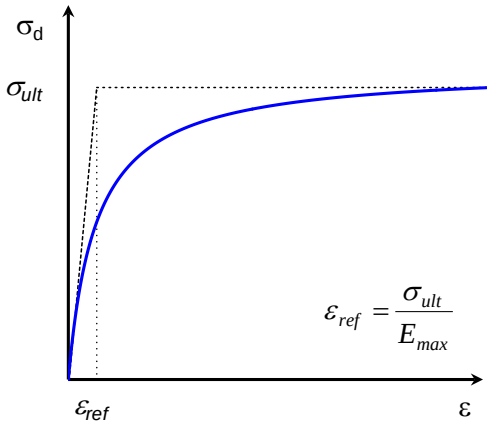

$$\sigma_d = \frac{\varepsilon}{a + b\varepsilon} = \frac{\varepsilon}{\frac{1}{E_{max}} + \frac{\varepsilon}{\sigma_{ult}}} = \frac{E_{max}\varepsilon}{1 + \frac{\varepsilon}{\varepsilon_{ref}}}$$

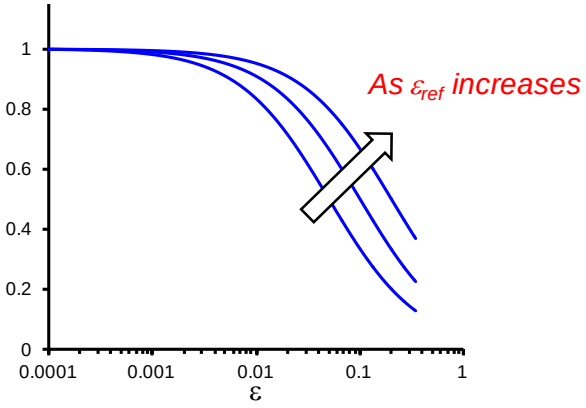

Secant stiffness:

$$\Pi = \frac{E_{sec}}{E_{max}} = \frac{1}{1 + \frac{\varepsilon}{\varepsilon_{ref}}}$$

Figure 7-55. Modulus reduction - Hyperbolic model

Model Calibration. The algorithm implements successive forward simulations where the modulus of each layer is reduced as a function of the strain mobilized in the layer, until the computed settlement matches the measured settlement. The procedure is as follows (Figure 7-56):

1. Model all layers using the elastic perfectly plastic Drucker-Prager model in a secant formulation
2. Determine the E_{max} for each layer from small-strain geophysical field data
3. Run the FEM and estimate strains in each element ε_{est}
4. Reduce the stiffness in each element according to the strain level using the hyperbolic formulation

5. Repeat steps 3 and 4 until subsurface strains convergence in subsequent iterations (example shown in Figure 7-57).
6. Compare the predicted settlement to measured surface settlements – If needed, adjust initial soil parameters as needed, but within the range of parameter uncertainty.
7. Repeat steps 3-to-6.

Final modulus reduction values computed for the SRS case history range from a factor of Π=7 in the shallowest layers (highest strains) to almost no reduction at depths z~B> 35 m. The reduced modulus compares well with the back-calculated global modulus (Figure 7-50 and Figure 7-58).

Foundation Stiffness. The mat foundation and the superstructure could be modeled in finite elements as well. To explore the effect of the mat-and-structure stiffness, we simulated and compared the two end-members: perfectly flexible (i.e., stress-controlled) and perfectly rigid (i.e., displacement controlled). Results in Figure 7-59 show limited effect of structural stiffness, with slight preference to rigid mat response (Stage C: structural and other loading; Stage D: post-completion). Displacement fields in Figure 7-60 and Figure 7-61 show the controlling effect of the shallower layers on surface settlement.

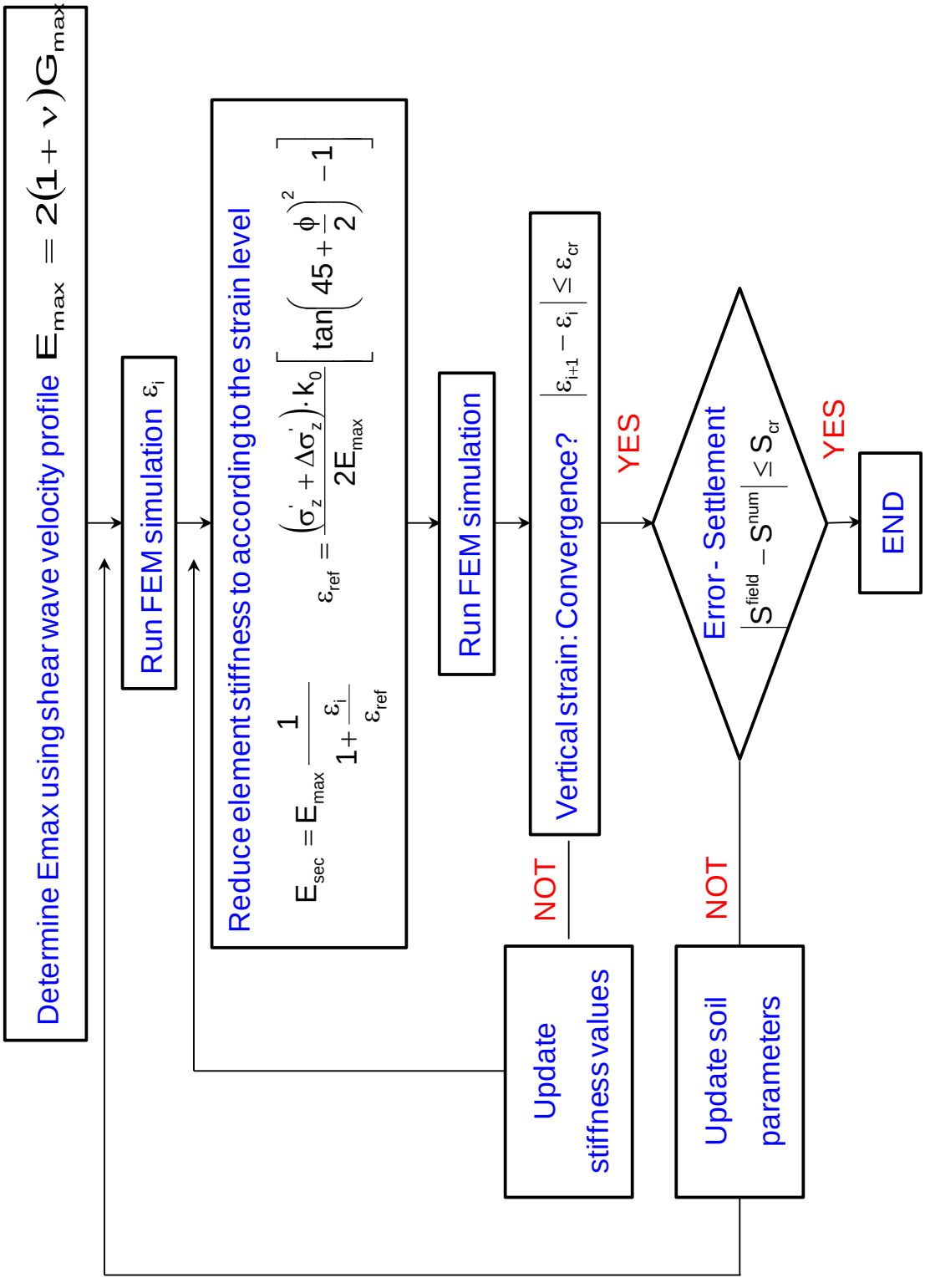

Figure 7-56. Back analysis and model calibration

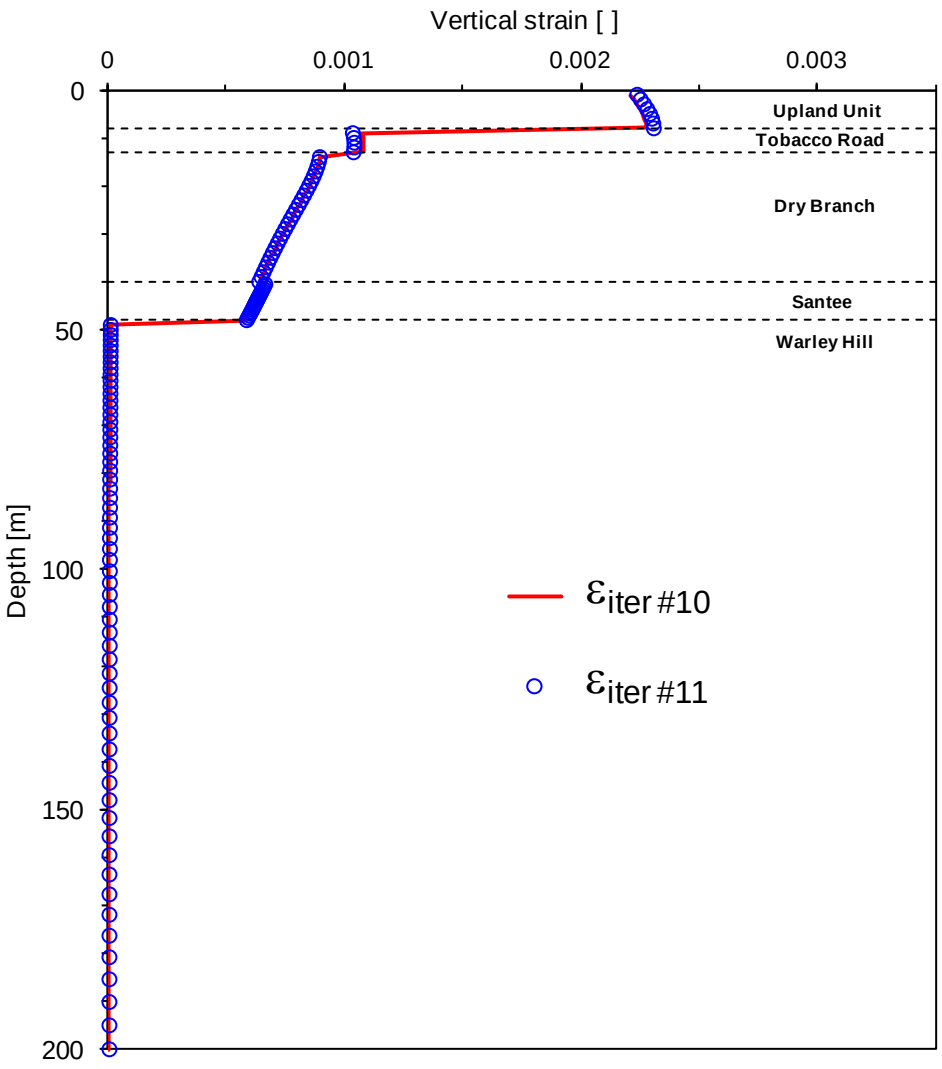

Figure 7-57. Convergence: $\varepsilon_{iter\ i}$ vs. $\varepsilon_{iter\ i+1}$

Parameter	Source	Upland Unit	Tobacco Road	Dry Branch	Santee	Warley Hill
Depth [m]		0 - 8	8 -13	13-40	40-48	48-200
Effective unit weight γ [kN/m^3]		20	10	10	10	10
Isotropic compression index λ	*min < back-calculated < max*	0.01	0.02	0.03	0.04	0.005
Void ratio at 1kPa e_{1kPa}	*Appendix (related to λ)*	0.56	0.63	0.71	0.78	0.52
Isotropic recompression index κ	Assumed (λ/10)	0.001	0.002	0.003	0.004	0.0005
OCR	Assumed	4	4	4	4	4
Shear velocity V_s [m/s]	*Shannon and Wilson (2007)*	350	300	300	250	500
Small-strain Poisson's ratio υ	Assumed	0.15	0.15	0.15	0.15	0.15
Young's modulus E_{max} [MPa]	*from Vs*	*574*	*422*	*422*	*293*	*1173*
Modulus degradation factor Π	*back-calculated*	*6.7*	*2.4*	*2.0*	*1.4*	*1.0*
Effective modulus E [MPa]	from back-analysis	*85*	*178*	*213*	*206*	*1142*
Drained Poisson's ratio υ	Assumed	0.2	0.2	0.2	0.2	0.2
Friction ϕ [^{o}]	*Shannon and Wilson (2007)*	37	35	34	24	43
MCC strength M (for AC)	*from ϕ*	1.51	1.42	1.38	0.94	1.77
Cohesion MC	*Shannon and Wilson (2007)*	0	0	0	0	0
Dilation Ψ [^{o}]	Assumed	0	0	0	0	0
Earth pressure k_0	Assumed	1.0	1.0	1.0	1.0	1.0

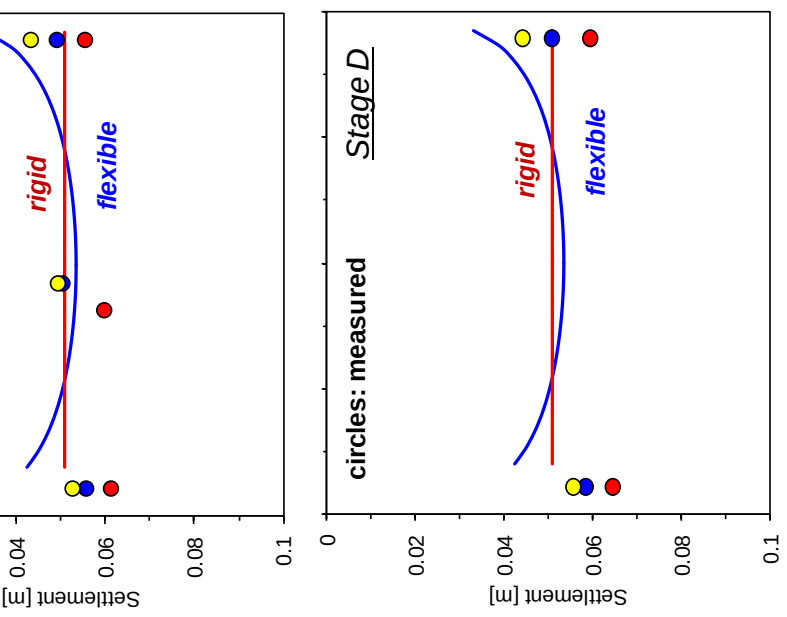

Figure 7-58. Selected material properties

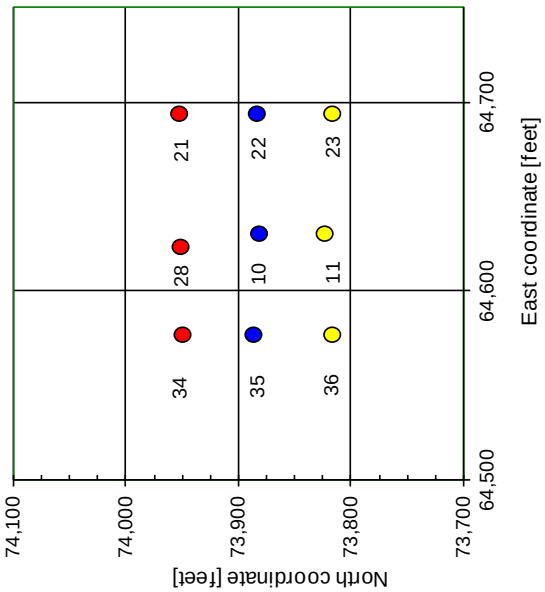

Figure 7-59. Measured vs. predicted settlements

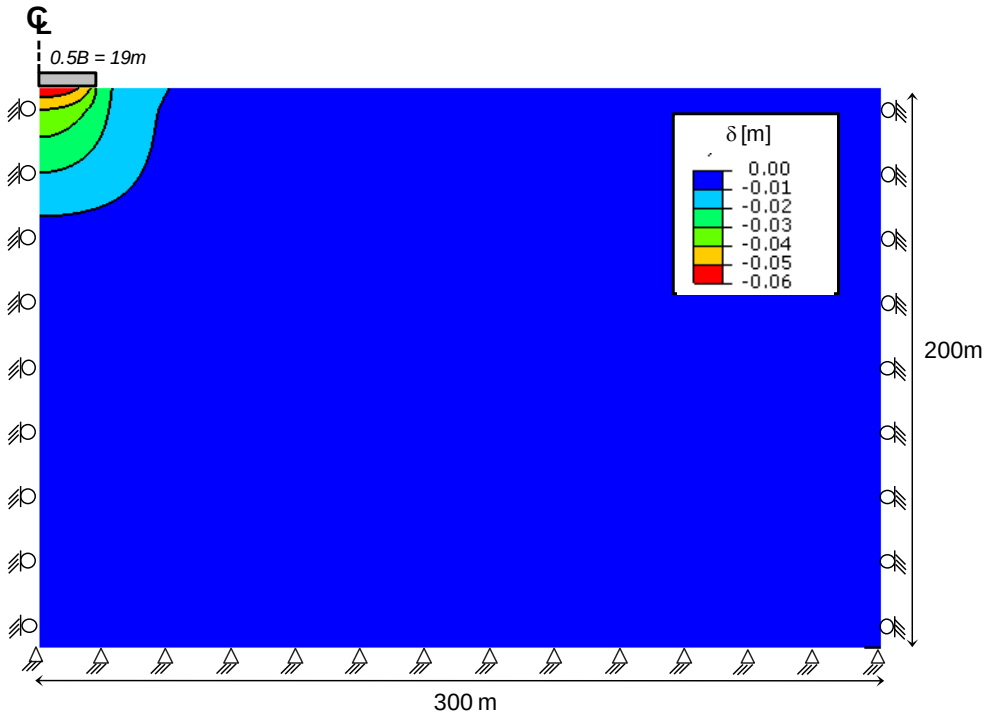

Figure 7-60. Displacement field - Building load (No soft zone); load applied in load-controlled mode (Flexible footing)

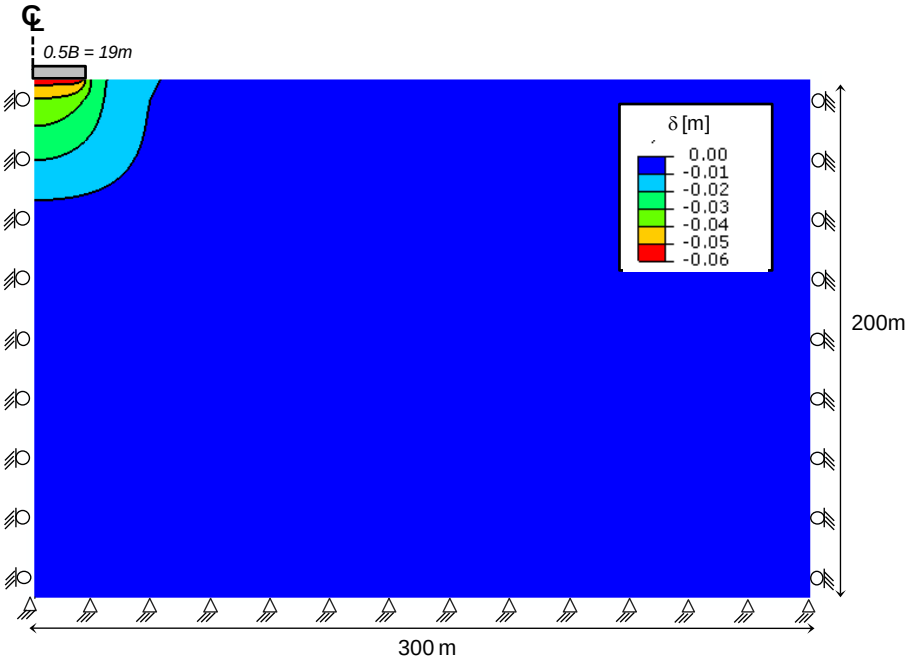

Figure 7-61. Displacement field - Building load (No soft zone); load applied in deformation-controlled mode (Rigid footing)

7.5.4. Possible Settlements Due to Cavities and Seismic Action

The calibrated subsurface model, including selected material parameters coupled with strain-dependent stiffness reduction, is taken as the initial condition (in-situ stresses and secant modulus of soil layers) to compute additional settlements due to the presence/formation of cavities and for seismic loading.

Parametric Studies. The carbonate rich sediments found in the lower Dry Branch and the Santee formation strata may experience dissolution. Three sets of hypothetical cavities are simulated to quantify the impact of dissolution features on the shallow mat foundation (Figure 7-62 - These cases are inspired by similar conditions encountered at the Vogtle excavation nearby – At the SRS, soft zones are mainly encountered in the Santee formation at a depth ≈ 40~48m). Two possible formation histories are considered: stress relaxation-before-structure and structure-before- stress relaxation.

Seismic action is added after soft zone formation in all cases. At the SRS, the horizontal component of the peak ground acceleration a_{max} on rock is between 0.06-0.09g (7%-75 year) and 0.09-0.12g (2%-50yr - See http://earthquake.usgs.gov/hazards/). Quasi-static analysis is adequate for these a_{max} values. Seismic wave propagation will induce a strain level that can be estimated as $\gamma = a_{max} / 2\pi V_s f$. For example, $\gamma \approx 5x10^{-4}$ for amax=0.1g, Vs=300 m/s and f=1Hz. Strain levels are approximately linearly proportional to a_{max} within this range. These strain range is similar to the expected threshold strain for cementation breakage in this material. However, cementation

breakage leads to a very dilative blocky structure, where blocks are composed of cemented grains. Therefore, higher accelerations do not necessarily imply risk of excess pore pressure generation. In summary, seismic action is modeled as a quasi-static horizontal load applied onto the mat foundation. The selected horizontal load is 10% of the vertical load.

The numerical methodology is summarized in Figure 7-63 (Cases 1, 2, and 3 refer to soft zone size and number of cavities, as sketched in Figure 7-62). Soft zone formation is simulated with different levels of internal stress reduction in order to capture different degrees of dissolution.

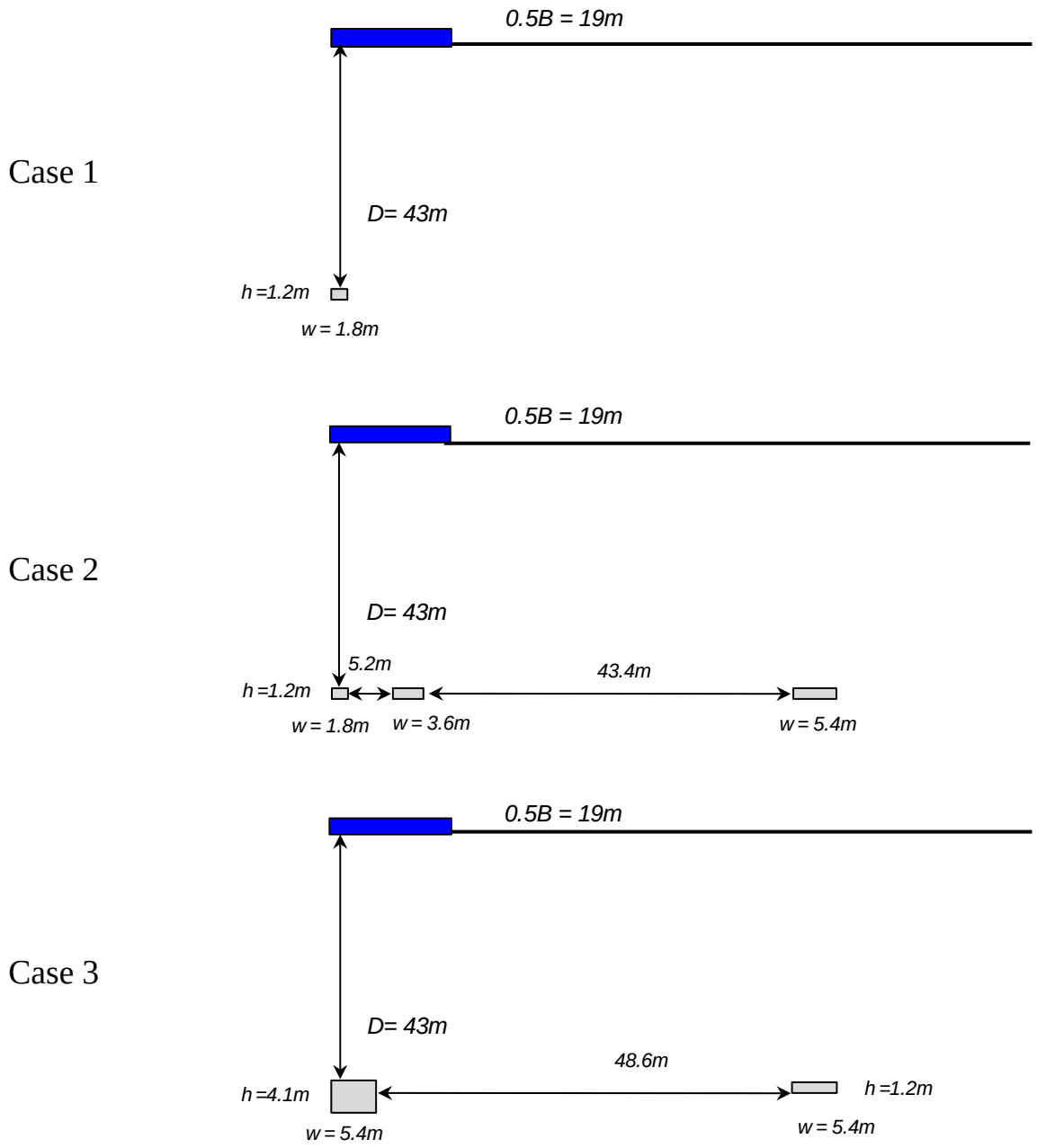

Figure 7-62. Hypothetical soft zones

	Stress Relaxation Before Load	Stress Relaxation After Load
Case 1	1) Form soft zone until specified ISR 2) Load footing to q_0 and q_1 3) Apply QS load over the footing 4) Repeat for ISR = 10,30,50	1) Load footing to q_0 and q_1 2) Form soft zone 3) Reduce the internal stress until specified ISR 4) Apply QS load over the footing 5) Repeat for ISR = 10,30,50
Case 2		
Case 3		

Surcharge: q_0 = 10 kPa

Building load: q = 220 kPa

QS horizontal load: QS = 22 kPa

Figure 7-63. Soft zone formation histories (Cases 1, 2, and 3 refer to soft zone size and number sketched in Figure 5.17)

Results. Computed settlements for complete histories are shown in Figure 7-64. The main observations follow:

- The structure-induced settlement is the largest component [OB or AC paths]; the formation of cavities or soft zones may increase settlements by less than 10-20 % [OA or BC paths]. The validity of this observation is limited to hypothetical geometries.
- Soft zone formation before the structure [OACD paths] produces slightly larger settlements than soft zone formation after the structural load [OBCD paths]. Thus, differences in formation history can be disregarded for all practical purposes at the SRS.
- Seismic loading the structure (a_h=0.1g) sitting on top of the sediment with cavities will cause negligible additional settlement (less than 5% of the total settlement due to the static load in all 24 cases).
- On the bases of these results, more complex seismic models that take into consideration inertial effects are not necessary at this point and for the purposes of this analysis. Furthermore, other consequences of seismic action such as liquefaction are unlikely given the measured penetration resistance and shear wave velocity profiles everywhere in the sediment except in the localized soft zones.

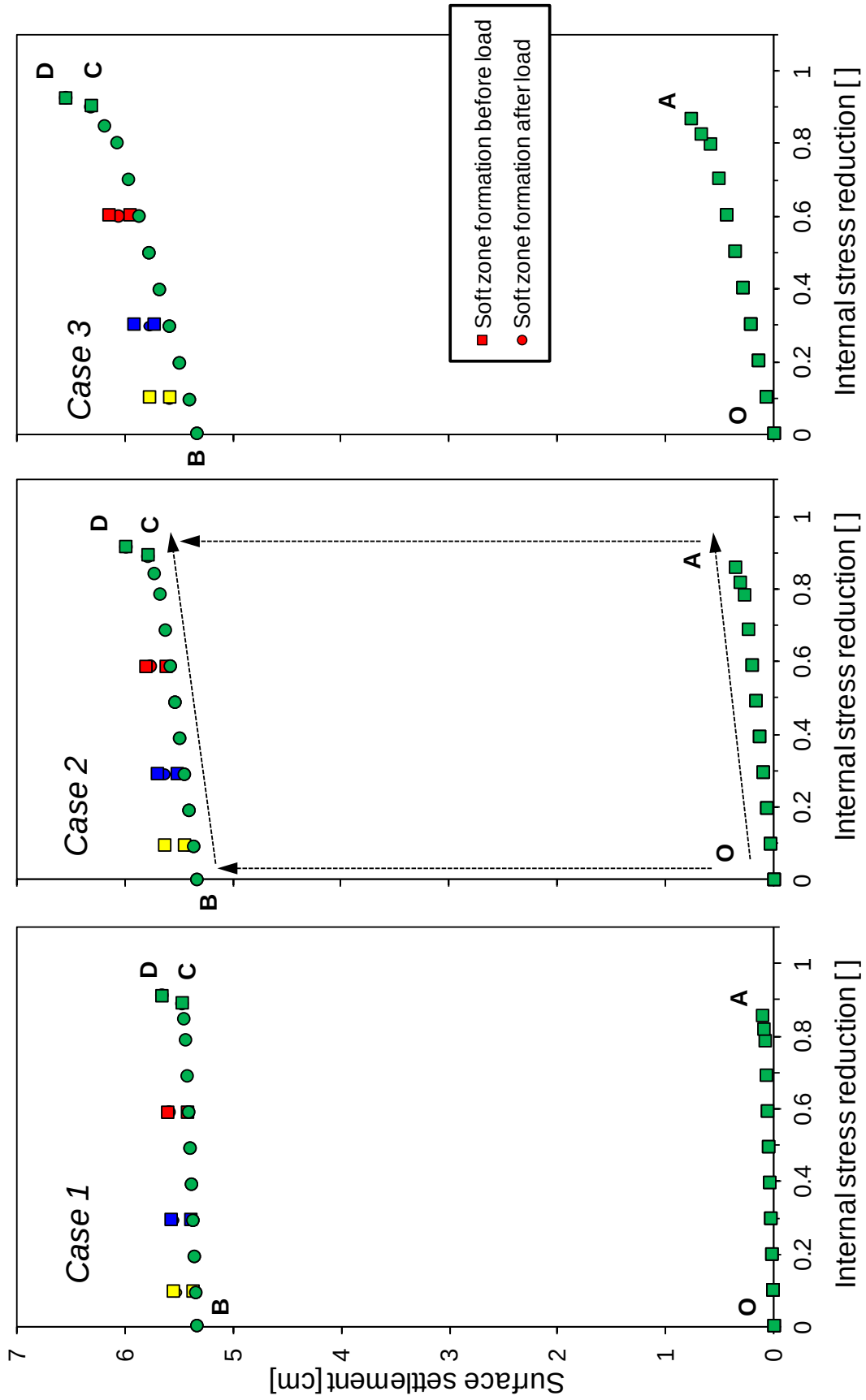

Figure 7-64. Settlement: Footing load, soft zone formation, and seismic load (z_0 = 43m)

7.5.5. Conclusions

Back analysis faces inherent difficulties with convergence and non-uniqueness of the solution. These are exacerbated by the stress-dependent, nonlinear soil behavior, spatial variability, and typically limited information available in most field cases. The approach developed and implemented in this study was guided by Ockham's criterion, involved a simple secant formulation using a robust elasto-plastic numerical model and was anchored on credible field measured parameters.

The "SRS subsurface model" was calibrated through the back-analysis of settlement data gathered during the construction of the Defense Waste Processing Facility at SRS. Emphasis was placed on small-strain geophysical field measurements.

Results for this facility at SRS show that structure-induced settlements overwhelm all other effects. The formation of cavities or soft zones either before or after the building load may cause an increase in settlement less than 10-20 % (for the simulated conditions). Seismic loading the structure (a_h=0.1g) after soft zone formation adds an additional settlement smaller than 5% of the settlement induced by the static load (for the simulated conditions).

Preliminary analyses conducted with compressibility parameters gathered in consolidation tests overpredicted settlements possibly due to sampling effects and procedural difficulties (core-ring gap, cap seating effects magnified by thin specimens).

For the given geometry (B=34 m, layered stratigraphy, most compressible layers in upper <50 m), the 1D analysis provides an excellent first order estimate. Furthermore, parameter

selection is much more important than the choice to capture this case history using a 1D or 2D representation.

It is important to highlight that no cohesion was considered in any of the layers. However, open pipes and tensile fractures observed at the Vogtle excavation suggest cementation in the host layer and/or the layer above. The addition of cementation to the frictional strength overlying layers should dramatically diminish the impact of soft zones on shallow foundations.

7.6. Hypothetical Cases

7.6.1. Introduction – Field case and model

In this section we utilize the soft zone formation module (developed and tested in Section 2), to conduct a comprehensive study (parallel to Section 5) of a hypothetical shallow foundation system suggested by the project Leadership at SRS, using the calibrated SRS subsurface model (Section 4). Several soft zone topologies and formation histories are simulated to explore the impact of dissolution features on bearing capacity and settlement.

The plane-strain numerical simulation is performed using plane-strain, eight-node biquadratic reduced integration elements. The model geometry is: 200m high and 300m wide (i.e., due to symmetry, the effective width is 600m). The subsurface consists of five distinct strata. All strata are modeled using the elastic perfectly plastic Drucker-Prager model. Material properties are tabulated in Figure 7-65. No cohesion and zero dilation are assumed for all layers to define a conservative condition for the subsurface.

The very long structure is 120m wide (plane strain condition - due to symmetry, a 60m wide footing is shown on Figure 7-66 – Figure 7-68, and will apply a load q=380 kPa. A surcharge load q_0=20kPa is added everywhere on the free surface to reflect a nominal burial depth. The mat and structural stiffness have a secondary effect (refer to results in Section 5); hence, the mat is not explicitly modeled as a structural element, but as a rough and perfectly rigid footing. The numerical methodology is the same as the one summarized in the previous section.

Parameter	Source	Upland Unit	Tobacco Road	Dry Branch	Santee	Warley Hill
Depth [m]		0 - 8	8 -13	13-40	40-48	48-200
Effective unit weight γ [kN/m^3]		20	10	10	10	10
Shear velocity V_s [m/s]	*Shannon and Wilson (2007)*	350	300	300	250	500
Small-strain Poisson's ratio υ	Assumed	0.15	0.15	0.15	0.15	0.15
Young's modulus E_{max} [MPa]	*from Vs*	*574*	*422*	*422*	*293*	*1173*
Modulus degradation factor Π	*back-calculated*	*6.9*	*2.7*	*2.5*	*2.2*	*1.0*
Effective modulus E [MPa]	from back-analysis	*84*	*156*	*170*	*130*	*1165*
Drained Poisson's ratio υ	Assumed	0.2	0.2	0.2	0.2	0.2
Friction ϕ [^{o}]	*Shannon and Wilson (2007)*	37	35	34	24	43
MCC strength M (for AC)	*from ϕ*	1.51	1.42	1.38	0.94	1.77
Cohesion MC	*Shannon and Wilson (2007)*	0	0	0	0	0
Dilation Ψ [^{o}]	Assumed	0	0	0	0	0
Earth pressure k_0	Assumed	1.0	1.0	1.0	1.0	1.0

Figure 7-65. Selected material properties

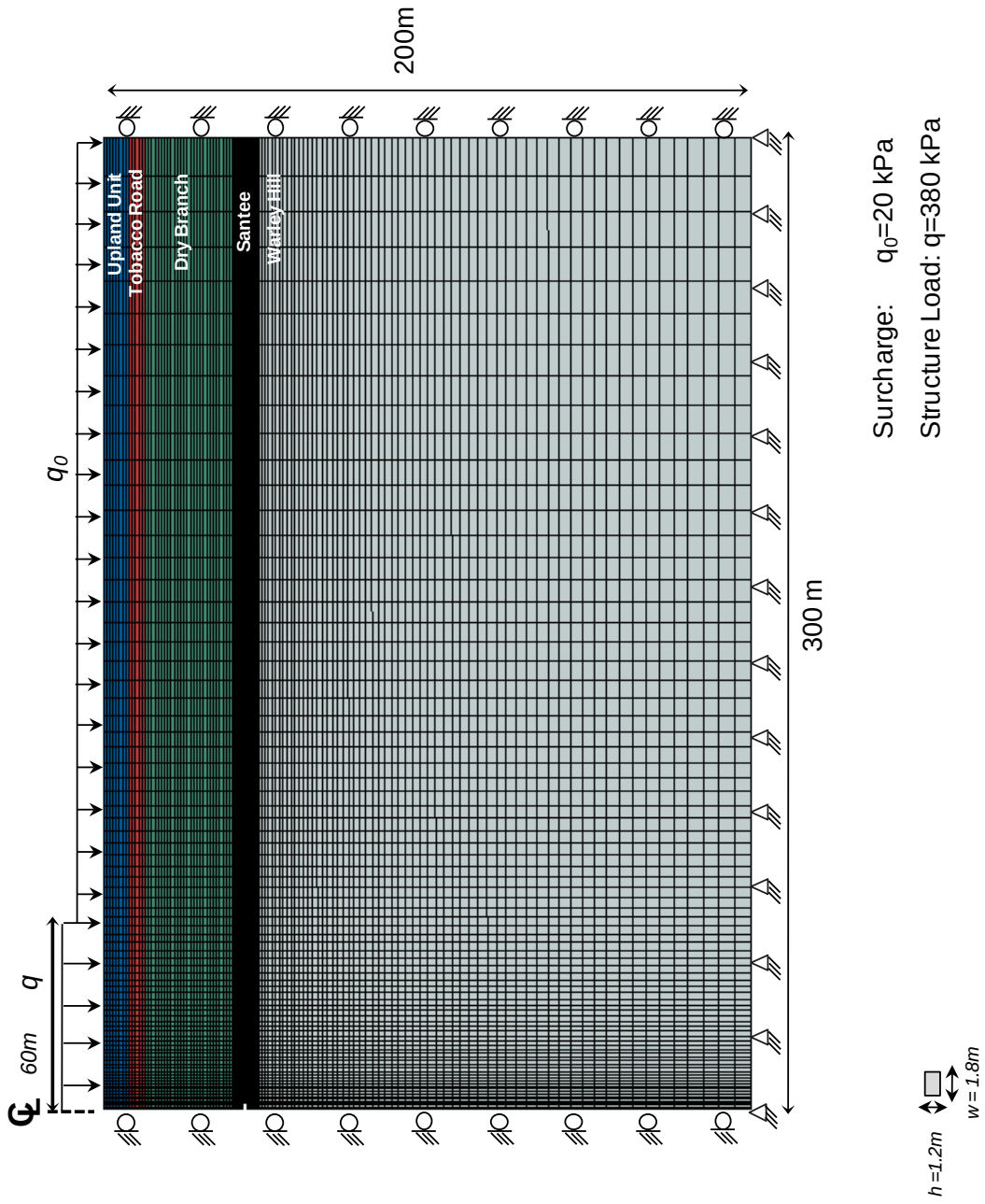

Figure 7-66. Geometry - Boundary conditions (Case 1)

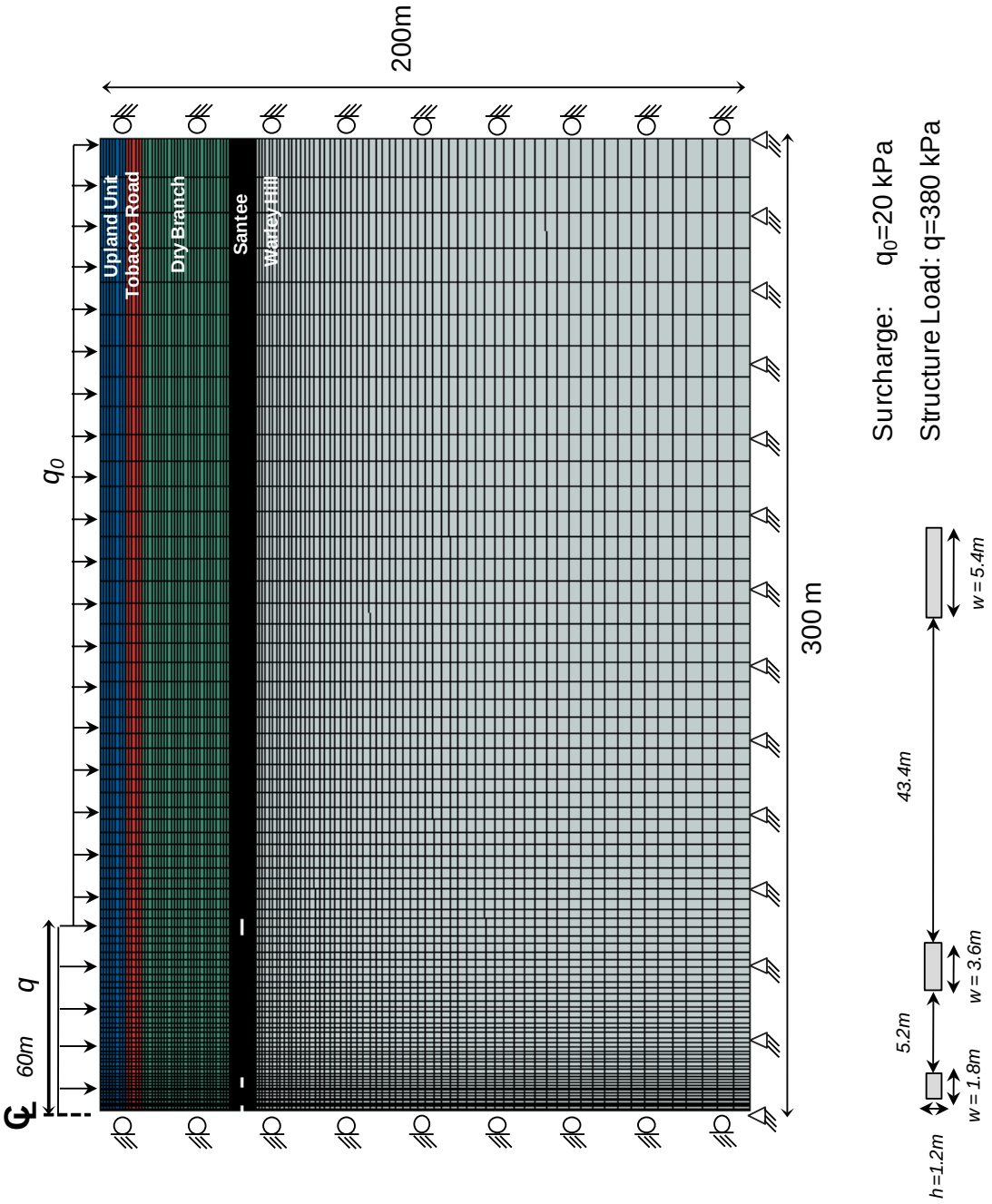

Figure 7-67. Geometry - Boundary conditions (Case 2)

218

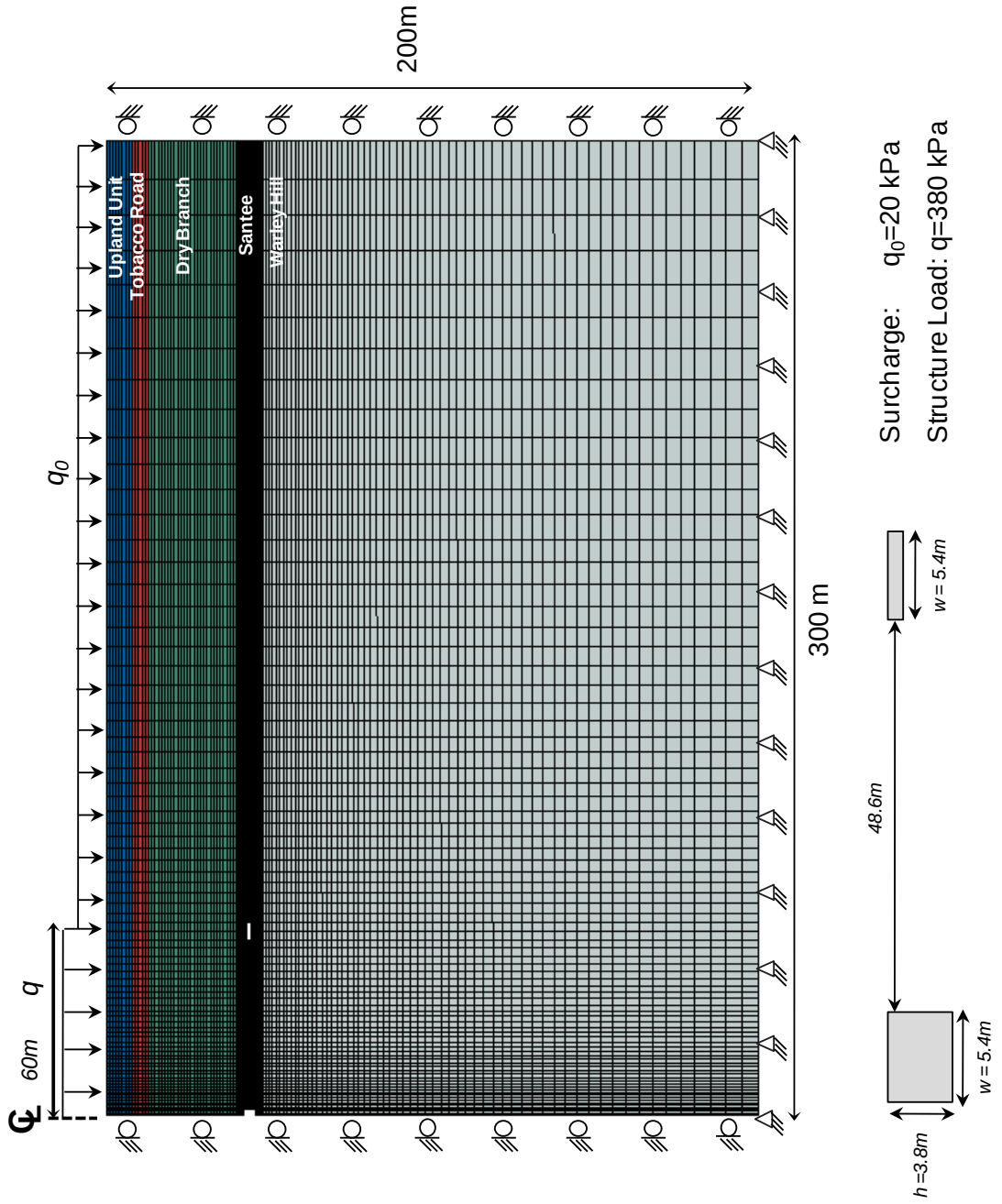

Figure 7-68. Geometry - Boundary conditions (Case 3)

7.6.2. Parametric study – Results

Model Calibration. The calibration procedure is revisited to reduce the modulus of each layer as a function of the strain mobilized in the layer (Figure 7-55 and Figure 7-56). The subsurface strains converge with subsequent iterations (Figure 7-69). Final modulus reduction values computed from the hypothetical cases show the range from a factor of Π=7 in the shallowest layers (highest strains) to almost no reduction at depths z > 48 m. The vertical displacement is plotted in Figure 7-70.

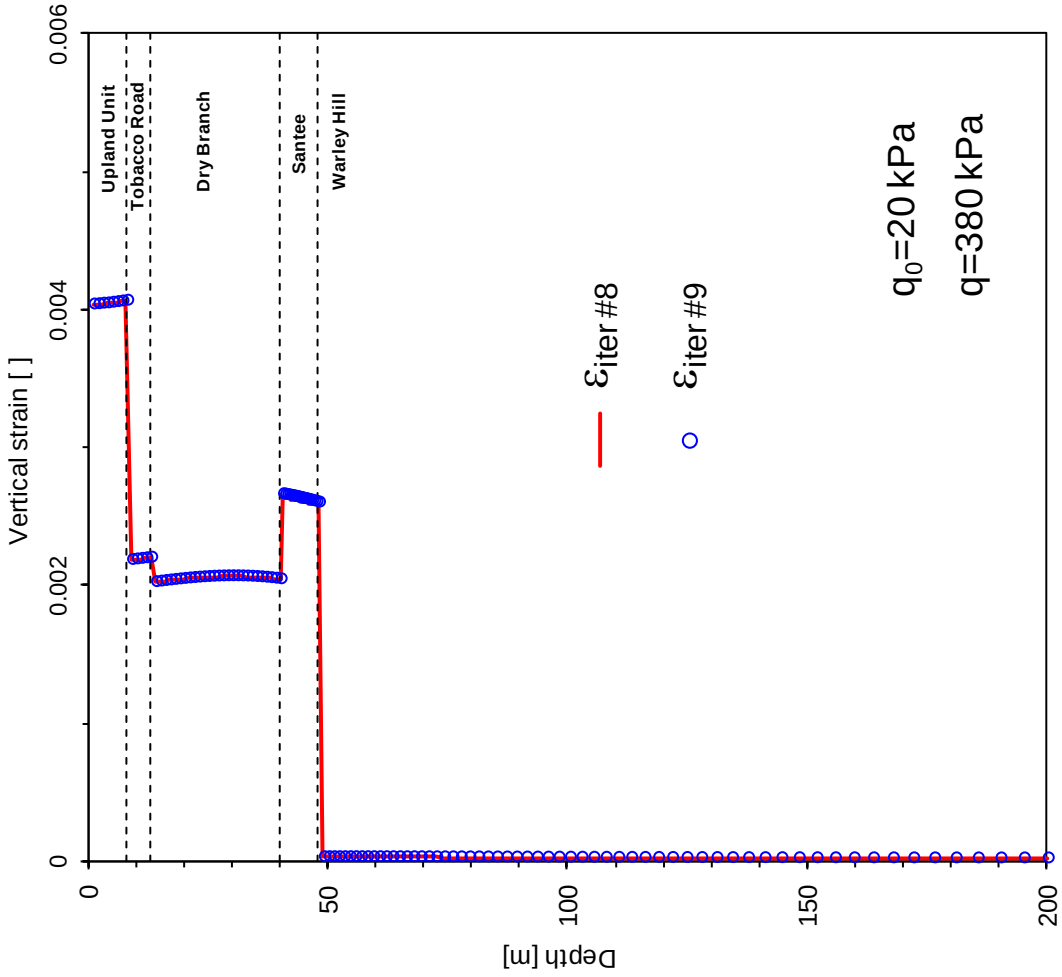

Figure 7-69. Convergence: $\varepsilon_{iter\ i}$ vs. $\varepsilon_{iter\ i+1}$ (No Soft zone)

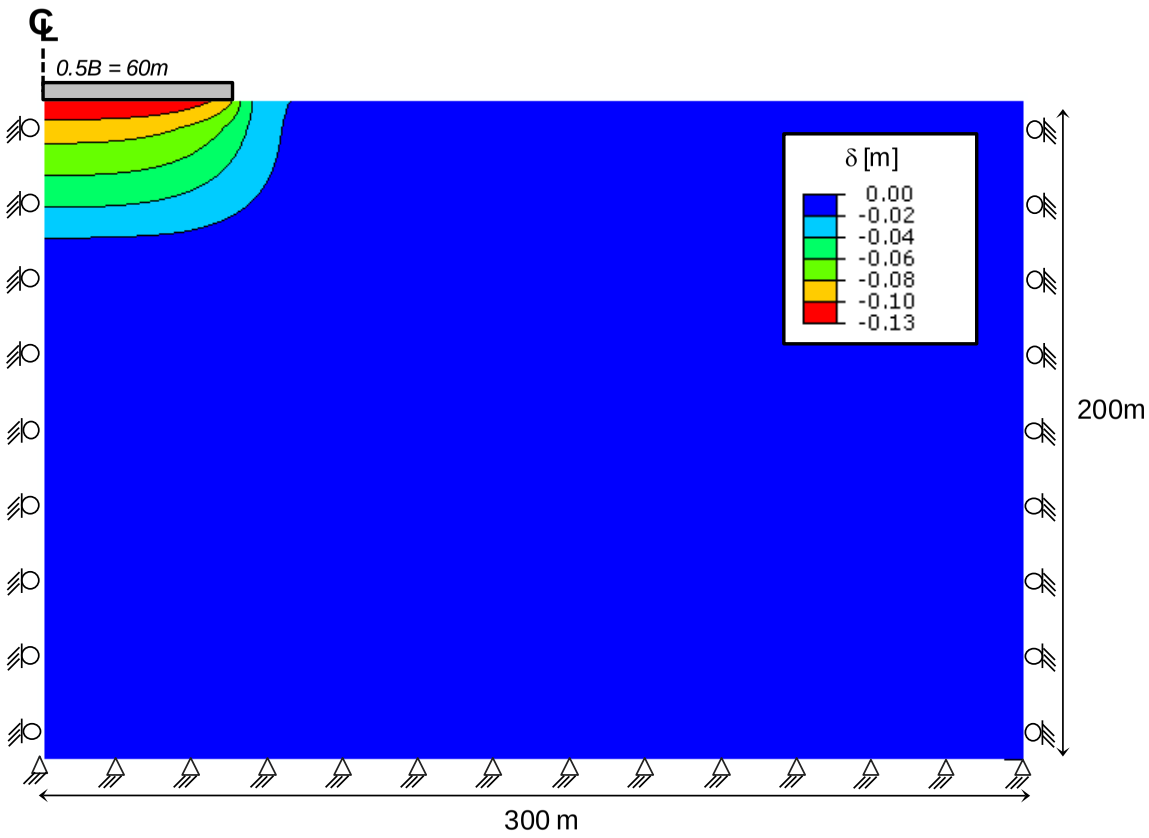

Figure 7-70. Displacement field - Building load (No soft zone) applied in load-controlled mode (flexible footing)

Load at yield. Three sets of subsurface cavities are modeled; these cases are inspired on similar conditions encountered at the Vogtle excavation nearby (Figure 7-71). Different levels of internal stress reduction ISR capture different degrees of dissolution. Following

simulations in previous Sections, the two formation histories considered in these simulations include cavities-before-loading and loading-before-stress relaxation.

Results in (Figure 7-71) show yield i.e., a break in the load-deformation curve during loading. The yield load decreases as the internal stress in cavities is reduced to emulate dissolution and soft zone formation. The yield load does not necessarily mean global bearing capacity failure in these hypothetical cases (the mat foundation is very large compared to the size of soft zone - B/w<120/5.4). The structural load q=380 kPa -shown on the figure- is relatively small in all cases. The yield load is normalized by the bearing capacity in the medium without cavities and plotted in Figure 7-72; the severity of Case 3 is readily seen.

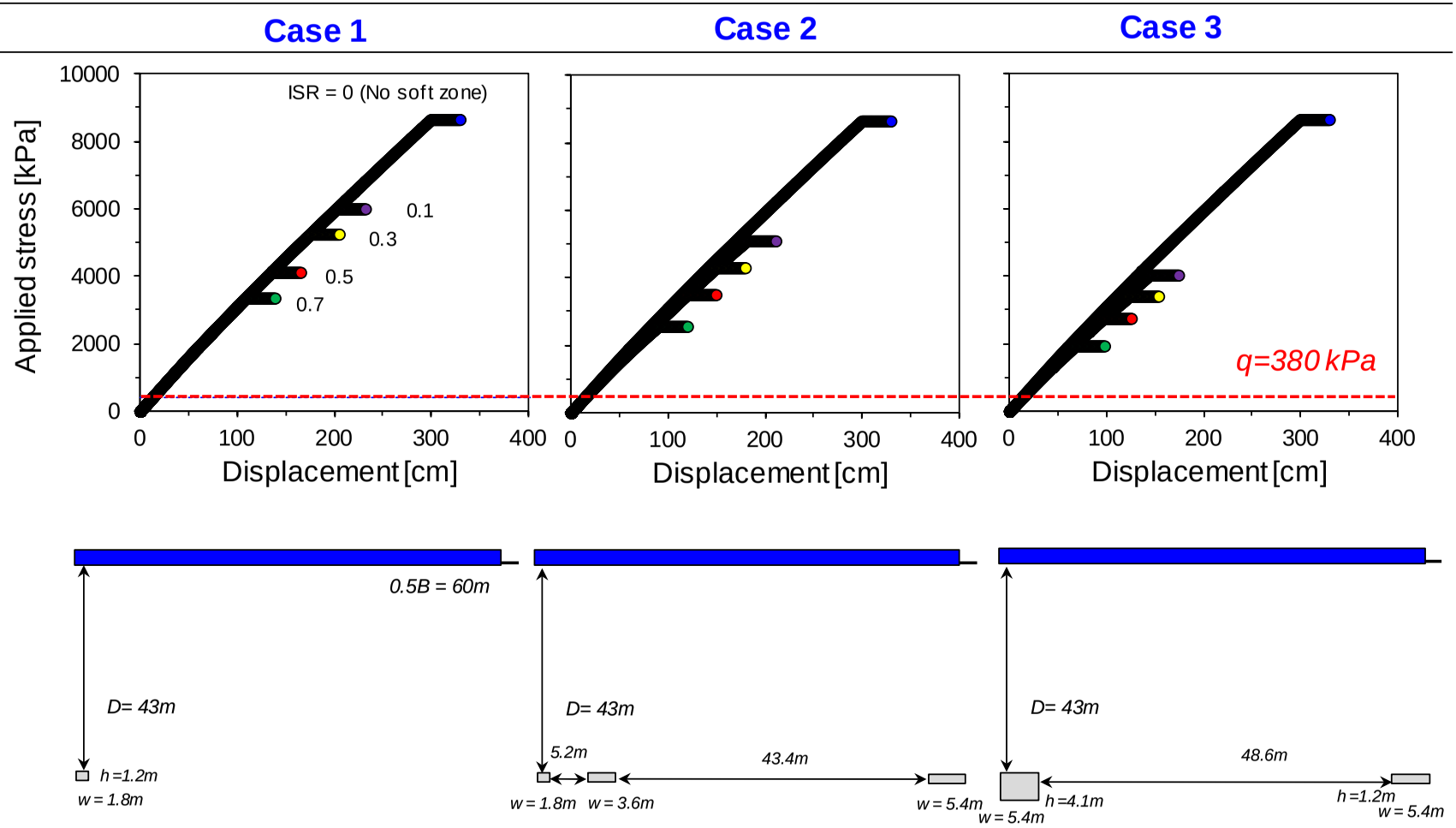

Figure 7-71. Load –Settlement

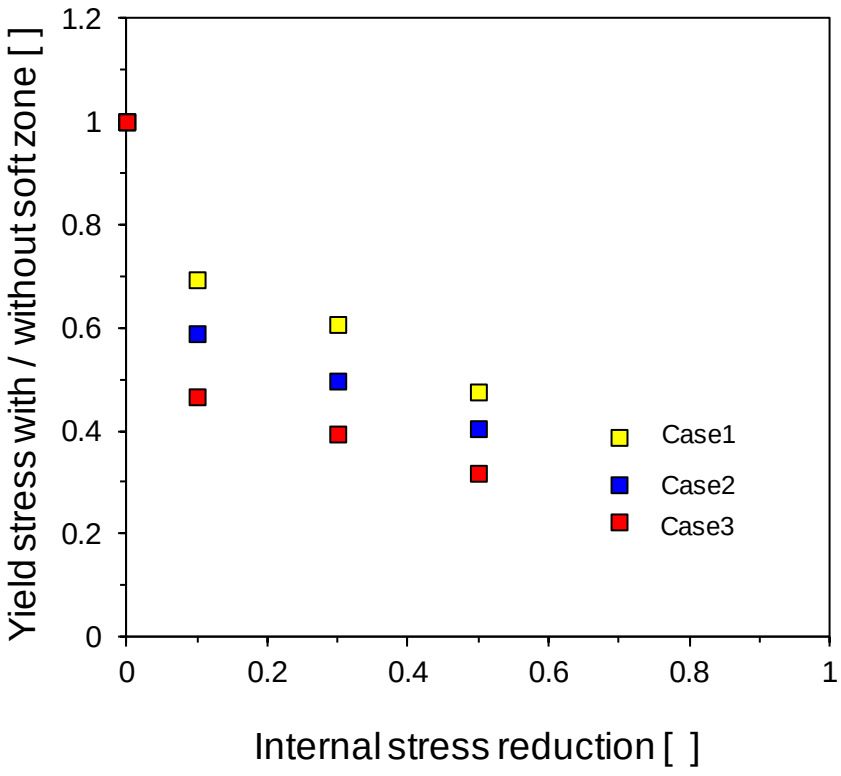

Figure 7-72. Soft zones: Normalized yield stress

Settlements. The stiffness reduction technique developed in Section 4 is applied to estimate settlements for these hypothetical cases, and to estimate additional settlements due to soft zone formation and seismic action. Simulations are run for stress relaxation-before-footing and footing-before-stress relaxation. Furthermore, footing load is imposed at different degrees of internal stress reduction to reflect different degrees of dissolution. A total of 24 cases are summarized in Figure 7-73. All cases include a final stage when quasi-static horizontal load is added to simulate seismic action (a_h=0.1g – refer to discussion and justification in previous section). Results resemble those obtained in the previous section for the case history. Larger settlements reflect the larger foundation size and higher load (Figure 7-73.). It can be observed that:

- The structure-induced settlement is the largest component [OB or AC paths]. In the absence of cavities, the structural load produces a settlement of about 12 cm (B points)
- The formation of cavities or soft zones may increase settlements by as much as 20 % in the very severe Case 3 [OA or BC paths]. The validity of this observation is limited to hypothetical geometries.
- Soft zone formation before the structure [OACD paths] produces slightly larger settlements than soft zone formation after the structural load [OBCD paths], in agreement with conclusions in previous sections. However, the differences in formation history can be disregarded for all practical purposes at the hypothetical cases.
- Seismic loading the structure (a_h=0.1g) sitting on top of the sediment with cavities (either formation history) will cause negligible additional settlement (<5% of settlement caused by the static load) and a minor reduction of stiffness. Furthermore, for a seismic induced settlement of 1cm, the average subsurface strain underneath such a large mat would be lower than 10^{-4} and no major reduction of stiffness or strength properties would be expected.

7.6.3. Conclusions

A very large structure and soft zones/cavities of several size and numbers were simulated in this section. The presence of cavities lowers the yield load (yet, not necessarily the global bearing capacity for this geometry). The yield load is sensitive to the cavities/soft zones, yet, it is significantly higher than the target structural load in most cases.

No cohesion was added to any of the layers. However, open pipes and tensile fractures observed at the Vogtle excavation suggest cementation in the host layer and/or the layer above. Adding cohesion to the overlying layer will dramatically diminish the impact of soft zones on shallow foundations.

Once again, these results suggest that: differences in formation history can be disregarded for all practical purposes at the hypothetical cases, and that more complex dynamic analyses that take into consideration inertial effects may not be necessary from a foundation response point of view.

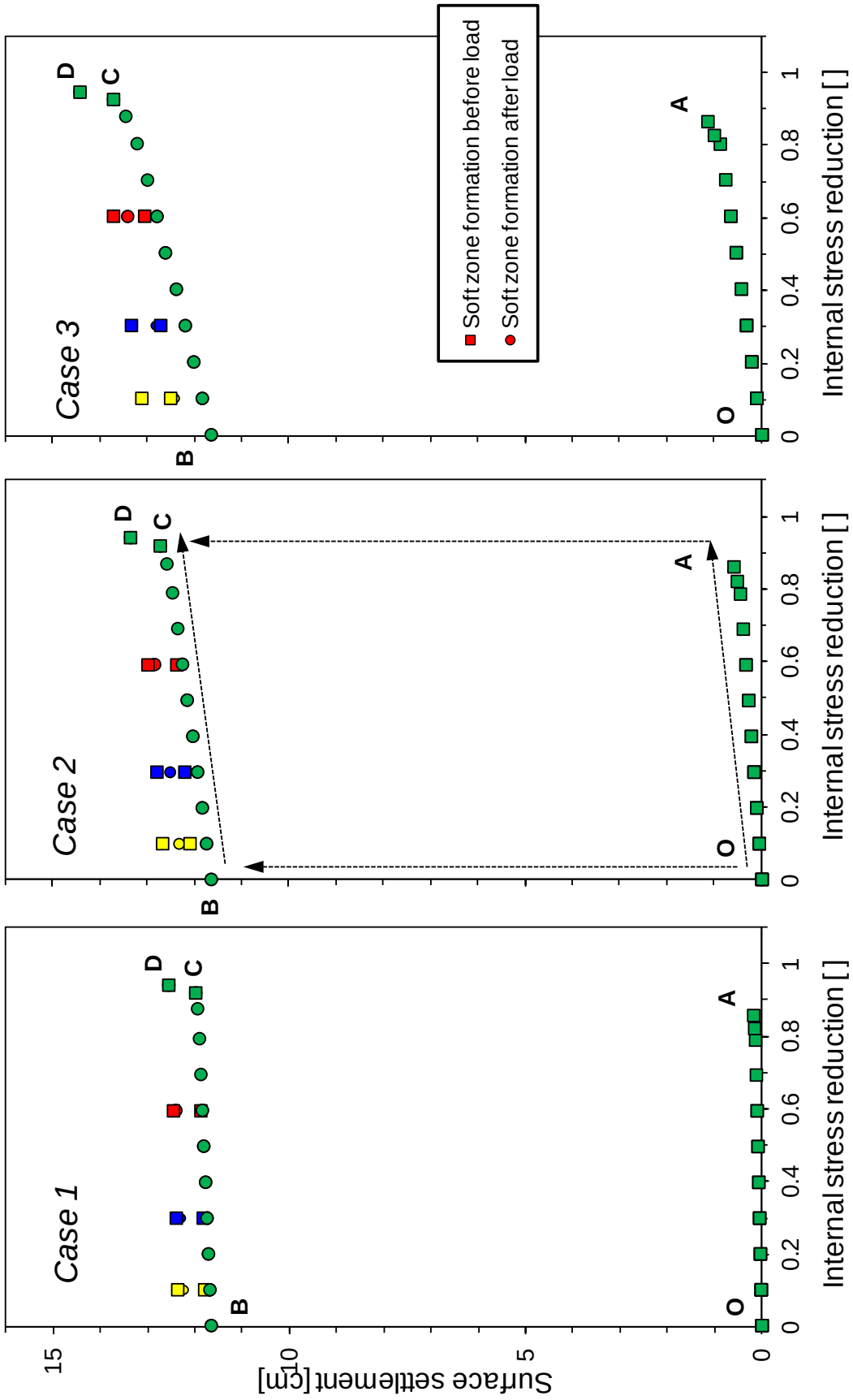

Figure 7-73. Settlement: Footing load, soft zone formation, and seismic load (z_0 = 43m)

7.7. CONCLUSIONS

This part of the project focused on macroscale analyses within the framework of finite element simulations. The salient conclusions from this study follow.

Constitutive model

- Given the complexity of the stratigraphy and the load-dissolution history, a simple model was adopted to capture a wide range of possible stress paths and conditions.
- Elastic, elasto-plastic with Drucker-Prager yield criterion, and Modified Cam Clay models were used throughout this study. These selected models require a small number of physically meaningful parameters that can be reliably estimated from characterization studies.

Dissolution cavities

- Subsurface volume loss and soft zone formation can be numerically simulated by gradually reducing the anisotropic insitu state of stress in the predefined soft zone. The developed module is validated with analytical solutions. Careful mesh refinement is required to avoid numerical effects.

Soft zone-footing interaction - Settlements

- Smaller and deeper cavities, higher friction angles and higher preconsolidation ratio lead to lower settlements at all depths.
- Surface and subsurface settlements are quite regular and can be adequately fitted with a two parameter Gaussian function in the absence of pronounced shear distortions and localizations.
- The linear superposition of surface settlements caused by neighboring cavities overestimates deformations.

- Shallow cavities interact with the footing, lower the bearing capacity, increase settlements, and promote local-punching failures. When the footing size is much wider than the soft zone size B>>w, failure remains global (and embodies the soft zone); global shear failures also develop when B<<w and z_0>w. Hence, the worst condition corresponds to B~w when punching shear failures prevail.
- The critical depth that separates shallow from deep cavities depends on soft zone depth to footing width z_0/B, anomaly size B/w, dilatancy ψ, and the internal stress reduction ISR in the soft zone. As a guiding rule, cavities deeper than z_0~3B-to-4B would be deep soft zones when B/w~1 (the most critical case).

Material Parameters

- Preliminary analyses conducted with compressibility parameters gathered in consolidation tests overpredicted settlements, possibly due to sampling effects and procedural difficulties (core-ring gap, cap seating effects magnified by thin specimens). Thus, the selection of stiffness and compressibility at the SRS site must be based on field stiffness measurements. Laboratory-based parameters may overestimate settlements by a factor of 10 or higher.
- The back analysis of measured settlement for the estimation of material parameters faces inherent difficulties with convergence and non-uniqueness of the solution. These are exacerbated by the stress-dependent, nonlinear soil behavior, spatial and temporal variability, and typically limited information available in most field cases.
- The approach developed and implemented in this study involved a simple secant formulation using a robust elasto-plastic numerical model and was anchored on credible field measured parameters.

Simplified surface settlement estimation for large mats (no soft zone)

- Determine the shear wave velocity profile with depth (conduct measurements after rainy season to avoid unnecessarily high suction-controlled values above the water table). Compute the small strain constrained modulus M_{max} from Vs (use a small-strain value for Poisson's $\nu \approx 0.15$).

- Estimate the load-induced vertical stresses on different layers
- Estimate vertical strains in each layer
- Reduce the modulus using the computed strains (hyperbolic formulation)
- Recalculate strains. Repeat until convergence
- Integrate strains to determine surface settlements

Predictions specific to SRS

- The SRS subsurface model was calibrated through back-analysis of settlement data gathered during the construction of the Defense Waste Processing Facility at SRS. The initial stiffness adopted for layers was based on small-strain geophysical field measurements.
- Results for this facility at SRS show that load-induced settlements overwhelm settlements induced by soft zone formation (before or after) and seismic events.
- The formation of cavities or soft zones either before or after the application of the building load may cause an increase in settlement less than 10-20 % (for the simulated conditions, which disregard cementation and dilation). Thus, the differences in formation history can be disregarded for all practical purposes, within the limitations of the hypothetical cases analyzed in this study.
- Seismic loading the structure (a_h=0.1g) sitting on top of the sediment with cavities (either formation history) will cause negligible additional settlement (<5% of settlement caused by the static load). Furthermore, anticipated seismic induced strains are low and no major reduction of stiffness or strength properties would be expected. On the bases of these results, more complex seismic models that take into consideration inertial effects are not necessary at this point and for the purposes of this analysis.
- No cohesion was considered in any of the layers throughout this study. Stable open cavities and tensile fractures observed at the Vogtle excavation suggest cementation. Adding cohesion to overlying layers would dramatically diminish the impact of soft zones on shallow foundations.

8. Summary of Findings

A number of unusual features are found in the old Eocene sediments at SRS that are due in part to a complex geo-bio-hydro-chemical history for the Santee Formation that occurs at depths of around 40 ± m below grade. Calcareous components of the Santee have resulted in partial to full dissolution as well as partial to complete encapsulation of voids-soft zones, resulting in karstic-like manifestations in localized yet consistent areas at SRS. In a number of instances, these voids-caves-soft zones have collapsed and altered the stress regime in the overlying soil column, thus affecting the stress history profile. One consequence appears due to the rather high lateral (and vertical) variability in the yield stress, or preconsolidation stress, as measured by laboratory consolidation tests and/or inferred from in-situ tests (CPT, DMT, SPT). Additional uncertainties and masking of interpreted results in the soil column may be due to: (1) a high degree of weathering of the old Eocene sandy sediments that has caused a high clay content (apparent gap-graded particle size distribution), high specific surface, and high plasticity of the fines content; and (2) presence of carbonates and calcareous constituency that results in particle breakage and/or crushing, thus affecting measured penetration resistances and readings. As it now stands, a complete understanding of the soil column, stress state, and engineering properties of the geologic strata at SRS is not yet fully appreciated, therefore uncertainties will remain for future geotechnical investigations.

In regard to the predictions of settlement:

- The formation of cavities or soft zones either before or after the application of the building load may cause an increase in settlement less than 10-20 % (for the simulated conditions, which disregard cementation and dilation).

- On the bases of these results, more complex seismic models that take into consideration inertial effects are not necessary at this point and for the purposes of this analysis.
- Adding cohesion to overlying layers would dramatically diminish the impact of soft zones on shallow foundations.
- The linear superposition of surface settlements caused by neighboring cavities overestimates deformations.

In new studies at SRS, some of the following field testing programs might be considered to help clarify the stress regime and geostatic stress state:

a. Pressuremeter tests (PMT), particularly self-boring type pressuremeter tests (SBPMT), offer a direct means to evaluate the in-situ K_0 stress condition. A series of pressuremeter tests at locations both inside and outside of potentially-identified collapsed soil columns would be necessary to quantify K_0 profiles within these regions. The PMT also provides an independent opportunity to assess the ground stiffness (e.g., E' or G') and shear strength characteristics of the soils (ϕ' and/or s_u).

b. Hydro-fracture (HF) is another independent means that can be useful in assessing K_0 states in soils and in rocks. Similar to above, HF testing would need to be performed both within and outside of collapsed soil column regions.

c. Matched series of HH and VH shear wave velocities have been shown to assist in the assessment of stress history (e.g., OCR, σ_p') as well as lateral stress state (K_0). The VH shear wave is obtained from standard downhole tests (DHT) in boreholes or by direct push technologies (SCPT, SDMT). The HH shear wave is procured through crosshole testing arrays

using a special horizontal source such as rotary hammer, vane source, or sparker (Ku and Mayne, 2013a, 2013b, 2013c).

d. The use of electromagnetic geophysics and/or mechanical wave geophysics may be able to help discern the caprock and/or voids-soft zones that are buried at SRS locations (Wightman et al. 2003). Continual improvements in the resolution and delineation of surface features and anomalies are being made with these technologies. Therefore, the utilization of refraction surveys, surface and/or subsurface resistivity measurements, and/or electromagnetic conductivity arrays may prove to be a viable means to track the unusual and difficult karstic features in and above the Santee Formation. It would appear some degree of success has already been achieved at SRS with these methods albeit the focus of those studies was towards contaminant plume migration (Cameron-González, et al. 2010).

e. Results of additional new testing by pressuremeters (PMT, SBPMT) and/or geophysical paired shear wave velocities (VsHH and VsVH) can be performed at several locations at SRS to either confirm or refute that low Ko condtions (even near KA active) associated with collapsed structure, or alternatively, that high Ko (indicative of overconsolidated soils) are present in the upper strata. Once these tests have been performed, analyzed, and reviewed, a workshop may be planned to discuss the impacts and consequences on future geotechnical programs at SRS, so that a reasonable consensus can be reached.

9. Recommendations for Subsurface Detection and Characterization of Soft Zones

Exploration methods should always be selected based on the objectives of the characterization program, anticipated subsurface conditions, site conditions and data quality/resolution requirements. As such, typical geotechnical programs at the SRS evolved from primarily boring programs to cone penetrometer sounding programs with focused, secondary boring programs. This methodology is still valid while applying some lessons from the Vogtle excavations summarized in Section 3.0 of this report.

The CPT provides an excellent tool for detecting soft zones and developing the site stratigraphy and stiffness profile. Based on the initial site screening with CPT soundings, an appropriate exploration plan should also include strategically located borings for obtaining Standard Penetration Test (SPT) N-values and undisturbed samples. This methodology enables a strong complement between the different techniques. Surface and subsurface geophysical methods should also be considered based on the program requirements and considerations listed above.

Specific exploration program considerations and recommendations:

1. In areas where early refusal of CPT soundings occurs, consideration should be made for the potential existence of cemented layers arching over softer materials beneath. These conditions are not likely a static loading issue but the thickness of the arch and underlying materials may warrant definition. Further, this should also be considered in any site response analysis, as these conditions can result in amplification of ground motions if these layers are laterally continuous beneath the structure footprint, greater

than about 5 feet thick, and have a high shear wave velocity. CPT soundings should be spaced at an interval of 30 m on a grid.

The objective should be to characterize the 3-dimensional geometry of the refusal interval as well as the shear wave velocity. The first step should be to determine the thickness. If the thickness is less than about 5 feet, it may not be a concern for the site response. Penetrating the refusal interval will also provide data for the bottom half of the Santee formation.

1a. If it is required to define the thickness of these cemented zones, coring is a preferred method to retrieve the most coherent samples for evaluation. SPT borings provide relative strength values but tend to break up the material or simply refuse requiring the interval simply be drilled without sampling.

1b. If it is required to define the lateral extent of the cemented zones, a combination of soundings, borings and shallow seismic reflection/refraction may provide an efficient methodology, however existing interferences both above and below ground should be evaluated.

2. Undisturbed sampling should also include the CPT sampler to retrieve soft zone materials. Although the diameter of these samples is too small for strength and consolidation testing, this technique is very efficient and provides better recovery rates than standard thin walled tube sampling and provides ample material for index testing including unit weight.

3. A core boring would help define the site stratigraphy and potentially identify if the soft zone conditions are actually genetically similar to the Utley Limestone as noted in

the Vogtle excavation. Previous investigations in several locations throughout the SRS have successfully cored the Santee utilizing a HQ Triple Barrel system.

4. A surface geophysical technique such as seismic refraction may be useful to delineate the lateral extent of cemented layers in the Santee. Detection of low-impedance anomalies in these conditions is exceedingly difficult because they are inherently hidden, due to diffraction healing in wave-based techniques. However, the zones may be detectable if it is possible to change the nature of the anomaly to allow detection through the use of a method such as injection of a conductivity tracer. Alternatively, it may be possible to detect the impact of soft zones on the overlying soil column, even if it is not possible to detect the soft zones per se.

Seismic methods will not easily detect soft zones (cross hole tomography may work, but only if boreholes are ~3B apart max, where B is the size of the soft zone), and while high resolution imaging with reflection and refraction will not show the soft zones, it may be possible to use the method to detect the impact of soft zones on shallow layers. Electrical detection methods may be employed with success if the soft zones are high conductivity zones, such as in the case of filled cavities with high clay content. The method may be successful if it is possible to find upstream depressions (possible inlet points) and pump brine into the soft zone to enhance the contrast with the surrounding medium.

5. Also for consideration would be utilization of the newer hydraulic continuous-push samplers (Geoprobe, Powerprobe, Geostar) that obtain small-diameter continuous samples for inspection and index testing, as well as sonic drilling methods which obtain larger diameter continuous cores of soil and rock (Boartlongyear, Terrasonic, Sonic-

Drill). Both HCPS and Sonic drilling do not use water which tends to wash away important soil particles. In addition, both HCPS and Sonic can penetrate thru hard cemented zones that may be encountered in the soil profile.

According to summaries provided by Dr. Frank Syms, carbonates are much less prevalent in the northwestern parts of SRS and increase in the southeasternmost portions of SRS. Of interest then would be a review study of CPTs in these areas in the northwestern parts of SRS (e.g., A-area; M-area) to confirm the lack of Santee soft zones/voids and/or quantification of these features as well as refusal depths. In addition, new series of CPTs could be performed in these areas to investigate further the lack of carbonates and therefore better define the localized region and extent of carbonates and calcareous sediments.

As discussed previously, a first order potential existence of soft zones for existing facilities or areas of interest can generally be determined from geographic location. A second order prediction can be determined from regional subsurface maps and cross-sections (Aadland, Harris, Syms). It is recommended that a third order prediction could be developed by additional mapping using the 1950's USCOE geomorphic maps, existing SRS LiDAR coverage, Vogtle data and existing regional subsurface boring and CPT sounding measurements.

10. REFERENCES

Aadland, R.K., Cumbest, R.J., Gelinas, R.L., Parker, W., Syms, F.H., Rothammer, C. and Whaley, K. (1999). Significance of Soft Zone Sediments at the Savannah River Site (U). *Document WSRC-TR-99-4083, Rev. 0*, Westinghouse Savannah River Co., Aiken, SC submitted to US Dept. of Energy: 135 p.

Ahmed, M., and Iskander, M. (2011). "Analysis of Tunneling-Induced Ground Movements Using Transparent Soil Models." Journal of Geotechnical And Geoenvironmental Engineering, 137(5), 525-535.

Alonso, E. E., Pinyol, N. M., and Puzrin, A. M. (2010). Geomechanics of failures: Advanced topics, Springer.

Andrus, R.D., Zhang, J., Ellis, B.S. and Juang, C-H. 2003. Guide for estimating the dynamic properties of South Carolina for ground response analysis. *FHWA Report No. SC-03-07*, South Carolina Dept. of Transportation, Columbia.

Andrus, R.D., Mohanan, N.P., Piratheepan, P., Ellis, B.S. and Holzer, T.L. 2007. Predicting shear wave velocity from cone penetration resistance. *Proc. 4th International Conferences on Earthquake Geotechnical Engineering*, Thessaloniki, Greece: Paper No. 1454.

Atkinson, J. H., Brown, E. T., and Potts, D. M. (1975). "Collapse of Shallow Unlined Tunnels in Dense Sand." Tunnels and Tunnelling, 7(3), 81-87.

Atkinson, J. H., and Potts, D. M. (1977a). "Subsidence Above Shallow Tunnels In Soft Ground." Journal of the Geotechnical Engineering Division, 103(GT4), 307-325.

Atkinson, J. H., and Potts, D. M. (1977b). "Stability of a shallow circular tunnel in cohesionless soil." Geotechnique, 203-215.

Azam, G., Hsieh, C. W., and Wang, M. C. (1991). "Performance of Strip Footing on Stratified Soil Deposit with Void." Journal of Geotechnical Engineering, 117(5), 753-772.

Badie, A., and Wang, M. C. (1984). "Stability of Spread Footing Above Void in Clay." Journal of Geotechnical Engineering, 110(11), 1591-1605.

Baus, R. L., and Wang, M. C. (1983). "Bearing Capacity of Strip Footing above Void." Journal of Geotechnical Engineering, 109(1), 1-14.

Bagwell, L. (2008). *Geophysical Data*. DOE-SRS-Georgia Tech Soft Zone Review Meeting, Savannah River Nuclear Solutions, LLC, A Fluor Daniel Partnership, 13 pages.

Becker, D.B., Crooks, J.H.A., Been, K., and Jefferies, M.G. (1987). Work as a criterion for determining in situ and yield stresses in clays. *Canadian Geotechnical Journal* 24 (4): 549–564.

Bobet, A. (2001). "Analytical Solutions for Shallow Tunnels in Saturated Ground." Journal of Engineering Mechanics, 127(12), 1258-1266.

Boone, S.J. (2010). A critical reappraisal of preconsolidation pressure interpretations using the oedometer test. *Canadian Geotechnical Journal* 47 (3): 281-296.

Borja, R. I., and Lee, S. R. (1990). "Cam-Clay plasticity, Part 1: Implicit integration of elasto-plastic constitutive relations." Computer Methods in Applied Mechanics and Engineering, 78(1), 49-72.

Brown, L.T., Boore, D.M., and Stokoe, K.H. (2002). Comparison of shear wave slowness profiles at 10 strong-motion sites from noninvasive SASW measurements and measurements made in boreholes. *Bulletin of the Seismological Society of America*, 92(8): 3116-3133.

Buechel, G.J. (2007). *Geotechnical Investigation Phase II, Salt Waste Processing Facility*. Parsons Subcontract 744910-30030 Report prepared by Shannon & Wilson, Seattle: 1548 pages.

Burd, H. J., Houlsby, G. T., Chow, L., Augarde, C. E., and Liu, G. (1994). "Analysis of settlement damage to masonry structures." Proceeding of the 3rd European Conference on Numerical Methods in Geotechnical Engineering, 203-208.

Burns and Roe Enterprises Inc. (2001). *Final geotechnical investigation report – APT Volume I.* U.S. Department of Energy, Westinghouse Savannah River, SC: 333p.

Calvello, M., and Finno, R. J. (2004). "Selecting parameters to optimize in model calibration by inverse analysis." Computers and Geotechnics, 31(5), 410-424.

Cameron-González, A.E., Knapp, C.C., Waddell, M.G., Addison, A.D., and Shafer, J.M. (2010). Structural and stratigraphic control on the migration of a contaminant plume at the P Reactor area, Savannah River site, South Carolina. *Environmental Geosciences* Vol. 17 (2): 77-98.

Camp, W.M., (2004). Site characterization and subsurface conditions for the Cooper River Bridge. *Proc. Geo-Trans Conference*, Geo-Institute of ASCE, Los Angeles, Vol. 1: 347-360.

Casagrande, A. (1936). The determination of the preconsolidation load and its practical significance. *Proceedings of the First International Conference on Soil Mechanics and Foundation Engineering*, Harvard Printing Office, Cambridge, Mass. Vol. 3: 60–64.

Cooke, M.F., Lancaster, W.A., and Depree, P.J. (2007). *Geotechnical Data Report – Attachment D – Geophysical Test Data. Vogtle Units 3 and 4 COL Project*. MACTEC Report 6141-06-0286 to Georgia Power Company, Burke County, GA: 329 pages.

Celestino, T. B., Gomes, R. A. M. P., and Bortolucci, A. A. (2000). "Errors in ground distortions due to settlement trough adjustment." Tunnelling and Underground Space Technology, 15(1), 97-100.

Chen, S. L., Gui, M. W., and Yang, M. C. (2012). "Applicability of the principle of superposition in estimating ground surface settlement of twin- and quadruple-tube tunnels." Tunnelling and Underground Space Technology, 28(0), 135-149.

Chen, W. F. (1975). Limit analysis and soil plasticity, Elsevier, Amsterdam.

Cho, G. C., Dodds, J., and Santamarina, J. C. (2006). "Particle Shape Effects on Packing Density, Stiffness, and Strength: Natural and Crushed Sands." Journal of Geotechnical and Geoenvironmental Engineering, 132(5), 591-602.

Cividini, A., Jurina, L., and Gioda, G. (1981). "Some aspects of 'characterization' problems in geomechanics." International Journal of Rock Mechanics and Mining Sciences & Geomechanics Abstracts, 18(6), 487-503.

Clough, W., and Schmidt, B. (1981). Design and performance of excavations and tunnels in soft clay, Elsevier.

Cording, E. J. (1991). "Control of ground movements around tunnels in soil." Proceedings of the 9th Pan American Conference on Soil Mechanics and Foundation Engineering, 2195-2244.

Crapps, D. K. (2010). "The Effects of Cavities upon Foundation Design & Construction." Art of Foundation Engineering Practice, 206-223.

Cumbest, R.J., Parra, J.O., Zook, B.J., Addington, C., and Price, V. (1996). Reverse VSP and crosswell seismic imaging at the Savannah River Site: United States. extended abstract, *Proc. SEG Annual Meeting*, Denver, Society of Society of Exploration Geophysicists: 34 p.

Das, B. (1999). Shallow foundations: Bearing capacity and Settlement, CRC Press LLC.

Day, R. A., and Potts, D. M. (2000). "Discussion: Observations on the computation of the bearing capacity factor Nγ by finite elements." Geotechnique, 301-303.

Drucker, D. C., and Prager, W. (1952). "Soil mechanics and plastic analysis or limit design." Quarterly of Applied Mathematics, 10(2), 157-165.

Duncan, J. M., and Chang, C. Y. (1970). "Non-linear analysis of stress and strain in soils." Journal of the soil mechanics and foundations division, Proceedings of the american society of civil engineers, 96(5).

Ebelhar, R.J., Young, A.G. and Stieben, G.P. (1988). Cone penetrometer and conductor pullout tests in carbonate soils offshore Africa. *Proceedings of the International Conference on Calcareous Sediments*, Perth, 1, 155-163.

Fares, N. F. (1987). "Green's Functions for Plane-layered Elastostatic and Viscoelastic Regions with Application to 3-D Crack Analysis." Ph.D, Massachusetts Institute of Technology.

Fernandez, A. L., and Santamarina, J. C. (2001). "Effect of cementation on the small-strain parameters of sands." Canadian Geotechnical Journal, 38(1), 191-199.

Finno, R., and Calvello, M. (2005). "Supported Excavations: Observational Method and Inverse Modeling." Journal of Geotechnical and Geoenvironmental Engineering, 131(7), 826-836.

Foti, S. (2012). “Combined use of geophysical methods in site characterization,” *Geotechnical and Geophysical Site Characterization 4* (ISC-4, Brazil), Vol. 1, Taylor & Francis Group, London: 43-61.

Franzius, J., and Potts, D. (2005). "Influence of Mesh Geometry on Three-Dimensional Finite-Element Analysis of Tunnel Excavation." International Journal of Geomechanics, 5(3), 256-266.

Frydman, S., and Burd, H. J. (1997). "Numerical Studies of Bearing Capacity Factor Nγ." Journal of Geotechnical and Geoenvironmental Engineering, 123(1), 20-29.

Gioda, G. (1980a). "Indirect identification of the average elastic characteristics of rock masses." International Conference on Structural Foundations on Rock, Sydney, Australia.

Gioda, G., and Locatelli, L. (1999). "Back analysis of the measurements performed during the excavation of a shallow tunnel in sand." International Journal for Numerical and Analytical Methods in Geomechanics, 23(13), 1407-1425.

Gioda, G., and Maier, G. (1980b). "Direct search solution of an inverse problem in elastoplasticity: Identification of cohesion, friction angle and in situ stress by pressure tunnel tests." International Journal for Numerical Methods in Engineering, 15(12), 1823-1848.

Gioda, G., and Sakurai, S. (1987). "Back analysis procedures for the interpretation of field measurements in geomechanics." International Journal for Numerical and Analytical Methods in Geomechanics, 11(6), 555-583.

Greenspan, M. (1944). "Effect of a small hole on the stresses in a uniformly loaded plate." Quarterly Applied Math, 2(1), 60-71.

Griffiths, D. V. (1982). "Computation of bearing capacity factors using finite elements." Geotechnique, 195-202.

Guedes, P. F. M., and Santos Pereira, C. (2000). "The role of the soil k0 value in numerical analysis of shallow tunnels." Proceedings of International Symposium on Geotechnical Aspects of Underground Construction in Soft Ground, Rotterdam, 379-384.

Hashash, Y. M. A., Phillips, C., and Groholski, D. R. (2010). "Recent advances innon-linearsiteresponseanalysis." Fifth international conference on recent advances in geotechnical engineering and soil dynamics, San Diego.

Hjiaj, M., Lyamin, A. V., and Sloan, S. W. (2005). "Numerical limit analysis solutions for the bearing capacity factor Nγ." International Journal of Solids and Structures, 42(5–6), 1681-1704.

Hollowell, W. T., Pilkey, W. D., and Sieveka, E. M. (1988). "System identification of dynamic structures." Finite Elements in Analysis and Design, 4(1), 65-77.

Hsieh, C. W. (1991). "Footing behavior and stability analysis method for strip surface footing above continuous circular void."Ph.D., The Pennsylvania State University, Ann Arbor.

Jacobsz, S. W., Standing, J. R., Mair, R. J., Hagiwara, T., and Sugiyama, T. (2004). "Centrifuge modelling of tunnelling near driven piles." Soils and foundations, 44(1), 49-56.

Jefferies, M. and Been, K. (2006). *Soil Liquefaction – A critical state approach*. Taylor and Francis, New York, NY, pp. 580.

Kavanagh, K. T. (1973). "Experiment versus analysis: computational techniques for the description of static material response." International Journal for Numerical Methods in Engineering, 5, 503-515.

Kirsch, G. (1898). "Die theorie der elastizitat und die bedurfnisse der festigkeitslehre." Zeitschrift des Vereines deutscher Ingenieure, 42(28), 797-807.

Kochanov, W. E. (1999). "Sinkholes in Pennsylvania: Pennsylvania Geological Survey." Educational Series 11, Department of Conservations and Natural resources.

Kondner, R. L. (1963). "Hyperbolic Stress-Strain Response: Cohesive Soils." Journal of the soil mechanics and foundations division, Proceedings of the american society of civil engineers, 89(1).

Ku, T., Mayne, P.W., and Gutierrez, B.J. (2012). Shear wave profiles in Tertiary marine sediments in west central South Carolina. *Geotechnical and Geophysical Site Characterization 4*, Vol. 2 (ISC'4, Recife, Brazil), Taylor & Francis Group, London: 1259-1265.

Ku, T. (2012). Geostatic stress state evaluation by directional shear wave velocities, with application towards geocharacterization at Aiken, SC. *PhD Dissertation*, School of Civil & Environmental Engineering, Georgia Institute of Technology, Atlanta, GA: 380 p.

Ku, T. and Mayne, P.W. (2013a). Evaluating the in-situ lateral stress coefficient (K_0) of soils via paired shear wave velocity modes. *J. Geotechnical & Geoenvironmental Engineering* 139 (5): 775-787.

Ku, T. and Mayne, P.W. (2013b). Yield stress history evaluated from paired in-situ shear moduli of different modes. *Engineering Geology* 152, Elsevier: 122-132.

Ku, T. and Mayne, P.W. (2013c). Profiling of K_0 lateral stress coefficient in soils using paired directional G0 ratios. *Journal of Applied Geophysics* 94, Elsevier: 15-21.

Ladd, C. C., and DeGroot, D. J. (2003). "Recommended practice for soft ground site characterization: The Arthur Casagrande Lecture." Proceedings of the 12th Panamerican Conference on Soil Mechanics and Geotechnical Engineering, Boston, 1-55.

Larrahondo-Cruz J.M. (2011). Carbonate diagenesis and chemical weathering in the southeastern United States: some implications on geotechnical behavior, *Ph.D. Dissertation*, School of Civil and Environmental Engineering, Georgia Institute of Technology, 320 pp.

Lew, M. and Campbell, K.W. (1985). "Relationships between shear wave velocity and depth of overburden," *Measurement and Use of Shear Wave Velocity for Evaluating Dynamic Soil Properties*, ASCE, Reston, Virginia: 63-76.

Lewis, M.R., McHood, M.D. and Arango, I. (2004). Liquefaction evaluations at the Savannah River Site: a case history. *Proc. 5th Intl. Conf. on Case Histories in Geotechnical Engineering*, New York: Paper 3.21; 10 p.

Li, W., Mason, J. and Williams, R. (2010). *Probabilistic seismic hazard assessment available data and current analyses*. Internal Report, Savannah River Nuclear Solutions, Aiken, SC: 37 slides.

Loukidis, D., and Salgado, R. (2009). "Bearing capacity of strip and circular footings in sand using finite elements." Computers and Geotechnics, 36(5), 871-879.

Lunne, T., and Long, M. (2006). "Review of long seabed samplers and criteria for new sampler design." Marine Geology, 226(1–2), 145-165.

Lunne, T., Robertson, P.K., and Powell, J.J.M. (1997). *Cone Penetration Testing in Geotechnical Practice*. Blackie-EF Spon, Rutledge Publishing, London: 318 p.

Mair, R. J. (2008). "Tunnelling and geotechnics: new horizons." Geotechnique, 695-736.

Mair, R. J., Gunn, M. J., and O'Reilly, M. P. (1981). "Ground movements around shallow tunnels in soft clay." Proceedings of 10th International Conference on Soil Mechanics and Foundation Engineering, Stockholm, 1, 323-328.

Mair, R. J., Taylor, R. N., and Bracegirdle, A. (1993). "Subsurface settlement profiles above tunnels in clays." Geotechnique, 43(2), 315-320.

Manoharan, N., and Dasgupta, S. P. (1995). "Bearing capacity of surface footings by finite elements." Computers & Structures, 54(4), 563-586.

Marchetti, S., (1980). "In-situ tests by flat dilatometer," *Journal of Geotechnical Engineering*, ASCE, 107 (3): 832-837.

Marshall, A. M., Farrell, R., Klar, A., and Mair, R. J. (2012). "Tunnels in sands: the effect of size, depth and volume loss on greenfield displacements." Geotechnique, 62(5), 385-399.

Martin, R.E. and Drahos, E. (1986). Calvert clay formation, Richmond, Virginia. *Use of In-Situ Tests in Geotechnical Engineering* (GSP 6), ASCE, Reston, VA.

Mayne, P.W. (1989). Site characterization of Yorktown formation for new accelerator. *Foundation Engineering: Current Principles and Practices* (GSP No. 22), Vol. 1, ASCE, Reston, Virginia: 1-15.

Mayne, P. W., and Kulhawy, F. H. (1982). "k0-OCR relationships in soil." Journal of Geotenical Engineering Division, 108(6), 851-872.

Mayne, P.W., Kulhawy, F.H., and Kay, J.N. (1990). Observations on the development of porewater pressures during piezocone penetration in clays. Canadian Geotechnical J. 27 (4): 418-428.

Mayne, P.W. (2007a). "In-situ test calibrations for evaluating soil parameters," *Characterization and Engineering Properties of Natural Soils*, Vol. 3, Taylor & Francis: 1601-1652.

Mayne, P.W. (2007b). *NCHRP Synthesis 368 on Cone Penetration Test*. Transportation Research Board, National Academies Press, Washington, D.C., 118 pages. Download from: www.trb.org

Mayne, P.W. (2010). Regional report for North America. *Proceedings, 2nd Intl. Symposium on Cone Penetration Testing* (CPT'10, Huntington Beach, California), Vol. 1, Omnipress: 275-312.

Mayne, P.W. (2014). “Generalized CPT method for rvaluating yield stress in soils” *Proceedings GeoCongress 2014*, (Atlanta), ASCE GSP, Reston, VA.

McNulty, G. and Harney, M.D. (2010). Comparison of CPT- and DMT-correlated effective friction angle in clayey and silty sands. *Proc. 2nd Intl. Symposium on Cone Penetration Testing*, Huntington Beach (Omnipress: www.cpt10.com): File 2-53: 8 p.

Meyerhof, G. G. (1963). "Some Recent Research on the Bearing Capacity of Foundations." Canadian Geotechnical Journal, 1(1), 16-26.

Moh, Z. C., Daniel, H. J., and Hwang, R. N. (1996). "Ground movements around tunnels in soft ground." Proceedings of International Symposium on Geotechnical Aspects of Underground Construction in Soft Ground, London, 36-42.

O’ Reilly, M. P., and New, B. M. (1982). "Settlements above tunnels in the United Kingdom: their magnitude and prediction." Proceedings of Tunneling, 173-181.

Pang, C. H., Yong, K. Y., and Dasari, G. R. (2005). "Some considerations in finite element analysis of tunnelling." Proceedings of the International World Tunnel Congress and the 31st ITA General AssemblyIstanbul, Turkey, 7-12 May 2005.

Peck, R. B. (1969). "Deep Excavations and Tunneling in Soft Ground." Proceedings of the Seventh International Conference on Soil Mechanics and Foundation Engineering, 225 - 290.

Potts, D. M. (2003). "Numerical analysis: a virtual dream or practical reality?" Geotechnique, 535-573.

Rajendran, S. (2010). "A technique to develop mesh-distortion immune finite elements." Computer Methods in Applied Mechanics and Engineering, 199(17–20), 1044-1063.

Rinaldi, V. A., and Santamarina, J. C. (2008). "Cemented soils: small strain stiffness." Deformational Characteristics of Geomaterials, 267-274.

Robertson, P.K. (2009). Interpretation of cone penetration tests: a unified approach. *Canadian Geotechnical Journal*, 46 (11): 1337-1355.

Robertson, P.K. and Wride, C.E. (1998). “Evaluating cyclic liquefaction potential using the cone penetration test,” *Canadian Geotechnical Journal*, 35 (3): 442-459.

Rodrıguez-Roa, F. (2000). "Observed and calculated load–settlement relationship in a sandy gravel." Canadian Geotechnical Journal, 37(2), 333-342.

Rodrıguez-Roa, F. (2002). "Ground Subsidence due to a Shallow Tunnel in Dense Sandy Gravel." Journal of Geotechnical and Geoenvironmental Engineering, 128(5), 426-434.

Roscoe, K. H., and Burland, J. B. (1968). On the generalized stress–strain behaviour of wet clay., London: Cambridge University Press.

Rowe, P. W., and Peaker, K. (1965). "Passive Earth Pressure Measurements." Geotechnique, 57-78.

Sakurai, S., and Takeuchi, K. (1983). "Back analysis of measured displacements of tunnels." Rock Mechanics and Rock Engineering, 16(3), 173-180.

Santagata, M., and Germaine, J. (2002). "Sampling Disturbance Effects in Normally Consolidated Clays." Journal of Geotechnical and Geoenviromental Engineering, 128(12), 997-1006.

Santamarina, J. C., and Fratta, D. (2005). Discrete Signals and Inverse Problems: An Introduction for Engineers and Scientists, ASCE Press.

Santamarina, J. C., and Shin, H. S. (2009). "Frictional Phenomena in Granular Media." Batsheva de Rothschild Seminar on Shear Physics at the Meso-scale in Earthquake and Landslide Mechanics.

Schmidt, B. (1969). "Settlements and ground movements associated with tunneling in soil." Ph.D., University of Illinois at Urbana-Champaign.

Schneider, J.A. and Lehane, B.M. (2010). Evaluation of cone penetration test data from a calcareous dune sand. *Proc. 2nd International Symposium on Cone Penetration Testing*, Huntington Beach (Omnipress: www.cpt10.com): File 2-28: 8 p.

Semple, R. (1988). State of the art report on engineering properties of carbonate soils. *Proceedings of the International Conference on Calcareous Sediments*, Perth, Vol. 2: 807-836.

Shannon & Wilson, Inc. (2007). *Geotechnical Engineering Report - Geotechnical Investigation Phase II: Salt Waste Processing Facility*. U.S. Department of Energy, Savannah River Site: 1945 p.

Shin, H. S., and Santamarina, J. C. (2009). "Mineral Dissolution and the Evolution of k0." Journal of Geotechnical and Geoenvironmental Engineering, 135(8), 1141-1147.

SNOC (2008). *Vogtle Early Site Permit Application, Part 2 – Site Safety Analysis Report*, Southern Nuclear Operating Company, Revision 5 (Dec. 2008), 126 p. Reference link location: http://pbadupws.nrc.gov/docs/ML0915/ML091540887.pdf

Sowers, G.F. (1996). *Building on Sinkholes: Design and Construction of Foundations in Karst Terrain*, ASCE Press, Reston/VA: 202 p.

SRNS (2011). "Settlement of the vitrification building at the Defense Waste Processing Facility: K-ESR-S Area." U.S. Department of Energy.

SRS Report (2005). *Compilation of SRS soil shear wave velocity data for soil parameterization model*, Savannah River Site, Aiken, SC: 97p.

Syms, F.H. (2002). Calibration of the electric piezocone penetrometer for predicting sediment character and geologic mapping of Eocene Carolina coastal plain sediments. *PhD Dissertation*. Dept. of Geological Sciences, Univ. of South Carolina: 121 p.

Syms, F.H. (2010). K-Area – Vogtle Geologic Comparative Study: Assessment of 105-K Subsurface Conditions. *Project Report 04.79214* by Fugro-William Lettis & Associates, Augusta, GA to SRS PDC, Aiken, SC: 34 pages.

Terzaghi, K. (1943). Theoretical Soil Mechanics, John Wiley & Sons, New York.

Terzaghi, K., and Richart, R. E. (1952). "Stresses in Rock About Cavities." Geotechnique, 3(2), 57-90.

Terzaghi, K., Peck, R.B. and Mesri, G. (1996). *Soil Mechanics in Engineering Practice*, 3rd edition, John Wiley & Sons, Inc., New York: 549 p.

UniStar Nuclear Services, LLC (UNS) Report. (2010). *Calvert Cliffs Nuclear Power Plant Unit 3, Part 2: Final Safety Analysis Report*. Maryland.

Verruijt, A., and Booker, J. R. (1996). "Surface settlements due to deformation of a tunnel in an elastic half plane." Geotechnique, 753-756.

Vesic, A. S. (1973). "Analysis of ultimate loads of shallow foundations." Journal of Soil Mechanics and Foundation Division, 93(SM3), 45-73.

Vorster, T., Klar, A., Soga, K., and Mair, R. (2005). "Estimating the Effects of Tunneling on Existing Pipelines." Journal of Geotechnical and Geoenvironmental Engineering, 131(11), 1399-1410.

Wang, M. C., and Badie, A. (1985). "Effect of Underground Void on Foundation Stability." Journal of Geotechnical Engineering, 111(8), 1008-1019.

Wang, M. C., and Hsieh, C. W. (1987). "Collapse Load of Strip Footing Above Circular Void." Journal of Geotechnical Engineering, 113(5), 511-515.

Washington Savannah River Company (WSRC). (2007). *Salt waste processing facility (SWPF) dynamic settlement evaluation (U).* United States Department of Energy, Savannah River Site, Aiken, South Carolina.

Wightman, W.E., Jalinoos, F., Sirles, P. and Hanna, K. (2003). *Application of Geophysical Methods to Highway Related Problems*. Contract No. DTFH68-02-P-00083, Federal Highway Administration, Washington, DC: 742 p.

Woodward, P. K., and Griffiths, D. V. (1998). "Observations on the computation of the bearing capacity factor Nγ by finite elements." Geotechnique, 137-141.

WSRC (1999). "Historical review of significant investigations and current understanding of soft zone origin, extent and stability." Project Report, U.S. Department of Energy.

WSRC (2007). "Salt Waste Processing Facility Dynamic Settlement Evaluation." U.S. Department of Energy.

Yun, T., and Santamarina, J. (2005). "Decementation, Softening, and Collapse: Changes in Small-Strain Shear Stiffness in Loading." Journal of Geotechnical and Geoenvironmental Engineering, 131(3), 350-358.